UNIVERSITY OF NOVA GORICA
GRADUATE SCHOOL

MODELLING OF SOLID-SOLID PHASE TRANSFORMATIONS IN ALUMINIUM ALLOYS

DISSERTATION

M.Sc. Igor Kovačević

Mentor: Prof.Dr. Božidar Šarler

Nova Gorica, 2008

Modelling of Solid-Solid Phase Transformations in Aluminium Alloys

M.Sc. I. Kovačević

Abstract

The solid-solid phase transformations during the homogenisation of aluminium alloys are modelled and simulated by the phase-field model. The two-domain approach and the phase-field approach, two distinct physical models, are derived for the simulation of phase transformations in heat treatment processes. A comparison of the phase-field model with the two-domain approach for the validation of both models is performed in one-dimensional geometry. Special attention is paid to the connection of the physical models with thermodynamic database. Thermodynamic conditions on the interphase interface between a stoichiometric or a nonstoichiometric phase and aluminium matrix for physical models are analysed. Isothermal diffusion-controlled dissolutions of the Al_3Mg_2, θ, Al_2CuMg and Mg_2Si phase in the aluminium phase for Al-Mg, Al-Cu, Al-Cu-Mg and Al-Mg-Si systems are computed, respectively. The spheroidisation kinetics of elongated Si-particle is estimated by the phase-field model. The influences of the homogenisation temperature and the interface energy on the spheroidisation kinetics are analysed. The model is applied on the dissolution kinetics of the interdendritic, artificial eutectic phase in the aluminium matrix in Al-Cu alloy. The Gibbs free energy of homogenous eutectic phase is calculated as the heterogeneous mixture of eutectic phases present. The dissolution kinetics of the eutectic phase under the industrial condition of the heating step of homogenisation is estimated. The strong-form local meshfree method is implemented for the solution of governing equations of the phase-field model. The solution procedure based on the local collocation with radial basis functions on the r-adaptive node arrangement for the solution to the involved moving boundary problems is derived.

Keywords:

solid-solid phase transformations, homogenisation, aluminium alloys, physical models, phase-field model, meshfree methods, r-adaptivity

Modeliranje trdno-trdnih faznih sprememb v aluminijevih zlitinah

Mag. I. Kovačević

Povzetek

Z metodo faznega polja modeliramo in simuliramo trdno-trdne fazne spremembe med homogenizacijo aluminijevih zlitin. Razvili smo dvoobmočno metodo in metodo faznega polja za simulacijo faznih sprememb pri toplotni obdelavi. Izdelali smo primerjavo med metodo faznega polja in dvoobmočno metodo za validacijo obeh metod v enodimenzionalni geometriji. Posebno pozornost smo posvetili povezavam fizikalnih modelov z bazo termodinamičnih podatkov. Podrobno smo analizirali termodinamične pogoje na medfaznem robu med stehiometrično ali nestehiometrično fazo in aluminijevo matriko pri obeh metodah. Izračunali smo izotermno difuzijsko kontrolirano raztapljanje Al_3Mg_2, θ, Al_2CuMg in Mg_2Si faz v aluminijevo matriko za Al-Mg, Al-Cu, Al-Cu-Mg in Al-Mg-Si sisteme. Obravnavali smo sferoidizacijo palice čistega silicija z metodo faznega polja. Analizirali smo vpliv temperature homogenizacije in površinske energije na kinetiko sferoidizacije podaljšanega silicijevega delca. Uporabili smo model faznega polja za modeliranje raztapljanja interdendritske, umetne evtektične faze v aluminijevo matriko za zlitino Al-Cu. Gibbsovo prosto energijo evtektične faze smo izračunali kot heterogeno mešanico faz v evtektiku. Izračunali smo raztapljanje evtektične faze pri industrijskih pogojih med časom segrevanja v homogenizacijski peči. Uporabili smo lokalno brezmrežno metodo z močno formulacijo za reševanje vodilnih enačb metode faznega polja. Razvili smo numerični postopek, ki temelji na lokalni kolokaciji z radialnimi baznimi funkcijami za reševanje problemov premičnih robov na podlagi r-prilagodljive porazdelitve točk.

Ključne besede:

trdno-trdno fazne spremembe, homogenizacija, aluminijeve zlitine, fizikalni modeli, model faznega polja, brezmrežne metode, r-prilagodljivost.

Contents

List of Figures

List of Tables

List of Symbols

Latin Symbols

a	activity
a_{φ}^{m}	activity of component m in the phase φ
A	predefined constant in Arrhenius relation
$\mathbf{A}_i$	system matrix for local support of reference node i
$\mathbf{b}_i$	right-hand side vector for reference node i
$\mathcal{B}$	boundary differential operator
c	concentration
$\bar{c}$	shape parameter in multiquadric radial basis function
c_p	specific heat
Δc	concentration difference
$\mathbf{c}$	mixture concentration vector
$\mathbf{c}_{\varphi}$	concentration vector in the phase φ
c_{φ}^{m}	concentration of component m in the phase φ
$\bar{d}$	capillarity length
d	dimension of problem
D	diffusion coefficient
D_0	preexponential constant
$\tilde{\mathbf{D}}_{\varphi}$	interdiffusion coefficient matrix in phase φ
D_{φ}^{m}	diffusion coefficient of component m in the phase φ
F	number of degrees of freedom
f	free-energy density
f_{φ}	free-energy density of the phase φ
F	function
$\mathcal{F}$	total free energy
$\bar{f}_{\alpha}^{\mathrm{m}}$	activity coefficient of component m in the phase φ
g	Gibbs free energy
g_{φ}	Gibbs free energy of the phase φ
g_0^{m}	partial Gibbs free energy of reference state for component m
Δg_{κ}	increase of molar free energy influenced by particle curvature
$\Delta g_{\beta\alpha}$	driving force for phase transformation of phase β to α
Δg	driving force
Δg_{sl}	driving force for freezing
$h(\phi)$	double-well function

h_{ef}	effective heat transfer coefficient
$\vec{i}$	unit vector in x direction
$\vec{j}$	unit vector in y direction
$\vec{J}^{\mathrm{m}}_{\varphi}$	mass flux of component m in phase φ
$\vec{J}$	mass flux
K	solubility product
k	conductivity
$\bar{K}$	parameter related to interface mobility
$\mathbf{K}$	tensor property
$l_{\beta\alpha}$	interface position
l_{Γ}	position of system boundary
L	Onsager coefficient
L_P	length of augmented polynom
L_{M}	latent heat for melting
$\vec{L}$	vector
$\mathcal{L}$	domain linear differential operator
M_{ζ}	positive kinetic coefficient
$M_{\mathrm{S^m}}$	molar mass of element $\mathrm{S^m}$
M_{mix}	local molar mass of mixture
M	number of components
n	variable normal to interface position
$\vec{n}_{\Gamma}$	normal vector on exterior boundary Γ
N	number of points
$\vec{n}_{l}$	vector normal to interface
n_{m}	stoichiometric constant
$\bar{n}$	order of radial basis function
$\bar{N}$	size of matrix
p	pressure
$\vec{p}$	vector position
Δp	pressure difference
P	number of phases
$p\left(\phi\right)$	interpolation function
P	augmented polynomial term
P	prescribed control function
Q_D	activitation energy for diffusion
$Q_{\mu_{\mathrm{k}}}$	activitation energy for interface-kinetic coefficient
Q_{M}	heat absorbed when an one mole of phase β dissolves in phase α
r	distance between node and reference node
r_c	radial cylindrical coordinate
r_{κ}	radius of particle
R	universal gas constant
$\bar{R}_i$	support radius in compact support radial basis function
$\Re$	set of real numbers
s	interpolation form
$\mathbf{S}$	data set
$\mathrm{S^m}$	chemical component of species m

S	source term
s_i	solid phase in eutectic reaction
t	time
Δt	time-step length
time	final time
$\tilde{t}_D$	diffusion time
T	temperature
T_A	surrounding air temperature
T_S	surface temperature
T_{M}	melting temperature
T_0	initial temperature
ΔT	undercooling
u	unknown field
V_{m}	molar volume
$\vec{v}$	velocity
V	volume of domain
V_{FTM}	value computed by the front-tracking method
V_{PFM}	value computed by the phase-field model
$\bar{x}$	molar fraction
X	molar concentration
X_{φ}^{m}	molar concentration of component m in phase φ
Δx	discretization distance
Δx_{in}	discretization distance mesh in the interface region
Δx_{out}	discretization distance mesh out the interface region
x	horizontal Cartesian coordinate
y	vertical Cartesian coordinate
Δy	discretization distance
z	axial cylindrical coordinate
w_l	basis of polynomial
w	height of energy hump

Greek Symbols

α	phase
β	phase
γ	function
$\bar{\gamma}$	free parameter in Gaussian radial basis function
Γ	boundary of domain
Γ_u	part of the boundary where Dirichlet boundary condition is defined
Γ_d	part of the boundary where derivative boundary conditions are defined
δ	interface thickness
δ_n	transition zone thickness
Δ	relative difference between numerical results
ϵ	convergence criteria

ε_ζ	energy gradient coefficient
η	transformation coordinate
ζ	order parameter
θ	angle
ρ	density
ϱ	general coordinate for transformation coordinate ξ, η
σ	interface energy
σ_n	function for controlling node distribution
σ_n'	the norm for controlling node distribution
ς	coefficient for radial basis function interpolation
$\boldsymbol{\varsigma}$	coefficient vector for radial basis function interpolation
κ	mean curvature
$\bar{\kappa}$	control function
κ_1, κ_2	principal curvature
λ	measure of interface thickness
μ	chemical potential
$\mu_{\varphi}^{\mathrm{m}}$	chemical potential of component m in the phase φ
μ_{k}	interface-kinetic coefficient
$\Delta\mu$	chemical potential difference
ξ	transformation coordinate
$\Delta\xi$	discretization transformation coordinate distance
ϕ	phase-field variable
Φ	local diffusion potential
$\mathbf{\Phi}$	interpolation matrix
φ	phase
$\bar{\varphi}$	complement phase of the phase φ
χ	general coordinate for Cartesian coordinate x, y
ψ	radial basis function
Ω	domain

Subscripts

Al	Aluminium phase
bulk	bulk phase
c	value related to concentration
eq	equilibrium
Eu	eutectic
i	interface mobility
I	interface
int	interface region
Liq	liquid
max	maximum value
min	minimum value
n	normal component

n_{m}	stoichiometrc constant
α	phase
β	phase
Γ_d	part of the boundary where derivative boundary conditions are defined
Γ_u	part of the boundary where Dirichlet boundary condition is defined
ϕ	value related to phase-field variable
φ	general phase
κ	curvature
μ_{k}	value related to interface-kinetic coefficient
Ω	domain

Superscripts

0	reference node
A	component A
B	component B
ch	chemical
d	spacial dimension
h	homogenous
k	previous time step
$k+1$	new time step
m	general component m
n	new iteration
st	stoichiometric phase

Acronyms

CS	compact support
DC	diffusion-controlled
FCC	face-centred cubic crystal structure
FDM	finite difference method
FTM	front-tracking method
GRBFCM	global radial basis function collocation method
IC	interface-controlled
MFM	meshfree method
MQ	multiquadric
LRBFCM	local radial basis function collocation method
PDE	partial differential equation
PFV	phase-field variable
PFM	phase-field model
RBF	radial basis function
TDA	two-domain approach
TPS	thin-plate spline

1 Introduction

Investigations of phase transformations in materials science and engineering are of great importance for the quality of final metal products. Most metals used for technical applications are alloys, mixtures composed of several chemical components. Aluminium alloys, a spectrum of alloys based on aluminium, have had an increasingly wide application in recent times. Phase transformations take place at various points throughout the materials processing of aluminium alloys. If the magnitude of phase change occurs at the micrometer scale, we are talking about a micro level; consequently, the structure is called microstructure. The microstructure has a big influence on mechanical properties of alloys. During the alloy casting, various particles grow in a very complex morphology and in non-uniform concentrations, in a phenomenon named microsegregation. Particles have varied crystal lattices; therefore their metallurgical and mechanical properties are different. In the present context, a phase represents a segment of a system with the same crystal lattice.

After casting, solution heat treatment is often necessary to optimize the mechanical properties of aluminium alloys for the following mechanical treatment processes. The main goal of this heat treatment is to homogenize the alloy elements (components) into aluminium grains, therefore the process is referred to as *Homogenisation*. Under the heat treatment, the metallurgical state of the alloys changes. This change either involves the creation of phases and/or the morphology of the various phases. The maximum temperature at which the annealing should take place can be determined from a thermodynamic analysis of the phases present. Another important process parameter is the minimum annealing time. The homogenisation time is not constant, and depends on the composition of the alloy, the characteristics of the phases present, the size and morphology of the particles, etc. Whereas the equilibrium phases can often be predicted quite accurately from computational thermodynamic models, presently, there are neither general models for microstructural changes nor general models for the kinetics of these transformations.

The basic goal of this presented thesis is to model the solid-solid phase transformations during heat treatment processes, especially during the homogenisation of aluminium alloys. These phase transformations, or in mathematical terminology, phase-change problems, belong to a wide spectrum of moving boundary problems. Many different physical models have been derived to solve moving boundary problems. In the context of simultaneously solving the phase transformations for a complex morphology, a phase-field model has been derived. The main advantage of the phase-field model is its excellent ability to mathematically describe complex problems such as those usually seen for microstructure topology. In general, the phase-field model belongs to the group of one-domain approaches, where the same governing equations hold over the whole domain. A great advantage of the one-domain approaches is the possibility of using the fixed mesh numerical schemes throughout computation. The major drawback of the phase-field model is the current lack of knowledge of the physical parameters involved. In two-domain approaches, the governing equations are solved separately in every domain occupied by a phase. Due to the capture of the moving boundary position, the moving grid or the front-tracking numerical schemes have to be used. These numerical procedures are difficult to implement in a complex multidimensional geometry.

Phase transformation modelling is closely related to thermodynamic data. Several thermodynamic quantities must be incorporated into physical models. The thermodynamic data for a specific alloy are obtained from software which calculates phase diagrams, and the data are then collected in a thermodynamic database.

Mathematical models of physical phenomena are described by a set of partial differential equations. In most cases, the solution needs to be found by a numerical computation. Partial differential equations can be solved using the finite difference, finite element, finite volume or boundary element methods, to name a few. These methods belong to the spectrum of classical numerical methods, and they require the definition of a mesh (domain and boundary discretization) where the functions are approximated locally. A number of meshfree methods have been developed to circumvent the problem of polygonisation encountered in the classical numerical methods. In meshfree methods, the discretization is constructed on a set of nodes only.

The local collocation with radial basis functions, a representative of meshfree strong-form methods, was derived several years ago. This method is truly meshfree, very simple and easy to implement for solving various differential equations. The method introduces the local support of each domain and boundary node. The field approximation and its partial derivatives in the domain and on the boundary are obtained by using a small set of the radial basis functions with centres in the local support of the reference node where the solution needs to be found.

Searching for an appropriate numerical procedure for the mathematical modelling of phase-change problems is very important. Solving the partial differential equations obtained from the phase-field model by the meshfree methods is an interesting, challenging task. In particular, the possibility of using meshfree methods for numerical computations of adaptive node arrangements is closely related to the moving boundary problems.

1.1 Heat Treatment Processes in the Production of Aluminium Alloys

The basic idea of heat treatment processes is the formation of a non-equilibrium microstructure at room temperature. This condition is established by holding the alloy for some time at an increased temperature, followed by rapid cooling. The phase distribution of an alloy depends on temperature. The annealed temperature can be determined from thermodynamic analysis of the phases present [Ragone, 1992]. Kinetics of materials [Ballufi *et al.*, 2005], a rapidly growing branch of materials science and engineering, tries to answer the question of how much time the heat treatment process must last to establish a desired microstructure. The computational description of phase transformation kinetics is an important step towards a better understanding of microstructure changes during heat treatment.

Two basic heat treatment processes are well established in heat-treatable aluminium alloy production: homogenisation and age-hardening [aluMATTER, 2007]. The primary particles formed during casting are attempted to be dissolved into the aluminium phase during homogenisation, because the pure aluminium phase with a Face-Centred Cubic (FCC) crystal lattice has very high ductility and formability. Such a heat-treated semi-product is well-prepared for subsequent mechanical treatment. The homogenisation occurs at approximately 500 °C or even higher temperatures and thus is a high-temperature treatment. When the final shape of the product is formed, its strength is adapted to the required application by the age-hardening treatment. The age-hardening treatment propagates precipitation in order to significantly increase the final product strength. This heat treatment occurs at approximately 200 °C, and is a low-temperature treatment. The temperature profile during the production of the extruded aluminium products is presented in Fig.(1.1).

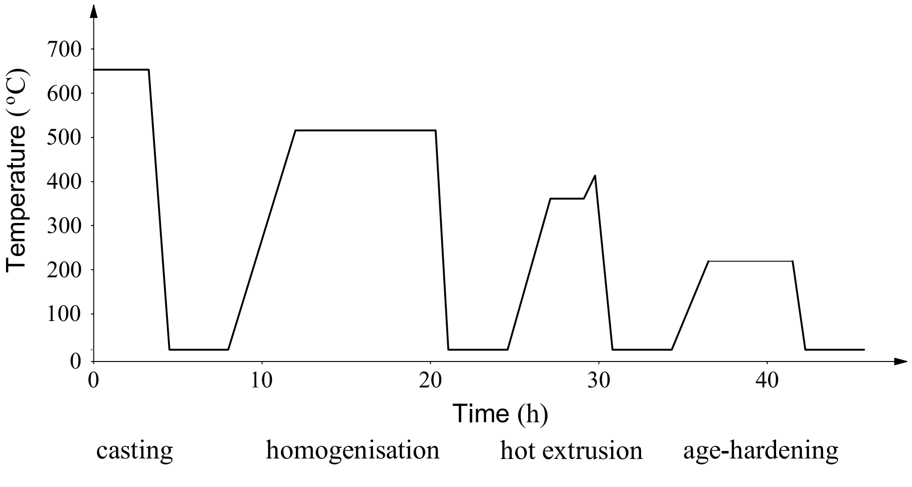

Figure 1.1: Time-temperature diagram of the processing of aluminium alloys [Pérez, 2006].

1.1.1 Homogenisation

The homogenisation follows the casting process. During casting, several primary particles are solidified in the interdendritic region between the aluminium grains. The industrial solidification is so fast that there is little time for the diffusion of alloying elements in the aluminium phase, because the solid solution of the aluminium phase is strongly supersaturated at room temperature after casting. The purpose of homogenisation is to [Dons, 2001]:

- dissolve Cu, Mg, Si - bearing particles,
- obtain a uniform distribution of alloying elements in the aluminium phase,
- remove particles and segregation gradients that will lead to areas with low melting temperatures,
- spheroidisate undissolvable particles and
- nucleate the secondary particles.

The secondary particles nucleate during the homogenisation [Li and Arnberg, 2003]. The secondary particles or dispersoids usually nucleate on the grain boundaries, because of the heterogeneous nucleation. They control the grain size during further mechanical treatment, for example extrusion or rolling.

Homogenisation of aluminium alloys is a three-step process consisting of heating, holding at the homogenisation temperature and subsequent cooling. When the heating starts at the room temperature, the solid solution is supersaturated. The major phase transformations during the heating step are nucleation and precipitation of secondary particles. During the holding time, the major phase transformation is the dissolution of primary Cu, Mg, Si - bearing particles. Other important reactions are the coarsening of dispersoids, spheroidisation of undissolvable primary particles, transformation of Mn, Fe - bearing particles from one phase to another, and the smoothing of the concentration gradients in aluminium grains. The cooling after the holding time occurs as quickly as possible in order to prevent the nucleation and precipitation of Mn, Fe, Si - bearing particles. For the fast cooling step, the term quenching is usually preferred [Kammer, 1999].

The as-cast and as-homogenised micrographs of Al-5 wt%Cu alloy, obtained from the Slovenian aluminium company IMPOL, d.d., are presented in Fig.(1.2). The interdendritic eutectic network in the as-cast micrograph is represented by the darker colour (left in Fig.(1.2)). This network has a strong negative influence on the ductility, and the basic purpose of homogenisation of this alloy is the dissolution of this phase [Mondolfo, 1976]. The copper-rich phase is evenly distributed in the form of particles in the as-homogenised micrograph (right in Fig.(1.2)).

The most important homogenisation parameters are the homogenisation temperature and time. For economic reasons, industrial heat treatments should be as short as possible and occur at the lowest possible temperature. The homogenisation is extremely time and energy consuming, and there is a substantial potential for its optimisation. The estimation of the phase transformation kinetics provides a better insight for controlling and optimizing this process.

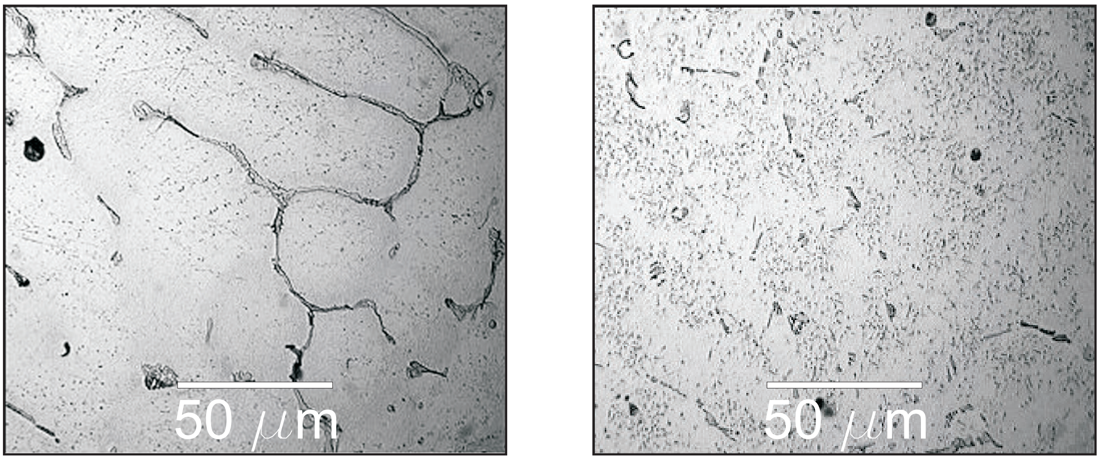

Figure 1.2: The as-cast and as-homogenised micrograph of Al-5 wt%Cu alloy at billet centre obtained from the Slovenian aluminium company IMPOL, d.d..

1.2 Literature Review

The literature review focuses on the modelling of phase transformations in the solid phase during heat treatment processes. In particular, the phase-field model is analysed in more detail as a tool for the modelling of solid-solid phase transformations in complex geometries. A numerical procedure based on the meshfree methods for solution of the phase-field model is developed. This thesis is founded on the following literature, separated into three research areas: modelling of phase transformations, the phase-field model and the meshfree methods.

1.2.1 Modelling of Phase Transformations

A basic literature survey on the subject of heat treatment processes in alloys can be found in the textbook [Callister, 2003]. The influence of alloying elements on the microstructure morphology and its influence on the properties of aluminium alloys are described in [Mondolfo, 1976]. The influence of the homogenisation of various aluminium alloys on microstructure is elaborated in [Sheppard, 1999]. [Mondolfo, 1976; Sheppard, 1999] can be a good starting literature for understanding what is the purpose of the homogenisation of aluminium alloys. [Kostorz, 2001; Jackson, 2004] focus on phase transformations in materials. A specialized study of phase transformations in metals and alloys are available in [Porter and Easterling, 1990]. The comprehensive textbook [Porter and Easterling, 1990] is a basic tool for understanding phase transformations in general. The microstructural phenomena in metallic systems are explained in [Matrin *et al.*, 1997]. The basic thermodynamics and kinetics of solid-solid interfaces are described in [Howe, 1997]. The theory of structural transformations in solids is described in [Khachaturyan, 1983]. Principles of diffusion in solids are described in [Glicksman, 2000]. A mathematical description of diffusion is available in [Crank, 1995].

Phase transformations are closely related to phase equilibria and phase diagrams [Hillert, 1998], which are related to the thermodynamics of materials [Ragone, 1992; DeHoff, 1993]. Today, thermodynamic data are obtainable from specific calculation phase diagrams (CALPHAD) software. The most well known and frequently used thermodynamic databases are Thermocalc [Thermocalc, 2007] and MTDATA [MTDATA, 2007]. The thermodynamic data in this thesis are obtained from the recently developed JMatPro software for aluminium alloys [JMatPro, 2007].

The modelling of phase transformations in heat treatment process began approximately forty years ago. The process is very complex, and a general physical and mathematical description has still not been developed. A mathematical description leads to the class of moving boundary problems. Many numerical methods for the solution of moving boundary problems can be found in [Crank, 1984]. Dissolution of particles in binary Al-Cu alloys described by the two-domain approach is found in [Aaron and Kotler, 1971]. The diffusion-controlled phase transformation in ternary alloys is presented in [Vitek *et al.*, 1995], in connection with a thermodynamic database, and solved by the moving grid method. A front-tracking method for phase transformation is presented in [Jacot and Rappaz, 1997]. This model is used for the description of austenitisation, homogenisation and grain growth in steels [Jacot and Rappaz, 1999], and solidification microstructures in multicomponent alloys [Jacot and Rappaz, 2002].

The model for the dissolution of stoichiometric particles in ternary aluminium systems during homogenisation based on the two-domain approach is presented in [Vermolen *et al.*, 1998a]. This model is implemented for dissolution kinetics under industrial conditions in [Vermolen *et al.*, 1998b]. The model [Vermolen *et al.*, 1998a] is extended for multicomponent systems in [Vermolen *et al.*, 2002], and the numerical procedures for solving the mathematical model are described in [Vermolen and Vuik, 1998; Vermolen and Vuik, 2000]. Later, the one-domain level set method was used to solve the same physical problem in [Javierre *et al.*, 2007; Vermolen *et al.*, 2007].

Also, many scientific papers are available in the literature which give an experimental treatment of the homogenisation of aluminium alloys. A few of these studies are listed here covering the dissolution kinetics of second particle in Al-Cu alloy [Baty *et al.*, 1970], the effect of solution heat treatment and quenching rates on Mg_2Si coarsening [Usta *et al.*, 2004], and the mechanical properties of Al-Si-Mg foundry alloys [Pedersen and Arnberg, 2001] and solid-solid intermetallic phase transformation in Al-Mn-Fe [Alexander and Greer, 2002].

1.2.2 Phase-Field Model

Today, one of the most frequently used models for describing phase transformations is the phase-field model. The applications of the phase-field model have expanded very quickly, so a comprehensive literature review of the model is difficult. Solidification is the most attractive application of the phase-field model, and it is used in solidification in binary alloys in [Boettinger *et al.*, 2002]. The concepts, applications, difficulties and perspectives of the model for multiphase solidification in multicomponent alloys are summarized in [Hechta *et al.*, 2004].

The phase-field model for isothermal phase transformation in binary alloys is developed in [Wheeler *et al.*, 1992]. The phase-field model is extended for anisotropic interfaces in [McFadden *et al.*, 1993]. The first numerical implementations of the model were the grain growth simulations [Warren and Boettinger, 1995; Karma and Rappel, 1998]. The influence of convection in liquid on the dendrite shape is presented in [Beckermann *et al.*, 1999]. In the model [Wheeler *et al.*, 1992], singe continuous concentration is defined in the diffuse-interface region, because the free energy density of the alloy is extrapolated as a mixture of the free energies of the pure materials. This model has serious disadvantages in applied numerical simulations, because interface contributions do not allow scaling with the interface thickness independently of other parameters, which is necessary for application at the thin interface limit.

The multiphase-field model is derived to model phase transformations in multiphase systems in [Steinbach *et al.*, 1996; Steinbach and Pezzolla, 1999]. An integrated concept of the multiphase-field model with solute diffusion is derived in [Tiaden *et al.*, 1998]. In this model, the interface region is assumed to be a mixture of solid and liquid with different concentrations, but the phase fraction is held constant. There is no limit on the interface thickness for numerical application. This concept is applied for modelling eutectic and peritectic solidification [Tiaden, 1999; Nestler and Wheeler, 2000], and the solid-solid phase transformations in steel [Pariser *et al.*, 2001].

The different definition of free-energy density in the diffuse-interface region in binary alloys is presented in [Kim *et al.*, 1999]. The phase diffusion potentials in both phases are locally equal in the diffuse-interface region. This model is extended for multicomponent alloys in [Cha *et al.*, 2001; Cha *et al.*, 2005]. The multiphase-field with this constraint in the diffuse-interface region was presented recently in [Eiken *et al.*, 2006].

Over the last few years, a major research focus has been the coupling of the phase-field model with a thermodynamic database. The phase-field model is integrated with the CALPHAD software Thermocalc in [Grafe *et al.*, 2000] and with MTDATA in [Qin and Wallach, 2003].

The incorporation of elastic strain energy in the phase-field model for solid-solid phase transformations is another challenging task for phase-field research. The two papers with incorporated elastic strain energy in the phase-field model are listed here [Steinbach and Apel, 2006; Yeon *et al.*, 2005].

Connection of the phase-field model with the JMatPro software for computation of the dissolution of primary particles in binary Al-Cu alloys is demonstrated in [Kovačević and Šarler, 2004]. Concentration in phases with a constant phase fraction between them in the diffuse-interface region is implemented in the model. Later, an effective way of computing the constraint that phase diffusion potentials are equal was presented in [Kovačević and Šarler, 2006b]. The numerical results for the isothermal diffusion-controlled dissolution of stoichiometric and nonstoichiometric primary particles in binary and multicomponent aluminium systems computed by the phase-field model and the two-domain approach are compared in [Kovačević and Šarler, 2006b]. Dissolution of Mg_2Si and Si particles in the Al-Mg-Si system described by the multiphase-field model is demonstrated in [Kovačević and Šarler, 2006c]. The dissolution of the artificial eutectic phase in binary Al-Cu alloy during homogenisation is presented in [Kovačević and Šarler, 2006a].

1.2.3 Meshfree Methods

The spectrum of meshfree methods along with their application in different solid and fluid dynamics problems are collected and demonstrated in [Liu, 2003]. Their basic programming principles are described in [Liu and Gu, 2005]. A detailed summary of research on meshless methods in solid and fluid mechanics, especially for the weak-form meshfree methods, is presented in [Atluri, 2004].

A class of strong-form meshfree methods is based on collocation with radial basis functions. Kansa used radial basis functions for a scattered data interpolation [Kansa, 1990a], and afterwards for a solution of the partial differential equations [Kansa, 1990b]. The global radial basis function collocation method is successfully applied in many scientific and engineering disciplines. It was initially used in a heat-transport context for diffusion problems [Zerroukat *et al.*, 1998], and later for advection-diffusion problems in [Zerroukat *et al.*, 2000]. The method has been applied to the solution of Navier-Stokes equations [Mai-Duy and Tran-Cong, 2001], the natural convection problem [Šarler *et al.*, 2001], and the steady natural convection problem with a free boundary associated with the solid-liquid phase change [Perko *et al.*, 2001]. The solutions of the Stefan problem and the temperature field in direct-chill cast slabs and billets with the radial basis function collocation method are presented in [Kovačević *et al.*, 2003] and [Kovačević *et al.*, 2004], respectively. A comparative analysis between unsymmetric and symmetric radial basis function collocation methods for the numerical solution of partial differential equations is presented in [Power and Barraco, 2002].

Local multiquadric collocation for solving boundary value problems is developed in [Lee *et al.*, 2003]. The local radial basis function differential quadrature method and its application to solve two-dimensional incompressible Navier-Stokes equations is presented in [Shu *et al.*, 2003]. The local radial basis function collocation method is presented as a solution for diffusion problems in [Šarler and Vertnik, 2006] and for convective-diffusive solid-liquid phase change problems in [Vertnik and Šarler, 2006]. The solution of the phase-field model for the dissolution of primary particles in binary aluminium alloys on an r-adaptive meshfree method is presented in [Kovačević and Šarler, 2005]. Error estimation of the local multiquadric collocation method throughout numerical experiments is presented in [Ding *et al.*, 2005].

1.3 Thermodynamic Background of Phase Transformations

Basic thermodynamic knowledge is necessary to model phase transformations. The Gibbs phase rule and the thermodynamic equilibrium state, essential for phase transformation modelling, are briefly explained here. The influence of the capillarity effect and the interface mobility on the interface condition obtained from the thermodynamic equilibrium state are explained later.

1.3.1 The Gibbs Phase Rule

The number of degrees of freedom F in a thermodynamic system depends on the number of components M and the number of phases P:

$$\mathrm{F} = \mathrm{M} - \mathrm{P} + 2. \tag{1.1}$$

The solid-solid phase transformations in the heat treatment processes usually occur at constant pressure. If the pressure is maintained constant, then one degree of freedom is lost and the Gibbs phase rule becomes

$$\mathrm{F} = \mathrm{M} - \mathrm{P} + 1. \tag{1.2}$$

If the two-phase system is considered ($\mathrm{P} = 2$), the number of degrees of freedom is

$$\mathrm{F} = \mathrm{M} - 1. \tag{1.3}$$

Therefore, the number of degrees of freedom in isobaric two-phase systems is $\mathrm{F} = 1$ in a binary system ($\mathrm{M} = 2$), $\mathrm{F} = 2$ in a ternary system ($\mathrm{M} = 3$), $\mathrm{F} = 3$ in a quaternary system ($\mathrm{M} = 4$), etc.

When three phases in a binary system are in thermodynamic equilibrium, there are no degrees of freedom and the compositions of the phases and the temperature of the system are uniform. Three phases in binary alloys occur during an eutectic or peritectic reaction where the liquid phase exists or during an eutectoid or peritectoid reaction in the solid state.

1.3.2 Thermodynamic Equilibrium State

The Gibbs free energy of the phase φ in a multicomponent system with M components is

$$g_\varphi = \sum_{\mathrm{m}=1}^{\mathrm{M}} X_\varphi^{\mathrm{m}} \mu_\varphi^{\mathrm{m}}, \tag{1.4}$$

where X_φ^{m} and μ_φ^{m} represent the molar composition and chemical potential of component m in the phase φ, respectively[1].

The thermodynamic equilibrium state in a two-phase α-β system is established when the chemical potentials of each component in the system are equal in both phases [DeHoff, 1993], i.e.,

$$\mu_\alpha^{\mathrm{m}} = \mu_\beta^{\mathrm{m}}; \quad \mathrm{m} = 1, 2, \dots, \mathrm{M}. \tag{1.5}$$

The number of conditions obtained from the thermodynamic equilibrium state is equal to the number of the components in the system, M.

The chemical potential, expressed in terms of the activity a_φ^{m}, is

$$\mu_\varphi^{\mathrm{m}} = g_0^{\mathrm{m}} + RT \ln a_\varphi^{\mathrm{m}}, \tag{1.6}$$

where g_0^{m}, R and T represent the partial Gibbs free energy of the reference state for component m, the universal gas constant and temperature, respectively. The thermodynamic equilibrium state can also be written in terms of activities as

$$a_\alpha^{\mathrm{m}} = a_\beta^{\mathrm{m}}; \quad \mathrm{m} = 1, 2, \dots, \mathrm{M}. \tag{1.7}$$

The thermodynamic equilibrium state of a binary A-B two-phase α-β system is presented on a the molar free energy versus concentration diagram in Fig.(1.3). In this figure, the equilibrium chemical potentials of components A and B in both phases are denoted by $\mu_{\mathrm{eq}}^{\mathrm{A}}$ and $\mu_{\mathrm{eq}}^{\mathrm{B}}$, respectively. The chemical potential of the components in both phases are equal, i.e.,

$$\mu_\alpha^{\mathrm{A}} = \mu_\beta^{\mathrm{A}} = \mu_{\mathrm{eq}}^{\mathrm{A}}, \quad \mu_\alpha^{\mathrm{B}} = \mu_\beta^{\mathrm{B}} = \mu_{\mathrm{eq}}^{\mathrm{B}}. \tag{1.8}$$

Equilibrium component concentrations in both phases are obtained by the common tangent line construction.

1.3.3 Capillarity Effect

The interface condition obtained from the thermodynamic equilibrium state neglects the interface shape. The interface curvature shifts the interface condition from the thermodynamic equilibrium. The spherical particle β exerts an extra local pressure in comparison with the phase α, because of the particle curvature. If the interface energy and the mean curvature of the interface are denoted as $\sigma\,[\mathrm{J/m^2}]$ and $\kappa\,[1/\mathrm{m}]$, respectively, then the pressure difference is

$$\Delta p = 2\sigma\kappa. \tag{1.9}$$

The mean curvature of the interface is defined as

$$\kappa = \frac{(\kappa_1 + \kappa_2)}{2}, \tag{1.10}$$

---

[1] The superscript and subscript denote a component and a phase, respectively.

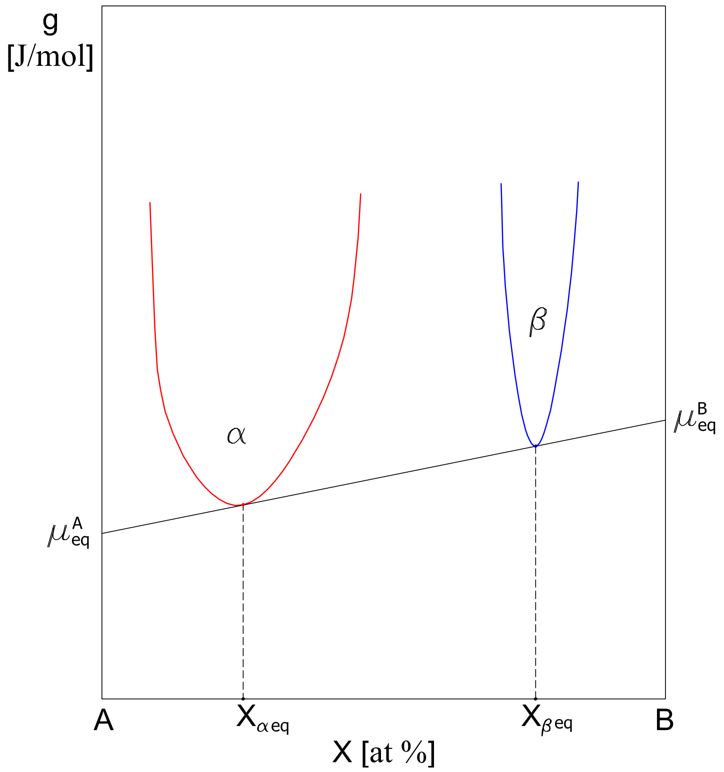

Figure 1.3: The thermodynamic equilibrium state for a binary two-phase α-β system.

where κ_1 and κ_2 are the principal interface curvatures. For two-dimensional geometry, the mean curvature is inversely proportional to the curvature radius r_κ

$$\kappa = \frac{1}{r_\kappa}\,. \tag{1.11}$$

The increase of local pressure causes an increase of the molar free energy of the particle β by

$$\Delta g_\kappa = 2\sigma\kappa V_\mathrm{m}, \tag{1.12}$$

where V_m [m^3/mol] is the molar volume of the phase β. Here, we assume that the phase β is a pure, incompressible component. The curvature effect on the molar free energy versus concentration diagram is depicted in Fig.(1.4). The free energy increase due to the interface curvature is known as the capillarity effect or the Gibbs-Thomson effect. The departure from the equilibrium chemical potential because of the interface curvature is

$$\Delta\mu_\kappa = \mu^\mathrm{B}_\kappa - \mu^\mathrm{B}_\mathrm{eq} = RT\ln\frac{a^\mathrm{B}_\kappa}{a^\mathrm{B}_\mathrm{eq}} = 2\sigma\kappa V_\mathrm{m}. \tag{1.13}$$

The solubility of component B in the phase α shifted by the interface curvature is

$$X_{\alpha\kappa} = X_{\alpha\mathrm{eq}}\exp\left(\frac{2\sigma\kappa V_\mathrm{m}}{RT}\right), \tag{1.14}$$

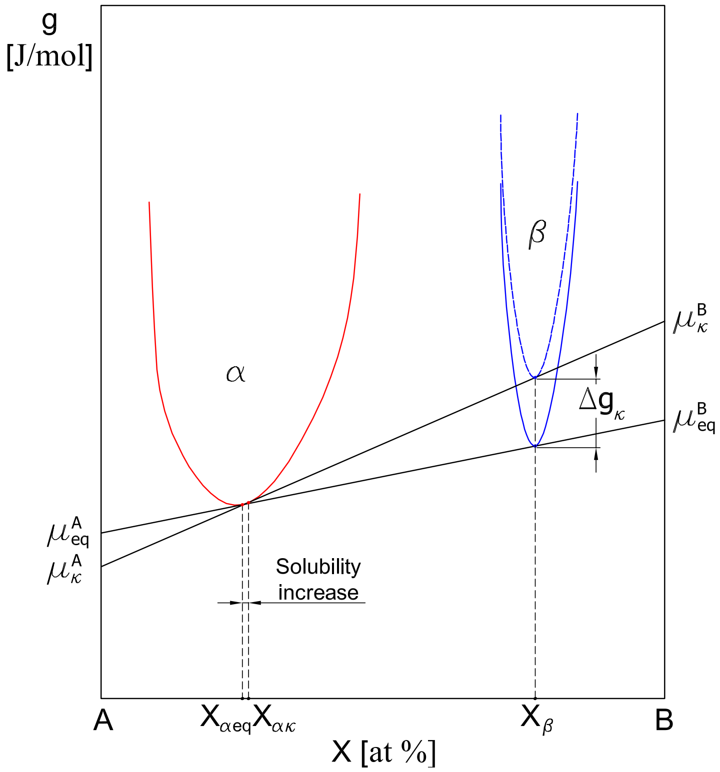

Figure 1.4: The influence of the interface curvature on the thermodynamic equilibrium state [Glicksman, 2000].

where it is assumed that the phase α is a dilute solution[2]. The solubility is shifted by

$$X_{\alpha\kappa} \approx X_{\alpha\mathrm{eq}} \left(1 + \frac{2\sigma V_\mathrm{m}}{RTr_\kappa}\right) = X_{\alpha\mathrm{eq}} \left(1 + \frac{\bar{d}}{r_\kappa}\right); \quad \bar{d} = \frac{2\sigma V_\mathrm{m}}{RT}, \tag{1.15}$$

where the capillary length $\bar{d}$ is introduced.

The interphase interface is extremely important for the early stage of growth when the phase β is in the form of fine precipitates embedded in the matrix α. The solubility changes with curvature influence the precipitation interaction. The enhanced solubility of fine particles leads to the growth of the larger particles at the expense of the smaller in a process known as coarsening or Ostwald ripening. The free energy of the two-phase system decreases with the decrease of the interface area. Also, the enhancement of solubility by the curvature is the driving force for the rounding of elongated (needle-shape) particles.

---

[2] In the binary A-B system, the superscript B on mass or molar concentration is omitted.

1.3.4 Interface Mobility

The departure of chemical potential from the thermodynamic equilibrium state influenced by the interface mobility is

$$\Delta\mu_{\mathrm{i}} = \mu_{\mathrm{i}}^{\mathrm{B}} - \mu_{\mathrm{eq}}^{\mathrm{B}} = \frac{v_n V_{\mathrm{m}}}{\mu_{\mathrm{k}}}\,, \tag{1.16}$$

where the interface-kinetic coefficient μ_{k} [m^4/Js] is introduced, and v_n [m/s] represents the velocity component normal to the interface. The magnitude of the normal component velocity is positive in the example of the growth of the phase β, and negative in the example of dissolution. The interface-kinetic coefficient quantifies the interface mobility. The solubility in the phase α, including the influence of interface mobility is

$$X_{\alpha\mathrm{i}} = X_{\alpha\mathrm{eq}} \exp\left(\frac{\Delta\mu_{\mathrm{i}}}{RT}\right) \approx X_{\alpha\mathrm{eq}}\left(1 + \frac{\Delta\mu_{\mathrm{i}}}{RT}\right). \tag{1.17}$$

If the interface mobility is very high, then the chemical potential departure $\Delta\mu_{\mathrm{i}}$ is very small, and the solubility is approximately equal to the solubility in the thermodynamic equilibrium state, $X_{\alpha\mathrm{i}} \approx X_{\alpha\mathrm{eq}}$. Under these circumstances, the interface moves as quickly as diffusion allows, and the phase transformation occurs in the diffusion-controlled mode. When the interface mobility is lower, a greater difference in chemical potential is required to drive the interface reaction, and the phase transformation occurs in the mixed-controlled mode. At the limit of a very low mobility, it is possible that the solubility is equal to the initial composition. This phase transformation is said to be in the interface-controlled mode, and a maximum possible driving force $\Delta\mu_{\mathrm{i}}$ exists across the interface [Porter and Easterling, 1990].

The interphase interface type influences the interface mobility. If the interface is incoherent, then atom transfer across the interface is easier. The presence of good atomic fit across the interface (coherent interface) poses a significant growth barrier for atom transfer across the interface.

1.4 Objectives of the Thesis

The following objectives are addressed in this thesis:

- Development of a general physical model to simulate solid-solid phase transformations at the micro level during the homogenisation of aluminium alloys. Realization of the model using the phase-field model, and coupling of the model with JMatPro software as a thermodynamic database for aluminium alloys. The model is to use at least three alloying elements.

- Validation of the model realized through the phase-field model by comparison with the two-domain approach. Explanation of the difference in the premises of the mentioned models through computed results. Analysis of the influence of the physical and model parameters on the accuracy and stability of the results.

- Implementation of the local collocation with the radial basis function as a numerical procedure for the solution of the phase-field model. Analysis of the stability and applicability of using the meshfree method in the phase-field model. Comparison of the results computed by the classical numerical scheme and the meshfree method.
- Investigation of the influence of homogenisation parameters on the microstructure and phase behaviour.

1.5 Outline of the Thesis

Chapter 2 deals with the physical models for solid-solid phase transformations. The two-domain approach and the phase-field approach for the description of phase transformations in the solid state are explained, and advantages and drawbacks of the models are pointed out.

Chapter 3 is devoted to the solution procedures used in this thesis. The front-tracking method for the solution of the two-domain approach and the classical finite difference method for the solution of the phase-field model are described. Also, the local strong-form meshfree method on r-adaptive node arrangements for the solution of moving boundary problems are explained. The procedure for very accurate computation of the driving force for phase transformations in multicomponent systems simulated by the phase-field model is demonstrated.

Chapter 4 focuses on the dissolution of primary particles in different aluminium systems. The numerical results computed by the two different physical models are compared for validation of the models. The influence of model parameters used in the phase-field model on the results are analysed and commented. The capability of the phase-field model for simulation of a complex topology is demonstrated. The numerical results computed by the local collocation with radial basis functions for the solution of the phase-field model are also provided.

Spheroidisation of the elongated Si-particle simulated by the phase-field model is demonstrated in Chapter 5. The influences of the interface energy and temperature on the rounding kinetics are simulated, and the influence of interface energy anisotropy on the particle shape is provided at the end of this chapter.

Chapter 6 focuses on the application of the phase-field model for simulation of the homogenisation of commercial Al-Cu alloys. This application concentrates on the dissolution kinetics of the interdendritic eutectic phases into the aluminium matrix.

Finally, Chapter 7 summarizes the conclusions of this thesis and further developments.

A list of the phase transformation examples computed in this thesis is presented in Tab.(1.1).

Table 1.1: List of examples computed in the presented thesis.

Description of Phase Transformation	System	Physical Model	Numerical Procedure	Geometry	Page
Chapter 4					
Dissolution of Al_3Mg_2 in Al phase	Al-Mg	Two-Domain Approach	Finite-Difference Method	1D	(94)
		Phase-Field Model			
Dissolution of θ in Al phase	Al-Cu	Two-Domain Approach	Finite-Difference Method	1D	(95)
		Phase-Field Model			
Dissolution of Mg_2Si in Al phase	Al-Mg-Si	Two-Domain Approach	Finite-Difference Method	1D	(96)
		Phase-Field Model			
Dissolution of Al_2CuMg in Al phase	Al-Cu-Mg	Two-Domain Approach	Finite-Difference Method	1D	(98)
		Phase-Field Model		2D	(102)
Dissolution of Al_3Mg_2 in Al phase	Al-Mg	Phase-Field Model	Finite-Difference Method	1D	(105)
				2D	(109)
			Meshfree Method	1D	(105)
				2D	(107)
Chapter 5					
Spheroidisation of Si-particle	Al-Si	Phase-Field Model	Finite-Difference Method	2D	(121)
Chapter 6					
Dissolution of Eu in Al Phase	Al-Cu	Phase-Field Model	Finite-Difference Method	1D	(140)
				2D	(146)

Part I

Physical Models and Solution Procedures

2 Physical Models for Solid-Solid Phase Transformations

This chapter deals with the physical models, related to solid-solid phase transformations. These physical models, in the mathematical terminology, belong to the group of moving-boundary problems. Wide spectra of physical models exist, along with numerical procedures for solving them [Crank, 1984]. The models are divided into two major groups: the two-domain approaches and the one-domain approaches.

The fields are solved separately in the domains occupied by the different phases in the two-domain approaches, and the interface conditions are explicitly taken into account. The major numerical problem is the boundary condition implementation at geometrically complex moving interphase interfaces.

The phase-field approach has been developed as a basis for powerful computational modelling of complex phase-change problems at the micro level. The phase-field approach belongs to the group of one-domain approaches, where the governing equations hold over the whole domain, and the interface conditions are implicitly taken into account through a major non-linearity.

2.1 General Characteristics of the Physical Models

A domain Ω of volume V with exterior boundary Γ, filled with a multicomponent alloy with M components and two different solid phases α and β is considered. The phases have different crystal structures and/or compositions. The boundary between the phases in the solid state is denoted in materials science as the interface [Porter and Easterling, 1990]. The system is in thermal and mechanical equilibrium. The scheme of the considered two-phase system is presented in Fig.(2.1).

In heat treatment processes, the temperature changes influence changes of the thermodynamic conditions in the system. The phase transformations between phases in the system are consequences of these changes. The description of the related phase transformation kinetics is the goal of the physical models.

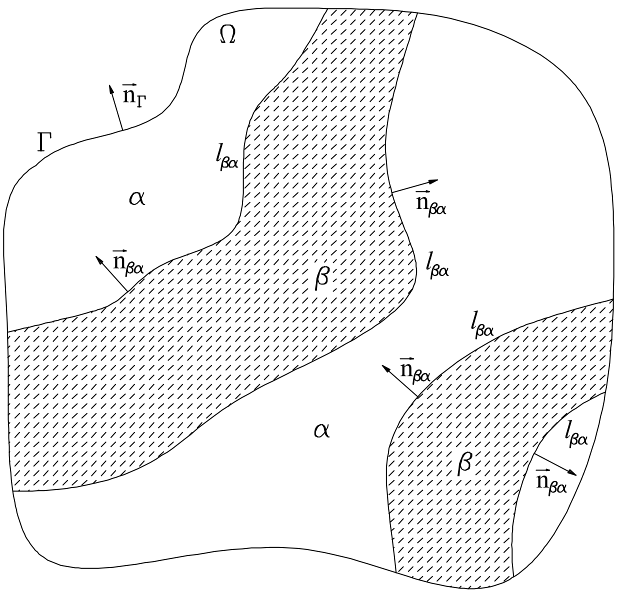

Figure 2.1: Schematic presentation of the considered two-phase system.

The typical time scale of phase transformations in the solid state is much larger than the time scale of the temperature changes. A time dependent but spatially uniform temperature distribution in the observed system can be assumed. The temperature changes in time are usually known from the macroscopic level

$$T = T(t)\,. \tag{2.1}$$

Computation of the component concentration fields $c_\varphi^{\mathrm{m}}(\vec{p}, t)$ [wt%] in the phase φ, $\varphi = \alpha$, β, and the interface position $l_{\beta\alpha}$ as a function of temperature change $T = T(t)$ is the main purpose of the physical models. The vector position and time are denoted as $\vec{p}$ and t, respectively. Our consideration is confined to the two-dimensional geometry, where the Cartesian coordinate system is used, $\vec{p} = \vec{p}(x, y)$. The schematic presentation of the purpose of the physical models is drawn in Fig.(2.2). The $\mathrm{M} - 1$ independent concentration fields have to be computed in both phases, because the constitutive relation holds

$$\sum_{\mathrm{m}=1}^{\mathrm{M}} c_\varphi^{\mathrm{m}} = 1. \tag{2.2}$$

The major component of the system is component M, in our case aluminium (Al). The concentration vector in the phase φ is denoted as $\mathbf{c}_\varphi = \begin{bmatrix} c_\varphi^1 \, c_\varphi^2 \, \ldots \, c_\varphi^{(\mathrm{M}-1)} \end{bmatrix}^{\mathrm{T}}$[1]. The major component is explicitly not included due to the constraint Eq.(2.2). Components are denoted with S^{m}, $\mathrm{m} = 1, 2, \ldots, \mathrm{M}$.

---

[1] The superscript T denotes the matrix transpose.

Initial conditions at time t_0 are prescribed: the concentration vectors in both phases $\mathbf{c}_\varphi(\vec{p},t_0)$ and the interface position $l_{\beta\alpha}(t_0)$. All boundary conditions on the exterior boundary Γ are assumed to be of the Neumann type, that is, no diffusion across the system boundary (closed system)

$$\nabla c_\varphi^{\mathrm{m}} \cdot \vec{n}_\Gamma = 0\,; \quad \mathrm{m} = 1, 2, \ldots, \mathrm{M}-1, \tag{2.3}$$

where $\vec{n}_\Gamma$ is the normal vector on the exterior boundary Γ.

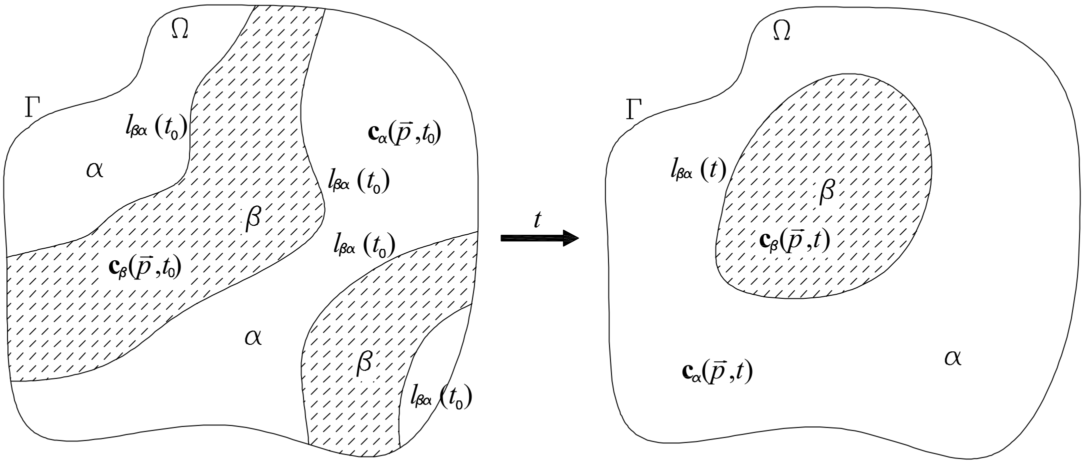

Figure 2.2: Schematic presentation of the purpose of the physical models.

2.2 The Two-Domain Approach

The description of the Two-Domain Approach (TDA) for diffusion-controlled solid-solid phase transformations is divided into three different segments: (i) the mass diffusion equations in the bulk phases, (ii) the thermodynamic equilibrium at the interface and (iii) the mass conservation at the interface. The departure from the local thermodynamic equilibrium at the interface, influenced by the local curvature as well as the local interface reaction, is described at the end of this section.

2.2.1 Mass Diffusion Equations in the Bulk Phases

The mass diffusion equation of component m in the bulk phase φ is obtained from Fick's second law [Glicksman, 2000]

$$\frac{\partial c_\varphi^{\mathrm{m}}}{\partial t} = -\nabla \cdot \vec{J}_\varphi^{\mathrm{m}}\,; \quad \mathrm{m} = 1, 2, \ldots, \mathrm{M}-1\,, \tag{2.4}$$

where $\vec{J}_{\varphi}^{\mathrm{m}}$ is the mass flux[2] of component m in the phase φ. The mass flux vector in the phase φ is denoted as $\vec{\mathbf{J}}_{\varphi} = \left[\vec{J}_{\varphi}^{1}\, \vec{J}_{\varphi}^{2} \ldots \vec{J}_{\varphi}^{(\mathrm{M}-1)}\right]^{\mathrm{T}}$ with size $d \times (\mathrm{M}-1)$, where d represents the dimension of the problem. The mass flux vector represents a product of the interdiffusion coefficient matrix and the concentration gradient vector:

$$\vec{\mathbf{J}}_{\varphi} = -\tilde{\mathbf{D}}_{\varphi} \nabla \mathbf{c}_{\varphi}\,, \tag{2.5}$$

where the isotropic interdiffusion square coefficient matrix of the size $(\mathrm{M}-1)$ and the concentration gradient vector are

$$\tilde{\mathbf{D}}_{\varphi} = \begin{bmatrix} \tilde{D}_{\varphi}^{11} & \tilde{D}_{\varphi}^{12} & \ldots & \tilde{D}_{\varphi}^{1(\mathrm{M}-1)} \\ \tilde{D}_{\varphi}^{21} & \tilde{D}_{\varphi}^{22} & \ldots & \tilde{D}_{\varphi}^{2(\mathrm{M}-1)} \\ \ldots & \ldots & \ldots & \ldots \\ \tilde{D}_{\varphi}^{(M-1)1} & \tilde{D}_{\varphi}^{(M-1)2} & \ldots & \tilde{D}_{\varphi}^{(\mathrm{M}-1)(\mathrm{M}-1)} \end{bmatrix}, \quad \nabla \mathbf{c}_{\varphi} = \begin{bmatrix} \nabla c_{\varphi}^{1} \\ \nabla c_{\varphi}^{2} \\ \ldots \\ \nabla c_{\varphi}^{(\mathrm{M}-1)} \end{bmatrix}. \tag{2.6}$$

The off-diagonal entries $\tilde{D}_{\varphi}^{\mathrm{nm}}$ $(\mathrm{n} \neq \mathrm{m})$ of the interdiffusion coefficient matrix, also referred to as the cross-terms, are measures for the interaction between consecutive components in the phase φ. When $\tilde{D}_{\varphi}^{\mathrm{nm}} < 0$, component m deteriorates diffusion of the element n in the phase φ, whereas $\tilde{D}_{\varphi}^{\mathrm{nm}} > 0$ implies that component m facilitates the diffusion of element n in the phase φ.

The assumption that the diffusion of the component is independent of the presence of the other component $(\tilde{D}_{\varphi}^{\mathrm{nm}} \equiv 0, \mathrm{n} \neq \mathrm{m})$ is used in the reminder of this thesis. There are two reasons for making this assumption: the first is that the cross-diffusion coefficients $\tilde{D}_{\varphi}^{\mathrm{nm}}$ are much lower than the diagonal diffusion coefficients $\tilde{D}_{\varphi}^{\mathrm{mm}}$, and the second one is that the cross-diffusion coefficients of the interdiffusion coefficient matrix in the solid phases cannot be easily obtained from the available literature. The DICTRA software with different mobility databases represents one of the ways to obtain the interdiffusion coefficient matrices for various phases [DICTRA, 2007]. In the following, the interdiffusion diffusion coefficients are denoted without tildes, and the superscript mm is replaced with the superscript m, $D_{\varphi}^{\mathrm{m}} = \tilde{D}_{\varphi}^{\mathrm{mm}}$.

If we take into account the above mentioned assumptions, the component mass flux does not dependent on the concentration gradients of other components

$$\vec{J}_{\varphi}^{\mathrm{m}} = -D_{\varphi}^{\mathrm{m}} \nabla c_{\varphi}^{\mathrm{m}} \tag{2.7}$$

and the mass diffusion equation of component m becomes

$$\frac{\partial c_{\varphi}^{\mathrm{m}}}{\partial t} = \nabla \cdot \left(D_{\varphi}^{\mathrm{m}} \nabla c_{\varphi}^{\mathrm{m}}\right)\,. \tag{2.8}$$

If we make the further simplification that diffusion coefficients do not depend on concentration, then the mass diffusion equation of component m in the phase φ is

$$\frac{\partial c_{\varphi}^{\mathrm{m}}}{\partial t} = D_{\varphi}^{\mathrm{m}} \nabla^{2} c_{\varphi}^{\mathrm{m}}\,. \tag{2.9}$$

---

[2] Multidimensional vector fields in this thesis are denoted with an arrow above them. Vector fields that correspond to concentration components are denoted in bold.

Eq.(2.9) represents a classical parabolic Partial Differential Equation (PDE).

2.2.2 Thermodynamic Equilibrium at the Interface

In the diffusion-controlled transformation mode, the local thermodynamic variables at the interface are determined by thermodynamic equilibrium. The number of degrees of freedom is determined in Section 1.3.1, and it determines the number of conditions that can be obtained from thermodynamic analysis. The two-phase isobaric system is considered, consequently the number of degrees of freedom is

$$\mathrm{F} = \mathrm{M} - 1\,. \tag{2.10}$$

The unknown thermodynamic variables at the interphase interface are

$$T\,, c_{\alpha\mathrm{I}}^{\mathrm{m}}\,, c_{\beta\mathrm{I}}^{\mathrm{m}}\,;\ \ \mathrm{m} = 1, 2, \ldots, \mathrm{M} - 1\,.^{3} \tag{2.11}$$

The number of unknown thermodynamic variables at the interface is $1+2(\mathrm{M}-1)$.

The number of unknown thermodynamic variables $1 + 2\,(\mathrm{M} - 1)$ minus the number of degrees of freedom $\mathrm{M} - 1$ is equal to the number of conditions that can be obtained from thermodynamic analysis M. The general condition of the thermodynamic equilibrium [DeHoff, 1993] in a multicomponent two-phase system (Eq.(1.5)) is

$$\mu_{\alpha}^{\mathrm{m}}\,(T, \mathbf{c}_{\alpha\mathrm{I}}) = \mu_{\beta}^{\mathrm{m}}\,(T, \mathbf{c}_{\beta\mathrm{I}})\,;\ \ \mathrm{m} = 1, 2, \ldots, \mathrm{M}. \tag{2.12}$$

Eq.(2.12) holds for each component in the system. These equations represent the conditions that have to be satisfied in order for any two phases to coexist in thermodynamic equilibrium.

Also, different system of independent equations can be selected from thermodynamics. If we use a thermodynamic database, M equations can be chosen as

$$\begin{aligned} g_{\alpha}\,(T, \mathbf{c}_{\alpha\mathrm{I}}) &= 0, \\ g_{\beta}\,(T, \mathbf{c}_{\beta\mathrm{I}}) &= 0, \\ F_{j}\,(T, \mathbf{c}_{\alpha\mathrm{I}}, \mathbf{c}_{\beta\mathrm{I}}) &= 0, \quad j = 1, 2, \ldots, \mathrm{M} - 2, \end{aligned} \tag{2.13}$$

where g_{φ} is the mathematical description of the M-dimensional Gibbs free energy surface of the phase φ. The mathematical description of tie-lines can be written as independent $\mathrm{M} - 2$ equations, F_j.

Stoichiometric Phase

An intermetallic compound with uniform concentration is known as a stoichiometric phase. Numerous stoichiometric phases are present in ferrous and nonferrous alloys. Thermodynamic equilibrium interface conditions between the stoichiometric and the nonstoichiometric phases are different [Hillert, 1998], therefore these are separately described.

---

[3] The subscript I denote local values on the interface.

The stoichiometry compound of the particle is denoted as

$$\left(\mathrm{S}^1\right)_{\mathrm{n}_1}\left(\mathrm{S}^2\right)_{\mathrm{n}_2}\ldots\left(\mathrm{S}^{\mathrm{M}}\right)_{\mathrm{n}_{\mathrm{M}}}\,, \tag{2.14}$$

where the numbers $\mathrm{n}_1, \mathrm{n}_2 \ldots \mathrm{n}_{\mathrm{M}}$ are stoichiometric constants, for example $\mathrm{Al_2CuMg}$.

The number of degrees of freedom at the interface is equal to

$$\mathrm{F} = \mathrm{M} - 1\,, \tag{2.15}$$

the same as in the previous case.

The unknown thermodynamic variables at the interface are

$$T, c_{\alpha\mathrm{I}}^{\mathrm{m}}\,; \quad \mathrm{m} = 1, 2, ..., \mathrm{M} - 1. \tag{2.16}$$

The number of unknown thermodynamic variables is $1 + (\mathrm{M} - 1)$, because the composition of the stoichiometric β phase is known ($\mathbf{c}_\beta = \mathbf{c}_\beta^{\mathrm{st}}$). The number of unknown thermodynamic variables minus the number of degrees of freedom is one. Only one condition or equation has to be satisfied in order for the stoichiometric and the matrix phases to coexist in thermodynamic equilibrium. Hence, the general thermodynamic condition for the physical model Eq.(2.13) in the present case is

$$g_\alpha\left(T, \mathbf{c}_{\alpha\mathrm{I}}\right) = 0\,, \tag{2.17}$$

which guarantees that the interface concentrations are on the M-dimensional Gibbs free energy surface of the phase α.

The other thermodynamic condition, solubility product, is introduced in [Vermolen *et al.*, 2002]. The assumption that the matrix phase is a dilute solution is used for the derivation of this condition.

Solubility Product. The Gibbs free energy of the phase β introduced in Eq.(1.4) is

$$g_\beta = \sum_{\mathrm{m}=1}^{\mathrm{M}} X_\beta^{\mathrm{m}} \mu_\beta^{\mathrm{m}} \tag{2.18}$$

and the chemical potential of component m introduced in Eq.(1.6) is

$$\mu_\beta^{\mathrm{m}} = g_0^{\mathrm{m}} + RT \ln a_\beta^{\mathrm{m}}\,. \tag{2.19}$$

The interphase interface, where the thermodynamic equilibrium state (Eq.(2.12)) exists, can be obtained from Eqs.(2.18,2.19)

$$\prod_{\mathrm{m}=1}^{\mathrm{M}} \left(a_\alpha^{\mathrm{m}}\right)^{X_\beta^{\mathrm{m}}} = \exp\left(\frac{\Delta g}{RT}\right); \quad \Delta g = g_\beta - \sum_{\mathrm{m}=1}^{\mathrm{M}} X_\beta^{\mathrm{m}}\, g_0^{\mathrm{m}}\,. \tag{2.20}$$

From Henry's law, valid for dilute solutions, the activity of the minor component is approximately proportional to the molar composition, i.e.,

$$a_\alpha^{\mathrm{m}} = \bar{f}_\alpha^{\mathrm{m}} X_\alpha^{\mathrm{m}} \approx X_\alpha^{\mathrm{m}}; \quad \mathrm{m} = 1, 2, \ldots, \mathrm{M} - 1, \tag{2.21}$$

where $\bar{f}_{\alpha}^{\mathrm{m}}$ is the activity coefficient of component m in the phase α. From Raoult's law, the activity coefficient of the major component is approximately one, $f_{\alpha}^{\mathrm{M}} \approx 1$. By using Eq.(2.21), Eq.(2.20) is

$$\prod_{\mathrm{m}=1}^{\mathrm{M}} (X_{\alpha\mathrm{I}}^{\mathrm{m}})^{X_{\beta}^{\mathrm{m}}} = \exp\left(\frac{\Delta g}{RT}\right) / \prod_{\mathrm{m}=1}^{\mathrm{M}-1} (f_{\alpha}^{\mathrm{m}})^{X_{\beta}^{\mathrm{m}}}. \tag{2.22}$$

The right-hand side of Eq.(2.22) is regarded as the solubility product and is denoted by K. The solubility product depends on temperature according to an Arrhenius relationship.

At the end, if we assume that the phase α is the dilute solution, the hyperbolic relationship between the interface compositions is valid

$$\prod_{\mathrm{m}=1}^{\mathrm{M}-1} (X_{\alpha\mathrm{I}}^{\mathrm{m}})^{X_{\beta}^{\mathrm{m}}} = K\left(T\right). \tag{2.23}$$

The Vermolen model [Vermolen *et al.*, 1998b; Vermolen *et al.*, 2002] for dissolution of the multicomponent stoichiometric phases in the aluminium matrix during homogenisation of aluminium alloys is based on this kind of interface condition.

The physical models are posed in specific mass quantities, and only the thermodynamic data are in specific molar quantities. The relation between them is

$$c_{\varphi}^{\mathrm{m}} = \frac{M_{\mathrm{S^m}}}{M_{\mathrm{mix}}} X_{\varphi}^{\mathrm{m}}; \quad M_{\mathrm{mix}} = \sum_{\mathrm{m}=1}^{\mathrm{M}} M_{\mathrm{S^m}} X_{\varphi}^{\mathrm{m}}, \tag{2.24}$$

where $M_{\mathrm{S^m}}$ and M_{mix} are the molar mass of element $\mathrm{S^m}$ and the mass of the local mixture, respectively.

2.2.3 Mass Conservation at the Interface

The mass conservation of component m at the interface is written as

$$\left(c_{\beta\mathrm{I}}^{\mathrm{m}} - c_{\alpha\mathrm{I}}^{\mathrm{m}}\right) v_n = \vec{J}_{\beta\mathrm{I}}^{\mathrm{m}} \cdot \vec{n}_{\beta\alpha} - \vec{J}_{\alpha\mathrm{I}}^{\mathrm{m}} \cdot \vec{n}_{\beta\alpha}\,, \quad v_n = \vec{v} \cdot \vec{n}_{\beta\alpha}. \tag{2.25}$$

$\vec{J}_{\varphi\mathrm{I}}^{\mathrm{m}}$ is the interface mass flux of component m in phase φ, $\vec{n}_{\beta\alpha}$ is the unit normal vector on the interface pointing outward with respect to the phase β, and $\vec{v}$ is the interface velocity.

If phase β is stoichiometric, then the mass conservation of component m at the interface Eq.(2.25) is reduced to

$$\left(c_{\beta\mathrm{I}}^{\mathrm{m}} - c_{\alpha\mathrm{I}}^{\mathrm{m}}\right) v_n = -\vec{J}_{\alpha\mathrm{I}}^{\mathrm{m}} \cdot \vec{n}_{\beta\alpha}. \tag{2.26}$$

In binary alloys, this equation is known as the classical Stefan problem [Šarler, 1995]. In multicomponent alloys, the number of components to be conserved is $\mathrm{M} - 1$, and in the literature, this set of equations is known as a vector-valued

Stefan problem. The one-phase classical or vector-valued Stefan problem can be solved for binary or multicomponent alloys, respectively, if the phase β is stoichiometric.

The number of mass conservation equations at the interface is the number of independent components $\mathrm{M}-1$, and only one additional unknown variable is introduced, the interface velocity $\vec{v}$.

The major drawback of the TDA is necessary tracking of the interface position where the mass conservation (Eq.(2.25) or Eq.(2.26)) has to be computed. Tracking of the interface position is very difficult in a complex multidimensional topology, usually seen during heat treatment processes of commercial alloys at the micro level.

In the one-dimensional geometry, Eq.(2.25) and Eq.(2.26) are

$$\left(c^{\mathrm{m}}_{\beta\mathrm{I}} - c^{\mathrm{m}}_{\alpha\mathrm{I}}\right) v = -D^{\mathrm{m}}_{\beta} \frac{\partial c^{\mathrm{m}}_{\beta}}{\partial x}\bigg|_{\mathrm{I}} + D^{\mathrm{m}}_{\alpha} \frac{\partial c^{\mathrm{m}}_{\alpha}}{\partial x}\bigg|_{\mathrm{I}}, \tag{2.27}$$

$$\left(c^{\mathrm{m}}_{\beta\mathrm{I}} - c^{\mathrm{m}}_{\alpha\mathrm{I}}\right) v = D^{\mathrm{m}}_{\alpha} \frac{\partial c^{\mathrm{m}}_{\alpha}}{\partial x}\bigg|_{\mathrm{I}}, \tag{2.28}$$

respectively. In the one-dimensional geometry, $v \equiv dl_{\beta\alpha}/dt$.

2.2.4 Capillarity Effect and Interface Reaction

In Section 2.2.2, the interface concentrations are determined from the thermodynamic equilibrium. However, the interface concentrations in real systems are also a function of the interface curvature and mobility.

The solubility of component m in the phase α at the interface is related to the local interface curvature through the capillarity effect

$$X^{\mathrm{m}}_{\alpha\kappa} = X^{\mathrm{m}}_{\alpha\mathrm{eq}} \exp\left(\frac{2\sigma\kappa V_{\mathrm{m}}}{RT}\right). \tag{2.29}$$

The local interface conditions derived from the thermodynamic equilibrium do not include the influence of the local curvature, and are only valid for the planar interface. Regions with positive curvature have a higher interface concentration than the regions with negative curvature. Therefore, regions of positive curvature move faster in cases of dissolution and slower in cases of growth than the regions of negative curvature.

The interface reaction also influences the interface condition. When the interface mobility is lower, a higher driving force is required to drive the interface reaction, and a departure from equilibrium appears at the interface. The solubility of component m is determined by

$$X^{\mathrm{m}}_{\alpha\mathrm{i}} = X^{\mathrm{m}}_{\alpha\mathrm{eq}} \exp\left(\frac{v_n V_{\mathrm{m}}}{\mu_{\mathrm{k}} RT}\right). \tag{2.30}$$

The interface concentrations in the phase α obtained from thermodynamic equilibrium have to be corrected in order to include the capillarity effect or the interface mobility by Eq.(2.29) or Eq.(2.30), respectively. The capillarity effect and the interface reaction effect on the interface conditions in the binary system are explained in more detail in Sections 1.3.3 and 1.3.4, respectively.

The influence of the interface reaction on the dissolution kinetics in binary aluminium alloys has already been implemented in [Aaron and Kotler, 1971]. The implementation of the TDA in multidimensional geometry for the grain growth is presented in [Juric, 1996]. Calculation of the curvature by the TDA is extremely difficult for multidimensional geometries, because of which it is only implemented for one-dimensional geometry. However, the results computed by the TDA are used as reference solutions for the results computed by the phase-field approach.

2.2.5 Summary

The total number of unknowns at the interface between two phases in the thermodynamic equilibrium state is $2(\mathrm{M}-1)+1+1 = 2\mathrm{M}$, which are the thermodynamic variables in Eq.(2.11) and the interface velocity in Eq.(2.25). Therefore, the unknowns in the TDA are:

$$T, c_{\alpha\mathrm{I}}^{\mathrm{m}}, c_{\beta\mathrm{I}}^{\mathrm{m}}, \vec{v}\,; \quad \mathrm{m} = 1, 2, \ldots, \mathrm{M}-1. \tag{2.31}$$

Temperature evaluation during heat treatment processes is known

$$T = T(t). \tag{2.32}$$

The physical model based on the TDA consists of the following system of equations:

- the concentration equation of each component in the bulk phases

$$\frac{\partial c_{\varphi}^{\mathrm{m}}}{\partial t} = D_{\varphi}^{\mathrm{m}} \nabla^2 c_{\varphi}^{\mathrm{m}}, \quad \mathrm{m} = 1, 2, \ldots, \mathrm{M}-1, \tag{2.33}$$

- the local thermodynamic equilibrium conditions at the interface

$$\mu_{\alpha}^{\mathrm{m}}\left(T, \mathbf{c}_{\alpha\mathrm{I}}\right) = \mu_{\beta}^{\mathrm{m}}\left(T, \mathbf{c}_{\beta\mathrm{I}}\right); \quad \mathrm{m} = 1, 2, \ldots, \mathrm{M}, \tag{2.34}$$

- the mass conservation equations at the interface

$$\left(c_{\beta\mathrm{I}}^{\mathrm{m}} - c_{\alpha\mathrm{I}}^{\mathrm{m}}\right) v_n = \vec{J}_{\beta\mathrm{I}}^{\mathrm{m}} \cdot \vec{n}_{\beta\alpha} - \vec{J}_{\alpha\mathrm{I}}^{\mathrm{m}} \cdot \vec{n}_{\beta\alpha}; \quad \mathrm{m} = 1, 2, \ldots, \mathrm{M}-1. \tag{2.35}$$

Stoichiometric phase

The total number of unknowns at the interface between a stoichiometric phase and the matrix is $(\mathrm{M}-1)+1+1 = \mathrm{M}+1$, the thermodynamic values in Eq.(2.16) and the interface velocity in Eq.(2.26). The unknowns are:

$$T, c_{\alpha\mathrm{I}}^{\mathrm{m}}, \vec{v}\,; \quad \mathrm{m} = 1, 2, \ldots, \mathrm{M}-1. \tag{2.36}$$

The physical model based on the TDA for the phase transformations of the stoichiometric phase consists of:

- the concentration equations of each component in the matrix phase α

$$\frac{\partial c_\alpha^{\mathrm{m}}}{\partial t} = D_\alpha^{\mathrm{m}} \nabla^2 c_\alpha^{\mathrm{m}}\,, \quad \mathrm{m} = 1, 2, \ldots, \mathrm{M}-1\,, \tag{2.37}$$

- the local thermodynamic equilibrium condition at the interface

$$g_\alpha\left(T, \mathbf{c}_{\alpha\mathrm{I}}\right) = 0 \quad \text{or} \quad \prod_{\mathrm{m}=1}^{\mathrm{M}-1} \left(X_{\alpha\mathrm{I}}^{\mathrm{m}}\right)^{X_\beta^{\mathrm{m}}} = K\left(T\right), \tag{2.38}$$

- the mass conservation equations at the interface

$$\left(c_{\beta\mathrm{I}}^{\mathrm{m}} - c_{\alpha\mathrm{I}}^{\mathrm{m}}\right) v_n = -\vec{J}_{\alpha\mathrm{I}}^{\mathrm{m}} \cdot \vec{n}_{\beta\alpha}\,; \quad \mathrm{m} = 1, 2, \ldots, \mathrm{M}-1\,. \tag{2.39}$$

The general model based on the TDA is presented here. The numerical procedures for the computation of such models are very well developed, and the implementation of the procedures is relatively simple and straightforward for one-dimensional geometry.

2.3 The Phase-Field Approach

The phase-field approach is based on a nonconserved order parameter named the Phase-Field Variable (PFV), which is continuous over in the computational domain. The fixed values of PFV represent bulk phases, whereas highly localized changes of this variable represent the interphase diffuse interface. The behavior of this variable is governed by a particular phase-field equation that is coupled to the heat and solute transport equations.

2.3.1 Diffuse-Interface Approach

Let $\zeta\left(\vec{p}\right)$ represent either a conserved or a nonconserved order parameter, such as concentration $c\left(\vec{p}\right)$ in a binary system or PFV $\phi\left(\vec{p}\right)$ [−]. The field $f\left(\vec{p}\right) = f\left(\zeta\left(\vec{p}\right), \nabla\zeta\left(\vec{p}\right)\right)$ [J/m^3] can represent the free-energy density at position $\vec{p}$. The homogeneous free-energy density $f^{\mathrm{h}}\left(\zeta, \nabla\zeta = 0\right)$ is the free-energy density in the absence of gradients, and is related to the Gibbs free energy. Expanding the free-energy density about its homogenous value in powers of gradients in the general coordinate system (x_1, x_2, x_3), the free-energy is

$$f\left(\zeta, \nabla\zeta\right) = f^{\mathrm{h}}\left(\zeta, 0\right) + \vec{L} \cdot \nabla\zeta + \nabla\zeta \cdot \mathbf{K}\nabla\zeta + \ldots \tag{2.40}$$

where

$$\vec{L} = \left[L_{x_1}, L_{x_2}, L_{x_3}\right], \quad L_{x_i} = \frac{\partial f}{\partial\left(\partial\zeta/\partial x_i\right)} \tag{2.41}$$

is a vector at zero gradient, and $\mathbf{K}$ is a tensor property known as the gradient-energy coefficient with the components

$$K_{ij} = \frac{1}{2}\frac{\partial^2 f}{\partial\left(\partial\zeta/\partial x_i\right)\partial\left(\partial\zeta/\partial x_j\right)}\,. \tag{2.42}$$

The free-energy density should not depend on the choice of coordinate system, therefore $\vec{L} = \vec{0}$ and **K** is a symmetric tensor. Furthermore, if the homogeneous material is isotropic or cubic, **K** is a diagonal tensor with an equal component $\varepsilon_\zeta^2/2$ [J/m]. The free-energy density truncated up to the second order is

$$f(\zeta, \nabla\zeta) \approx f^{\mathrm{h}}(\zeta) + \nabla\zeta \cdot \frac{\varepsilon_\zeta^2}{2}\nabla\zeta = f^{\mathrm{h}}(\zeta) + \frac{\varepsilon_\zeta^2}{2}|\nabla\zeta|^2. \tag{2.43}$$

The free-energy density is approximated as the first two terms in a series expansion in order-parameters gradients: the first term is related to homogeneous free-energy density and the second is proportional to the squared order parameter gradient [Ballufi *et al.*, 2005].

Diffusion Potential for Transformation

The local diffusion potential for a transformation, $\Phi(\vec{p})$, at time $t = t_0$, can be determined from the rate of change of total free energy, $\mathcal{F}$ [J], with respect to its current order-parameter field, $\zeta(\vec{p}, t_0)$. The total free energy at time $t = t_0$ is

$$\mathcal{F}(t_0) = \int\limits_\Omega \left[f^{\mathrm{h}}(\zeta(\vec{p}, t_0)) + \frac{\varepsilon_\zeta^2}{2}|\nabla\zeta|^2 \right] dV\,, \tag{2.44}$$

which defines the total free energy $\mathcal{F}$ as a functional of the order parameter $\zeta(\vec{p}, t_0)$. If the order parameter changes with local "velocity" $\partial\zeta/\partial t$ (i.e. such that $\zeta(\vec{p}, t) = \zeta(\vec{p}, t_0) + t\,\partial\zeta/\partial t(\vec{p}, t_0)$), then the rate of change of $\mathcal{F}$ can be summed from all the contributions of $f(\zeta, \nabla\zeta)$ due to changes in the order-parameter field and its gradient,

$$\left.\frac{d\mathcal{F}}{dt}\right|_{t_0} = \int\limits_\Omega \left(\frac{\partial f^{\mathrm{h}}}{\partial\zeta}\frac{\partial\zeta}{\partial t} + \varepsilon_\zeta^2 \nabla\zeta \cdot \nabla\frac{\partial\zeta}{\partial t} \right) dV. \tag{2.45}$$

Using the relation

$$\nabla\zeta \cdot \nabla\frac{\partial\zeta}{\partial t} = \nabla \cdot \left(\frac{\partial\zeta}{\partial t}\nabla\zeta \right) - \frac{\partial\zeta}{\partial t}\nabla^2\zeta, \tag{2.46}$$

Eq.(2.45) can be written as

$$\left.\frac{d\mathcal{F}}{dt}\right|_{t_0} = \int\limits_\Omega \left(\frac{\partial f^{\mathrm{h}}}{\partial\zeta} - \varepsilon_\zeta^2\nabla^2\zeta \right) \frac{\partial\zeta}{\partial t} dV + \varepsilon_\zeta^2 \int\limits_\Omega \nabla \cdot \left(\frac{\partial\zeta}{\partial t}\nabla\zeta \right) dV. \tag{2.47}$$

Applying the divergence theorem to the second integral in Eq.(2.47)

$$\left.\frac{d\mathcal{F}}{dt}\right|_{t_0} = \int\limits_\Omega \left(\frac{\partial f^{\mathrm{h}}}{\partial\zeta} - \varepsilon_\zeta^2\nabla^2\zeta \right) \frac{\partial\zeta}{\partial t} dV + \varepsilon_\zeta^2 \int\limits_\Gamma \left(\frac{\partial\zeta}{\partial t}\nabla\zeta \right) \cdot \vec{n}_\Gamma dA. \tag{2.48}$$

The boundary integral on the right-hand side of Eq.(2.48) is zero, if

- $\zeta(\Gamma)$ has constant boundary values (constant Dirichlet boundary condition) or

- the projections of the gradients onto the boundary vanish (Neumann insolation boundary condition).

Therefore, if the order parameter changes by a small amount $\delta\zeta = (\partial\zeta/\partial t)\,\delta t$, the change in total free energy is the sum of the local changes:

$$\delta\mathcal{F} = \int\limits_{\Omega} \left(\frac{\partial f^{\mathrm{h}}}{\partial\zeta} - \varepsilon_{\zeta}^{2}\nabla^{2}\zeta \right) \delta\zeta dV. \tag{2.49}$$

The quantity

$$\Phi\left(\vec{p}\right) = \frac{\partial f^{\mathrm{h}}}{\partial\zeta} - \varepsilon_{\zeta}^{2}\nabla^{2}\zeta \tag{2.50}$$

is the localized density of free-energy change due to the variation in the order-parameter field $\delta\zeta$, and is therefore the potential of change ζ. Eq.(2.50) is the starting point for the development of kinetic equations for conserved and non-conserved order-parameter fields [Ballufi *et al.*, 2005].

Evolution Equations for Conserved and Non-Conserved Order Parameters

Cahn-Hilliard Equation. The Cahn-Hilliard equation [Cahn and Hilliard, 1958] applies to conserved order-parameter kinetics. For a binary A-B alloy, the quantity Φ in Eq.(2.50) is the change in homogeneous and gradient energy due to the change of the local concentration and is related to flux by

$$\vec{J} = -L\nabla\frac{\delta\mathcal{F}}{\delta c} = -\frac{D}{\frac{\partial^{2} f^{\mathrm{h}}}{\partial c^{2}}}\nabla\left(\frac{\partial f^{\mathrm{h}}}{\partial c} - \varepsilon_{c}^{2}\nabla^{2}c\right), \tag{2.51}$$

where L is the Onsager coefficient. The kinetic equation for concentration $c\left(\vec{p}, t\right)$ in a binary alloy is

$$\frac{\partial c}{\partial t} = -\nabla\cdot\vec{J} = \nabla\cdot\left[\frac{D}{\frac{\partial^{2} f^{\mathrm{h}}}{\partial c^{2}}}\nabla\left(\frac{\partial f^{\mathrm{h}}}{\partial c} - \varepsilon_{c}^{2}\nabla^{2}c\right)\right]. \tag{2.52}$$

Eq.(2.52) is the Cahn-Hilliard equation. The Cahn-Hiliard equation is often linearized for concentration around the average value of the positive kinetic coefficient $M_c = \left\langle D/\left(\partial^{2} f^{\mathrm{h}}/\partial c^{2}\right)\right\rangle$ [m^5/Js]

$$\frac{\partial c}{\partial t} = M_c\left(\frac{\partial^{2} f^{\mathrm{h}}}{\partial c^{2}}\nabla^{2}c - \varepsilon_{c}^{2}\nabla^{4}c\right). \tag{2.53}$$

The first term on the right-hand side in Eq.(2.53) is the diffusion term. The second term accounts for the interface energy potential for concentration gradients.

Allen-Cahn Equation. The Allen-Cahn equation [Cahn and Allen, 1977] applies to the kinetics of a diffuse-interface model for a nonconserved order parameter. The increase in local free-energy density $\Phi\left(\vec{p}\right)$, does not require any additional macroscopic flux. In a linear model, the local rate of change is proportional to its energy-density decrease,

$$\frac{\partial \phi}{\partial t} = -M_\phi \frac{\delta \mathcal{F}}{\delta \phi} = -M_\phi \left(\frac{\partial f^{\mathrm{h}}}{\partial \phi} - \varepsilon_\phi^2 \nabla^2 \phi \right). \tag{2.54}$$

where M_ϕ [m^3/Js] is positive kinetic coefficient referred to as the phase-field mobility, and is related to the microscopic rearrangement kinetics. According to the Allen-Cahn equation, Eq.(2.54), the PFV ϕ will be attracted to the local minima of the homogeneous free-energy density f^{h}.

2.3.2 Phase-Field Model

Numerical models of conserved and nonconserved order-parameter kinetics produce simulations that might capture many aspects of microstructure evolution. These equations, as derived from variational principles, constitute the Phase-Field Model (PFM). In our example, the nonconserved and conserved order-parameters are the PFV ϕ and the component concentration c^{m} in the system, respectively.

The total free energy of such an observed system is

$$\mathcal{F}\left(\phi, \mathbf{c}, T\right) = \int\limits_V \left(f^{\mathrm{ch}}\left(\phi, \mathbf{c}, T\right) + \frac{\varepsilon_\phi^2}{2} \left|\nabla \phi\right|^2 \right) dV, \tag{2.55}$$

where the energy-gradient coefficient related to concentrations is neglected ($\varepsilon_c \approx 0$).

In this thesis, the order parameter PFV represents the matrix phase α where $\phi = 0$ and the phase β where $\phi = 1$. The strong gradient of the PFV between these values represents the diffuse-interface region. The PFV versus the coordinate normal to the interface is presented in Fig.(2.3(a)).

The PFMs for phase transformation are divided depending on the definition of free-energy density in the diffuse-interface region. The PFM is derived for solidification, and later on the model is implemented for different phase transformations as well as for transformations in the solid state.

The PFM for the solidification of binary alloys is derived in [Wheeler *et al.*, 1992]. In the model, any point within the interface region is assumed to be a mixture of solid and liquid phases with the same concentrations. A problem in this model, especially in numerical simulations where a finite interface thickness is assumed, is that the model parameters vary depending on the interface thickness. Due to the chemical energy contribution to the interface energy, there is a certain limit of the interface thickness, which is not only restricted by the interface energy, but also by the difference between the equilibrium liquid and solid compositions.

A different definition of the free-energy density is used in [Tiaden *et al.*, 1998]. In their model, the interface region is assumed to be a mixture of solid and liquid with different concentrations, but with a constant phase fraction. There is no limit to the interface thickness for numerical implementations.

In this thesis, the interface region is defined as a mixture of two phases with compositions different from each other, but with the same phase diffusion potential [Kim *et al.*, 1999]. In the model [Wheeler *et al.*, 1992], on the contrary, the interface region is defined as a mixture of solid and liquid with the same composition, but with different phase diffusion potentials. It does not matter which definition for the interface region is more physically reasonable, because the interface region in the PFMs cannot be regarded as a physical entity, but instead must be taken as a mathematical entity for technical convenience.

The thermodynamic condition in the interface region is that the phase diffusion potential in the phase α is equal to the phase diffusion potential in the phase β for each independent component, i.e.,

$$\frac{\partial f_\alpha}{\partial c_\alpha^{\mathrm{m}}} = \frac{\partial f_\beta}{\partial c_\beta^{\mathrm{m}}}; \quad \mathrm{m} = 1, 2, , \ldots, \mathrm{M} - 1 . \tag{2.56}$$

The concentration in the interface region is defined as a mixture of concentrations in the phase α and the phase β, as:

$$\mathbf{c} = (1 - p(\phi))\, \mathbf{c}_\alpha + p(\phi)\, \mathbf{c}_\beta, \tag{2.57}$$

where an interpolation function $p(\phi)$ is introduced.

The concentrations in phases are different from each other, but they have the same phase diffusion potential. The condition Eq.(2.56) does not imply that the phase diffusion potential is constant throughout the interface region; it is only constant across the interface region in thermodynamic equilibrium. The schematic presentation of concentrations in phases in the interface region is depicted in Fig.(2.3(b)).

The concentrations of each component in the phases α and β have to be computed from Eqs.(2.56,2.57). Solving the system of Eqs.(2.56,2.57) with tabular data from an thermodynamic database is very time consuming, and special attention is paid in the presented thesis to suitable solution.

If the phase β is an intermetallic compound with a constant concentration $\mathbf{c}_\beta = \mathbf{c}_\beta^{\mathrm{st}}$, then the concentration in the phase α can be straightforwardly computed by Eq.(2.57) through

$$\mathbf{c}_\alpha = \frac{\mathbf{c} - p(\phi)\, \mathbf{c}_\beta^{\mathrm{st}}}{1 - p(\phi)} . \tag{2.58}$$

Free-Energy Density

The chemical free-energy density $f^{\mathrm{ch}}(\phi, \mathbf{c}, T)$ of a two-phase system is postulated as

$$f^{\mathrm{ch}}(\phi, \mathbf{c}, T) = (1 - p(\phi))\, f_\alpha(\mathbf{c}_\alpha, T) + p(\phi)\, f_\beta(\mathbf{c}_\beta, T) + wh(\phi), \tag{2.59}$$

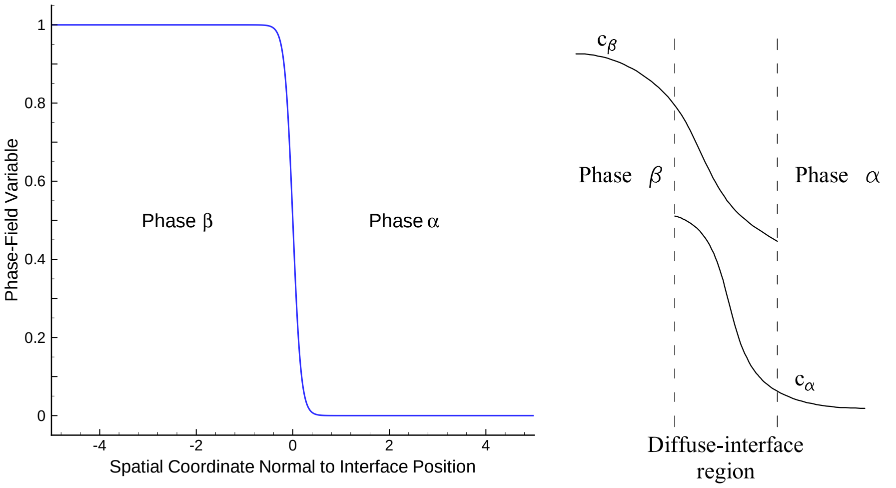

(a) The PFV. (b) Concentration Profiles.

Figure 2.3: Schematic presentation of the PFM.

where $f_\varphi(\mathbf{c}_\varphi, T)$ is the free-energy density of the phase φ and $wh(\phi)$ is the energy hump between them. The model parameter $w\,[\mathrm{J/m^3}]$ is four times higher than the height of the energy hump. The interpolation $p(\phi)$ and the double-well function $h(\phi)$ are explained later in this section.

The chemical free-energy density can be divided into two parts: the bulk and the interface part of chemical free energy

$$f^{\mathrm{ch}}(\phi, \mathbf{c}, T) = f^{\mathrm{ch}}_{\mathrm{bulk}} + f^{\mathrm{ch}}_{\mathrm{int}}, \tag{2.60}$$

where

$$f^{\mathrm{ch}}_{\mathrm{bulk}}(\phi, \mathbf{c}, T) = (1 - p(\phi))\, f_\alpha(\mathbf{c}_\alpha, T) + p(\phi)\, f_\beta(\mathbf{c}_\beta, T)\,,\; f^{\mathrm{ch}}_{\mathrm{int}}(\phi) = wh(\phi)\,, \tag{2.61}$$

respectively.

The derivative of the chemical free energy with respect to the PFV is

$$\frac{\partial f^{\mathrm{ch}}}{\partial \phi} = p'(\phi)\left[f_\beta - f_\alpha - \sum_{\mathrm{m}=1}^{\mathrm{M}-1} \frac{\partial f_\alpha}{\partial c^{\mathrm{m}}_\alpha}\left(c^{\mathrm{m}}_\beta - c^{\mathrm{m}}_\alpha\right)\right] + wh'(\phi)\,. \tag{2.62}$$

The last expression is derived by the following relationships

$$\frac{\partial c^{\mathrm{m}}_\varphi}{\partial c^{\mathrm{m}}} = \frac{\frac{\partial^2 f_{\bar\varphi}}{\partial c^{\mathrm{m}\,2}_{\bar\varphi}}}{(1 - p(\phi))\frac{\partial^2 f_\beta}{\partial c^{\mathrm{m}\,2}_\beta} + p(\phi)\frac{\partial^2 f_\alpha}{\partial c^{\mathrm{m}\,2}_\alpha}},\; \frac{\partial c^{\mathrm{m}}_\varphi}{\partial \phi} = -\frac{p'(\phi)\left(c^{\mathrm{m}}_\beta - c^{\mathrm{m}}_\alpha\right)\frac{\partial^2 f_{\bar\varphi}}{\partial c^{\mathrm{m}\,2}_{\bar\varphi}}}{(1 - p(\phi))\frac{\partial^2 f_\beta}{\partial c^{\mathrm{m}\,2}_\beta} + p(\phi)\frac{\partial^2 f_\alpha}{\partial c^{\mathrm{m}\,2}_\alpha}}. \tag{2.63}$$

In the first case, $\varphi = \alpha$, $\bar\varphi = \beta$ and in the second, $\varphi = \beta, \bar\varphi = \alpha$. $p'(\phi)$ represents the first derivative with respect to the PFV, $dp/d\phi$. The derivative of the chemical free-energy density with respect to the mixture concentration of component m is

$$\frac{\partial f^{\mathrm{ch}}}{\partial c^{\mathrm{m}}} = \frac{\partial f_{\alpha}^{\mathrm{ch}}}{\partial c_{\alpha}^{\mathrm{m}}} = \frac{\partial f_{\beta}^{\mathrm{ch}}}{\partial c_{\beta}^{\mathrm{m}}} \,. \tag{2.64}$$

For the evolution of the chemical contribution in conjunction with the thermodynamic database, Gibbs-molar free energies are preferred. If we neglect volume changes and assume that the molar volumes of phases are equal and independent of composition (V_{m}), then the free-energy densities can be replaced by molar free energies as

$$f_{\mathrm{bulk}}^{\mathrm{ch}}(\mathbf{c}, T) = \frac{1}{V_{\mathrm{m}}} \left[(1 - p(\phi))\, g_{\alpha}(\mathbf{X}_{\alpha}, T) + p(\phi)\, g_{\beta}(\mathbf{X}_{\beta}, T) \right]. \tag{2.65}$$

Now, the derivative of the chemical free energy with respect to the PFV in terms of the molar free energies is

$$\frac{\partial f^{\mathrm{ch}}}{\partial \phi} = \frac{p'(\phi)}{V_{\mathrm{m}}} \left[g_{\beta} - g_{\alpha} - \sum_{\mathrm{m}=1}^{\mathrm{M}-1} \frac{\partial g_{\alpha}}{\partial X_{\alpha}^{\mathrm{m}}} \left(X_{\beta}^{\mathrm{m}} - X_{\alpha}^{\mathrm{m}} \right) \right] + w h'(\phi) \,. \tag{2.66}$$

By using the condition Eq.(2.56) and the assumption that molar volumes of phases are equal, the derivatives of the molar free energies with respect to the molar compositions of each component are equal

$$\frac{\partial g_{\alpha}}{\partial X_{\alpha}^{\mathrm{m}}} = \frac{\partial g_{\beta}}{\partial X_{\beta}^{\mathrm{m}}} \,, \quad \mathrm{m} = 1, 2, \ldots, \mathrm{M} - 1 \,. \tag{2.67}$$

The molar phase diffusion potential of a component can be expressed by chemical potentials as

$$\frac{\partial g_{\varphi}}{\partial X_{\varphi}^{\mathrm{m}}} = \mu_{\varphi}^{\mathrm{m}} - \mu_{\varphi}^{\mathrm{M}}. \tag{2.68}$$

The presentation of Eq.(2.68) in binary systems can be seen in Fig.(1.3).

Driving Force for Phase Transformations. The expression in brackets in Eq.(2.66) is the driving force for the phase transformation of the phase β in the phase α [Hillert, 1998]

$$\Delta g_{\beta\alpha} = g_{\beta} - g_{\alpha} - \sum_{\mathrm{m}=1}^{\mathrm{M}-1} \frac{\partial g_{\alpha}}{\partial X_{\alpha}^{\mathrm{m}}} \left(X_{\beta}^{\mathrm{m}} - X_{\alpha}^{\mathrm{m}} \right). \tag{2.69}$$

The molar phase diffusion potential ($\partial g_{\varphi} / \partial X_{\varphi}^{\mathrm{m}}$) is the difference between the chemical potentials (Eq.2.68), and the driving force can be expressed in terms of thermodynamic variables as

$$\Delta g_{\beta\alpha} = g_{\beta} - g_{\alpha} - \sum_{\mathrm{m}=1}^{\mathrm{M}-1} \left(\mu_{\alpha}^{\mathrm{m}} - \mu_{\alpha}^{\mathrm{M}} \right) \left(X_{\beta}^{\mathrm{m}} - X_{\alpha}^{\mathrm{m}} \right). \tag{2.70}$$

The molar free energy of the phase and the chemical potential of components in phases can be obtained from a thermodynamic database. The schematic presentation of the driving force for the dissolution of the phase β in phase α is presented for the binary system in Fig.(2.4). The departure from the thermodynamic equilibrium state can be quantified by the molar driving force. If $\Delta g_{\beta\alpha} < 0$, then the phase β grows in phase α, and vice versa, i.e., if $\Delta g_{\beta\alpha} > 0$, then the phase β dissolves into the phase α. In the equilibrium state, the driving force is equal to zero:

$$\Delta g_{\beta\alpha} = 0\,. \tag{2.71}$$

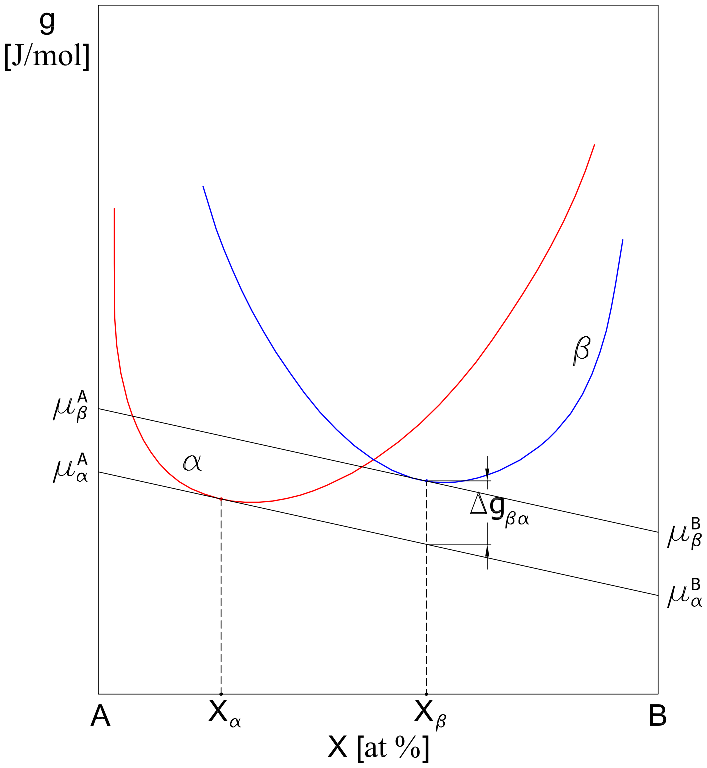

Figure 2.4: Thermodynamic driving force for phase transformation of β in α phase for binary system.

Interpolation and Double-well Function. The free-energy density of the system is defined by using the interpolation $p(\phi)$ and the double-well function $h(\phi)$. These functions have to satisfy the following conditions:

$$\begin{aligned} p(\phi=0)=0,\ \frac{dp(0)}{d\phi}=0, \quad h(0)=0,\ \frac{dh(0)}{d\phi}=0,\\ p(\phi=1)=1,\ \frac{dp(1)}{d\phi}=0, \quad h(1)=0,\ \frac{dh(1)}{d\phi}=0. \end{aligned} \tag{2.72}$$

The interpolation function and its derivative with respect to the PFV are

$$p\left(\phi\right)=\phi^3\left(6\phi^2-15\phi+10\right), \quad p'\left(\phi\right)=\frac{dp}{d\phi}=30\phi^2\left(1-\phi\right)^2 \tag{2.73}$$

and the double-well function and the derivative are

$$h\left(\phi\right)=\phi^2\left(1-\phi\right)^2, \quad h'\left(\phi\right)=\frac{dh}{d\phi}=2\phi\left(1-\phi\right)\left(1-2\phi\right). \tag{2.74}$$

Also, other functions which satisfy conditions in Eq.(2.72) could be used. The selection of these functions has no influence on the model. The double-well function in Eq.(2.74) is the most frequently used, whereas the interpolation function is also frequently expressed as

$$p\left(\phi\right)=\phi^2\left(3-2\phi\right), \quad p'\left(\phi\right)=6\phi\left(1-\phi\right). \tag{2.75}$$

Phase-Field Equation

The phase-field equation is derived by the Allen-Cahn equation Eq.(2.54), the definition of the free-energy density Eq.(2.59) and its derivative with respect to the PFV Eq.(2.66). The phase-field equation becomes

$$\frac{\partial\phi}{\partial t}=M_\phi\left(\varepsilon_\phi^2\nabla^2\phi-wh'\left(\phi\right)-p'\left(\phi\right)\frac{\Delta g_{\beta\alpha}}{V_\mathrm{m}}\right). \tag{2.76}$$

By choosing the interpolation and the double-well function Eqs.(2.73,2.74), the phase-field equation Eq.(2.76) becomes

$$\frac{\partial\phi}{\partial t}=M_\phi\left[\varepsilon_\phi^2\nabla^2\phi-2w\phi\left(1-\phi\right)\left(1-2\phi\right)-30\phi^2\left(1-\phi\right)^2\frac{\Delta g_{\beta\alpha}}{V_\mathrm{m}}\right]. \tag{2.77}$$

The phase-field equation in Eq.(2.77) controls the evolution of the PFV.

From a mathematical point of view, the driving force is the function of concentrations in the phases,

$$\Delta g_{\beta\alpha}=\Delta g_{\beta\alpha}\left(\mathbf{X}_\alpha,\mathbf{X}_\beta\right) \tag{2.78}$$

and it is part of the source term in the phase-field equation.

Concentration Equations

Concentration equations are derived from two different physical approaches in the literature. The first approach is the classical thermodynamic approach, derived from the Cahn-Hilliard equation Eq.(2.52). The second approach is based on the fact that the mixture concentration in a finite control volume can only change by external flux over the volume boundary. This is named the control-volume approach. Concentration equations derived from the Cahn-Hilliard equation are explained first.

Cahn-Hilliard Equation. The evolution equation for the concentration of component m in the system with the total free energy in Eq.(2.55) is [Cha *et al.*, 2005]:

$$\begin{aligned}\frac{\partial c^{\mathrm{m}}}{\partial t} &= \nabla\cdot\sum_{\mathrm{n}=1}^{\mathrm{M}-1} L^{\mathrm{mn}}\nabla\frac{\delta\mathcal{F}}{\delta c^{\mathrm{n}}} = \nabla\cdot\sum_{\mathrm{n}=1}^{\mathrm{M}-1} L^{\mathrm{mn}}\nabla\frac{\partial f^{\mathrm{ch}}}{\partial c^{\mathrm{n}}} = \\ \nabla\cdot\sum_{\mathrm{n}=1}^{\mathrm{M}-1}\sum_{\mathrm{l}=1}^{\mathrm{M}-1} L^{\mathrm{mn}}\frac{\partial^2 f^{\mathrm{ch}}}{\partial c^{\mathrm{n}}\partial c^{\mathrm{l}}}\nabla c^{\mathrm{l}} &+ \nabla\cdot\sum_{\mathrm{n}=1}^{\mathrm{M}-1} L^{\mathrm{mn}}\frac{\partial^2 f^{\mathrm{ch}}}{\partial c^{\mathrm{n}}\partial\phi}\nabla\phi.\end{aligned} \tag{2.79}$$

If we use the assumption that coefficients of the Onsager tensor are only non-zero on the main diagonal, which means that concentration of each component is independent of the presence of other components ($\partial^2 f^{\mathrm{ch}}/\left(\partial c^{\mathrm{m}}\partial c^{\mathrm{n}}\right)\approx 0$), Eq.(2.79) is reduced to

$$\begin{aligned}\frac{\partial c^{\mathrm{m}}}{\partial t} &= \nabla\cdot\left(L^{\mathrm{mm}}\frac{\partial^2 f^{\mathrm{ch}}}{\partial c^{\mathrm{m}2}}\nabla c^{\mathrm{m}}\right) + \nabla\cdot\left(L^{\mathrm{mm}}\frac{\partial^2 f^{\mathrm{ch}}}{\partial c^{\mathrm{m}}\partial\phi}\nabla\phi\right) = \\ \nabla\cdot\left(D^{\mathrm{m}}(\phi)\nabla c^{\mathrm{m}}\right) &- \nabla\cdot\left[D^{\mathrm{m}}(\phi)\,p'(\phi)\left(c^{\mathrm{m}}_{\beta}-c^{\mathrm{m}}_{\alpha}\right)\nabla\phi\right].\end{aligned} \tag{2.80}$$

Control-Volume Approach. This approach is based on the physical statement that the mixture concentration in an infinitesimally small volume or the finite control volume of the numerical model can only change by external fluxes over the boundary of this volume. These fluxes are superimposed according to the PFVs, which have to be evaluated at the boundary of the volume [Tiaden *et al.*, 1998].

The mass diffusion or concentration equation of the component m, valid over the whole system, is

$$\frac{\partial c^{\mathrm{m}}}{\partial t} = -\nabla\cdot\left[(1-\phi)\,\vec{J}^{\mathrm{m}}_{\alpha} + \phi\,\vec{J}^{\mathrm{m}}_{\beta}\right], \tag{2.81}$$

where $\vec{J}^{\mathrm{m}}_{\varphi}$ represents the mass flux of component m in the phase φ ($\varphi = \alpha, \beta$) introduced in Section 2.2.1.

The final mass diffusion equation or the concentration equation of component m in the system is

$$\frac{\partial c^{\mathrm{m}}}{\partial t} = \nabla\cdot\left[(1-\phi)\,D^{\mathrm{m}}_{\alpha}\nabla c^{\mathrm{m}}_{\alpha} + \phi D^{\mathrm{m}}_{\beta}\nabla c^{\mathrm{m}}_{\beta}\right]. \tag{2.82}$$

The mixture concentration in the finite volume approach can be defined as

$$c^{\mathrm{m}} = (1-\phi)\,c^{\mathrm{m}}_{\alpha} + \phi c^{\mathrm{m}}_{\beta}. \tag{2.83}$$

where the interpolation function is substituted by the PFV, $p(\phi)\equiv\phi$.

Comparison of Concentration Equations. Concentration equations in Eq.(2.80) and Eq.(2.82) are derived by different physical statements. The first equation is derived from the classical thermodynamic approach and the second one from the control-volume approach. Concentration equations derived by both concepts are compared here. By using Eq.(2.63), the following relationship can be computed:

$$\nabla c_{\varphi}^{\mathrm{m}} = \frac{\frac{\partial^2 f_{\bar{\varphi}}}{\partial c_{\bar{\varphi}}^{\mathrm{m}\,2}} \left[\nabla c^{\mathrm{m}} - p'(\phi)\left(c_{\beta}^{\mathrm{m}} - c_{\alpha}^{\mathrm{m}}\right)\nabla\phi\right]}{\left(1 - p(\phi)\right)\frac{\partial^2 f_{\beta}}{\partial c_{\beta}^{\mathrm{m}\,2}} + p(\phi)\frac{\partial^2 f_{\alpha}}{\partial c_{\alpha}^{\mathrm{m}\,2}}} \,. \tag{2.84}$$

The concentration equation derived by the control-volume approach (Eq.(2.82)) by using relationships in Eq.(2.84) can be rewritten as

$$\begin{gathered}\frac{\partial c^{\mathrm{m}}}{\partial t} = \nabla\cdot\left[\left(1-\phi\right)D_{\alpha}^{\mathrm{m}}\nabla c_{\alpha}^{\mathrm{m}} + \phi D_{\beta}^{\mathrm{m}}\nabla c_{\beta}^{\mathrm{m}}\right] = \\ \nabla\cdot\left(D^{\mathrm{m}}(\phi)\nabla c^{\mathrm{m}}\right) - \nabla\cdot\left[D^{\mathrm{m}}(\phi)\,p'(\phi)\left(c_{\beta}^{\mathrm{m}} - c_{\alpha}^{\mathrm{m}}\right)\nabla\phi\right],\end{gathered} \tag{2.85}$$

where the diffusion coefficient of component m in the diffusion-interface region $D^{\mathrm{m}}(\phi)$ is introduced as

$$D^{\mathrm{m}}(\phi) = \frac{\left(1-\phi\right)D_{\alpha}^{\mathrm{m}}\frac{\partial^2 f_{\beta}}{\partial c_{\beta}^{\mathrm{m}\,2}} + \phi D_{\beta}^{\mathrm{m}}\frac{\partial^2 f_{\alpha}}{\partial c_{\alpha}^{\mathrm{m}\,2}}}{\left(1 - p(\phi)\right)\frac{\partial^2 f_{\beta}}{\partial c_{\beta}^{\mathrm{m}\,2}} + p(\phi)\frac{\partial^2 f_{\alpha}}{\partial c_{\alpha}^{\mathrm{m}\,2}}} \,. \tag{2.86}$$

The concentration equation derived by the classical thermodynamic approach Eq.(2.80) is identical to the concentration equation derived by the control-volume approach Eq.(2.82), in case the diffusion coefficient in the diffuse-interface region is defined through Eq.(2.86).

2.3.3 Derivation of PFM Parameters

Relations between the model parameters and the physical properties are established here. The gradient-energy coefficient ε_{ϕ}, the height of the energy hump w and the phase-field mobility M_{ϕ} are model parameters, whereas the interface energy σ, the interface thickness δ, and the interface-kinetic coefficient μ_{k} are physical properties. Relations of the observed PFM have been explained for binary systems [Kim *et al.*, 1999]. Later, relations were derived for multicomponent systems in [Cha *et al.*, 2001; Cha *et al.*, 2005]. The PFV and concentration profile at the thermodynamic equilibrium state in the diffusion-interface region are explained first.

Equilibrium Solution. The concentration field and the PFV are independent of time at the equilibrium. The PFV and concentration profile at the equilibrium are denoted by $\phi_{\mathrm{eq}}(\vec{p})$ and $c_{\mathrm{eq}}(\vec{p})$, respectively. The kinetic equations Eqs.(2.76,2.79) for the binary system at the equilibrium for one-dimensional geometry are:

$$\varepsilon_{\phi}^{2}\frac{d^2\phi_{\mathrm{eq}}}{dx^2} - wh'(\phi_{\mathrm{eq}}) - p'(\phi_{\mathrm{eq}})\frac{\Delta g_{\beta\alpha}}{V_{\mathrm{m}}} = 0\,, \tag{2.87}$$

$$\frac{d}{dx}\left[\frac{D\left(\phi\right)}{\frac{\partial^2 f^{\mathrm{ch}}}{\partial^2 c_{\mathrm{eq}}}}\frac{d}{dx}\left(\frac{\partial f^{\mathrm{ch}}}{\partial c_{\mathrm{eq}}}\right)\right]=0\,. \tag{2.88}$$

The phase diffusion potential is constant throughout the system, hence Eq.(2.88) is equivalent to

$$\frac{\partial f^{\mathrm{ch}}}{\partial c_{\mathrm{eq}}}=\mathrm{const}\,. \tag{2.89}$$

From Eqs.(2.64,2.89), one can get

$$\frac{\partial f^{\mathrm{ch}}}{\partial c_{\mathrm{eq}}}=\frac{\partial f_\alpha}{\partial c_\alpha}=\frac{\partial f_\beta}{\partial c_\beta}\,. \tag{2.90}$$

Therefore, c_α and c_β are constant and equal to the equilibrium concentrations

$$c_\alpha=c_{\alpha\mathrm{eq}}\,,\quad c_\beta=c_{\beta\mathrm{eq}}\,. \tag{2.91}$$

The concentration profile at the equilibrium is

$$c_{\mathrm{eq}}\left(x\right)=\left(1-p\left(\phi\right)\right)c_{\alpha\mathrm{eq}}+p\left(\phi\right)c_{\beta\mathrm{eq}}\,. \tag{2.92}$$

Now, let us find solution $\phi_{\mathrm{eq}}\left(x\right)$ in Eq.(2.87). The driving force for phase transformation is zero (Eq.(2.71)), so the phase field equation at the equilibrium becomes:

$$\varepsilon_\phi^2\frac{d^2\phi_{\mathrm{eq}}}{d^2x}=wh'\left(\phi_{\mathrm{eq}}\right). \tag{2.93}$$

This equation can be transformed in

$$\frac{\varepsilon_\phi^2}{2}\left(\frac{d\phi_{\mathrm{eq}}}{dx}\right)^2=wh\left(\phi_{\mathrm{eq}}\right). \tag{2.94}$$

By integration of Eq.(2.94) from $x=-\infty$ to $x=\infty$ with the double-well function $h(\phi)=\phi^2(1-\phi)^2$ and the following boundary conditions

$$\begin{aligned} x=-\infty\,,\quad \phi=1\,,\quad h\left(1\right)=0\,,\\ x=\infty\,,\quad \phi=0\,,\quad h\left(0\right)=0\,, \end{aligned} \tag{2.95}$$

we can get the PFV profile at the equilibrium

$$\phi_{\mathrm{eq}}=\frac{1}{2}\left[1-\tanh\left(\frac{\sqrt{w}}{\varepsilon_\phi\sqrt{2}}x\right)\right]. \tag{2.96}$$

Interface Energy

The interface energy for an equilibrium interface, with the concentration profile $c_{\mathrm{eq}}\left(x\right)$ Eq.(2.92) and the PFV $\phi_{\mathrm{eq}}\left(x\right)$ Eq.(2.96), can be calculated by

$$\sigma=\int\limits_{-\infty}^{\infty}\left[\frac{\varepsilon_\phi^2}{2}\left(\frac{d\phi_{\mathrm{eq}}}{dx}\right)^2+wh\left(\phi_{\mathrm{eq}}\right)\right]dx\,. \tag{2.97}$$

There are two interface energy contributions: (i) the first one is due to the gradient-energy term; this contribution tends to spread the interface region and thereby reduce the order parameter gradient between its stable values in adjacent phases and (ii) the second one is due to the chemical free energy associated with the energy hump; this contribution tends to narrow the interface region.

By using Eq.(2.94) the interface energy is

$$\sigma = \varepsilon_\phi^2 \int\limits_{-\infty}^{\infty} \left(\frac{d\phi_{\text{eq}}}{dx} \right)^2 dx \,. \tag{2.98}$$

For an interface at equilibrium, the gradient-energy term is half of the total interface energy.

Analytical expressions for the interface energy in terms of the model parameters are only available for very simple cases when the analytical solution can be derived at equilibrium, i.e., where the profiles are known. In our case, the analytical solution of the interface energy can be obtained with the PFV at equilibrium Eq.(2.96) and the double-well function $h(\phi) = \phi^2 (1-\phi)^2$. From Eq.(2.94), we can obtain

$$dx = -\sqrt{\frac{\varepsilon_\phi^2}{2wh(\phi_{\text{eq}})}} d\phi \,. \tag{2.99}$$

Substituting Eqs.(2.94,2.99) into Eq.(2.98), and using the boundary conditions in Eq.(2.95), the interface energy is

$$\begin{aligned} \sigma = -\varepsilon_\phi^2 \int\limits_{1}^{0} \frac{2wh(\phi_{\text{eq}})}{\varepsilon_\phi^2} \sqrt{\frac{\varepsilon_\phi^2}{2wh(\phi_{\text{eq}})}} d\phi_{\text{eq}} = \\ -\sqrt{2w\varepsilon_\phi^2} \int\limits_{1}^{0} \phi_{\text{eq}} (1-\phi_{\text{eq}})\, d\phi_{\text{eq}} \,. \end{aligned} \tag{2.100}$$

By integrating Eq.(2.100), the relationship between the interface energy and model parameters can be obtained as

$$\sigma = \frac{\varepsilon_\phi \sqrt{w}}{3\sqrt{2}} \,. \tag{2.101}$$

Interface Thickness

The phase-field variable as a function of the one-dimensional coordinate at the equilibrium is written in Eq.(2.96). The inverse function is

$$x = \frac{\varepsilon_\phi \sqrt{2}}{\sqrt{w}} \operatorname{atanh}(1 - 2\phi_{\text{eq}}) \,. \tag{2.102}$$

The measure of the interface thickness δ, using the condition that the PFV is in the interval $(\lambda, 1-\lambda)$, can be written as

$$\delta = \frac{\varepsilon_\phi \sqrt{2}}{\sqrt{w}} \big\{ \operatorname{atanh}[1 - 2(1-\lambda)] - \operatorname{atanh}(1 - 2\lambda) \big\} \,. \tag{2.103}$$

The parameter λ determines the measure of the interface thickness. For example,

$$\lambda = 0.1\,, \quad \delta = 2.197\frac{\varepsilon_\phi\sqrt{2}}{\sqrt{w}}\,; \quad \lambda = 0.05\,, \quad \delta = 2.944\frac{\varepsilon_\phi\sqrt{2}}{\sqrt{w}}\,. \tag{2.104}$$

Usually, the measure of interface thickness is

$$\delta = 3\sqrt{2}\frac{\varepsilon_\phi}{\sqrt{w}}\,, \tag{2.105}$$

which guaranties that the PFV in the diffusion-interface region at equilibrium is in the interval $(0.05, 0.95)$. The measure of the interface thickness is written in the following text as the interface thickness only.

Phase-Field Mobility

The last model parameter explained in this section is the phase-field mobility. The relationship between the phase-field mobility and the interface-kinetic coefficient has to be found. The interface-kinetic coefficient is the proportional constant between the driving force for phase transformation and the interface velocity Eq.(1.16)

$$\frac{v_n}{\mu_\mathrm{k}} = -\frac{\Delta g_{\beta\alpha}}{V_\mathrm{m}}\,. \tag{2.106}$$

A relationship can be found at the thin-interface limit, where the interface thickness is small compared with the diffuse boundary layer. The complete derivation of the thin-interface limit of the presented model for solidification of binary alloys is derived in [Kim *et al.*, 1999]. The relationship between the interface-kinetic coefficient and the phase-field mobility is

$$\frac{1}{\mu_\mathrm{k}} = \frac{\sigma}{M_\phi\varepsilon_\phi^2} - \frac{\varepsilon_\phi}{D_\mathrm{int}\sqrt{2w}}\gamma\left(c_{\alpha\mathrm{eq}}, c_{\beta\mathrm{eq}}\right). \tag{2.107}$$

This relationship was derived under the assumption that the diffusivity is negligible in the phase β, and that the diffusivity D_int is constant within the interface region. The function γ is

$$\begin{aligned}\gamma\left(c_{\alpha\mathrm{eq}}, c_{\beta\mathrm{eq}}\right) \;=\;& \frac{\partial^2 f_\beta}{\partial c_\beta^2}\frac{\partial^2 f_\alpha}{\partial c_\alpha^2}\left(c_{\beta\mathrm{eq}} - c_{\alpha\mathrm{eq}}\right)^2 \\ & \int_0^1 \frac{p\left(\phi_\mathrm{eq}\right)\left(1 - p\left(\phi_\mathrm{eq}\right)\right)}{\left(1 - p\left(\phi_\mathrm{eq}\right)\right)\frac{\partial^2 f_\beta}{\partial c_\beta^{\mathrm{m}\,2}} + p\left(\phi_\mathrm{eq}\right)\frac{\partial^2 f_\alpha}{\partial c_\alpha^{\mathrm{m}\,2}}}\frac{d\phi_\mathrm{eq}}{\phi_\mathrm{eq}\left(1 - \phi_\mathrm{eq}\right)}.\end{aligned} \tag{2.108}$$

If we take that $\delta \sim \varepsilon_\phi/\sqrt{w} \rightarrow 0$, Eq.(2.107) is reduced to the sharp-interface limit condition

$$\mu_\mathrm{k} = \frac{M_\phi\varepsilon_\phi^2}{\sigma} = M_\phi\delta. \tag{2.109}$$

Model Parameters

The PFV profile related by the interface thickness at the equilibrium is computed by substituting Eq.(2.105) in Eq.(2.96)

$$\phi_{\mathrm{eq}} = \frac{1}{2}\left[1 - \tanh\left(\frac{3x}{\delta}\right)\right]. \tag{2.110}$$

From the interface energy Eq.(2.101) and the interface thickness Eq.(2.105), the model parameters such as the gradient energy coefficient ε_ϕ and the height of energy hump w are

$$\varepsilon_\phi^2 = \sigma\delta\,, \quad w = \frac{18\sigma}{\delta}\,. \tag{2.111}$$

The phase-field mobility at the sharp-interface limit condition Eq.(2.109) is

$$M_\phi = \frac{\mu_{\mathrm{k}}}{\delta}\,. \tag{2.112}$$

The phase-field equation, expressed by the physical properties and the interface thickness is

$$\frac{\partial\phi}{\partial t} = \frac{\mu_{\mathrm{k}}}{\delta}\left\{\sigma\left[\delta\nabla^2\phi - \frac{36}{\delta}\phi\left(1-\phi\right)\left(1-2\phi\right)\right] - 30\phi^2\left(1-\phi\right)^2\frac{\Delta g_{\beta\alpha}}{V_{\mathrm{m}}}\right\}. \tag{2.113}$$

2.3.4 Geometry Description of the Phase-Field Equation

A simple geometrically motivated derivation of the phase-field equation starting from the Gibbs-Thomson interface relation is presented in [Beckermann *et al.*, 1999]. The Gibbs-Thomson relation for an isotropic interface energy can be written as

$$\frac{v_n}{\mu_{\mathrm{k}}} = -2\sigma\kappa - \frac{\Delta g_{\beta\alpha}}{V_{\mathrm{m}}}\,. \tag{2.114}$$

The normal component of the interface velocity is

$$v_n = \vec{v}\cdot\vec{n}_{\beta\alpha} = \vec{v}\cdot\left(-\frac{\nabla\phi}{|\nabla\phi|}\right) = \frac{1}{|\nabla\phi|}\frac{\partial\phi}{\partial t}\,, \tag{2.115}$$

and the curvature is given by

$$\kappa = \frac{1}{2}\nabla\cdot\vec{n}_{\beta\alpha} = -\frac{1}{2|\nabla\phi|}\left(\nabla^2\phi - \frac{(\nabla\phi\cdot\nabla)|\nabla\phi|}{|\nabla\phi|}\right). \tag{2.116}$$

The PFV in the diffusion interface is

$$\phi = \frac{1}{2}\left[1 - \tanh\left(\frac{3n}{\delta}\right)\right], \tag{2.117}$$

where n is the coordinate normal to the interface. From Eq.(2.117), the following relationships can be obtained

$$|\nabla\phi| = \frac{\partial\phi}{\partial n} = \frac{6}{\delta}\phi\left(1-\phi\right), \quad \frac{(\nabla\phi\cdot\nabla)|\nabla\phi|}{|\nabla\phi|} = \frac{\partial^2\phi}{\partial^2 n} = \frac{36}{\delta^2}\phi\left(1-\phi\right)\left(1-2\phi\right). \tag{2.118}$$

The phase-field equation is derived by substituting Eqs.(2.115,2.116,2.118) into the Gibbs-Thomson relation Eq.(2.114). The phase-field equation becomes

$$\frac{\partial \phi}{\partial t} = \frac{\mu_{\mathrm{k}}}{\delta}\left\{\sigma\left[\delta\nabla^2\phi - \frac{36}{\delta}\phi\left(1-\phi\right)\left(1-2\phi\right)\right] - 6\phi\left(1-\phi\right)\frac{\Delta g_{\beta\alpha}}{V_{\mathrm{m}}}\right\}. \tag{2.119}$$

The first two terms in the phase-field equation are caused by the curvature effect: (i) the first contribution tends to spread and (ii) the second one tends to narrow the interface region. The third term is related to the thermodynamic driving force.

The phase-field equation derived directly from the Gibbs-Thomson interface relation Eq.(2.119) is identical to the phase-field equation derived from the Allen-Cahn equation Eq.(2.113), if we choose the interpolation function as $p\left(\phi\right) = \phi^2\left(3-2\phi\right)$ (Eq.(2.75)).

2.3.5 Summary

The phase-field equation for the evolution of the PFV is

$$\frac{\partial \phi}{\partial t} = M_\phi\left[\varepsilon_\phi^2\nabla^2\phi - 2w\phi\left(1-\phi\right)\left(1-2\phi\right) - 30\phi^2\left(1-\phi\right)^2\frac{\Delta g_{\beta\alpha}}{V_{\mathrm{m}}}\right]. \tag{2.120}$$

The model parameters in the phase-field equation are determined by the interface thickness and physical properties as

$$\varepsilon_\phi^2 = \sigma\delta, \quad w = \frac{18\sigma}{\delta}, \quad M_\phi = \frac{\mu_{\mathrm{k}}}{\delta}. \tag{2.121}$$

The driving force in the phase-field equation is computed from a thermodynamic database as

$$\Delta g_{\beta\alpha} = g_\beta - g_\alpha - \sum_{\mathrm{m}=1}^{\mathrm{M}-1}\frac{\partial g_\alpha}{\partial X_\alpha^{\mathrm{m}}}\left(X_\beta^{\mathrm{m}} - X_\alpha^{\mathrm{m}}\right), \tag{2.122}$$

and it is a function of concentration in the phases of the diffuse-interface region.

The concentrations in phases are computed by the definition of mixture concentration

$$c^{\mathrm{m}} = \phi c_\beta^{\mathrm{m}} + \left(1-\phi\right)c_\alpha^{\mathrm{m}}, \tag{2.123}$$

and by the condition that the phase diffusion potentials are equal in the phases

$$\frac{\partial f_\alpha}{\partial c_\alpha^{\mathrm{m}}} = \frac{\partial f_\beta}{\partial c_\beta^{\mathrm{m}}}. \tag{2.124}$$

If the phase β is stoichiometric with constant concentrations in the phase β, $\mathbf{c}_\beta = \mathbf{c}_\beta^{\mathrm{st}}$, then the concentration in the phase α can be computed using Eq.(2.123) only

$$c_\alpha^{\mathrm{m}} = \frac{c^{\mathrm{m}} - \phi c_\beta^{\mathrm{mst}}}{1-\phi}. \tag{2.125}$$

The concentration equations derived by the control-volume approach are used in this thesis. The concentration equation of component m, when the cross-diffusion terms in the interdiffusion coefficient matrix are neglected, is

$$\frac{\partial c^{\mathrm{m}}}{\partial t} = \nabla \cdot \left[(1-\phi) D_{\alpha}^{\mathrm{m}} \nabla c_{\alpha}^{\mathrm{m}} + \phi D_{\beta}^{\mathrm{m}} \nabla c_{\beta}^{\mathrm{m}} \right] . \tag{2.126}$$

As conclusions, the set of governing equations arising from the two physical models, initial and boundary conditions are summarized in Table 2.1.

Table 2.1: The set of equations arising from the two physical models, initial and boundary conditions.

TDA		**PFM**	
General	Stoichiometric Phase	General	Stoichiometric Phase
Concentration Equations in Phases		Concentration Equations in Whole System	
$\frac{\partial c_\varphi^{\mathrm{m}}}{\partial t} = D_\varphi^{\mathrm{m}} \nabla^2 c_\varphi^{\mathrm{m}} \;\; \varphi = \alpha, \beta$ $\mathrm{m} = 1, 2, \ldots, \mathrm{M}-1$	$\frac{\partial c_\alpha^{\mathrm{m}}}{\partial t} = D_\alpha^{\mathrm{m}} \nabla^2 c_\alpha^{\mathrm{m}}$ $\mathrm{m} = 1, 2, \ldots, \mathrm{M}-1$	$\frac{\partial c^{\mathrm{m}}}{\partial t} = \nabla \cdot \left[(1-\phi) D_\alpha^{\mathrm{m}} \nabla c_\alpha^{\mathrm{m}} + \phi D_\beta^{\mathrm{m}} \nabla c_\beta^{\mathrm{m}}\right]$ $\mathrm{m} = 1, 2, \ldots, \mathrm{M}-1$	
Local Thermodynamic Equilibrium at Interface		Phase-Field Equation	
$\mu_\alpha^{\mathrm{m}}\left(T, \mathbf{c}_{\alpha\mathrm{I}}\right) = \mu_\beta^{\mathrm{m}}\left(T, \mathbf{c}_{\beta\mathrm{I}}\right)$	$g_\alpha\left(T, \mathbf{c}_{\alpha\mathrm{I}}\right) = 0$ $\prod_{\mathrm{m}=1}^{\mathrm{M}-1} \left(X_{\alpha\mathrm{I}}^{\mathrm{m}}\right)^{X_\beta^{\mathrm{m}}} = K\left(T\right)$	$\frac{\partial \phi}{\partial t} = M_\phi [\varepsilon_\phi^2 \nabla^2 \phi - 2w\phi\left(1-\phi\right)\left(1-2\phi\right) -$ $30\phi^2\left(1-\phi\right)^2 \frac{\Delta g_{\beta\alpha}}{V_{\mathrm{m}}}]$	
Mass Conservation Equations at Interface		Driving Force for Phase Transformation	
$\left(c_{\beta\mathrm{I}}^{\mathrm{m}} - c_{\alpha\mathrm{I}}^{\mathrm{m}}\right) v_n = \vec{J}_{\beta\mathrm{I}}^{\mathrm{m}} \cdot \vec{n}_{\beta\alpha} - \vec{J}_{\alpha\mathrm{I}}^{\mathrm{m}} \cdot \vec{n}_{\beta\alpha}$ $\mathrm{m} = 1, 2, \ldots, \mathrm{M}-1$	$\left(c_{\beta\mathrm{I}}^{\mathrm{m}} - c_{\alpha\mathrm{I}}^{\mathrm{m}}\right) v_n = -\vec{J}_{\alpha\mathrm{I}}^{\mathrm{m}} \cdot \vec{n}_{\beta\alpha}$ $\mathrm{m} = 1, 2, \ldots, \mathrm{M}-1$	$\Delta g_{\beta\alpha} = g_\beta - g_\alpha - \sum_{\mathrm{m}=1}^{\mathrm{M}-1} \frac{\partial g_\alpha}{\partial X_\alpha^{\mathrm{m}}} \left(X_\beta^{\mathrm{m}} - X_\alpha^{\mathrm{m}}\right)$	
		Concentrations in Phases	
		$c^{\mathrm{m}} = \phi c_\beta^{\mathrm{m}} + \left(1-\phi\right) c_\alpha^{\mathrm{m}}$	
		$\frac{\partial f_\alpha}{\partial c_\alpha^{\mathrm{m}}} = \frac{\partial f_\beta}{\partial c_\beta^{\mathrm{m}}}$	$c_\alpha^{\mathrm{m}} = \frac{c^{\mathrm{m}} - \phi c_\beta^{\mathrm{mst}}}{1-\phi}$
Initial Conditions			
$c_\varphi^{\mathrm{m}}(\vec{p}, t_0)\,; \quad \mathrm{m} = 1, 2, \ldots, \mathrm{M}-1$ $l_{\beta\alpha}(t_0)$			
Boundary Conditions			
$\nabla c_\varphi^{\mathrm{m}} \cdot \vec{n}_\Gamma = 0\,; \quad \mathrm{m} = 1, 2, \ldots, \mathrm{M}-1$			

3 Solution Procedures

The solution procedures for solving the physical models are explained in this chapter. The governing equations of the TDA and PFM are deeply different, consequently the solution procedures of the mentioned methods are different, and are separately explained.

The TDA requires the use of the so-called moving-grid or front-tracking numerical schemes in order to capture the moving boundary. The well-known front-tracking method for the solution of the governing equations of the TDA in one-dimensional geometry is shortly presented. The results computed by this procedure are used as the reference results for the estimation of the results computed by the PFM.

The PFM is solved by the two solution procedures, the classical finite difference method and the advanced meshfree method. The finite difference discretization of the governing equations is briefly presented.

The local collocation by radial basis functions, as new solution procedure, for solving the general PDE are explained in more detail. This advanced numerical scheme is implemented for the solution of the PFM. Application of the meshless method on an r-adaptive node arrangement strategy is pointed out.

3.1 Solution of the TDA using the Front-Tracking Method

The TDA requires the existence of a discrete boundary between phases in the computational domain. The primary difficulty associated with its implementation is tracking the moving interphase interface. The solution procedure is presented for the phase transformations with a stoichiometric phase only, but expanding to general phase transformations is straightforward. The physical model based on the TDA for the phase transformations of the stoichiometric phase consists of:

- mass diffusion equations in the phase α

$$\frac{\partial c_\alpha^{\mathrm{m}}}{\partial t} = D_\alpha^{\mathrm{m}} \frac{\partial^2 c_\alpha^{\mathrm{m}}}{\partial x^2}\,; \quad \mathrm{m} = 1, 2, \ldots, \mathrm{M} - 1, \tag{3.1}$$

- the local thermodynamic equilibrium condition at the interface

$$g_\alpha \left(T, \mathbf{c}_{\alpha\mathrm{I}}\right) = 0, \tag{3.2}$$

- mass conservation equations at the interface

$$\left(c_{\beta}^{\mathrm{m,st}} - c_{\alpha\mathrm{I}}^{\mathrm{m}}\right) v = D_{\alpha}^{\mathrm{m}} \frac{\partial c_{\alpha}^{\mathrm{m}}}{\partial x}\bigg|_{\mathrm{I}}; \quad \mathrm{m} = 1, 2, \ldots, \mathrm{M}-1. \tag{3.3}$$

The left side of the mass conservation equation for each component is equal, and the system Eq.(3.3) can be reorganised such that the interface velocity does not exist in $\mathrm{M}-2$ independent equations:

$$D_{\alpha}^{\mathrm{m}-1} \frac{\partial c_{\alpha}^{\mathrm{m}-1}}{\partial x}\bigg|_{\mathrm{I}} = D_{\alpha}^{\mathrm{m}} \frac{\partial c_{\alpha}^{\mathrm{m}}}{\partial x}\bigg|_{\mathrm{I}}; \quad \mathrm{m} = 2, \ldots, \mathrm{M}-1\,, \tag{3.4}$$

$$\left(c_{\beta}^{1,\mathrm{st}} - c_{\alpha\mathrm{I}}^{1}\right) v = D_{\alpha}^{1} \frac{\partial c_{\alpha}^{1}}{\partial x}\bigg|_{\mathrm{I}}. \tag{3.5}$$

The above system, that represents the mass conservation at the interface is used in the solution procedure.

The one-dimensional system with length l_{Γ} is considered. The interphase interface position between the phases is denoted by $l_{\beta\alpha}$. Since the interface is moved, the variable $l_{\beta\alpha}$ changes with time while l_{Γ} remains constant. The moving grid transformation is implemented to allow the grid to move with the interphase interface, an approach introduced in [Murray and Landis, 1959]. The method is referred to in this thesis as the Front-Tracking Method (FTM). The moving grid enables the implementation of the moving boundary conditions described by Eq.(3.3) very easily, because the node in the moving grid coincides with the moving interface position $l_{\beta\alpha}$. Numerical modelling of the diffusion-controlled phase transformation in a ternary system based on coordinate transformation is presented in [Vitek *et al.*, 1995]. The coordinate transformation is done as

$$\xi_{\alpha}(t) = \frac{x - l_{\beta\alpha}(t)}{l_{\Gamma} - l_{\beta\alpha}(t)}\,, \tag{3.6}$$

where x and ξ_{α} are the horizontal Cartesian coordinate and spatial transformation coordinates, respectively. The spatial transformation coordinate is a function of time, $\xi_{\alpha} = \xi_{\alpha}(t)$. The coordinate transformation transforms the partial derivatives in the governing equations Eqs.(3.1,3.3) into the forms

$$\begin{aligned}
\frac{\partial c_{\alpha}^{\mathrm{m}}(x,t)}{\partial t} &= \frac{\partial c_{\alpha}^{\mathrm{m}}(\xi_{\alpha},t)}{\partial \xi_{\alpha}} \frac{\partial \xi_{\alpha}}{\partial t} + \frac{\partial c_{\alpha}^{\mathrm{m}}(\xi_{\alpha},t)}{\partial t}\,, \\
\frac{\partial c_{\alpha}^{\mathrm{m}}}{\partial x} &= \frac{\partial c_{\alpha}^{\mathrm{m}}}{\partial \xi_{\alpha}} \frac{\partial \xi_{\alpha}}{\partial x} = \frac{1}{(l_{\Gamma} - l_{\beta\alpha})} \frac{\partial c_{\alpha}^{\mathrm{m}}}{\partial \xi_{\alpha}}\,, \\
\frac{\partial^2 c_{\alpha}^{\mathrm{m}}}{\partial x^2} &= \frac{\partial^2 c_{\alpha}^{\mathrm{m}}}{\partial \xi_{\alpha}^2} \frac{\partial^2 \xi_{\alpha}}{\partial x^2} = \frac{1}{(l_{\Gamma} - l_{\beta\alpha})^2} \frac{\partial^2 c_{\alpha}^{\mathrm{m}}}{\partial \xi_{\alpha}^2}.
\end{aligned} \tag{3.7}$$

Now, the mass diffusion equations (Eq.(3.1)) and the mass conservation equations at the interface (Eq.(3.3)) described by the transformation coordinate are

$$\frac{\partial c_{\alpha}^{\mathrm{m}}}{\partial t} = \frac{D_{\alpha}^{\mathrm{m}}}{(l_{\Gamma} - l_{\beta\alpha})^2} \frac{\partial^2 c_{\alpha}^{\mathrm{m}}}{\partial \xi_{\alpha}^2} - \frac{\partial c_{\alpha}^{\mathrm{m}}}{\partial \xi_{\alpha}} \frac{\partial \xi_{\alpha}}{\partial t}\,, \tag{3.8}$$

$$\left(c_\beta^{\mathrm{m,st}} - c_{\alpha\mathrm{I}}^{\mathrm{m}}\right) v = \frac{D_\alpha^{\mathrm{m}}}{\left(l_\Gamma - l_{\beta\alpha}\right)} \frac{\partial c_\alpha^{\mathrm{m}}}{\partial \xi_\alpha}\bigg|_{\mathrm{I}}. \tag{3.9}$$

The first term on the right hand side of Eq.(3.8) corresponds to the right hand side of Eq.(3.1), while the second term is the correction due to the Murray-Landis coordinate transformation (Eq.(3.6)).

The fields in the matrix phase α are discretized by the equidistant $N_\alpha + 1$ nodes. By using the transformation Eq.(3.6), the nodes $\xi_{\alpha,1}$ and $\xi_{\alpha,N_\alpha+1}$ coincide with the interface position $l_{\beta\alpha}$ and the exterior boundary l_Γ, respectively. The time dependent spatial step and the position at the point i, expressed by the transformation coordinate are

$$\Delta\xi_\alpha\left(t\right) = \frac{l_\Gamma - l_{\beta\alpha}}{N_\alpha}, \quad \xi_{\alpha,i} = \frac{\left(i-1\right)\Delta\xi_\alpha}{l_\Gamma - l_{\beta\alpha}}. \tag{3.10}$$

The discretization in the one-dimensional system with the concentration profile of component m is presented in Fig.(3.1).

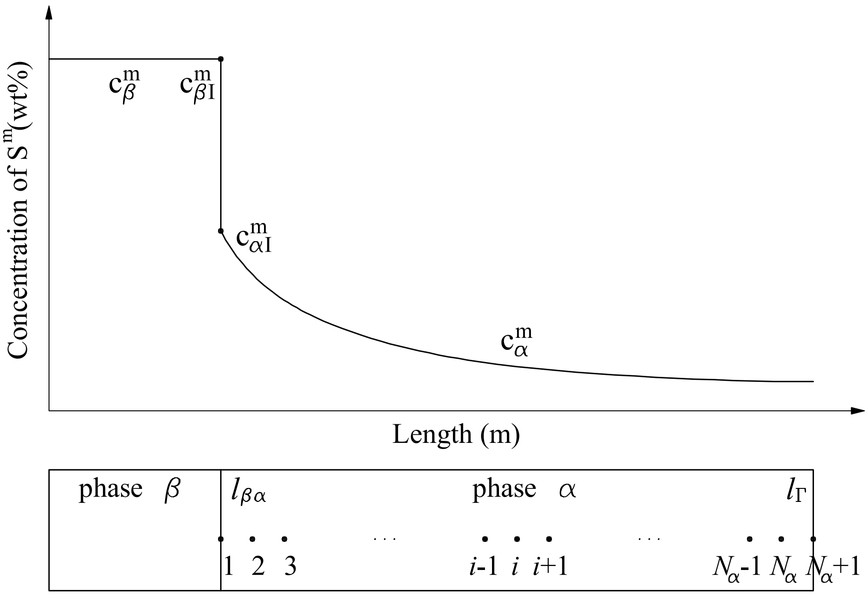

Figure 3.1: The transformation coordinate discretization in the phase α and concentration profile of component m in the one-dimensional geometry.

The governing equations are discretized by the implicit scheme in time. The first derivative in time at node i is discretized as

$$\frac{\partial u}{\partial t}\bigg|_i^{k+1} \propto \frac{u_i^{k+1} - u_i^k}{\Delta t}, \tag{3.11}$$

where u represents an unknown field, Δt represents the time-step length, and the superscripts k and $k+1$ represent the previous and new time steps, respectively.

An iterative solution procedure is performed, because the nonlinearity is introduced throughout the thermodynamic equilibrium condition at the interface (Eq.3.2). For the first iteration, the interface velocity v and the interface concentrations in the phase α $c^{\mathrm{m}}_{\alpha\mathrm{I}}$ in the new time step are presumed from the previous time step values. This enables the spatial discretization of mass diffusion equations, because the starting grid in the new time step is formed. The second-order finite difference discretization of mass diffusion equations in the phase α at nodes $2, \dots, \mathrm{N}_\alpha$ are

$$\begin{aligned}\frac{c^{\mathrm{m},k+1}_{\alpha,i}-c^{\mathrm{m},k}_{\alpha,i}}{\Delta t} = {} & \frac{D^{\mathrm{m}}_{\alpha}}{\left(l_\Gamma - l^{k+1}_{\beta\alpha}\right)^2}\frac{c^{\mathrm{m},k+1}_{\alpha,i+1}-2c^{\mathrm{m},k+1}_{\alpha,i}+c^{\mathrm{m},k+1}_{\alpha,i-1}}{\Delta\xi^{k+1^2}_{\alpha}} - \\ & \frac{c^{\mathrm{m},k+1}_{\alpha,i+1}-c^{\mathrm{m},k+1}_{\alpha,i-1}}{2\Delta\xi^{k+1}_{\alpha}}\frac{\xi^{k+1}_{\alpha,i}-\xi^{k}_{\alpha,i}}{\Delta t}; \quad i=2,3,\dots,N_\alpha.\end{aligned} \tag{3.12}$$

The discretization of the Neumann boundary condition on the exterior boundary by the second-order finite difference scheme [Özisik, 1994] is

$$\frac{3c^{\mathrm{m},k+1}_{\alpha,N_\alpha+1}-4c^{\mathrm{m},k+1}_{\alpha,N_\alpha}+c^{\mathrm{m},k+1}_{\alpha,N_\alpha-1}}{2\Delta\xi^{k+1}_{\alpha}} = 0\,. \tag{3.13}$$

From Eqs.(3.12,3.13), the concentration of each component m and at each node at the new time step $k+1$ can be computed.

The thermodynamic interface condition Eq.(3.2) and the reorganised system of interface conditions Eq.(3.4) consists of the system of $\mathrm{M}-1$ nonlinear equations with $\mathrm{M}-1$ unknowns: interface concentrations $c^{\mathrm{m},k+1}_{\alpha\mathrm{I}}$, $\mathrm{m}=1,2,\dots,\mathrm{M}-1$. The discretized system by the second-order finite difference scheme is

$$g_\alpha\left(c^{\mathrm{m},k+1}_{\alpha\mathrm{I}},\ \mathrm{m}=1,2,\dots,\mathrm{M}-1\right)=0\,, \tag{3.14}$$

$$D^{\mathrm{m}-1}_{\alpha}\frac{-3c^{\mathrm{m}-1,k+1}_{\alpha\mathrm{I}}+4c^{\mathrm{m}-1,k+1}_{\alpha,2}-c^{\mathrm{m}-1,k+1}_{\alpha,3}}{2\Delta{\xi_\alpha}^{k+1}} = D^{\mathrm{m}}_{\alpha}\frac{-3c^{\mathrm{m},k+1}_{\alpha\mathrm{I}}+4c^{\mathrm{m},k+1}_{\alpha,2}-c^{\mathrm{m},k+1}_{\alpha,3}}{2\Delta{\xi_\alpha}^{k+1}}\,. \tag{3.15}$$

In order to solve such a system of equations, an analytical function that represents the thermodynamic interface condition Eq.(3.2) needs to be carefully prepared. The interpolation is implemented by the radial basis function for accurate representation of the thermodynamic interface condition. This interpolation allows for the very accurate and simple calculation of the partial derivatives with respect to the particular component concentration. Such a defined interface condition enables the solution of the system of equations Eqs.(3.15,3.14) by the Newton-Rapson numerical procedure.

When the interface concentrations are calculated, the interface velocity at the new iteration $dl/dt^{k+1,n}$ is computed from Eq.(3.5):

$$\left(c^{1,\mathrm{st}}_{\beta}-c^{1}_{\alpha\mathrm{I}}\right)v^{k+1,n} = \frac{D^{1}_{\alpha}}{l_\Gamma - l^{k+1}_{\beta\alpha}}\frac{-3c^{1,k+1}_{\alpha,\mathrm{I}}+4c^{1,k+1}_{\alpha,2}-c^{1,k+1}_{\alpha,3}}{2\Delta{\xi_\alpha}^{k+1}}, \tag{3.16}$$

the superscript n represents the value at the new iteration. If the difference between the interface velocity in the new and previous iteration is higher than the prescribed small value ϵ, the computation at time step $k+1$ is performed again. The interface velocity in the new iteration is used for the new grid redistribution, $v^{k+1} = v^{k+1,n}$.

This computation is performed until the computation time is equal to the final time. The algorithm of the proposed solution procedure is presented in Fig.(3.2).

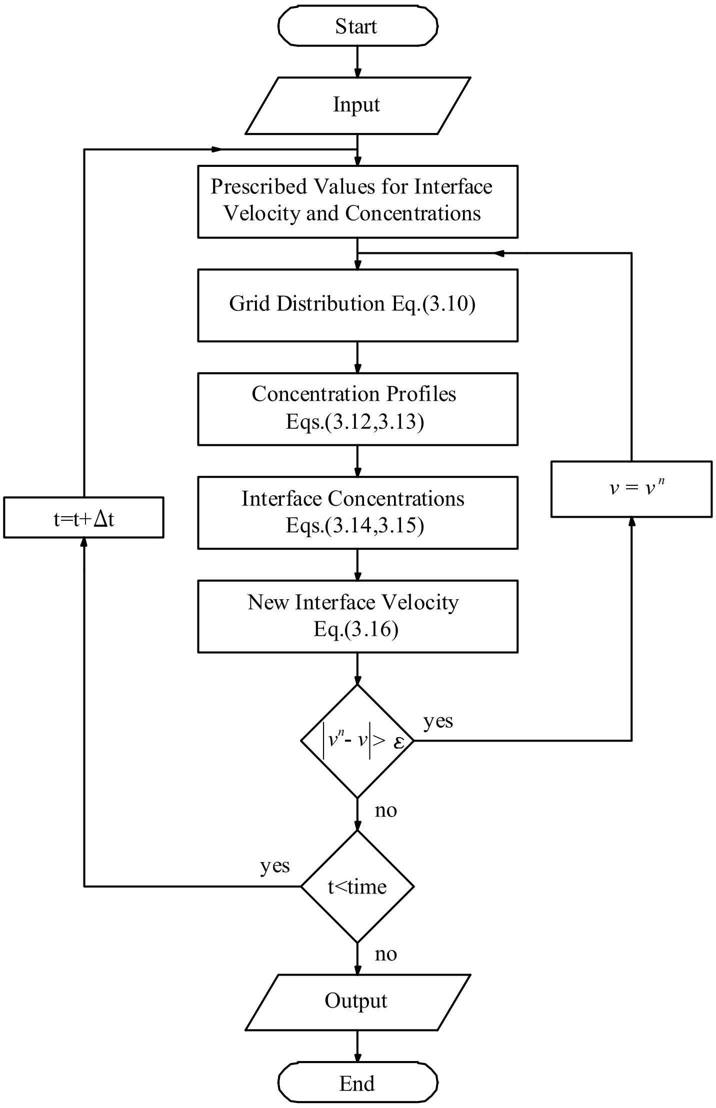

Figure 3.2: Flow chart of the solution procedure for the FTM.

3.2 Solution of the PFM using the Finite Difference Method

The PFM consists of the phase-field equation and the concentration equation for each independent component. The phase-field equation for the evolution of the PFV is

$$\frac{\partial \phi}{\partial t} = M_\phi \left[\varepsilon_\phi^2 \nabla^2 \phi - 2w\phi \left(1-\phi\right)\left(1-2\phi\right) - 30\phi^2 \left(1-\phi\right)^2 \frac{\Delta g_{\beta\alpha}}{V_\mathrm{m}} \right] \tag{3.17}$$

and the concentration equation for component m, derived by the control-volume approach, is

$$\frac{\partial c^\mathrm{m}}{\partial t} = \nabla \cdot \left[(1-\phi) D_\alpha^\mathrm{m} \nabla c_\alpha^\mathrm{m} + \phi D_\beta^\mathrm{m} \nabla c_\beta^\mathrm{m} \right]. \tag{3.18}$$

The solution procedure for computation of the molar driving force for phase transformation $\Delta g_{\beta\alpha}$ in Eq.(3.17) is needed to solve these equations, and it is explained first. The same procedure is used for both solution procedures for solving the PFM.

The molar driving force for the isothermal phase transformation introduced in Eq.(2.69) is

$$\Delta g_{\beta\alpha} \left(\mathbf{X}_\alpha, \mathbf{X}_\beta\right) = g_\beta \left(\mathbf{X}_\beta\right) - g_\alpha \left(\mathbf{X}_\alpha\right) - \sum_{\mathrm{m}=1}^{\mathrm{M}-1} \frac{\partial g_\alpha}{\partial X_\alpha^\mathrm{m}} \left(\mathbf{X}_\alpha\right) \left(X_\beta^\mathrm{m} - X_\alpha^\mathrm{m}\right). \tag{3.19}$$

It is, in general, a function of the concentration in both phases, where the temperature is known.

If the second phase β is stoichiometric, then the concentration vector in the phase α is computed explicitly from the mixture concentration vector in the interface region (Eq.(2.123)):

$$\mathbf{c}_\alpha = \frac{\mathbf{c} - \phi \mathbf{c}_\beta^\mathrm{st}}{1-\phi}. \tag{3.20}$$

In this example, the molar driving force is the function of concentration vector in the phase α only:

$$\Delta g_{\beta\alpha} = \Delta g_{\beta\alpha} \left(\mathbf{c}_\alpha\right). \tag{3.21}$$

We do not use a direct link to a thermodynamic database, and the specific data for the phase transformation have to be prepared before modelling. The molar driving force is calculated for the concentration vector in the phase α in a discretized or tabular form, where the data are obtained from the thermodynamic database. The values are calculated over the finite number of points N:

$$\Delta g_{\beta\alpha,n} = \Delta g_{\beta\alpha} \left(\mathbf{c}_{\alpha,n}\right); \quad n = 1, 2, \ldots N. \tag{3.22}$$

The accurate calculation of the molar driving force for an arbitrary concentration vector in the phase α is crucial for qualitative simulation by the PFM. The values of the molar driving force need to be accurately approximated. This is enabled by using the radial basis function interpolation to get a very accurate analytical function of the molar driving force as a function of the concentration vector in the phase α. The interpolation is in the form

$$\Delta g_{\beta\alpha}\left(\mathbf{c}_{\alpha}\right)=\sum_{n=1}^{N}\varsigma_{n}\psi_{n}\left(\left\|\mathbf{c}_{\alpha}-\mathbf{c}_{\alpha,n}\right\|\right), \tag{3.23}$$

where ψ_n and ς_n are the radial basis function and its coefficient, respectively. The radial basis function is the function of distance between the concentration vector $\mathbf{c}_\alpha$ where the value of the driving force needs to be computed and its centre $\mathbf{c}_{\alpha,n}$. By using this interpolation, the number of points N where the values of the molar driving force are calculated can be reasonably small. The implementation for multicomponent systems is straightforward. Also, temperature can be included in the interpolation.

If the phase β is nonstoichiometric, concentration vectors of the phases need to be solved from the system of nonlinear equations:

$$c^{\mathrm{m}}=\left(1-\phi\right)c_{\alpha}^{\mathrm{m}}+\phi c_{\beta}^{\mathrm{m}}\,;\quad \mathrm{m}=1,2,\ldots,\mathrm{M}-1, \tag{3.24}$$

$$\mu_{\alpha}^{\mathrm{m}}\left(\mathbf{c}_{\alpha}\right)-\mu_{\alpha}^{\mathrm{M}}\left(\mathbf{c}_{\alpha}\right)=\mu_{\beta}^{\mathrm{m}}\left(\mathbf{c}_{\beta}\right)-\mu_{\beta}^{\mathrm{M}}\left(\mathbf{c}_{\beta}\right);\quad \mathrm{m}=1,2,\ldots,\mathrm{M}-1. \tag{3.25}$$

The first equation Eq.(3.24) represents the definition of the mixture concentration vector, and the second one Eq.(3.25) requires that the local phase diffusion potentials in phases are equal. The solution of this system is the concentration vectors in phases. This system needs to be solved at each point in the diffuse-interface region. For the solution of this system, the chemical potentials of components, in particular phases as functions of the concentration vector, need to be approximated. The chemical potentials of components in the particular phase are prepared in a discretized or tabular form for a finite number of points

$$\mu_{\varphi,n}^{\mathrm{m}}=\mu_{\varphi}^{\mathrm{m}}\left(\mathbf{c}_{\varphi,n}\right);\quad n=1,2,\ldots,N_{\varphi}\,. \tag{3.26}$$

Now, the radial basis functions interpolation of the component chemical potentials in the phases is

$$\mu_{\varphi}^{\mathrm{m}}\left(\mathbf{c}_{\varphi}\right)=\sum_{n=1}^{N_{\varphi}}\varsigma_{\varphi,n}^{\mathrm{m}}\psi_{n}\left(\left\|\mathbf{c}_{\varphi}-\mathbf{c}_{\varphi,n}\right\|\right). \tag{3.27}$$

This interpolation allows for the very accurate and simple calculation of the partial derivatives with respect to the component concentration:

$$\frac{\partial\mu_{\varphi}^{\mathrm{m}}}{\partial c_{\varphi}^{\mathrm{m}}}\left(\mathbf{c}_{\varphi}\right)=\sum_{n=1}^{N_{\varphi}}\varsigma_{\varphi,n}^{\mathrm{m}}\frac{\partial\psi_{n}}{\partial c_{\varphi}^{\mathrm{m}}}\left(\left\|\mathbf{c}_{\varphi}-\mathbf{c}_{\varphi,n}\right\|\right). \tag{3.28}$$

The global interpolation by a multiquadric radial basis function is performed. These approximations enable using fast iterative solvers for the solution of the system of nonlinear equations Eqs.(3.24,3.25). The modified Powell hybrid algorithm from the IMSL library is used as a solver for the fast computation of concentration vectors at each point in the diffuse-interface region.

The molar driving force for phase transformation is computed with calculated concentration vectors in both phases from Eq.(3.19).

The governing equations (Eqs.(3.17,3.18)) are discretized by the explicit Euler scheme. The source term, which includes the driving force for phase transformation, is calculated at previous time step. The time discretization at the point (i,j) by the explicit Euler numerical scheme is

$$\left.\frac{\partial u}{\partial t}\right|_{i,j}^{k} \propto \frac{u_{i,j}^{k+1} - u_{i,j}^{k}}{\Delta t}. \tag{3.29}$$

The differential operators in the PFM (Eqs.(3.17,3.18)) are discretized in the two-dimensional Cartesian coordinate system by the Finite Difference Method (FDM) as

$$\begin{aligned}\nabla u &= \frac{\partial u}{\partial x}\vec{i} + \frac{\partial u}{\partial y}\vec{j}\,,\\ \nabla^2 u = \nabla\cdot(\nabla u) &= \left(\frac{\partial}{\partial x}\vec{i} + \frac{\partial}{\partial y}\vec{j}\right)\cdot\left(\frac{\partial u}{\partial x}\vec{i} + \frac{\partial u}{\partial y}\vec{j}\right) = \frac{\partial^2 u}{\partial x^2} + \frac{\partial^2 u}{\partial y^2}\,,\\ \nabla\cdot\vec{J}_u &= \left(\frac{\partial}{\partial x}\vec{i} + \frac{\partial}{\partial y}\vec{j}\right)\cdot\left(J_{u,x}\vec{i} + J_{u,y}\vec{j}\right) = \frac{\partial J_{u,x}}{\partial x} + \frac{\partial J_{u,y}}{\partial y}\,.\end{aligned} \tag{3.30}$$

The PFM is solved on the mesh with the spatial distance between points Δx and Δy on the x and y coordinates, respectively. The differential operators discretized at the point (i,j) by the spatial central finite difference are

$$\begin{aligned}\nabla u|_{i,j} &\propto \frac{u_{i+1/2,j} - u_{i-1/2,j}}{\Delta x}\vec{i} + \frac{u_{i,j+1/2} - u_{i,j-1/2}}{\Delta y}\vec{j}\,,\\ \nabla^2 u|_{i,j} &\propto \frac{u_{i+1,j} - 2u_{i,j} + u_{i-1,j}}{\Delta x^2} + \frac{u_{i,j+1} - 2u_{i,j} + u_{i,j-1}}{\Delta y^2}\,,\\ \nabla\cdot\vec{J}_u|_{i,j} &\propto \frac{J_{u,x,i+1/2,j} - J_{u,x,i-1/2,j}}{\Delta x} + \frac{J_{u,y,i,j+1/2} - J_{u,y,i,j-1/2}}{\Delta y}\,.\end{aligned} \tag{3.31}$$

The values between grid points are calculated by the linear interpolation, for example for x coordinate:

$$u|_{i\pm1/2,j} = \frac{u_{i\pm1,j} + u_{i,j}}{2}\,. \tag{3.32}$$

The Neumann boundary condition in the two-dimensional Cartesian coordinate system is written as

$$\nabla u\cdot\vec{n}_\Gamma = \left(\frac{\partial u}{\partial x}\vec{i} + \frac{\partial u}{\partial y}\vec{j}\right)\cdot\left(n_{\Gamma x}\vec{i} + n_{\Gamma y}\vec{j}\right) = \frac{\partial u}{\partial x}n_{\Gamma x} + \frac{\partial u}{\partial y}n_{\Gamma y}. \tag{3.33}$$

The first derivatives in the boundary conditions, discretized by the second-order finite difference scheme, are

$$\nabla u \cdot \vec{n}_\Gamma|_{i,j} \propto \frac{\mp 3u_{i,j} \pm 4u_{i\pm1,j} \mp u_{i\pm2,j}}{2\Delta x} n_{\Gamma x} + \frac{\mp 3u_{i,j} \pm 4u_{i,j\pm1} \mp u_{i,j\pm2}}{2\Delta y} n_{\Gamma y}, \quad (3.34)$$

where the upper sign is used when the corresponding component of unit vector is negative, $n_{\Gamma\chi} < 0, \chi = x, y$ and vice versa.

The phase-field equation (Eq.(3.17)) with the pronounced source term S_ϕ is:

$$\frac{\partial \phi}{\partial t} = M_\phi \left[\varepsilon_\phi^2 \nabla^2 \phi - S_\phi\right], \; S_\phi = 2w\phi(1-\phi)(1-2\phi) + 30\phi^2(1-\phi)^2 \frac{\Delta g_{\beta\alpha}}{V_\mathrm{m}}. \quad (3.35)$$

The phase-field equation at the point (i, j) is discretized by the central finite difference in space and by the explicit Euler in time as:

$$\phi_{i,j}^{k+1} = \phi_{i,j}^k + \Delta t M_\phi \left[\varepsilon_\phi^2 \left(\frac{\phi_{i+1,j}^k - 2\phi_{i,j}^k + \phi_{i-1,j}^k}{\Delta x^2} + \frac{\phi_{i,j+1}^k - 2\phi_{i,j}^k + \phi_{i,j-1}^k}{\Delta y^2}\right) - S_{\phi,i,j}^k\right], \quad (3.36)$$

where the source term is

$$\begin{aligned} S_{\phi,i,j}^k &= 2w\phi_{i,j}^k\left(1-\phi_{i,j}^k\right)\left(1-2\phi_{i,j}^k\right) + 30{\phi_{i,j}^k}^2\left(1-\phi_{i,j}^k\right)^2 \frac{\Delta g_{\beta\alpha,i,j}^k}{V_\mathrm{m}}, \\ \Delta g_{\beta\alpha,i,j}^k &= \Delta g_{\beta\alpha}\left(\mathbf{c}_{\alpha,i,j}^k, \mathbf{c}_{\beta,i,j}^k\right). \end{aligned} \quad (3.37)$$

The concentration equation for component m (Eq.(3.18)), introducing the component flux $\vec{J}^\mathrm{m}$, is rewritten as

$$\frac{\partial c^\mathrm{m}}{\partial t} = \nabla \cdot \vec{J}^\mathrm{m}, \quad \vec{J}^\mathrm{m} = (1-\phi) D_\alpha^\mathrm{m} \nabla c_\alpha^\mathrm{m} + \phi D_\beta^\mathrm{m} \nabla c_\beta^\mathrm{m}. \quad (3.38)$$

The component flux in the two-dimensional Cartesian coordinate system is

$$J_x^\mathrm{m} = (1-\phi) D_\alpha^\mathrm{m} \frac{\partial c_\alpha^\mathrm{m}}{\partial x} + \phi D_\beta^\mathrm{m} \frac{\partial c_\beta^\mathrm{m}}{\partial x}, \quad J_y^\mathrm{m} = (1-\phi) D_\alpha^\mathrm{m} \frac{\partial c_\alpha^\mathrm{m}}{\partial y} + \phi D_\beta^\mathrm{m} \frac{\partial c_\beta^\mathrm{m}}{\partial y}. \quad (3.39)$$

The component flux is discretized at the point (i, j) by Eq.(3.31), where the fluxes are

$$\begin{aligned} J_{x,i+1/2,j}^\mathrm{m} &= \left(1 - \frac{\phi_{i,j} + \phi_{i+1,j}}{2}\right) D_\alpha^\mathrm{m} \frac{c_{\alpha,i+1,j}^\mathrm{m} - c_{\alpha,i,j}^\mathrm{m}}{\Delta x} + \frac{\phi_{i,j} + \phi_{i+1,j}}{2} D_\beta^\mathrm{m} \frac{c_{\beta,i+1,j}^\mathrm{m} - c_{\beta,i,j}^\mathrm{m}}{\Delta x} \\ J_{x,i-1/2,j}^\mathrm{m} &= \left(1 - \frac{\phi_{i-1,j} + \phi_{i,j}}{2}\right) D_\alpha^\mathrm{m} \frac{c_{\alpha,i,j}^\mathrm{m} - c_{\alpha,i-1,j}^\mathrm{m}}{\Delta x} + \frac{\phi_{i-1,j} + \phi_{i,j}}{2} D_\beta^\mathrm{m} \frac{c_{\beta,i,j}^\mathrm{m} - c_{\beta,i-1,j}^\mathrm{m}}{\Delta x} \\ J_{y,i,j+1/2}^\mathrm{m} &= \left(1 - \frac{\phi_{i,j} + \phi_{i,j+1}}{2}\right) D_\alpha^\mathrm{m} \frac{c_{\alpha,i,j+1}^\mathrm{m} - c_{\alpha,i,j}^\mathrm{m}}{\Delta y} + \frac{\phi_{i,j} + \phi_{i,j+1}}{2} D_\beta^\mathrm{m} \frac{c_{\beta,i,j+1}^\mathrm{m} - c_{\beta,i,j}^\mathrm{m}}{\Delta y} \\ J_{y,i,j-1/2}^\mathrm{m} &= \left(1 - \frac{\phi_{i,j-1} + \phi_{i,j}}{2}\right) D_\alpha^\mathrm{m} \frac{c_{\alpha,i,j}^\mathrm{m} - c_{\alpha,i,j-1}^\mathrm{m}}{\Delta y} + \frac{\phi_{i,j-1} + \phi_{i,j}}{2} D_\beta^\mathrm{m} \frac{c_{\beta,i,j}^\mathrm{m} - c_{\beta,i,j-1}^\mathrm{m}}{\Delta y}. \end{aligned} \quad (3.40)$$

The discretization of the concentration equation of component m at the point (i, j) by the second-order finite difference scheme in space and the explicit Euler in time is

$$
\begin{aligned}
c_{i,j}^{\mathrm{m},k+1} &= c_{i,j}^{\mathrm{m},k} + \Delta t \\
\Bigg\{ &\left(1 - \frac{\phi^k_{i,j} + \phi^k_{i+1,j}}{2}\right) D^{\mathrm{m}}_{\alpha} \frac{c^{\mathrm{m},k}_{\alpha,i+1,j} - c^{\mathrm{m},k}_{\alpha,i,j}}{\Delta x^2} + \frac{\phi^k_{i,j} + \phi^k_{i+1,j}}{2} D^{\mathrm{m}}_{\beta} \frac{c^{\mathrm{m},k}_{\beta,i+1,j} - c^{\mathrm{m},k}_{\beta,i,j}}{\Delta x^2} - \\
&\left(1 - \frac{\phi^k_{i-1,j} + \phi^k_{i,j}}{2}\right) D^{\mathrm{m}}_{\alpha} \frac{c^{\mathrm{m},k}_{\alpha,i,j} - c^{\mathrm{m},k}_{\alpha,i-1,j}}{\Delta x^2} + \frac{\phi^k_{i-1,j} + \phi^k_{i,j}}{2} D^{\mathrm{m}}_{\beta} \frac{c^{\mathrm{m},k}_{\beta,i,j} - c^{\mathrm{m},k}_{\beta,i-1,j}}{\Delta x^2} + \\
&\left(1 - \frac{\phi^k_{i,j} + \phi^k_{i,j+1}}{2}\right) D^{\mathrm{m}}_{\alpha} \frac{c^{\mathrm{m},k}_{\alpha,i,j+1} - c^{\mathrm{m},k}_{\alpha,i,j}}{\Delta y^2} + \frac{\phi^k_{i,j} + \phi^k_{i,j+1}}{2} D^{\mathrm{m}}_{\beta} \frac{c^{\mathrm{m},k}_{\beta,i,j+1} - c^{\mathrm{m},k}_{\beta,i,j}}{\Delta y^2} - \\
&\left(1 - \frac{\phi^k_{i,j-1} + \phi^k_{i,j}}{2}\right) D^{\mathrm{m}}_{\alpha} \frac{c^{\mathrm{m},k}_{\alpha,i,j} - c^{\mathrm{m},k}_{\alpha,i,j-1}}{\Delta y^2} + \frac{\phi^k_{i,j-1} + \phi^k_{i,j}}{2} D^{\mathrm{m}}_{\beta} \frac{c^{\mathrm{m},k}_{\beta,i,j} - c^{\mathrm{m},k}_{\beta,i,j-1}}{\Delta y^2} \Bigg\}.
\end{aligned}
\tag{3.41}
$$

The molar driving force is computed by Eq.(3.19) when the concentration vector in both phases are calculated. The values of the PFV and the concentration of each independent component in the domain points are computed by Eq.(3.36) and Eq.(3.41), respectively. The values at the boundary points are computed by Eq.(3.34). The solution procedure for solving the PFM by the FDM is presented in Fig.(3.3).

3.3 An Alternative to the Solution of the PFM: Implementing the Meshfree Method

In recent decades, a number of MeshFree Methods (MFMs) have been developed to circumvent the problem of polygonisation encountered in the classical numerical methods. In meshless or meshfree methods, the discretization is entirely constructed in a set of gridpoints. The MFMs can be classified into two major categories based on the formulation procedure: MFMs based on strong-form [Kansa, 1990a; Kansa, 1990b] and MFMs based on weak-form [Atluri, 2004]. Recently, MFMs based on strong and weak forms which use advantages of both categories have been developed [Liu and Gu, 2003]. The meshfree strong-form method is regarded as a truly MFM as the mesh is neither used in discretization nor in integration. The formulation procedure is rather simple and straightforward, compared to the weak-form method, but according to the literature [Liu, 2003; Liu and Gu, 2005], the strong-form methods are often found to be less stable than the weak-form methods.

The collocation with radial basis functions, a representative of meshfree strong-form methods, is analysed in this thesis. The method is truly meshfree, very simple, and easy to implement for solving various PDEs. The development and implementation of the method for an adaptive analysis is a logical step forward.

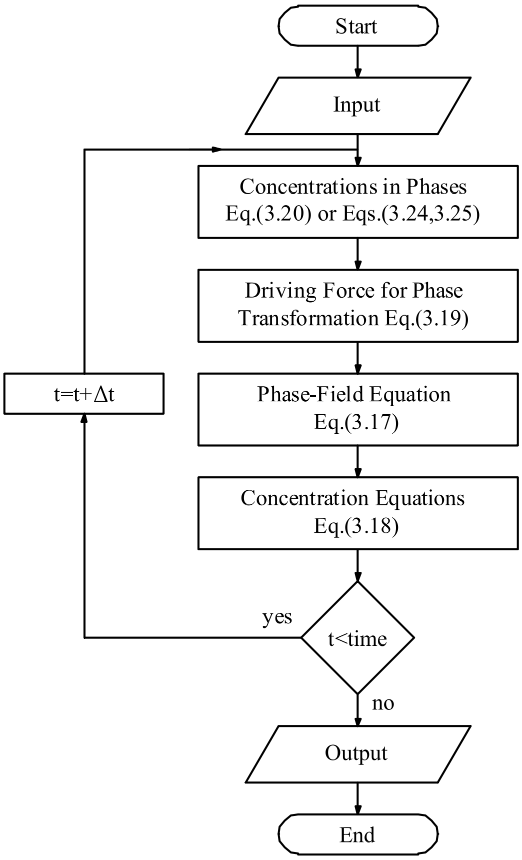

Figure 3.3: Flow chart of the solution procedure for the PFM.

Although, the collocation with radial basis functions could suffer from instability, we demonstrate that it can be sufficiently implemented for a carefully selected r-adaptive analysis. In the r-adaptation, the number of nodes remains constant throughout computations whereas positions of nodes are redistributed. Recently, authors [Liu *et al.*, 2006] claimed that the implementation for adaptive analysis is impossible and proposed a stabilized scheme based on least-squares when using collocation methods for adaptive analysis.

Radial Basis Functions (RBFs) were first intensively researched [Franke, 1982] in the areas of multivariate data and function interpolation. Franke found that global interpolation methods generally outperformed local interpolation methods in his elaborated analysis. Out of all the methods tested, Hardy's multiquadric RBFs gave the most accurate results on a spectrum of benchmark problems. Considering these results, Kansa focused on the multiquadric RBFs and argued that PDEs are intrinsically related to the interpolation scheme from which PDEs solvers are derived [Kansa, 1990a; Kansa, 1990b].

Interpolation of the fields on the boundary and in the domain by the Global

Radial Basis Function Collocation Method (GRBFCM) is obtained by a set of global functions and a subsequent representation of the partial derivatives by the partial derivatives of them. In these methods, the discretization is represented only on gridpoints, in contrast to finite element and finite volume methods (where the approximate polygonisation also needs to be generated) or FDM (where the points are constrained to the coordinate lines). The main disadvantage of the GRBFCM is in dealing with full large-sized matrices that can be ill-conditioned. Consequently, the implementation is confined to a relatively small number of gridpoints in the computational domain. The matrix of the system of linear equations arising from the GRBFCM usually has a very large condition number, and becomes increasingly ill-conditioned as the number of gridpoints increases. Also, the free parameter in RBFs has to be carefully selected in the collocation with the multiquadric RBFs.

Keeping in mind the drawback of implementation of the global interpolation numerical methods for solving PDEs, different approaches for overcoming the issues are proposed, such as compactly supported RBFs [Jumarhon *et al.*, 2000], domain decomposition [Kansa and Hon, 2000], local interpolation [Lee *et al.*, 2003; Lazzaro and Montefusco, 2002]... Currently, the most attractive and the most frequently used concept for meshfree strong-form method is local approximation of the solution, which easily overcomes problems with large full matrices. The concept of local approximation is extended for the collocation by RBFs, and the Local Radial Basis Function Collocation Method (LRBFCM) is derived for the solution of PDEs. Approximation of the fields and partial derivatives in the domain and on the boundary are obtained by using a small set of the RBFs with centres in the vicinity of the reference node where the solution needs to be found. This concept introduces local support of each domain and boundary node. The selection of points in the local support needs to be done earlier. Determination of the local support for each node, which may differ from node to node, represents another degree of freedom in the LRBFCM.

In the local MFMs, the function and its derivatives are approximated by a linear combination of a small number of RBFs with centres in the local support of the reference node and their coefficients. For every reference node, linear equations with a small number of unknown coefficients need to be solved. The system of obtained linear equations can be solved in two different ways. In the first one, each discretization equation for every reference node is assembled in a global, but most importantly, sparse matrix. The matrix size is equal to the total number of nodes in the computational system, the same as in the global collocation method [Liu, 2003]. The solution can be found by a sparse matrix solver. In the second one, for every reference node, a small system of linear equations is solved. The size of the system is equal to the number of nodes in the local support of the reference node [Lee *et al.*, 2003; Šarler and Vertnik, 2006]. The interpolation in the local concept is more difficult because of local support overlapping. If a point corresponds to several local supports, the value of the function at this point is collocated as the mean of the values from corresponding local supports. Here, the second way is chosen because of the matrix size.

This local concept of MFMs introduces the local support of each domain and boundary node. Two approaches for selection of the supporting nodes in a uniformly distributed node arrangement are well established. However, the selection of supporting points in a scattering node arrangement, especially in an adaptive node arrangement, is another poorly analysed problem that exists today. The selection procedure for supporting points in highly r-adaptive node arrangements needs to be developed.

In this thesis, the local interpolation or collocation for determination of unknown coefficients is performed. The local characteristics of the method enable the system to be employed with a large number of nodes. Also, it requires no extra effort in the division of the computational domain. Parallel with the collocation, the coefficients can be obtained from the approximation using the least squares formulation. In the literature, the method is known as the diffuse-approximate method. The implementation of this method in various transport phenomena is demonstrated in [Perko, 2005].

Instability is a fatal shortcoming of meshfree strong-form methods. Instability and poor accuracy (usually on the boundary) often arise, especially when derivative boundary conditions exist, and several techniques have been proposed to overcome instability in the meshfree strong-form methods [Liu and Gu, 2005]. The stability of the results is very sensitive to the determination of the local support, especially in the boundary nodes. Therefore, the local support for boundary nodes with the only one node, a reference node, is proposed on the boundary. Also, better stability of the results at the boundary is accomplished by using the collocation based on Hermite-type interpolation.

A very fine grid in the diffuse-interface region must be used for proper solving of the governing equations obtained by the PFM. If one uses a sufficiently fine equidistant mesh, the majority of the nodes are not coincident with the vicinity of the diffuse-interface region, and the computation time turns out to be enormous. This fact represents a principal motivation for introducing adaptive grids which could follow the migration of the interface. Adaptive approaches of finite element and FDM for the solution of the PFM have been applied in [Provatas *et al.*, 1999; Nestler *et al.*, 2005].

3.3.1 Radial Basis Functions

A RBF is a function $\psi : \Re^d \to \Re$, $\psi_i(r) = \psi(\|\vec{p} - \vec{p}_i\|)$, which depends only on the distance between the vector point $\vec{p} \in \Re^d$ and the fixed vector point $\vec{p}_i \in \Re^d$, referred to as a reference node. A RBF is a continuous, bounded function on any bounded subdomain $\Omega \subseteq \Re^d$. The function ψ_i is radial and symmetric about the vector point $\vec{p}_i$. The most frequently used RBFs to date are generalized MultiQuadric (MQ)

$$\psi(r) = \left(r^2 + \bar{c}^2\right)^{\bar{n}/2}, \tag{3.42}$$

with free parameters $\bar{c}$ and $\bar{n}$, the Thin-Plate Spline (TPS) of order $\bar{n}$

$$\psi(r) = r^{2(\bar{n}-1)} \log r \tag{3.43}$$

and Gaussian

$$\psi(r) = \exp\left(-\bar{\gamma} r^2\right) \tag{3.44}$$

with free parameter $\bar{\gamma}$. For example, in the case of the two-dimensional Cartesian coordinate system

$$\vec{p} = x\vec{i} + y\vec{j}, \tag{3.45}$$

x, y denote the Cartesian coordinates (base vectors $\vec{i}$, $\vec{j}$) of the vector point $\vec{p}$. The norm $\|\cdot\|$ is usually taken to be the Euclidean norm

$$\|\vec{p} - \vec{p}_i\| = \vec{p} \cdot \vec{p}_i = \sqrt{(x - x_i)^2 + (y - y_i)^2}, \tag{3.46}$$

although other norms are possible.

MQ functions with the values $\bar{n} = 1$ and $\bar{c} = 0$ are often referred to as conicals whilst those with $\bar{n} = 3$ and $\bar{c} = 0$ are referred to as Duchon cubics. All above RBFs are globally supported. If globally supported RBFs are used in the GRBFCM, the coefficient matrix is a full matrix, and usually poorly conditioned. The Gaussian and inverse MQ (i.e. $\bar{n} < 0$ in Eq.(3.42)) are positive definite functions, while TPS and MQ (i.e. $\bar{n} > 0$ in Eq.(3.42)) are conditionally positive definite functions of order $\bar{n}$. These functions require additional polynomial terms and homogeneous constraint conditions in order to assure an invertible coefficient matrix.

Hardy derived the two-dimensional MQ scheme to approximate geographical surfaces ($\bar{n} = 1$ in Eq.(3.42)), and today these RBFs are most frequently used

$$\psi(r) = \sqrt{r^2 + \bar{c}^2}\,. \tag{3.47}$$

Another frequently used form of MQ is the reciprocal MQ, $\bar{n} = -1$ in Eq.(3.42)

$$\psi(r) = \frac{1}{\sqrt{r^2 + \bar{c}^2}}\,. \tag{3.48}$$

MQ functions ware largely unknown to mathematicians until the publication of Franke's review paper [Franke, 1982]. Most mathematicians have not seriously studied this method because the mathematical analysis of MQ is very difficult, and it is presently not known why MQ performs so well for interpolation problems.

The value of the parameter $\bar{c}$ controls the shape of the MQ RBFs, and is denoted as a shape parameter. A large value of $\bar{c}$ gives rise to a flat sheet-like basis function, an intermediate $\bar{c}$ value gives rise to a bowl-like basis function, and small $\bar{c}$ values give rise to narrow cone-like basis functions.

The second group of the RBFs are compactly supported. If Compactly Supported (CS) positive definite RBFs are used, the coefficient matrix in the GRBFCM is sparse and positive definite. The additional polynomial term is not required when using the CS RBFs.

The most frequently used CS RBFs originate from Wendland, and are for the two-dimensional problems, [Jumarhon *et al.*, 2000]:

$$\psi(r) = (1-r)_+^3 (3r+1), \quad \psi(r) = (1-r)_+^5 \left(8r^2 + 5r + 1\right), \tag{3.49}$$

where

$$(1-r)_+ = \begin{cases} 1-r, & \text{if} \quad 0 \le r \le 1 \\ 0, & \text{if} \quad r > 1. \end{cases} \tag{3.50}$$

For upper functions, the size of the support of the CS RBFs is one. In a practical applications, a transformation

$$r = \|\vec{p} - \vec{p}_i\| = \sqrt{\left(\frac{x - x_i}{\bar{R}_i}\right)^2 + \left(\frac{y - y_i}{\bar{R}_i}\right)^2} \tag{3.51}$$

can be used to define the support for the CS RBFs, with a free parameter $\bar{R}_i$. The idea of using the CS RBFs is very good because the coefficient matrix is sparse, but the accuracy of the results obtained by the CS RBFs is lower than with the above defined global RBFs.

In the following, the MQ RBFs (Eq.(3.47)) are selected as the RBFs due to their excellent performance for the interpolation and very accurate results in PDEs computed by collocation on scattered node arrangements [Vertnik, 2007].

3.3.2 Interpolation by RBFs

In approximation problems, scattered data set $\mathbf{S} = \{(\vec{p}_i, F(\vec{p}_i)), \vec{p}_i \in \Omega, i = 1, 2, \ldots, N\}$ is assumed to be known. The local standard interpolation of a function $F(\vec{p})$ at an arbitrary point $\vec{p}$, close to the reference node $\vec{p}_i$, can be written in the following form

$$s(\vec{p}) \equiv \sum_{j=1}^{N_i} \varsigma_j \psi(\|\vec{p} - \vec{p}_j\|) + P(\vec{p}), \tag{3.52}$$

where N_i is the number of nodes in the local support of the reference node $\vec{p}_i$, ς_j are coefficients that must be determined, $\vec{p}_j$ are centres of RBFs in the same local support, and $P(\vec{p})$ is the additional polynomial term.

In the global collocation method, the number of nodes in the local support of every node is equal to the total number of points in the whole domain, i.e. $N_i = N$. In the local collocation method, the number of nodes in the local support is a free parameter and can be different from one reference node to another, but always $N_i \le N$. Selection of the supporting points in the local support is described later.

The polynomial term used in the above equation is defined as

$$P(\vec{p}) = \sum_{l=1}^{L_P} \varsigma_{N_i+l} w_l(\vec{p}), \tag{3.53}$$

where L_P is the length of the polynomial and $w_l(\vec{p})$ are basis polynomials for the space of polynomials of degree up to $\bar{n}-1$ in $\Re^d$. The length of polynomials in relation to the order of the RBF ($\bar{n}$) and the dimension of space (d) is:

$$L_P = \left(\begin{array}{c} \bar{n}+d-1 \\ d \end{array} \right). \tag{3.54}$$

For example, for $\bar{n}=3$ and $d=2$, the basis of additional polynomials $w_l(\vec{p})$ are:

$$\begin{array}{ccc} w_1(\vec{p}) = 1, & w_2(\vec{p}) = (x-x^0), & w_3(\vec{p}) = \left(y-y^0\right), \\ w_4(\vec{p}) = \left(x-x^0\right)^2, & w_5(\vec{p}) = (x-x^0)(y-y^0), & w_6(\vec{p}) = \left(y-y^0\right)^2. \end{array} \tag{3.55}$$

The scaling constants x_0, y_0 are set to

$$x^0 = \frac{1}{2}\left(x^+ + x^-\right), \quad y^0 = \frac{1}{2}\left(y^+ + y^-\right), \tag{3.56}$$

where x^+, y^+ represent the maximum, and x^-, y^- the minimum coordinates x, y of the local support, respectively. The scaling constants can be simply set to the coordinate of the reference node $\vec{p}_i$, $x^0 = x_i$ and $y^0 = y_i$.

The local support of the node $\vec{p}_i$ in the local MFMs is not the whole domain, such as in the global interpolation by RBFs. To obtain the values of coefficients ς_j, $j = 1, 2, \ldots, N_i + L_P$, the interpolation at each node $\vec{p}_n$ in the local support has been done by Eq.(3.52)

$$F(\vec{p}_n) = \sum_{j=1}^{N_i} \varsigma_j \psi\left(\|\vec{p}_n - \vec{p}_j\|\right) + \sum_{l=1}^{L_P} \varsigma_{N_i+l} w_l(\vec{p}_n); \quad n = 1, 2, \ldots, N_i. \tag{3.57}$$

In order to ensure the uniqueness of the interpolation, the following constraints are necessary,

$$\sum_{j=1}^{N_i} \varsigma_j w_l(\vec{p}_j) = 0; \quad l = 1, 2, \ldots, L_P. \tag{3.58}$$

The matrix formulation of the above local interpolation procedure for the reference node $\vec{p}_i$ can be written as

$$\boldsymbol{\Phi}_i \boldsymbol{\varsigma}_i = \mathbf{b}_i. \tag{3.59}$$

The symmetric interpolation or coefficient matrix is defined as

$$\boldsymbol{\Phi}_i = \left[\begin{array}{cc} (\psi_{nj})_{N_i \times N_i} & (w_{nl})_{N_i \times L_P} \\ (w_{nl})^{\mathrm{T}}_{L_P \times N_i} & (0)_{L_P \times L_P} \end{array} \right]_{\bar{N}_i \times \bar{N}_i}, \tag{3.60}$$

where $\psi_{nj} \equiv \psi\left(\|\vec{p}_n - \vec{p}_j\|\right)$, $w_{nl} \equiv w_l(\vec{p}_n)$, $n, j = 1, \ldots, N_i$ and $l = 1, 2, \ldots, L_P$. The coefficient matrix size is equal to the sum of the number of nodes in the local support of the reference node $\vec{p}_i$ and the length of the additional polynomial term, $\bar{N}_i = N_i + L_P$. The coefficient vector $\boldsymbol{\varsigma}_i$ and the right-hand side vector $\mathbf{b}_i$ are

$$\boldsymbol{\varsigma}_i = \left[\varsigma_1\, \varsigma_2\, \ldots\, \varsigma_{N_i+L_P}\right]^{\mathrm{T}}, \quad \mathbf{b}_i = \left[F(\vec{p}_1)\, F(\vec{p}_2)\, \ldots\, F(\vec{p}_{N_i})\, 0\, \ldots\, 0\right]^{\mathrm{T}}. \tag{3.61}$$

The interpolation matrix is nonsingular when using the MQ RBFs if the shape parameter is not equal to zero and all the supporting points are distinct points [Lee *et al.*, 2003]. If the matrix is nonsingular, the coefficient vector is uniquely computed by

$$\boldsymbol{\varsigma}_i = \boldsymbol{\Phi}_i^{-1}\mathbf{b}_i. \tag{3.62}$$

Now, the interpolation of function at an arbitrary point in the local support of the reference node $\vec{p}_i$ is computed by Eq.(3.52) using the coefficients computed by Eq.(3.62).

The local standard interpolation by RBFs can also be used for approximation of derivatives at an arbitrary point in the domain. For example, the k-th partial derivative of the function F with respect to coordinate x at the point $\vec{p}$ in the local support $\vec{p}_i$ is

$$\frac{\partial^k F}{\partial x^k}(\vec{p}) \approx \sum_{j=1}^{N_i} \varsigma_j \frac{\partial^k \psi}{\partial x^k}\left(\|\vec{p} - \vec{p}_j\|\right) + \sum_{l=1}^{L_P} \varsigma_{N_i+l} \frac{\partial^k w_l}{\partial x^k}(\vec{p}). \tag{3.63}$$

A possible straightforward approximation of high-order derivatives represents one of the advantages of the interpolation by RBFs.

The shape function in the local and global MQ RBFs interpolation has a very high influence on the interpolation results. The effect of varying the shape parameter on the fit quality in the global interpolation is investigated in [Tarwater, 1985]. It was found that error is related to the shape parameter. When the shape parameter increases, the error drops to a minimum, called the optimum shape parameter, and then grows rapidly thereafter. By adjusting the shape parameter, the accuracy can be considerably improved. Also, the shape of the surface to be fitted is a factor in optimizing the accuracy. Various methods for estimating partial derivatives on scattered data are examined in [Stead, 1984]. Excellent results are obtained in regions with modest and large gradients, which are approximated by the MQ RBFs with small and intermediate values of the shape parameter. Today, almost all papers that deal with MQ RBFCM employ a constant shape parameter. Also, the shape parameter can be different from one reference node to another in local MFMs.

Early interpolations by MQ RBFs, without the additional polynomial term, involve noise in the regions with shallow gradient regions. The flat surface was represented by a linear combination of the RBFs with a very large shape parameter and large values of coefficients. A method for overcoming these noises is performed by adding the polynomial term Eq.(3.53) in the standard interpolation form Eq.(3.52). However, the additional polynomial term increases the size of the coefficient matrix, which consequently increases computational time.

Hermite-type Interpolation

The interpolation by MQ RBFs performs well in the inner region, but results in a significant error in the derivatives at the boundary nodes [Zhang *et al.*, 2000]. Consequently, using the collocation by the RBFs to solve a PDE could result in a significant error due to inaccurate approximation of the derivatives at the boundary points which involve Neumann or Robin-type (derivative) boundary conditions. The concept of collocation with RBFs based on a Hermite-type interpolation can significantly increase the accuracy of results at the boundary where derivative boundary conditions are defined.

In Hermite-type interpolation, the RBFs are not only used for the function interpolation, but its derivatives are also employed. Assume that the data sets $\mathbf{S}_1 = \{(\vec{p}_i, F(\vec{p}_i)), \vec{p}_i \in \Omega, i = 1, 2, \ldots, N_1\}$, and $\mathbf{S}_2 = \{(\vec{p}_i, \mathcal{L}[F(\vec{p}_i)]), \vec{p}_i \in \Omega, i = 1, 2, \ldots, N_2\}$ are known, where a linear differential operator is denoted as $\mathcal{L}$. The intersection of data sets cannot be the empty set. The interpolation of the function F by the local Hermite-type interpolation can be written as

$$s(\vec{p}) \equiv \sum_{j=1}^{N_{i1}} \varsigma_j \psi(\|\vec{p} - \vec{p}_j\|) + \sum_{k=1}^{N_{i2}} \varsigma_{N_i+k} \mathcal{L}^k [\psi(\|\vec{p} - \vec{p}_k\|)] + P(\vec{p}), \tag{3.64}$$

where N_{in} is the number of nodes in the local support of the reference node $\vec{p}_i$ from the set $\mathbf{S}_n$ $(N_{in} \leq N_n, n = 1, 2)$. The superscript k indicates that the functional $\mathcal{L}$ acts on the RBF ψ viewed as a function of the second argument $\vec{p}_k$. This form of the operator is chosen in order to guarantee symmetry of the coefficient matrix.

Imposing the interpolation conditions at each node of the local support of the reference node $\vec{p}_i$

$$\begin{aligned} F(\vec{p}_n) = \sum_{j=1}^{N_{i1}} \varsigma_j \psi(\|\vec{p}_n - \vec{p}_j\|) + \sum_{k=1}^{N_{i2}} \varsigma_{N_{i1}+k} \mathcal{L}^k [\psi(\|\vec{p}_n - \vec{p}_k\|)] + \\ \sum_{l=1}^{L_P} \varsigma_{N_{i1}+N_{i2}+l} w_l(\vec{p}_n); \quad \vec{p}_n \in \mathbf{S}_1, \end{aligned} \tag{3.65}$$

$$\begin{aligned} \mathcal{L}F(\vec{p}_n) = \sum_{j=1}^{N_{i1}} \varsigma_j \mathcal{L}[\psi(\|\vec{p}_n - \vec{p}_j\|)] + \sum_{k=1}^{N_{i2}} \varsigma_{N_{i1}+k} \mathcal{L}\mathcal{L}^k [\psi(\|\vec{p}_n - \vec{p}_k\|)] + \\ \sum_{l=1}^{L_P} \varsigma_{N_{i1}+N_{i2}+l} \mathcal{L}[w_l(\vec{p}_n)]; \quad \vec{p}_n \in \mathbf{S}_2. \end{aligned} \tag{3.66}$$

The following constraints are necessary for computing a unique set of coefficients

$$\sum_{j=1}^{N_{i1}} \varsigma_j w_l(\vec{p}_j) + \sum_{k=1}^{N_{i2}} \varsigma_{N_{i1}+k} \mathcal{L}^k [w_l(\vec{p}_k)] = 0; \quad l = 1, 2, \ldots, L_P. \tag{3.67}$$

The coefficient matrix from the Hermite-type interpolation scheme is

$$\boldsymbol{\Phi}_i = \begin{bmatrix} (\psi_{nj})_{N_{i1}\times N_{i1}} & \left(\mathcal{L}^k\left[\psi_{nk}\right]\right)_{N_{i1}\times N_{i2}} & (w_{nl})_{N_{i1}\times L_P} \\ \left(\mathcal{L}\left[\psi_{nj}\right]\right)_{N_{i2}\times N_{i1}} & \left(\mathcal{L}\mathcal{L}^k\left[\psi_{nk}\right]\right)_{N_{i2}\times N_{i2}} & \left(\mathcal{L}\left[w_{nl}\right]\right)_{N_{i2}\times L_P} \\ (w_{nl})^{\mathrm{T}}_{L_P\times N_{i1}} & \left(\mathcal{L}^k\left[w_{nl}\right]\right)^{\mathrm{T}}_{L_P\times N_{i2}} & (0)_{L_P\times L_P} \end{bmatrix}_{\bar{N}_i\times\bar{N}_i}, \tag{3.68}$$

where $\mathcal{L}\left[\psi_{nj}\right] \equiv \mathcal{L}\left[\psi\left(\|\vec{p}_n - \vec{p}_j\|\right)\right]$ and $\bar{N}_i = N_{i1}+N_{i2}+L_P$. The coefficient vector $\boldsymbol{\varsigma}_i$ and the right-hand side vector $\mathbf{b}_i$ are

$$\boldsymbol{\varsigma}_i = \left[\varsigma_1\,\varsigma_2\,\ldots\,\varsigma_{N_{i1}+N_{i2}+l}\right]^{\mathrm{T}},\ \mathbf{b}_i = \left[F\left(\vec{p}_n\right)\|\vec{p}_n \in \mathbf{S}_1\ \mathcal{L}[F]\left(\vec{p}_n\right)\|\vec{p}_n \in \mathbf{S}_2\ 0\,\ldots\,0\right]^{\mathrm{T}}. \tag{3.69}$$

The test shows that the accuracy of the derivatives is improved significantly by using Hermite-type interpolation, so it can be expected that the accuracy will be also improved by using the Hermite-type interpolation in solving PDEs.

3.3.3 Solution of PDEs by Collocation with RBFs

The local collocation method is introduced to solve a general PDE in the domain Ω imposed by the boundary conditions on the boundary Γ. The boundary Γ is divided into two parts, $\Gamma = \Gamma_u \cup \Gamma_d$, the part of the boundary Γ_u where the Dirichlet boundary condition is defined and the part of the boundary Γ_d where the derivative boundary conditions are defined.

Similar to the interpolation, the data set $\mathbf{S} = \{\vec{p}_i \in \Omega \cup \Gamma,\ i = 1, 2, \ldots, N\}$ can be scattered or equidistant. The above data set is divided into a set of domain points $\mathbf{S}_\Omega = \{\vec{p}_i \in \Omega,\ i = 1, 2, \ldots, N_\Omega\}$, a set of boundary points where Dirichlet boundary condition exists $\mathbf{S}_{\Gamma_u} = \{\vec{p}_i \in \Gamma_u,\ i = 1, 2, \ldots, N_{\Gamma_u}\}$, and a set of boundary points where derivative boundary conditions exist $\mathbf{S}_{\Gamma_d} = \{\vec{p}_i \in \Gamma_d,\ i = 1, 2, \ldots, N_{\Gamma_d}\}$. The total number of nodes in the whole computational domain is $N = N_\Omega + N_{\Gamma_u} + N_{\Gamma_d}$.

Consider the following general PDE in the form of

$$\frac{\partial u}{\partial t} + \mathcal{L}\left[u\right]\left(\vec{p}\right) = F_\Omega\left(\vec{p}\right); \quad \vec{p} \in \Omega, \tag{3.70}$$

$$u\left(\vec{p}\right) = F_{\Gamma_u}\left(\vec{p}\right); \quad \vec{p} \in \Gamma_u, \tag{3.71}$$

$$\mathcal{B}\left[u\right]\left(\vec{p}\right) = F_{\Gamma_d}\left(\vec{p}\right); \quad \vec{p} \in \Gamma_d, \tag{3.72}$$

where F_Ω, F_{Γ_u} and F_{Γ_d} are the known functions. The operators $\mathcal{L}$ and $\mathcal{B}$ are linear partial differential operators on the domain Ω and the part of the boundary Γ_d, respectively. The initial field $u\left(\vec{p}, t_0\right)$ is prescribed.

Approximation of the solution u by a standard or direct local collocation close to the reference node $\vec{p}_i$ is

$$u\left(\vec{p}, t\right) \approx \sum_{j=1}^{N_i} \varsigma_j\left(t\right)\psi\left(\|\vec{p} - \vec{p}_j\|\right) + \sum_{l=1}^{L_P} \varsigma_{N_i+l}\left(t\right) w_l\left(\vec{p}\right). \tag{3.73}$$

The unknown coefficient vector $\boldsymbol{\varsigma}$ is a function of time only in time dependent problems.

The number of nodes in the local support of the node $\vec{p}_i$ that belongs to the sets $\mathbf{S}_\Omega$, $\mathbf{S}_{\Gamma_u}$ and $\mathbf{S}_{\Gamma_d}$ are $N_{i\Omega}$, $N_{i\Gamma_u}$ and $N_{i\Gamma_d}$, respectively. The number of nodes in the local support is equal to the sum of the number of nodes in subsets, $N_i = N_{i\Omega} + N_{i\Gamma_u} + N_{i\Gamma_d}$.

The local collocation by RBFs for solving PDEs is performed by using the explicit Euler scheme in time. The explicit Euler scheme enables solution of the general PDE in a purely local character.

Time discretization of Eq.(3.70) in domain points $\vec{p}_i \in \Omega$ is

$$u\left(\vec{p}_i, t^{k+1}\right) = u\left(\vec{p}_i, t^k\right) + \Delta t\left\{F_\Omega\left(\vec{p}_i\right) - \mathcal{L}\left[u\right]\left(\vec{p}_i\right)\right\}, \tag{3.74}$$

The values of the field at the domain points and at the new time step is computed by Eq.(3.74).

After the computation of the field in the domain points, the values of the field on the boundary points that satisfied the boundary conditions are computed. The values of the field at boundary nodes are computed by the collocation. The supporting nodes $\vec{p}_n$ that belong to the local support of the reference boundary point $\vec{p}_i$ have to satisfy the following conditions:

$$\sum_{j=1}^{N_i} \varsigma_j^{k+1} \psi\left(\|\vec{p}_n - \vec{p}_j\|\right) + \sum_{l=1}^{L_P} \varsigma_{N_i+l}^{k+1} w_l\left(\vec{p}_n\right) = u\left(\vec{p}_n, t^{k+1}\right); \quad \vec{p}_n \in \mathbf{S}_\Omega\,, \tag{3.75}$$

$$\sum_{j=1}^{N_i} \varsigma_j^{k+1} \psi\left(\|\vec{p}_n - \vec{p}_j\|\right) + \sum_{l=1}^{L_P} \varsigma_{N_i+l}^{k+1} w_l\left(\vec{p}_n\right) = F_{\Gamma_u}\left(\vec{p}_n\right); \quad \vec{p}_n \in \mathbf{S}_{\Gamma_u}\,, \tag{3.76}$$

$$\sum_{j=1}^{N_i} \varsigma_j^{k+1} \mathcal{B}\left[\psi\left(\|\vec{p}_n - \vec{p}_j\|\right)\right] + \sum_{l=1}^{L_P} \varsigma_{N_i+l}^{k+1} \mathcal{B}\left[w_l\left(\vec{p}_n\right)\right] = F_{\Gamma_d}\left(\vec{p}_n\right); \quad \vec{p}_n \in \mathbf{S}_{\Gamma_d}\,. \tag{3.77}$$

The additional constraint conditions are

$$\sum_{j=1}^{N_i} \varsigma_j^{k+1} w_l\left(\vec{p}_j\right) = 0; \quad l = 1, 2, \ldots, L_P. \tag{3.78}$$

Eqs.(3.75,3.76,3.77,3.78) from the direct collocation consist of the system of linear algebraic equations with the unknown coefficients ς_j^{k+1}, $j = 1, 2, \ldots, N_i + L_P$ for the reference boundary node $\vec{p}_i$. The system can be written in the matrix form

$$\mathbf{A}_i\, \boldsymbol{\varsigma}_i^{k+1} = \mathbf{b}_i^{k+1}, \tag{3.79}$$

where

$$\mathbf{A}_i = \begin{bmatrix} \left(\psi_{nj}\right)_{N_{i\Omega}\times N_i} & \left(w_{nl}\right)_{N_{i\Omega}\times L_P} \\ \left(\psi_{nj}\right)_{N_{i\Gamma_u}\times N_i} & \left(w_{nl}\right)_{N_{i\Gamma_u}\times L_P} \\ \left(\mathcal{B}\left[\psi_{nj}\right]\right)_{N_{i\Gamma_d}\times N_i} & \left(\mathcal{B}\left[w_{nl}\right]\right)_{N_{i\Gamma_d}\times L_P} \\ \left(w_{nl}\right)^{\mathrm{T}}_{L_P\times N_i} & \left(0\right)_{L_P\times L_P} \end{bmatrix}_{\bar{N}_i\times\bar{N}_i},$$

$$\boldsymbol{\varsigma}_i^{k+1} = \left[\varsigma_1^{k+1}\, \varsigma_2^{k+1} \,\ldots\, \varsigma_{N_i+L_P}^{k+1}\right]^{\mathrm{T}}, \tag{3.80}$$

$$\mathbf{b}_i^{k+1} = \left[u\left(\vec{p}_n, t^{k+1}\right) \parallel \vec{p}_n \in \mathbf{S}_\Omega \;\; F_{\Gamma_u}\left(\vec{p}_n\right) \parallel \vec{p}_n \in \mathbf{S}_{\Gamma_u} \;\; F_{\Gamma_d}\left(\vec{p}_n\right) \parallel \vec{p}_n \in \mathbf{S}_{\Gamma_d} \;\; 0 \;\ldots\; 0\right]^{\mathrm{T}}.$$

The size of the matrix $\mathbf{A}_i$ is $\bar{N}_i = N_i + L_P$.

If the matrix $\mathbf{A}_i$ is nonsingular, the unknown coefficients $\boldsymbol{\varsigma}_i^{k+1}$ for the reference boundary point $\vec{p}_i$ in the new time step $k+1$ can be uniquely computed by

$$\boldsymbol{\varsigma}_i^{k+1} = \mathbf{A}_i^{-1}\mathbf{b}_i^{k+1}. \tag{3.81}$$

When the coefficients for the boundary nodes are computed, the field at the boundary nodes is computed as

$$u\left(\vec{p}_i, t^{k+1}\right) = \sum_{j=1}^{N_i} \varsigma_j^{k+1}\psi\left(\|\vec{p}_i - \vec{p}_j\|\right) + \sum_{l=1}^{L_P} \varsigma_{N_i+l}^{k+1} w_l\left(\vec{p}_i\right), \quad \vec{p}_i \in \Gamma. \tag{3.82}$$

The values of the field in the new time step are already determined and the coefficients for reference domain nodes are computed. The coefficients in the new time step $\boldsymbol{\varsigma}_i^{k+1}$ for the reference domain points, $\vec{p}_i \in \Omega$, are computed by

$$\boldsymbol{\varsigma}_i^{k+1} = \boldsymbol{\Phi}_i^{-1}\mathbf{b}_i, \tag{3.83}$$

where the coefficient matrix $\boldsymbol{\Phi}_i$ is introduced in Eq.(3.60) and the vector $\mathbf{b}_i$ is

$$\mathbf{b}_i^{k+1} = \left[u\left(\vec{p}_1, t^{k+1}\right)\; u\left(\vec{p}_2, t^{k+1}\right) \;\ldots\; u\left(\vec{p}_{N_i}, t^{k+1}\right)\; 0 \ldots 0\right]^{\mathrm{T}}. \tag{3.84}$$

In transient problems, the initial field in the computational domain is prescribed. The coefficients at the initial stage are computed in the same way as in the interpolation problem. For steady-state problems, the local collocation by RBFs solves the problem in the presented way by introducing the artificial transient term $\partial u/\partial t$ in the domain's governing equation. The initial condition is artificially prescribed. The solution for the time-independent problem is computed when the difference between two successive time steps is smaller than a prescribed small number which defines the accuracy of the result.

The influence of the shape parameter on the numerical results computed by the collocation with RBFs has been estimated by numerical experiments with the conclusion that the value of the shape parameter has a large influence on the accuracy of results. Generally, when the value of the shape parameter increases, errors decrease. In the GRBFCM, the growth of the shape parameter is confined because the value of the condition number of the coefficient matrix increases and the system of equations becomes ill-conditioned ([Kovačević *et al.*, 2003; Wang and Liu, 2002]). In the LRBFCM, when the value of the shape parameter reaches a certain value, the accuracy of the results are nonsensitive to its changes [Lee *et al.*, 2003].

The direct collocation method produces accurate results for various PDEs when the boundary conditions are all of Dirichlet type. If there is any derivative boundary condition, the accuracy of the solution deteriorates drastically and the solution can be unstable; small changes in the setup of the problem can lead to a large change in the solution. One of the proposed methods is collocation based on Hermite-type interpolation, as introduced in Section 3.3.2.

Hermite-type Interpolation

Collocation methods based on Hermite-type interpolation can significantly improve the numerical results of PDEs imposed by the derivative boundary conditions. The method was proposed by Fasshauer for global collocation [Fasshauer, 1997]. The collocation matrix is symmetric in this method and thus the method is also known as the symmetric GRBFCM. Comparison between the direct-unsymmetric and symmetric GRBFCM for the numerical solution of PDEs is presented in [Power and Barraco, 2002]. The system of algebraic equations obtained with the symmetric method is, in general, simpler to solve than one with the direct GRBFCM method, and the resulting algorithm performs better. However, the unsymmetric method is simpler to implement.

The implementation of local collocation methods based on the Hermite-type interpolation is not unique. A local collocation numerical scheme similar to the symmetric global collocation method can be introduced, but the stability and the accuracy of the results in the presence of the derivative boundary conditions are not much better than in the direct collocation method. We present the local collocation numerical scheme based on double interpretation of the derivative boundary points, proposed for global collocation in [Zhang *et al.*, 2000; Chen, 2002]. This numerical scheme is used for increasing the stability as well as the accuracy of results on the boundary where derivative boundary conditions exist. In this collocation, the derivative boundary nodes are double treated. The domain equation (Eq.(3.70)) and the derivative boundary conditions (Eq.(3.72)) have to be satisfied at the derivative boundary nodes.

The approximation of the solution u is based on Hermite-type interpolation with double treatment of the derivative boundary points close to the reference node $\vec{p}_i$

$$u\left(\vec{p},t\right) \approx \sum_{j=1}^{N_i} \varsigma_j\left(t\right)\psi\left(\|\vec{p}-\vec{p}_j\|\right) + \sum_{k=1}^{N_{i\Gamma_d}} \varsigma_{N_i+k}\left(t\right)\mathcal{B}^k\left[\psi\left(\|\vec{p}-\vec{p}_k\|\right)\right] + \sum_{l=1}^{L_P} \varsigma_{N_i+N_{i\Gamma_d}+l}\left(t\right)w_l\left(\vec{p}\right), \tag{3.85}$$

where $\mathcal{B}^k$ is the differential operator used in Eq.(3.72).

The values of the field in the new time step are computed at the domain and derivative boundary nodes as

$$u\left(\vec{p}_i,t^{k+1}\right) = u\left(\vec{p}_i,t^k\right) + \Delta t\big\{F_\Omega\left(\vec{p}_i\right) - \mathcal{L}\left[u\right]\left(\vec{p}_i\right)\big\}\,. \tag{3.86}$$

The values at the derivative boundary nodes in the domain nodes are used for the collocation, explained in the following. The conditions that must be satisfied at the boundary nodes in the local support of the reference node $\vec{p}_i$ are:

$$\begin{aligned}&\sum_{j=1}^{N_i} \varsigma_j^{k+1}\psi\left(\|\vec{p}_n-\vec{p}_j\|\right) + \sum_{k=1}^{N_{i\Gamma_d}} \varsigma_{N_i+k}^{k+1}\mathcal{B}^k\left[\psi\left(\|\vec{p}_n-\vec{p}_k\|\right)\right] + \\ &\sum_{l=1}^{L_P} \varsigma_{N_i+N_{i\Gamma_d}+l}^{k+1} w_l\left(\vec{p}_n\right) = u\left(\vec{p}_n,t^{k+1}\right); \quad \vec{p}_n \in \mathbf{S}_\Omega \cup \mathbf{S}_{\Gamma_d},\end{aligned} \tag{3.87}$$

$$\begin{gathered}\sum_{j=1}^{N_i} \varsigma_j^{k+1}\psi\left(\|\vec{p}_n-\vec{p}_j\|\right)+\sum_{k=1}^{N_{i\Gamma_d}} \varsigma_{N_i+k}^{k+1}\mathcal{B}^k\left[\psi\left(\|\vec{p}_n-\vec{p}_k\|\right)\right]+\\ \sum_{l=1}^{L_P} \varsigma_{N_i+N_{i\Gamma_d}+l}^{k+1} w_l\left(\vec{p}_n\right)=F_{\Gamma_u}\left(\vec{p}_n\right);\quad \vec{p}_n\in\mathbf{S}_{\Gamma_u},\end{gathered}\tag{3.88}$$

$$\begin{gathered}\sum_{j=1}^{N_i} \varsigma_j^{k+1}\mathcal{B}\left[\psi\left(\|\vec{p}_n-\vec{p}_j\|\right)\right]+\sum_{k=1}^{N_{i\Gamma_d}} \varsigma_{N_i+k}^{k+1}\mathcal{B}\mathcal{B}^k\left[\psi\left(\|\vec{p}_n-\vec{p}_k\|\right)\right]+\\ \sum_{l=1}^{L_P} \varsigma_{N_i+N_{i\Gamma_d}+l}^{k+1}\mathcal{B}\left[w_l\left(\vec{p}_n\right)\right]=F_{\Gamma_d}\left(\vec{p}_n\right);\quad \vec{p}_n\in\mathbf{S}_{\Gamma_d}.\end{gathered}\tag{3.89}$$

The additional constraint conditions are

$$\begin{gathered}\sum_{j=1}^{N_{i\Omega}+N_{i\Gamma_d}+N_{i\Gamma_u}} \varsigma_j^{k+1} w_l\left(\vec{p}_j\right)+\sum_{k=1}^{N_{\Gamma_d}} \varsigma_{N_{i\Omega}+N_{i\Gamma_d}+N_{i\Gamma_u}+k}\mathcal{B}^k\left[w_l\left(\vec{p}_k\right)\right]=0;\\ l=1,2,\ldots,L_P.\end{gathered}\tag{3.90}$$

The matrix form of the system of linear Eqs.(3.87,3.88,3.89,3.90) is

$$\mathbf{A}_i\,\boldsymbol{\varsigma}_i^{k+1}=\mathbf{b}_i^{k+1},\tag{3.91}$$

where

$$\mathbf{A}_i=\begin{bmatrix} \left(\psi_{nj}\right)_{\left(N_{i\Omega}+N_{i\Gamma_d}\right)\times N_i} & \left(\mathcal{B}^k\left[\psi_{nk}\right]\right)_{\left(N_{i\Omega}+N_{i\Gamma_d}\right)\times N_{i\Gamma_d}} & \left(w_{ml}\right)_{\left(N_{i\Omega}+N_{i\Gamma_d}\right)\times L_P}\\ \left(\psi_{nj}\right)_{N_{i\Gamma_u}\times N_i} & \left(\mathcal{B}^k\left[\psi_{nk}\right]\right)_{N_{i\Gamma_u}\times N_{i\Gamma_d}} & \left(w_{nl}\right)_{N_{i\Gamma_u}\times L_P}\\ \left(\mathcal{B}\left[\psi_{nj}\right]\right)_{N_{i\Gamma_d}\times N_i} & \left(\mathcal{B}\mathcal{B}^k\left[\psi_{nk}\right]\right)_{N_{i\Gamma_d}\times N_{i\Gamma_d}} & \left(\mathcal{B}\left[w_{nl}\right]\right)_{N_{i\Gamma_d}\times L_P}\\ \left(w_{nl}\right)^{\mathrm{T}}_{L_P\times\left(N_{i\Omega}+N_{i\Gamma_d}+N_{i\Gamma_u}\right)} & \left(\mathcal{B}^k\left[w_{nl}\right]\right)^{\mathrm{T}}_{L_P\times N_{i\Gamma_d}} & (0)_{L_P\times L_P} \end{bmatrix}_{\bar{N}_i\times\bar{N}_i},\tag{3.92}$$

$$\boldsymbol{\varsigma}_i^{k+1}=\left[\varsigma_1^{k+1}\;\varsigma_2^{k+1}\;\ldots\;\varsigma_{N_i+N_{i\Gamma_u}+L_P}^{k+1}\right]^{\mathrm{T}}$$

$$\mathbf{b}_i^{k+1}=\left[u\left(\vec{p}_n,t^{k+1}\right)\|\,\vec{p}_n\in\mathbf{S}_\Omega\cup\mathbf{S}_{\Gamma_d}\;F_{\Gamma_u}\left(\vec{p}_n\right)\|\,\vec{p}_n\in\mathbf{S}_{\Gamma_u}\;F_{\Gamma_d}\left(\vec{p}_n\right)\|\,\vec{p}_n\in\mathbf{S}_{\Gamma_d}\;0\;\ldots\;0\right]^{\mathrm{T}}.$$

The matrix size is equal to $\bar{N}_i=N_i+N_{\Gamma_d}+L_P$. The coefficient vector in the new time step $\boldsymbol{\varsigma}_i^{k+1}$ for the boundary reference node $\vec{p}_i$ is determined by

$$\boldsymbol{\varsigma}_i^{k+1}=\mathbf{A}_i^{-1}\mathbf{b}_i^{k+1}.\tag{3.93}$$

The values of the field at the boundary nodes are

$$\begin{gathered}u\left(\vec{p}_i\right)=\sum_{j=1}^{N_i} \varsigma_j^{k+1}\psi\left(\|\vec{p}_i-\vec{p}_j\|\right)+\sum_{k=1}^{N_{i\Gamma_d}} \varsigma_{N_i+k}^{k+1}\mathcal{B}^k\left[\psi\left(\|\vec{p}_i-\vec{p}_k\|\right)\right]+\\ \sum_{l=1}^{L_P} \varsigma_{N_i+N_{i\Gamma_d}+l}^{k+1} w_l\left(\vec{p}_i\right);\quad \vec{p}_i\in\Gamma.\end{gathered}\tag{3.94}$$

The coefficient vector for the domain nodes, $\vec{p}_i \in \Omega$, is computed by

$$\boldsymbol{\varsigma}_i^{k+1} = \boldsymbol{\Phi}_i^{-1} \mathbf{b}_i, \tag{3.95}$$

where the coefficient matrix $\boldsymbol{\Phi}_i$ and the vector $\mathbf{b}_i$ are

$$\boldsymbol{\Phi}_i = \begin{bmatrix} (\psi_{nj})_{N_i \times N_i} & \left(\mathcal{B}^k [\psi_{nk}]\right)_{N_i \times N_{i\Gamma_d}} & (w_{nl})_{N_i \times L_P} \\ (\mathcal{B}[\psi_{nj}])_{N_{i\Gamma_d} \times N_i} & \left(\mathcal{B}\mathcal{B}^k [\psi_{nk}]\right)_{N_{i\Gamma_d} \times N_{i\Gamma_d}} & (\mathcal{B}[w_{nl}])_{N_{i\Gamma_d} \times L_P} \\ (w_{nl})^{\mathrm{T}}_{L_P \times N_i} & \left(\mathcal{B}^k [w_{nl}]\right)^{\mathrm{T}}_{L_P \times N_{i\Gamma_d}} & (0)_{L_P \times L_P} \end{bmatrix}_{\bar{N}_i \times \bar{N}_i}, \tag{3.96}$$

$$\mathbf{b}_i^{k+1} = \left[u\left(\vec{p}_n, t^{k+1}\right) \|\vec{p}_n \in \mathbf{S}_\Omega \cup \mathbf{S}_{\Gamma_u} \cup \mathbf{S}_{\Gamma_d} \; F_{\Gamma_d}(\vec{p}_n) \|\vec{p}_n \in \Gamma_d \; 0 \; \ldots \; 0\right]^{\mathrm{T}}.$$

3.3.4 Selection of Local Support

Approximation of the function and its derivatives at the domain and boundary points is performed by using the local support. Selection of the local support for the domain and boundary nodes can be different and will be separately analysed here. At the start, the local supports for the domain nodes are determined.

Domain Local Support

Two approaches for selection of local support for domain nodes in the MFMs community are well established. The shape and the size of the local support is determined explicitly in the first approach. For example, the local support can be a circle in two dimensions and a sphere in three dimensions, i.e., for a reference node $\vec{p}_i$, its local support is defined as

$$S_i = \{\vec{p}_j, \|\vec{p}_j - \vec{p}_i\| < R_i\}, \tag{3.97}$$

where R_i is the radius of the circle and represents the size of the local support. The term domain of influence is very frequently used instead the term the local support for this situation. The number of supporting points within the local support is restricted to a given value in the second approach. The supporting points are chosen by their distance from the reference node, with the closer one having higher priority. The described approaches on two-dimensional equidistant grids are presented in Fig.(3.4). The domain of influence is determined with the radius of the circle R_i in Fig.(3.4(a)), and the number of supporting nodes in the second approach is five Fig.(3.4(b)). The domain, boundary, supporting nodes, and the reference node on the following schemes are presented by blue, red, green, and black colours, respectively.

These two approaches work well when the nodes in the domain are uniformly distributed or the local density of nodes varies smoothly. However, when the nodes are unevenly distributed locally, which is usual in an r-adaptive node distribution, these two methods may not be appropriate anymore [Ding *et al.*, 2005].

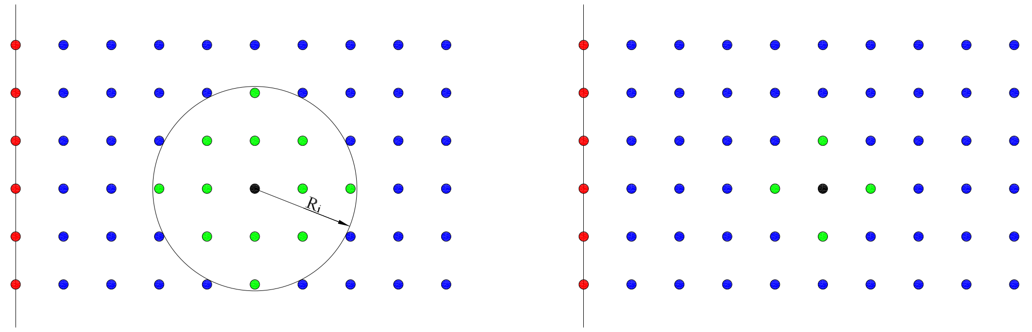

(a) The domain of influence determined by the circe with radius R_i.

(b) The local support with five supporting nodes.

Figure 3.4: Local supports for domain reference nodes on the equidistant grid.

Arbitrary Node Arrangements. If one tries to use the domain of influence in r-adaptivity node arrangements, where the nodes in the domain have a track-like distribution, then too many supporting nodes will be captured in one direction from the reference node and not enough in the others. The approximations of the function, and especially the derivatives, with such supporting nodes are very bad and cannot be used for solution of PDEs. Because of that, the second approach for determination of the local support, where the number of supporting nodes is previously determined, is better suited for r-adaptivity node arrangements. The number of supporting nodes is the input parameter in the local MFM. We will concentrate on the local support with five supporting nodes ($M_i = 5$) in the two-dimensional geometry. The local support with five supporting nodes, on the equidistant grid, is presented in Fig.(3.4(b)).

The possibility of MFMs for numerical computations on an arbitrary, and especially adaptive, node arrangement is used. Therefore, a useful and quick approach for determination of the local support for domain reference nodes in an arbitrary node arrangement is developed. The number of nodes in the supporting domain is five, but the approach can be generalized for an arbitrary number of nodes in the supporting domain. A schematic presentation of the approach is presented in Fig.(3.5). The first supporting node is the nearest node to the reference node, Fig.(3.5(a)). The second node has to be selected in the opposite quadrant ($90\,^{\circ}$) from the first selected node. The nodes outside of this quadrant (shaded on scheme) are not included in the selection. The second selected node in the local support is the nearest node in the opposite quadrant. The selection of the second node is presented in Fig.(3.5(b)). The selection of third supporting point is computed from the region which is influenced by the positions of the previous two. The total angle of this region is $90\,^{\circ}$. The third node is the nearest node in this region (Fig.(3.5(c))). The last node is selected in the same way, but now the region is constructed from the previously selected three nodes (Fig.(3.5(d))). The total angle of this region is between $90\,^{\circ}$ and $112.5\,^{\circ}$. In the proposed approach, the minimum angle that is formed between two supporting points and the reference node is higher than 45°.

The idea for such selection of the supporting points has emerged during solution of one-dimensional problems with the r-adaptive grids. Even in the one-dimensional geometry, the distance to the reference node is not the only priority for the selection of the local support. The local support has to consist of the same number of nodes from both sides of the reference node. The local support with three supporting nodes consists of the closest node from one side and the closest node from the other side of the reference node.

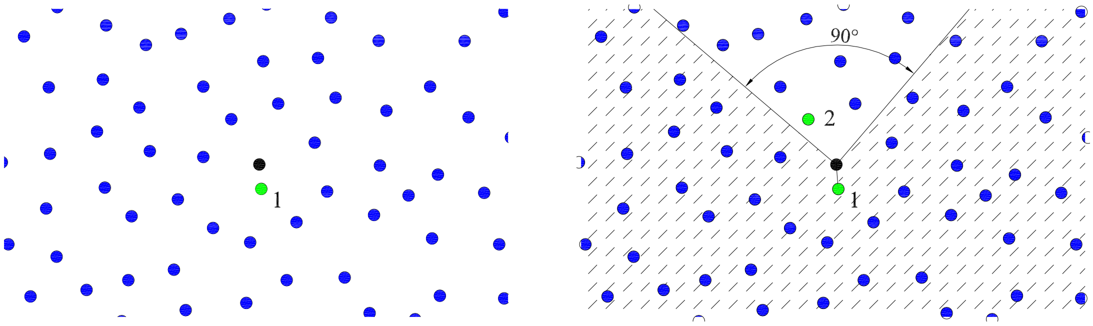

(a) The first supporting point.

(b) The second supporting point.

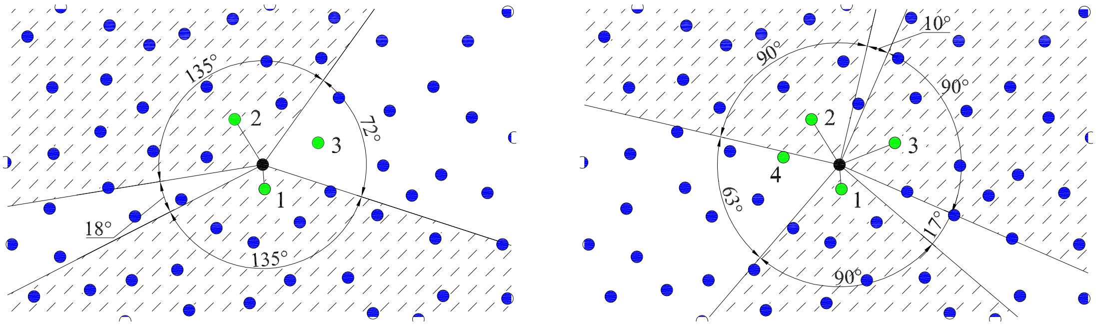

(c) The third supporting point.

(d) The fourth supporting point.

Figure 3.5: The new approach for selection of the local support with five supporting points in an arbitrary node arrangement.

Boundary Local Support

Implementation of boundary conditions in the local collocation by RBFs is still an open topic, and consequently, the general collocation numerical scheme does not exist. Also, the numerical results computed by the global collocation method on the boundary where derivative boundary conditions exist are less accurate than the results in the domain. Still in the global collocation, different strategies are proposed for increasing accuracy of the results on the boundary. The symmetric collocation approach based on Hermite-type interpolation proposed by Fasshauer [Fasshauer, 1997] and the double consideration of the boundary nodes proposed by Zhang [Zhang *et al.*, 2000] and Chen [Chen, 2002] are the two examples of these strategies. All strategies for global collocation can be translated on the local collocation. The only difference is that determination of the local support in the local collocation is another degree of freedom for consideration, especially on the boundary.

Theoretically, selection of the local support for boundary nodes could be the same as for domain nodes, and the two previously explained approaches can be easily implemented. In the direct local collocation, the only difference is that at the boundary nodes, the boundary conditions are implemented. The local support with six supporting points is presented in Fig.(3.6(a)). The stability of results computed by this boundary local support is not very good when the derivative boundary conditions are applied. The approximation of the first derivative at the boundary nodes is a key factor for accuracy of the results. The stability of results continues to decrease with increases in the number of boundary nodes in the local support. Because of this observation, the idea for using only one reference-boundary node in the local support has been proposed [Šarler and Vertnik, 2006], where the boundary condition is implemented. The such defined boundary local support with five supporting nodes is presented in Fig.(3.6(b)). Numerical experiments have shown that this boundary local support stabilizes numerical results.

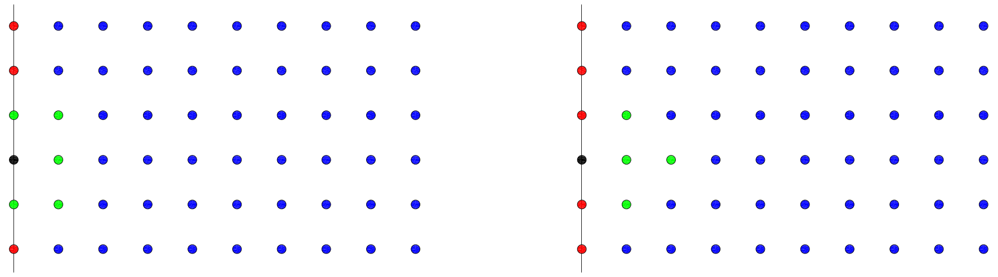
(a) The classical method for determination of the local support for boundary nodes.

(b) The local support with only one boundary node in the local support.

Figure 3.6: Local supports for boundary reference nodes.

3.3.5 R-adaptation

The possibility of MFMs for solving PDEs with arbitrary node arrangements could be very useful if the node arrangement is carefully prepared. The adaptation of node arrangements can be performed in different ways [Thompson *et al.*, 1999]. Two basic strategies are h-adaptivity and r-adaptivity. The number of nodes can be added and removed in the h-adaptation, whereas the number of nodes is constant throughout computations in the r-adaptation. The implementation of h-adaptivity for MFMs has been performed only recently [Rabczuk and Belytschko, 2005].

In the r-adaptation, the total number of nodes is constant and nodes are only redistributed in the computational domain. This was done for the first time in [Kovačević and Šarler, 2005]. The fine node arrangement is necessary in the phase-change region where the gradients of the field are highest. The method with an elliptic automatic adaptive node redistribution, designed to properly cope with the gradients in the phase-change region, is implemented. As a result, we have to solve one more differential equation to redistribute the nodes in the domain. On the other hand, the number of nodes is much smaller in comparison with the uniform distribution while retaining the same accuracy.

Grid generation for the computation position of the nodes is used. One of the most general methods for grid generation is the method with an elliptic generator, where the grid density is simply controlled. This adaptivity method in the framework of the finite volume method is demonstrated in [Mencinger, 2001].

Grid Generation with Elliptic Generator

Grid generation with the elliptic generator is based on solving the elliptic PDE, which is called the elliptic generator [Thompson *et al.*, 1999]. The standard method for grid generation with the elliptic generator is based on solving the Poisson equation:

$$\nabla^2 \zeta = \mathtt{P}. \tag{3.98}$$

The solution of this differential equation is controlled by the prescribed control function $\mathtt{P}$. In fact, the control function $\mathtt{P}$ together with the boundary conditions determines the solution as well as the shape and density of the grid generation. In general, this control function is not easily to be determined. The grid density is easier to control by solving another kind of PDE:

$$\nabla \cdot (\bar{\kappa} \nabla \zeta) = 0, \tag{3.99}$$

where the control function $\bar{\kappa}$ and the boundary conditions determine the solution.

An analogy between the coordinate lines and isotherms is used for an easier discussion. The steady temperature distribution T in the body is determined by the heat conduction equation and the boundary conditions (temperature or temperature flux):

$$\nabla \cdot (k \nabla T) = S, \tag{3.100}$$

where k and S are the thermal conductivity and the heat source density, respectively. For example, if the body is homogenous ($k = const$), the isotherm density is influenced only by the heat source S as well as the boundary conditions. In another example, if the inhomogeneous body is without heat sources ($S = 0$), the isotherm density in the body is inversely proportional to the thermal conductivity k. From comparison of both methods, our opinion is that the isothermal density could be easier to control with the prescribed thermal conductivity k, rather than the heat source S.

The influence of the control function $\bar{\kappa}$ on the grid density in Eq.(3.99) is the same as the influence of the thermal conductivity k on the temperature field in Eq.(3.100). In the region where the value of $\bar{\kappa}$ is lower, the grid density is higher, and vice versa. Other advantages of using this method are that temperature in the body is in the temperature interval confined by the boundary conditions and isotherm overlapping is avoided. Consequently, nodes that fall out of the computational domain and overlapping nodes are avoided [Mencinger, 2001].

Numerical Implementation

The grid generator (Eq.(3.99)) for the curvilinear coordinates ξ and η as dependent variables in the two-dimensional geometry are:

$$\nabla \cdot (\bar{\kappa} \nabla \varrho) = 0\,, \quad \varrho = \xi\,, \eta. \tag{3.101}$$

In fact, the position (x, y) of the intersection of curvilinear coordinate lines (ξ, η), which are independent variables in Eq.(3.101), has to be solved. The boundary conditions for the curvilinear coordinate ξ are the Dirichlet type in the x direction with values of the physical boundaries and the Neumann with no flux in the y direction, and vice versa for the curvilinear coordinate η.

These positions can be solved by two different approaches. In the first one, Eq.(3.101) are directly computed and the positions of the intersections of coordinate lines are computed thereafter. Eq.(3.101) is the classical elliptic PDE, and it is relatively simple to solve numerically. The implementation of the control function as a function of physical coordinates ($\bar{\kappa} = \bar{\kappa}\,(x, y)$) is straightforward. Because of this, the control function is computed only once at the start of the computation. An additional effort is the computation of the position (x, y) for computed values of the curvilinear coordinates (ξ, η). The solution is iteratively found by the global interpolation with RBFs. This approach is used in the one-dimensional geometry [Kovačević and Šarler, 2005], where only one equation of Eq.(3.101) is solved.

In the second approach, the position of the intersection of curvilinear coordinate lines can be solved straight away by using the inverse functions ($x = x(\xi, \eta), y = y(\xi, \eta)$). Eq.(3.101) that are transformed to

$$\begin{aligned}\gamma_1 \left[\frac{\partial^2 \chi}{\partial \xi^2} - \frac{1}{2\bar{\kappa}}\frac{\partial}{\partial \xi}\left(\bar{\kappa}\frac{\partial \chi}{\partial \xi}\right)\right] + \gamma_2 \left[\frac{\partial^2 \chi}{\partial \eta^2} - \frac{1}{2\bar{\kappa}}\frac{\partial}{\partial \eta}\left(\bar{\kappa}\frac{\partial \chi}{\partial \eta}\right)\right] - \\ \gamma_3 \left[2\frac{\partial^2 \chi}{\partial \xi \partial \eta} - \frac{1}{2\bar{\kappa}}\frac{\partial}{\partial \xi}\left(\bar{\kappa}\frac{\partial \chi}{\partial \eta}\right) - \frac{1}{2\bar{\kappa}}\frac{\partial}{\partial \eta}\left(\bar{\kappa}\frac{\partial \chi}{\partial \xi}\right)\right] = 0\,, \quad \chi = x, y,\end{aligned} \tag{3.102}$$

where geometric coefficients

$$\gamma_1 = \left(\frac{\partial x}{\partial \xi}\right)^2 + \left(\frac{\partial y}{\partial \xi}\right)^2, \quad \gamma_2 = \left(\frac{\partial x}{\partial \eta}\right)^2 + \left(\frac{\partial y}{\partial \eta}\right)^2, \quad \gamma_3 = \frac{\partial x}{\partial \xi}\frac{\partial x}{\partial \eta} + \frac{\partial y}{\partial \eta}\frac{\partial y}{\partial \xi} \tag{3.103}$$

are covariant components of a matrix tensor. The boundary conditions for the physical coordinate x are the Dirichlet type in the direction ξ with the value of the physical boundaries and the Neumann type with no flux in the direction η, and vice versa for the physical coordinate y.

If we use the curvilinear coordinate (ξ, η) as an independent coordinate (Eq.(3.102)), the simple square domain $(1, N+1; 1, N+1)$ is used, where $N+1$ represents the number of nodes in one direction. The distance between neighbouring nodes is one, $\Delta\varrho = 1$.

The control function is the function of physical coordinates ($\bar{\kappa} = \bar{\kappa}(x, y)$) and have to be computed in each time step. The computation of the control function is performed by local standard interpolation, explained in Section 3.3.2. Eq.(3.102) are solved by local standard collocation, explained in Section 3.3.3. The computation is performed iteratively by adding the transient term ($\partial\chi/\partial t$) on the right-hand side of Eq.(3.102). The equidistant node distribution which covers the whole computational domain is used as the initial node distribution (x, y position). The condition that the maximum difference between two subsequent grids is smaller than predefined small number (ϵ) is used as the convergence criteria. So, the convergence criteria is

$$\max_{i=1} \mid \chi_i^n - \chi_i^{\bar{n}} \mid \geq \epsilon\,, \quad \chi = x, y, \tag{3.104}$$

where index i represents the node in the computation domain, and superscripts $\bar{n}$ and n represent the positions in the previous and the new time step.

Examples of Mesh Generation

The control function $\bar{\kappa}$, as explained earlier in this section, is crucial for the node distribution, and the influence of the control function on the node distribution is demonstrated here. The control function can be defined in different ways as well. Our idea for definition of the control function emerged from the definition of the PFV in the PFM. The control function is defined as

$$\bar{\kappa}(x, y) = \bar{\kappa}_{\max} - \sigma_n(x, y)\left(\bar{\kappa}_{\max} - \bar{\kappa}_{\min}\right), \tag{3.105}$$

where $\bar{\kappa}_{\max}$ and $\bar{\kappa}_{\min}$ are predefined maximum and minimum values of the control function, and $\sigma_n(x, y)$ is the function for controlling the node distribution. A smooth transition from the maximum to minimum value, similar to the PFV, is obtained by using the function σ_n as

$$\sigma_n(x, y) = \frac{1}{2}\left[1 + \tanh\left(\frac{3\, n(x, y)}{\delta_n}\right)\right], \tag{3.106}$$

where n represents an independent variable normal to the interface position and δ_n represents the transition zone thickness. The function σ_n is prescribed in the interval $[0, 1]$; consequently the control function $\bar{\kappa}$ is confined in the interval $[\bar{\kappa}_{\min}, \bar{\kappa}_{\max}]$. The minimum value of the control function in each computation is equal to one.

Two basic examples of node arrangements influenced by the control function, defined in such a way, are demonstrated in Fig.(3.7). The square physical domain with the length 50 is used in both examples. The examples are computed on the equidistant 61×61 grid. The maximum of the control function in the examples is five. The transition zone thicknesses in the first and second example are ten and two, respectively. The interface positions in the examples are

$$1.\ l\ :\ x - x_c = 0, \quad 2.\ l\ :\ (x - x_c)^2 + (y - y_c)^2 - r_c^2 = 0, \tag{3.107}$$

where the parameters x_c, y_c and r_c are 25, 25, 10, respectively. The control function fields and the computed grids in the first and second examples are presented in Figs.(3.7(a),3.7(b)) and Fig.(3.7(c),3.7(d)), respectively. A fine grid is obtained in the region where the value of the control function is lower and vice versa. The transition zone in the first example is much thicker than in the second. Because of that, in the first example, transition between the fine and coarse grid is smoother than in the second one. The convergence criteria in the examples is $\epsilon = 2 \times 10^{-5}$.

Phase-change problems are focused on in this thesis, and therefore adaptive node arrangements for phase-change problems are specially derived. In phase-change problems, a fine grid is necessary in the phase-change region, which is the interphase interface position. Therefore, a correlation between the control function and the interface position is used to obtain denser node arrangement in the vicinity of the interface position, $l = l\,(x, y)$. For this purpose, we introduce a modified definition of the control function for phase-change problems in a form

$$\bar{\kappa} = \bar{\kappa}_{\max} - \sigma_n'\,(x, y)\,(\bar{\kappa}_{\max} - \bar{\kappa}_{\min})\ , \tag{3.108}$$

where the norm $\sigma_n' = \sigma_n'(x, y)$ is defined as

$$\sigma_n' = \frac{\left|\frac{d\sigma_n}{dn}\right|}{\max\left(\left|\frac{d\sigma_n}{dn}\right|\right)}\ , \quad \left|\frac{d\sigma_n}{dn}\right| = \frac{3}{2\delta_n \cosh^2\left(3n/\delta_n\right)}\ . \tag{3.109}$$

The node distribution of the proposed method for phase-change problems is controlled by two parameters: the maximum value of the control function $\bar{\kappa}_{\max}$ in Eq.(3.108) and the transition zone thickness δ_n in Eq.(3.109). The influence of the maximum value of the control function $\bar{\kappa}_{\max}$ is explained in the one-dimensional domain with length $50\,\mu$m. The interface position is located $15\,\mu$m from the left side of the system. The total number of nodes used in this example is 151. The transition zone thickness δ_n is chosen to be $6\,\mu$m. Node arrangements for three maximum values of the control function $10, 30$ and 50 are presented in Fig.(3.8). The node positions are computed by the first approach.

These adaptive grids are used for phase-change simulation by the phase-filed model. The very narrow interface thickness δ, 1.2×10^{-7} m in the PFM is used. The number of nodes in the vicinity of the diffuse interface is a function of the maximum value of the control function (Fig.(3.8)). The number of nodes in the narrow interface region is $2, 5$ and 8 and by using the maximum value of control function $10, 30$ and 50, respectively. As $\bar{\kappa}_{\max}$ increases, the relative number of nodes in the vicinity of the diffuse interface relative to the total number of nodes also increases. If one tries to solve the same problem with an equidistant node arrangement and to obtain the same number of nodes in the diffuse-interface

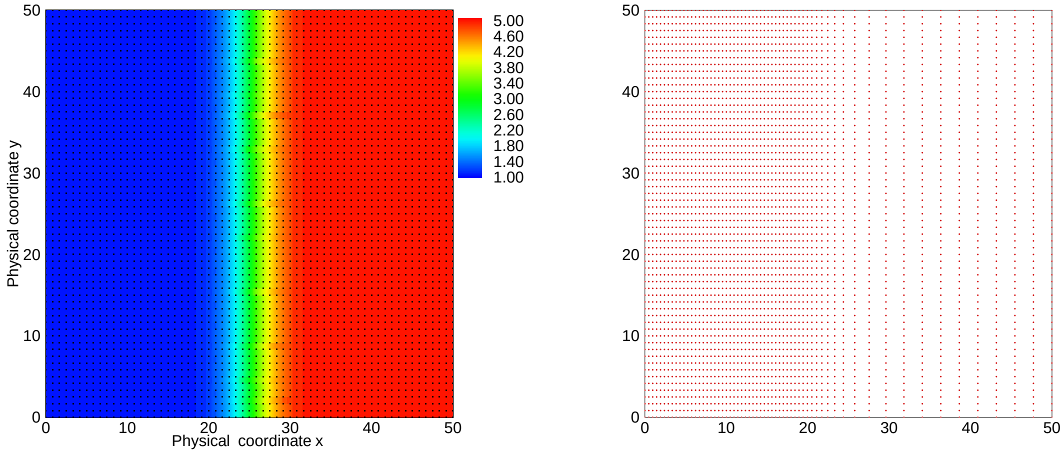

(a) The control function for selection of node arrangement.

(b) Grid computed by the elliptic generator.

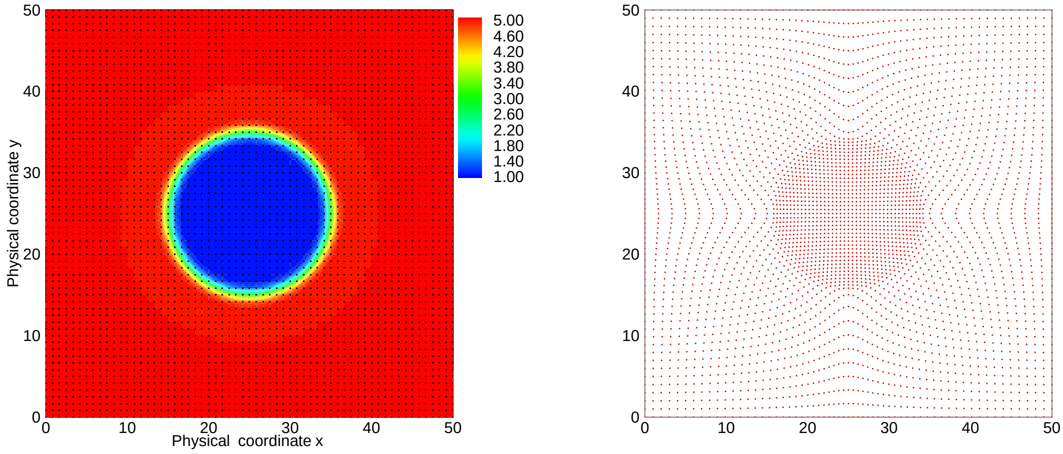

(c) The control function for selection of node arrangement.

(d) Grid computed by the elliptic generator.

Figure 3.7: Test examples for demonstration of r-adaptation.

region, the total number of nodes has to be much higher $834, 2084$ and 3334, respectively.

If one tries to compute problems with the microstructure geometry received from a micrograph, the interface position cannot be analytically written. In fact, the interface position, the boundary between phases, is obtained implicitly from the graph, as presented in Fig.(3.9(a)). The demonstration is done on the equidistant 76×76 grid. The interface between phases is sharp. To obtain a smooth control function, the transition zone between phases needs to be diffused. The diffusion is enabled by solving the Poisson equation:

$$\frac{\partial \sigma_n'}{\partial \tilde{t}} = \nabla^2 \sigma_n', \tag{3.110}$$

where the boundary conditions are of the Neumann type with zero flux. The parameter $\tilde{t}_D$ is named as the diffusion time. A relation between the diffusion time and time does not exist. The initial norm σ'_n is numerically computed. Here, the parameter for definition of the transition zone thickness is $\tilde{t}_D$, instead of δ_n. The time integration proceeds in the closed interval $\left[0, \tilde{t}_D\right]$. After the diffusion of the transition zone, the control function is computed from Eq.(3.108). Node distributions for three diffusion times $75, 150$ and 300 are presented in Figs.(3.9(b), 3.9(c), 3.9(d)), respectively.

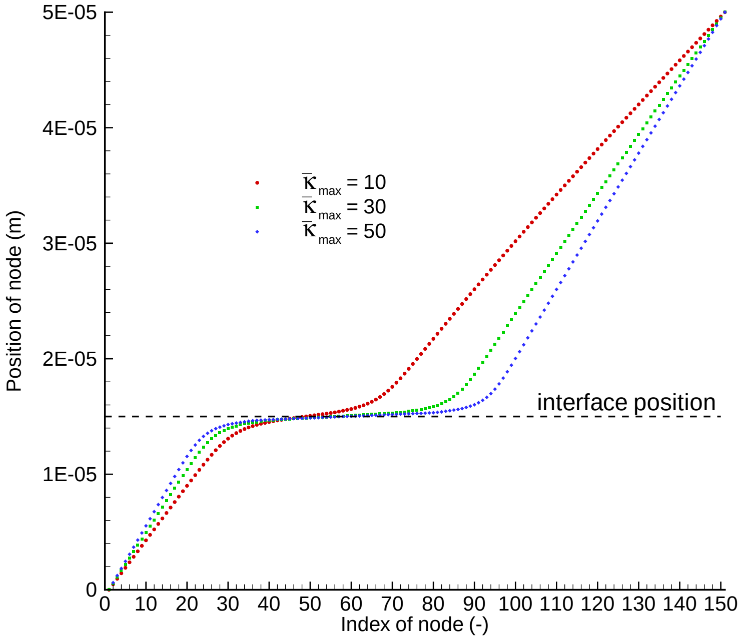

Figure 3.8: The influence of the maximum value of the control function on the node arrangement in the one-dimensional geometry.

3.3.6 Numerical Procedure

The numerical procedure of the r-adaptive LRBFCM for solving the phase-change problems simulated by the PFM is presented here. The algorithm for the r-adaptive numerical procedure is presented in Fig.(3.10). The driving force for phase transformation, the phase-field equation, and the concentration equations are solved in each-time step, the same as in other numerical procedures. The node arrangement is automatically redistributed after a transition time, denoted as t_p on a flow chart.

The input parameters in the proposed r-adaptive node arrangements are:

- the maximum value of control function $\bar{\kappa}_{\max}$ in Eq.(3.108),
- the convergence criteria ϵ in Eq.(3.104).

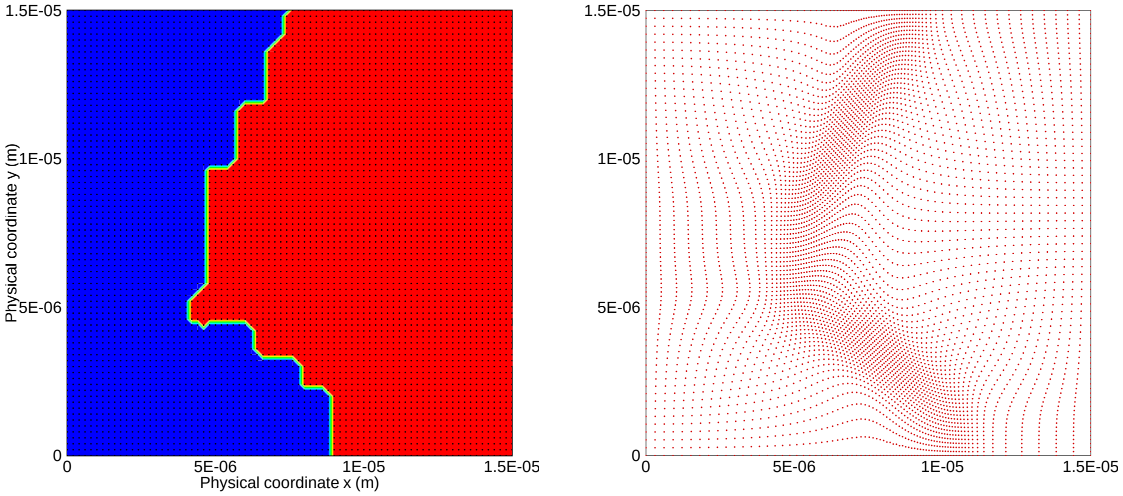

(a) The interphase interface position obtained from the micrograph.

(b) $\tilde{t}_D = 75$.

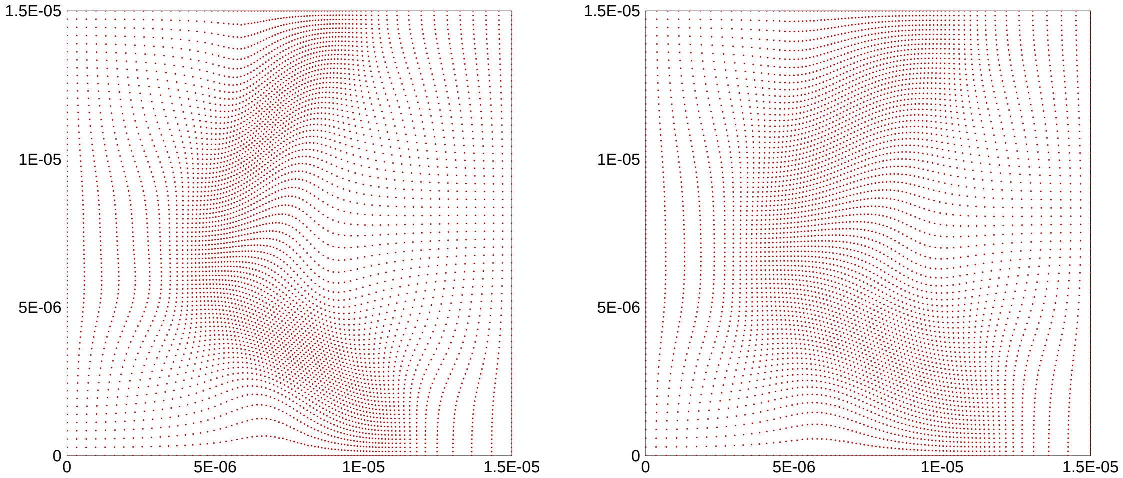

(c) $\tilde{t}_D = 150$.

(d) $\tilde{t}_D = 300$.

Figure 3.9: The influence of diffusion time $\tilde{t}_D$ on the node arrangements in the two-dimensional geometry.

- the diffusion time $\tilde{t}_D$ in Eq.(3.110) and
- the transition time t_p.

Node Redistribution

The computation is performed on the same adaptive node distribution during the transition time. The interface position moves in time, therefore the adaptive grid has to be redistributed. The new region with the fine grid is determined by the

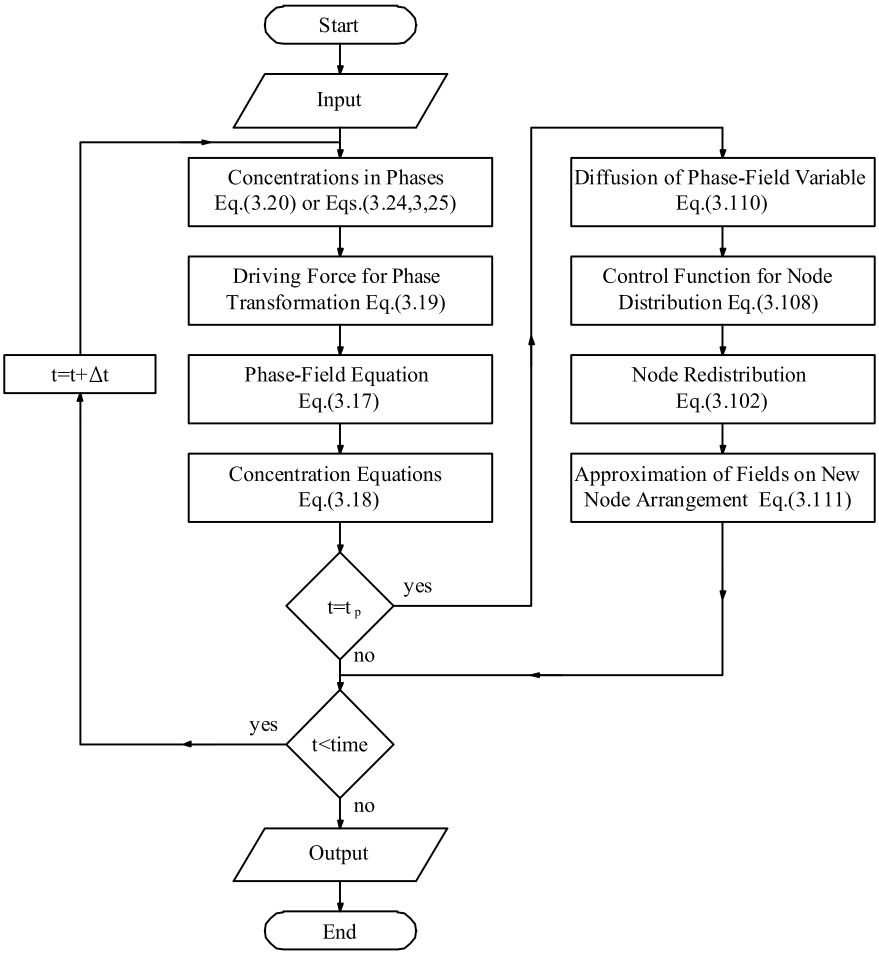

Figure 3.10: Flow chart of r-adaptivity strong-form MFM for solving phase-change problems simulated by the PFM.

PFV which implicitly defines the interface position in the PFM. The control function for the node distribution is computed by Eq.(3.108). The norm is computed by Eq.(3.109), where the function for controlling node distribution is equal to the PFV, $\sigma_n(x, y) \equiv \phi(x, y)$. To obtain a smooth transition in the node arrangement, the PFV needs to be diffused. The diffusion of the PFV is computed on the old node arrangement and this control function field is transformed on the equidistant grids ($\bar{\kappa} = \bar{\kappa}\,(x, y)$). The positions of the new node arrangement are computed by Eq.(3.102) by using the previously computed values of the control function. The positions for the new node arrangement are obtained when Eq.(3.104) is satisfied. After that, selection of the local support for every node is accomplished.

The values of the fields at the new node arrangement. The computational fields are translated at every node in the new node arrangement when the nodes are redistributed. The fields are computed from the values of the fields on the old grid. The closest node from the old node arrangement is used as the reference node. The local support of this reference node is used for computation of the fields at the new node. The schematic presentation of the computation of the values of the field in the new node arrangements is demonstrated on Fig.(3.11). The previous grid is plotted using unfilled circles and the new node, where the value of the field is computed, is presented by red circle. The values of the fields at the new node $\vec{p}_m$ are computed by the values in local support of the reference node $\vec{p}_i$ by

$$F\left(\vec{p}_m\right) = \sum_{j=1}^{N_i} \varsigma_j \psi\left(\|\vec{p}_m - \vec{p}_j\|\right) + \sum_{l=1}^{L_P} \varsigma_{N_i+l} w_l\left(\vec{p}_n\right), \qquad (3.111)$$

where the coefficient vector of the fields of the reference node $\vec{p}_i$ is known from the old node arrangement. The computed values at the new node arrangement are used for continuation of the computation at the new node arrangement.

Scaling of the MQ RBFs. The numerical results are computed by the MQ RBFs with the shape parameter $\bar{c}$ (Eq.(3.47)). When using the adaptive node arrangement, the classical MQ RBFs need to be modified. The modified MQ RBF in the two-dimensional geometry is:

$$\psi(\|\vec{p} - \vec{p}_j\|) = \sqrt{\frac{\left(x - x_j\right)^2}{x_{\max i}^2} + \frac{\left(y - y_j\right)^2}{y_{\max i}^2} + \bar{c}^2}\,, \qquad (3.112)$$

where the scaling parameters $x_{\max i}$ and $y_{\max i}$ are set to the maximum nodal distance in direction x and y in the local support of the reference node $\vec{p}_i$. The scaling parameters are

$$x_{\max i} = \max_i |x_j - x_k|\,, \quad y_{\max i} = \max_i |y_j - y_k|\,; \quad j, k = 1, \ldots, N_i. \qquad (3.113)$$

The scaling of the MQ RBFs is twofold. In the first one, the difference in distances between the supporting nodes decreases. In the second one, size differences of local supports also decrease. Because of this, the shape parameter in the MQ RBFs for each supporting point in the local support (and in each local support in the whole computational domain) can be constant.

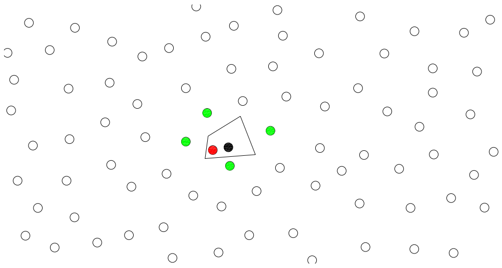

Figure 3.11: A schematic presentation of the computation of the values of the field in new node arrangements (Eq.(3.111)).

Part II

Validation and Simulation Results

4 Dissolution of Primary Particles

The primary purpose of homogenisation of aluminium alloys is to remove Cu, Mg, Si - bearing particles, formed during solidification. This chapter is dedicated to the estimation of the dissolution kinetics of primary particles into the aluminium phase for different heat-treatable aluminium systems. The phase transformations of stoichiometric and nonstoichiometric particles for binary and multicomponent systems are elaborated, commented and simulated by previously explained physical models. Also, the capability of using the local collocation by RBFs for solving phase transformations described by the PFM on r-adaptive node arrangements is presented, explained and commented.

The TDA and PFM are enforced for the dissolution of primary particles during homogenisation of aluminium alloys. Special attention is paid for linking data from a thermodynamic database to the physical models.

The numerical results for the isothermal diffusion-controlled dissolution of stoichiometric and nonstoichiometric primary particles in binary and multicomponent aluminium systems are compared for validation of physical models. A very nice agreement between the numerical results computed by the PFM and previously derived Vermolen model [Vermolen *et al.*, 1998b; Vermolen *et al.*, 2002] for the dissolution of multicomponent particles during homogenisation of aluminium alloys is demonstrated. Also, a very nice agreement between results computed by the PFM and the TDA based on the general thermodynamic interface condition are presented. The possibility of the PFM for simulation of the phase transformation in complex geometry is demonstrated. Advantages and disadvantages of using the r-adaptivity strong-form MFM for solving the PFM are pointed out.

The phase transformations in the solid state are between two extremes, known in the literature as the diffusion-controlled or the interface-controlled modes. In the diffusion-controlled mode, the main assumption is that the interface reaction proceeds quickly with respect to long-distance diffusion in the phases. Therefore, the interface concentrations are determined through the thermodynamic equilibrium state. If the interface reaction proceeds slower than long-distance diffusion in the phases, the phase transformations are interface-controlled. The transformation is in a mixed-mode character if both processes influence on the transformation kinetics. The transition between the modes depends upon the relative magnitude of the solute diffusion and the interface mobility.

The temperature dependence of the diffusion coefficient of element m in the aluminium phase is

$$D_{\mathrm{Al}}^{\mathrm{m}} = D_0^{\mathrm{m}} \exp\left(-\frac{Q_D^{\mathrm{m}}}{RT}\right), \tag{4.1}$$

where D_0^{m} is temperature-independent preexponential, and Q_D^{m} is the activation energy for diffusion. The impurity diffusion coefficients used in this thesis are computed with coefficients from Tab.(4.1). The coefficients are rewritten from Smithells Metals Reference Book [Brandes and Brook, 1992].

Table 4.1: The impurity diffusion coefficients used in this thesis [Brandes and Brook, 1992].

m	D_0^{m}	Q_D^{m}	Temp. range	$D_{\mathrm{Al}}^{\mathrm{m}}, (T = 500\,°\mathrm{C})$
–	[cm^2/s]	[kJ/mol]	°C	[m^2/s]
Cu	0.65	136.0	321 – 655	4.193×10^{-14}
Mg	1.24	130.4	394 – 655	1.741×10^{-13}
Si	2.48	137.0	480 – 620	1.369×10^{-13}

4.1 Diffusion-Controlled Dissolution

The physical models for the solid-solid phase transformations are analysed in Chapter 2. In the Diffusion-Controlled (DC) mode, the local interface condition is determined throughout the thermodynamic equilibrium state. Connections for the TDA and the PFM with a thermodynamic database for different aluminium systems are explained in detail at the beginning. The numerical results computed by the TDA and PFM for the validation of physical models are compared. The PFM as a one-domain approach enables relatively easy computation in the complex two-dimensional topology. A sensitive study of the influence of model parameters on the PFM results is done. The LRBFCM described in Section 3.3 is implemented for solving the PFM. Comparison with the numerical results computed by the fine-grid FDM in one and two-dimensional geometry is performed.

4.1.1 Connection of the Physical Models with a Thermodynamic Database

The major difficulty in modelling of phase transformations is the link between the model and the thermodynamic data. The JMatPro software for aluminium alloys [JMatPro, 2004] is used as the thermodynamic database in this thesis. The thermodynamic data for using the FTM and the PFM for binary, stoichiometric or nonstoichiometric second phases and multicomponent systems are explained in this section.

Binary Systems

The number of degrees of freedom in isobaric binary systems with two coexisting phases are equal to one (Eq.(1.3)). In heat treatment processes, the temperature is the known process parameter and the number of degrees is equal to zero at the interphase interface. Therefore, the interface conditions are completely determined by the equilibrium phase diagram.

Connection to the PFM with a thermodynamic database is different for stoichiometric or nonstoichiometric second phase. Because of this, it is necessary to separately treat it. The stoichiometric phase is considered first.

Stoichiometric phase. The link between the models and the thermodynamic database, where the second phase is stoichiometric, is explained in an example of a Al-Mg system. In the Al-Mg system, the aluminium phase and intermetallic compound Al_3Mg_2 phase exist in the two-phase solid-solid region. The concentration of Mg in the intermetallic stoichiometric Al_3Mg_2 phase is constant and equals to 36.06 wt%.

FTM. The solubility of Mg determines the interface concentration in the aluminium phase. Solubility as a function of temperature is presented on the binary equilibrium phase diagram by the solvus line. The solubility as a function of temperature is written in Tab.(4.2).

Table 4.2: The interface concentrations of Mg in the aluminium phase as a function of temperature, obtained from the thermodynamic database [JMatPro, 2004].

T	$c_{\mathrm{AlI}}^{\mathrm{Mg}}$	T	$c_{\mathrm{AlI}}^{\mathrm{Mg}}$	T	$c_{\mathrm{AlI}}^{\mathrm{Mg}}$	T	$c_{\mathrm{AlI}}^{\mathrm{Mg}}$
°C	[wt%]	°C	[wt%]	°C	[wt%]	°C	[wt%]
20	0.32	140	1.82	260	5.39	380	11.46
40	0.46	160	2.25	280	6.22	400	12.72
60	0.64	180	2.75	300	7.13	420	14.04
80	0.86	200	3.30	320	8.11	440	15.44
100	1.13	220	3.93	340	9.16	450.3	16.19
120	1.45	240	4.62	360	10.28		

PFM. The thermodynamic condition in the PFM is included via the thermodynamic driving force for phase transformation. The method for computation of the thermodynamic driving force is presented in Section 3.2. If the second phase is stoichiometric, the component concentration in the aluminium phase in the interface region is explicitly determined from the mixture concentration as:

$$c_{\mathrm{Al}} = \frac{c - \phi c_{\mathrm{Al_3Mg_2}}^{\mathrm{st}}}{1-\phi}\,, \tag{4.2}$$

because the concentration of the second phase is constant. The molar driving force is only a function of component concentration (Mg) in the aluminium phase during the isothermal phase transformation. The molar driving force, $\Delta g_{\beta\alpha}$, for the phase transformation of Al_3Mg_2 in the aluminium phase for three homogenisation temperatures is presented in Fig.(4.1). The system is at its thermodynamic equilibrium state, when the molar driving force is zero. If the driving force is positive, the second phase dissolves into the aluminium matrix, and vice versa. If the driving force is negative, the second phase grows into the matrix. This molar driving force represents the connection between the PFM and the thermodynamic database.

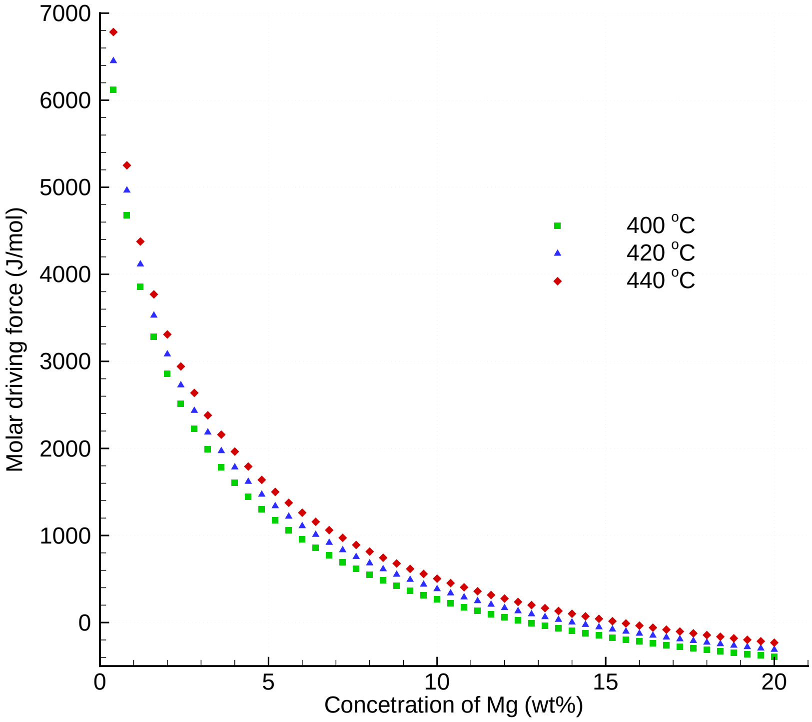

Figure 4.1: The molar driving force for phase transformation of Al_3Mg_2 in the aluminium phase for three homogenisation temperatures.

Nonstoichiometric phase. The connection between the models for phase transformations of the nonstoichiometric phase and aluminium matrix is explained in an example of the Al-Cu system. The aluminium and θ nonstoichiometric phase exist in two phase region in the solid state. The θ phase has approximately composition Al_2Cu, and in the literature is also denoted as Al_2Cu.

FTM. The interface concentrations in both phases are determined from the equilibrium phase diagram presented in Fig.(4.2). The interface concentration in aluminium and θ phase can be read from the light brown and sky blue line in the equilibrium phase diagram, respectively. The growth or dissolution of the second phase in the aluminium matrix is determined by the interface mass fluxes (Eq.(2.25)).

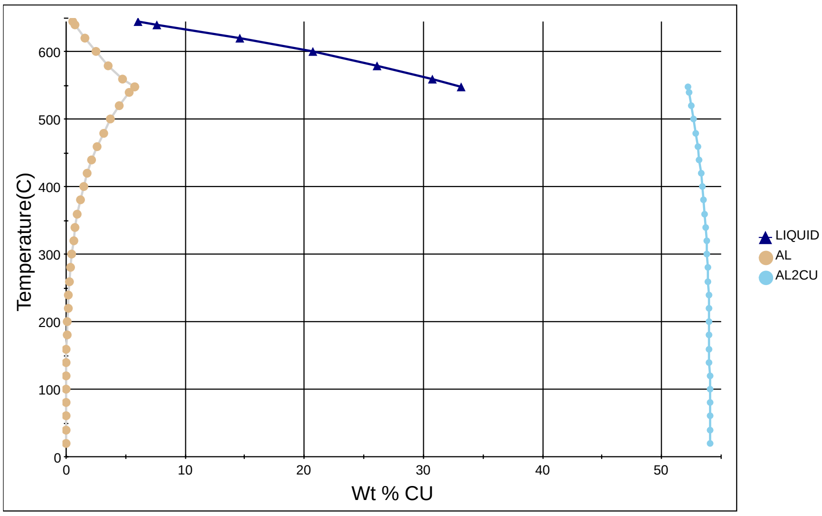

Figure 4.2: The equilibrium phase diagram of the binary Al-Cu system, obtained from [JMat-Pro, 2004].

PFM. When dealing with nonstoichiometric phases even in binary alloys, the connection between the explained PFM with a thermodynamic database is not as simple. Local concentrations of phases in the interface region need to be found from the following system of nonlinear equations:

$$\begin{aligned} c &= \phi\, c_\theta + (1-\phi)\; c_{\mathrm{Al}} \\ \mu_{\mathrm{Al}}^{\mathrm{Cu}} - \mu_{\mathrm{Al}}^{\mathrm{Al}} &= \mu_\theta^{\mathrm{Cu}} - \mu_\theta^{\mathrm{Al}}. \end{aligned} \tag{4.3}$$

The first equation is the definition of the mixture concentration and the second one represents the condition that phase diffusion potentials in both phases are equal. This system needs to be solved at each point in the diffuse-interface region. The chemical potentials of components as functions of concentration are necessary for the solution of this system. The chemical potentials of elements in both phases as a function of concentration of Cu, obtained by the thermodynamic database for temperature 500 °C are written in Tab.(4.3). These values are interpolated by the MQ RBFs for obtaining very accurate analytical functions of chemical potentials as functions of component concentration, as explained in the previous chapter. These approximations enable the use of solvers for the solution of the system of nonlinear equations. The molar driving force is computed from the values of the calculated concentrations of both phases.

Multicomponent Systems

Second phases are usually intermetallic compounds in multicomponent aluminium systems. The link between the physical models and thermodynamics is much simpler, if the second phase has a constant concentration.

Table 4.3: The chemical potentials of components as function of Cu concentration in the aluminium and θ phases at temperature 500 °C, obtained from [JMatPro, 2004].

$c_{\mathrm{Al}}^{\mathrm{Cu}}$ [wt %]	$\mu_{\mathrm{Al}}^{\mathrm{Al}}$ [J/mol]	$\mu_{\mathrm{Al}}^{\mathrm{Cu}}$ [J/mol]	c_{θ}^{Cu} [wt %]	$\mu_{\theta}^{\mathrm{Al}}$ [J/mol]	$\mu_{\theta}^{\mathrm{Al}}$ [J/mol]
2.0	−28761.5	−77761.7	30.0	−28845.7	−71327.2
6.0	−28840.4	−72668.7	34.0	−23791.5	−87913.4
10.0	−28890.3	−71249.6	38.0	−24136.6	−86471.6
14.0	−28913.5	−70830.9	42.0	−24602.5	−84831.1
18.0	−28913.7	−70821.7	46.0	−25299.5	−82752.5
22.0	−28896.6	−70981.0	50.0	−26583.1	−79507.4
26.0	−28870.2	−71178.0	54.0	−36233.3	−59496.5

FTM. The phase transformation of the Mg_2Si in the aluminium phase in the Al-Mg-Si system is used for expression of connections between FTM and thermodynamics. The interface concentrations in the aluminium phase need to be determined only from thermodynamics as an example of the second stoichiometric phase. The interface concentrations in the aluminium phase in the thermodynamic equilibrium with the Mg_2Si phase can be computed from the hyperbolic relation (Eq.(2.23)):

$$X_{\mathrm{Al}}^{\mathrm{Mg}^2} X_{\mathrm{Al}}^{\mathrm{Si}} = K\left(T\right), \tag{4.4}$$

where the aluminium phase is assumed as the dilute solution. The solubility product is computed from the pseudo-binary Al-Mg_2Si phase diagram of the ternary Al-Mg-Si system. The interface concentrations in the aluminium phase, computed by Eq.(4.4), are compared with the values directly obtained from the thermodynamic database. The interface concentrations, obtained from both methods and for three temperatures are presented in Fig.(4.3). The values are in very good agreement. We conclude that a hyperbolic relationship (Eq.(4.4)) can be used as the interface condition between the Mg_2Si and aluminium phase, if the JMatPro software [JMatPro, 2004] is used as the reference.

The aluminium phase can not be treated as the dilute solution in all phase transformations of aluminium systems. The interface condition is directly obtained from the thermodynamic database (Eq.(2.17)) in general. The phase transformation of the Al_2CuMg in the aluminium phase in the Al-Cu-Mg system is the example. This interface condition is used for modelling the phase transformation of the Al_2CuMg phase into aluminium phase.

PFM. In modelling the isothermal phase transformations with the PFM, if the second phase is stoichiometric, the molar driving force is the only function of the component concentrations in the aluminium phase. The molar driving force for the phase transformation of the Mg_2Si in the aluminium phase as a function of concentration of Mg and Si in the aluminium phase at temperature 560 °C is presented in Fig.(4.4). For accurate computation, the driving force as a function

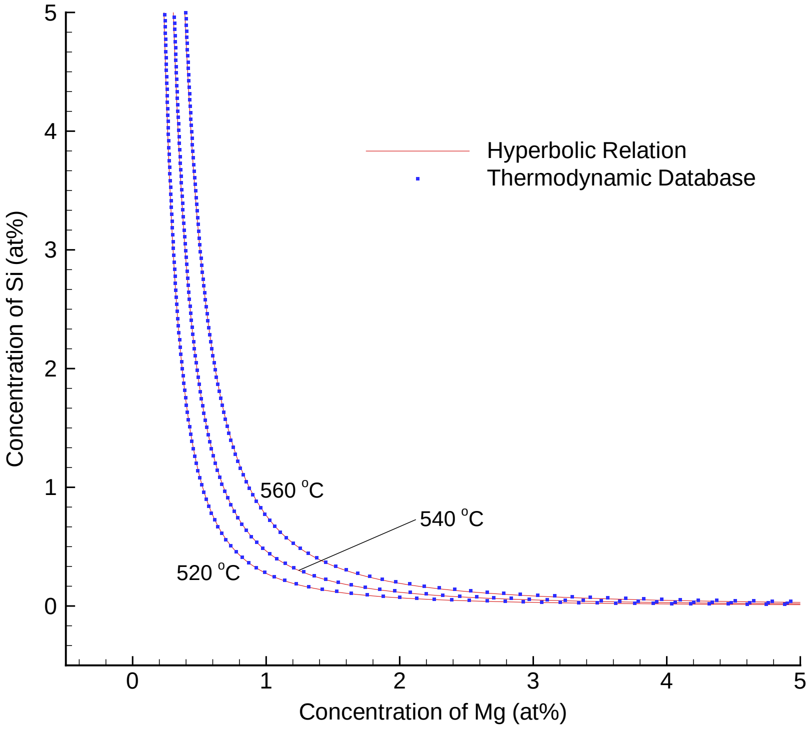

Figure 4.3: The interface concentrations in the aluminium phase during phase transformation between Mg_2Si and the aluminium phase at three temperatures.

of component concentrations in the aluminium phase needs to be very accurately approximated. Again, the interpolation by the MQ RBFs is incorporated here.

Summary

In the FTM, the interface condition for DC phase transformations is determined by the thermodynamic equilibrium state. For binary systems, the interface condition can be read from the equilibrium phase diagram. For multicomponent systems, the interface condition is determined in two ways. In the first one, the hyperbolic relationship between component concentrations in the aluminium phase is derived. This equation is derived throughout the solubility product, where the aluminium phase is assumed to be the dilute solution. In the second one, the interface condition is determined as an isothermal cross section of the solubility surface of the aluminium phase in the equilibrium phase diagram for multicomponent systems.

In the PFM, the connection of the model with a thermodynamic database is established via the driving force for the phase transformation. The molar driving force is the difference between the molar free energies of phases and gives information about the departure from the thermodynamic equilibrium state. In dealing with the stoichiometric second phase, the driving force is a function of component concentrations in the aluminium phase only. The accurate approximation

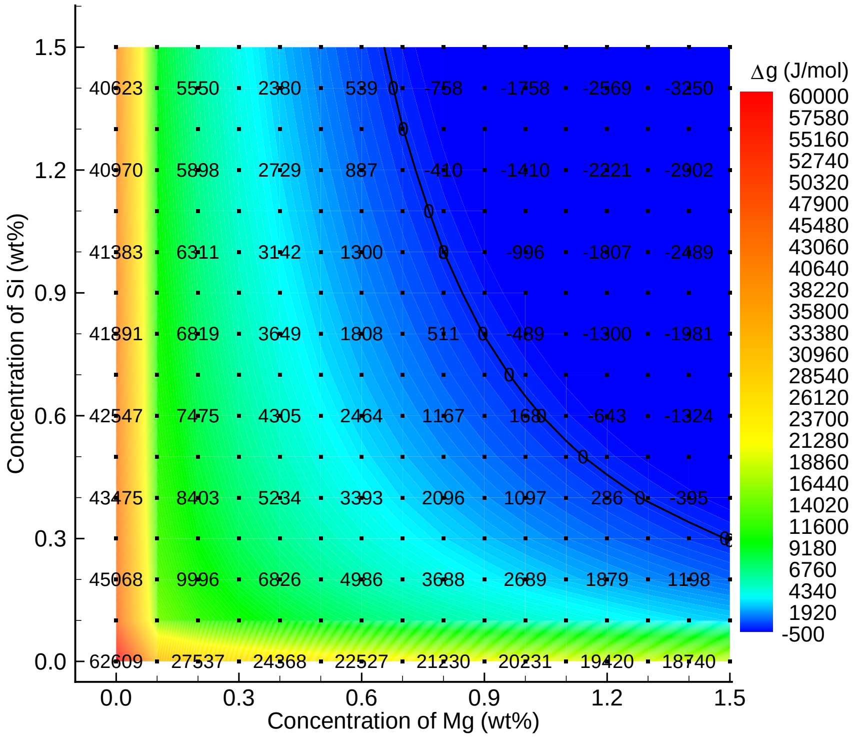

Figure 4.4: The molar driving force for phase transformation of Mg_2Si in the aluminium phase at temperature 560 °C.

of this function is essential for accurate computation of phase transformations by the PFM. In dealing with the nonstoichiometric second phase, the component concentrations in the phases have to be computed from the condition that phase diffusion potentials in both phases are equal. This condition at each node in the interface region has to be satisfied. The interpolation by MQ RBFs is implemented for accurate approximation of the thermodynamic data for computing the driving force.

4.1.2 Validation of the Physical Models

Comparison between the numerical results computed by the TDA and PFM in one-dimensional geometry is performed for validation of both physical models. It is performed in one-dimensional geometry only, because tracking of the interphase interface in the TDA in complex geometry is not a trivial task. On the other hand, the lack of knowledge about physical parameters, for example the interface-kinetic coefficient, makes the PFM difficult for quantitative simulations. Such a comparison can serve as a tool for estimation of the interface-kinetic coefficient in the PFM for the DC phase transformations.

The isothermal DC dissolutions of the Al_3Mg_2, θ, Mg_2Si and Al_2CuMg phase in the aluminium phase in the Al-Mg, Al-Cu, Al-Mg-Si and Al-Cu-Mg systems are computed, respectively. The numerical results computed by both models are presented on the same graphs to demonstrate the possibility of the PFM for quantitative phase transformations for modelling in the solid state. Because of the almost coincident results, the representative data of the following figures are written also in a tabular form. The FTM and FDM are used as solution procedures for the solution of the TDA and the PFM physical models, respectively.

The results are presented for the one-dimensional system with length $50\,\mu$m. The simulation time is one hour. Initial concentrations of components in the aluminium phase are assumed to be constant for simplicity. The boundary conditions are assumed to be of the Neumann type with zero flux.

Two equidistant fixed meshes are used for discretization of the PFM. The first mesh is around the interface and the coarser one out of the phase-change region. Distances between neighbouring nodes are for the first $\Delta x_{\mathrm{in}} = 2 \times 10^{-2}\,\mu$m and the second mesh $\Delta x_{\mathrm{out}} = 2 \times 10^{-1}\,\mu$m.

The interface thickness in each example is $1.2 \times 10^{-1}\,\mu$m. A very narrow interface region is used for getting sufficiently grid independent results. Therefore, the distance between the neighbouring nodes in the interface region has to be small. Consequently, the time-step length has to be short. The number of nodes in the diffuse-interface region is 6.

The interface energy and the interface-kinetic coefficient in the PFM have to be estimated. The interface energy depends on the type of particle-matrix interface [Porter and Easterling, 1990; Howe, 1997]. The interface energy has no big influence on the phase transformation kinetics in the DC mode and is chosen to be 5.0×10^{-1} J/m^2 in this section. The interface energy anisotropy significantly influences the particle shape.

The interface-kinetic coefficient in the PFM defines the mode of the phase transformation: DC, interface-controlled or mixed-mode. The interface-kinetic coefficient is proportionally constant between the driving force for phase transformation and the interface velocity (Eq.(1.16)). If the value of the interface-kinetic coefficient is high, the interface velocity has no influence on the transformation kinetics and the transformation is in the DC mode. The interface-kinetic coefficient is confined in application by the upper side, because it is proportional with phase-field mobility in the phase-field equation (Eq.(2.76)). The time-step length is inversely proportional with phase-field mobility during the numerical computation of the phase-field equation. The interface-kinetic coefficient for a particular phase transformation is an unknown parameter and it is adjusted by numerical experiments. The interface-kinetic coefficient is slowly increased until the difference in results computed with subsequent values becomes very small. Such approaches can determine the interface-kinetic coefficient as well as the phase-field mobility when the phase transformation is in the DC mode. The interface kinetic-coefficients for the validation of the PFM in DC mode and for different phase transformations are written in Tab.(4.4).

Table 4.4: The interface-kinetic coefficient for the phase transformations in the DC mode.

System	Phase Trans. between	μ_k [m^4/Js]
Al-Mg	Al_3Mg_2 and Al	5.0×10^{-13}
Al-Cu	θ and Al	5.0×10^{-14}
Al-Mg-Si	Mg_2Si and Al	5.0×10^{-15}
Al-Cu-Mg	Al_2CuMg and Al	5.0×10^{-14}

The relative difference between the numerical results is defined as

$$\Delta = \frac{\mid V_\mathrm{FTM} - V_\mathrm{PFM} \mid}{V_\mathrm{FTM}} \times 100\% \,, \tag{4.5}$$

where V_FTM and V_PFM are values computed by the FTM and PFM, respectively. The interface values in the PFM are computed implicitly from the isovalue of the PFV, $\phi = 0.50$. The interface values are computed by the linear interpolation between values at the neighbouring nodes.

The validation of physical models for each aluminium system is performed for three homogenisation temperatures with differences between them 20 °C. The numerical results computed by the FTM and PFM and relative differences between them are written in the Tables. The comparison of the results was presented in [Kovačević and Šarler, 2006b].

Al-Mg System

The one-phase classical Stefan problem needs to be solved in the TDA, because the Al_3Mg_2 is a stoichiometric phase. The diffusion length of Mg in this phase transformation ($D_\mathrm{Al}^\mathrm{Mg}/v$) is much smaller than the diffusion length of other components in binary systems. The total number of nodes for sufficiently accurate results in the FTM is 402, whereas the number of nodes in phases is equidistantly distributed in the initial condition.

The finer mesh in the PFM are between 6 μm and 16 μm. The total number of nodes in the domain is 701. The time-step lengths in the FTM and PFM are 5×10^{-2} s and 5×10^{-4} s, respectively.

The initial concentration of Mg in the aluminium phase is equal to 1.00 wt%. The initial interface position is chosen to be 15 μm. The numerical results are presented for following homogenisation temperatures 400 °C, 420 °C and 440 °C.

The Mg concentration profiles computed by the FTM and PFM after one hour of isothermal DC dissolution of the Al_3Mg_2 in the aluminium phase at three homogenisation temperatures are presented in Fig.(4.5(a)). The respective interface positions are presented in Fig.(4.5(b)). The values of the molar driving forces are interpolated from the values presented in Fig.(4.1). The data in Fig.(4.5(b)) and the relative differences between the numerical results computed by both physical models are written in Tab.(4.5). The interface positions and relative differences are calculated in ten equal time steps during the simulations.

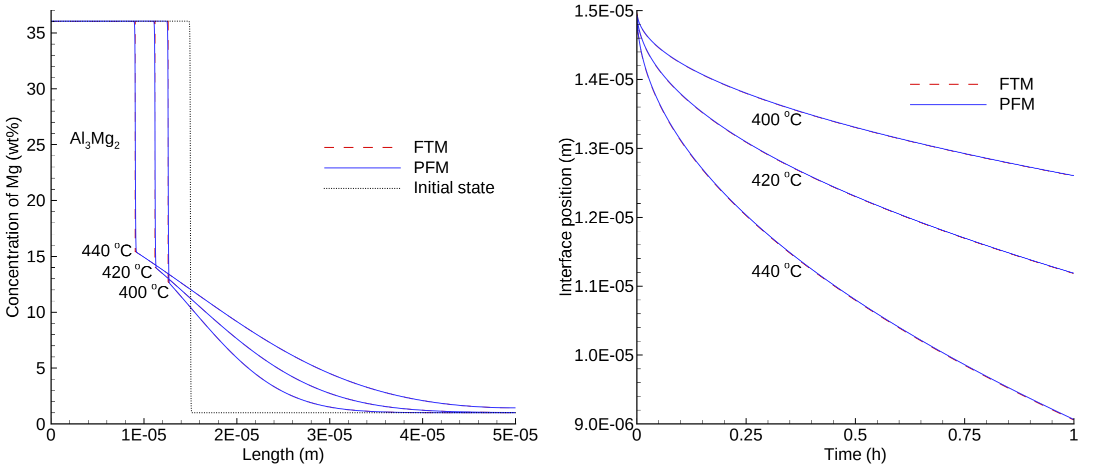

(a) The Mg concentration profiles after one hour of homogenisation.

(b) The interface positions during homogenisation.

Figure 4.5: Isothermal DC dissolution of the Al_3Mg_2 in the aluminium phase at three homogenisation temperatures.

Table 4.5: The numerical data for Fig.(4.5(b)) and the relative differences between the results of both methods.

	400 °C			420 °C			440 °C		
	FTM	PFM	Δ×	FTM	PFM	Δ×	FTM	PFM	Δ×
t [s]	l[μm]	l[μm]	10^2[%]	l[μm]	l[μm]	10^2[%]	l[μm]	l[μm]	10^3[%]
360	14.239	14.242	2.089	13.790	13.794	3.210	13.115	13.123	6.227
720	13.926	13.928	2.148	13.290	13.295	3.393	12.338	12.346	6.684
1080	13.685	13.688	2.252	12.907	12.912	3.608	11.741	11.749	6.940
1440	13.482	13.485	2.376	12.584	12.589	3.844	11.238	11.246	7.385
1800	13.303	13.306	2.411	12.299	12.304	4.066	10.795	10.803	7.723
2160	13.141	13.144	2.472	12.042	12.047	4.116	10.394	10.403	8.017
2520	12.992	12.995	2.206	11.805	11.810	4.072	10.026	10.034	7.974
2880	12.854	12.857	2.253	11.585	11.590	4.168	9.683	9.691	8.381
3240	12.724	12.727	2.532	11.378	11.383	4.425	9.361	9.369	8.789
3600	12.601	12.604	2.615	11.183	11.188	4.444	9.056	9.065	9.268

Al-Cu System

Copper is the most common element for aluminium alloys, and a variety of alloys (2xxx series) in which copper is the major addition were developed. Copper is solvable up to 5.74 wt% in the aluminium phase. The aluminium phase has the

FCC crystal structure and the phase θ has a complex body-centred tetragonal structure.

The basic purpose of homogenisation of 2xxx aluminium alloys is to dissolve the interdendritic eutectic, the mixture of the phases θ and Al. In this section, we demonstrate the numerical results of the dissolution of the θ phase in the aluminium phase, computed by the FTM and PFM. Dissolution of the eutectic phase in the aluminium phase during homogenisation is presented in Chapter 6, where the eutectic phase is treated as a heterogeneous mixture of solid phases.

The initial concentrations of Cu in the aluminium and θ phase are constant and equal to 0.50 wt% and 53.00 wt%, respectively. The position of the initial interface is chosen to be 10 μm. Temperatures 480 °C, 500 °C, and 520 °C are chosen as homogenisation temperatures.

The number of nodes in both models are the same as in the Al-Mg system. The time-step length in the PFM is 5×10^{-5} s. The time-step length is considerable lower than in the example with a stoichiometric phase, because the condition, that phase diffusion potentials in both phases are equal, is implemented.

The Cu concentration profiles after one hour of isothermal DC dissolution of the θ in the aluminium phase at three homogenisation temperatures computed by the FTM and PFM are presented in Fig.(4.6(a)). Interface positions are presented in Fig.(4.6(b)). The data in Fig.(4.6(b)) and the relative differences between the numerical results computed by both physical models are written in Tab.(4.6).

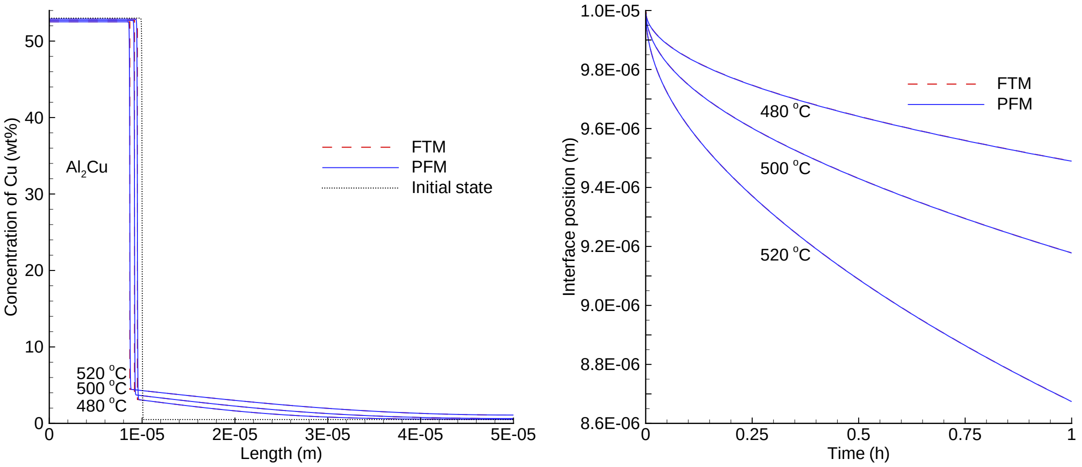

(a) The Cu concentration profiles after one hour of homogenisation.

(b) The interface positions during homogenisation.

Figure 4.6: Isothermal DC dissolution of the θ in the aluminium phase at three homogenisation temperatures.

Al-Mg-Si System

Aluminium alloys of the 6xxx heat-treatable series are most widely used for the production of extruded parts. The Al-Mg-Si system defines the 6xxx series of

Table 4.6: The numerical data for Fig.(4.6(b)) and the relative differences between the results of both methods.

	480 °C			500 °C			520 °C		
	FTM	PFM	$\Delta\times$	FTM	PFM	$\Delta\times$	FTM	PFM	$\Delta\times$
t [s]	$l[\mu\mathrm{m}]$	$l[\mu\mathrm{m}]$	$10^3[\%]$	$l[\mu\mathrm{m}]$	$l[\mu\mathrm{m}]$	$10^3[\%]$	$l[\mu\mathrm{m}]$	$l[\mu\mathrm{m}]$	$10^3[\%]$
360	9.840	9.839	5.984	9.749	9.748	2.847	9.607	9.607	0.274
720	9.774	9.773	6.841	9.644	9.644	1.535	9.441	9.441	0.555
1080	9.723	9.722	3.634	9.563	9.563	1.752	9.308	9.308	0.490
1440	9.680	9.679	6.008	9.493	9.493	4.953	9.192	9.192	3.075
1800	9.642	9.641	4.229	9.431	9.430	3.727	9.088	9.088	1.134
2160	9.607	9.606	3.388	9.373	9.373	5.056	8.993	8.993	3.899
2520	9.575	9.574	6.898	9.320	9.320	3.777	8.906	8.906	0.148
2880	9.545	9.544	2.845	9.270	9.270	3.410	8.824	8.824	0.024
3240	9.516	9.516	6.925	9.223	9.223	1.594	8.747	8.747	0.386
3600	9.490	9.489	4.316	9.178	9.178	5.096	8.674	8.674	4.066

aluminium alloys. Extrudability of these alloys is strongly influenced by the amount of Mg and Si in the solid solution, and the size of Mg_2Si precipitates.

The dissolution of the stoichiometric Mg_2Si phase in the aluminium phase during homogenisation is presented here. The hyperbolic relation (Eq.(4.4)) as the condition for the interface concentrations in the aluminium phase is used in the FTM. The molar driving force for dissolution of Mg_2Si in the aluminium phase used in the PFM at temperature 560 °C is presented in Fig.(4.4). The initial concentrations of Mg and Si in the aluminium phase are constant and equal to 0.01 wt% and 0.01 wt%, respectively. The initial concentrations of components are very low for making the dissolution kinetics as high as possible. The concentrations of Mg and Si in the Mg_2Si stoichiometric phase are 63.38 wt% and 36.62 wt%, respectively. The initial interface position is 6 μm. Homogenisation temperatures are 520 °C, 540 °C and 560 °C.

The total number of nodes in the FTM is 115, whereas the number of nodes in the Mg_2Si and the aluminium phase are 15 and 100, respectively. The boundary between the meshes in the PFM in both multicomponent system is 7 μm from the left boundary of the system. The total number of nodes is 566. The time-step lengths in the TDA and PFM are 1×10^{-1} s and 1×10^{-4} s, respectively.

The interface positions during isothermal DC dissolution of the Mg_2Si phase in the aluminium phase at three homogenisation temperatures are presented in Fig.(4.7(a)). The numerical results related to Fig.(4.7(a)) are written in Tab.(4.7). The interface concentrations of Mg and Si in the aluminium phase during homogenisation computed by both models are presented in Fig.(4.7(b)).

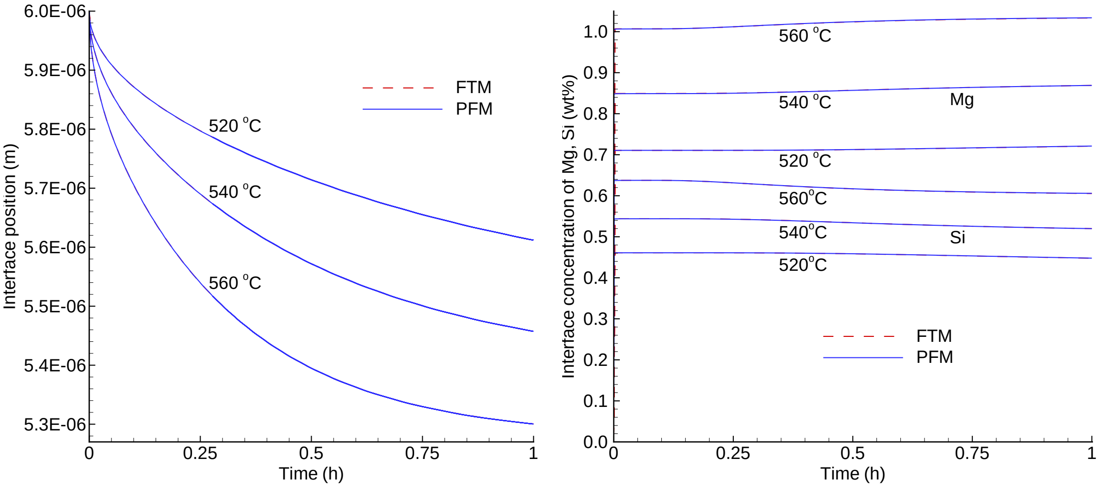

(a) The interface positions during homogenisation.

(b) The interface concentrations of Mg and Si in the Al phase during homogenisation.

Figure 4.7: Isothermal DC dissolution of the Mg_2Si in the aluminium phase at three homogenisation temperatures.

Table 4.7: The numerical data for Fig.(4.7(a)) and the relative differences between the results of both methods.

	520 °C			540 °C			560 °C		
	FTM	PFM	$\Delta\times$	FTM	PFM	$\Delta\times$	FTM	PFM	$\Delta\times$
t [s]	$l[\mu m]$	$l[\mu m]$	$10^3[\%]$	$l[\mu m]$	$l[\mu m]$	$10^3[\%]$	$l[\mu m]$	$l[\mu m]$	$10^3[\%]$
360	5.872	5.872	2.420	5.804	5.804	4.967	5.705	5.706	4.465
720	5.819	5.818	2.876	5.722	5.723	5.306	5.585	5.586	4.456
1080	5.778	5.778	3.665	5.661	5.661	4.599	5.501	5.501	1.730
1440	5.744	5.744	2.325	5.612	5.612	1.075	5.440	5.440	1.362
1800	5.714	5.714	4.439	5.572	5.572	1.160	5.395	5.395	5.137
2160	5.688	5.688	0.049	5.539	5.539	1.271	5.363	5.363	0.668
2520	5.666	5.666	1.580	5.512	5.512	0.472	5.339	5.339	4.885
2880	5.646	5.646	1.450	5.490	5.490	1.900	5.322	5.322	1.431
3240	5.628	5.628	0.004	5.472	5.472	0.185	5.310	5.309	4.086
3600	5.612	5.612	3.871	5.457	5.457	1.718	5.300	5.300	4.689

Al-Cu-Mg System

Dural alloys based on Al-Cu-Mg systems are important in structural applications where a combination of good damage tolerance and high strength is required. In this section, we estimate the transformation kinetics of the Al_2CuMg or S phase in the aluminium phase during solution heat treatment. The initial concentrations of Cu and Mg in the aluminium phase are constant and equal to 0.50 wt% and 1.20 wt%, respectively. The concentrations of Cu and Mg in the Al_2CuMg stoichiometric phase are 44.80 wt% and 17.14 wt%, respectively. The general thermodynamic condition for the interface concentrations in the aluminium phase is used from Eq.(2.17). If we use this interface condition, additional assumptions are not needed. Homogenisation temperatures are 450 °C, 470 °C and 490 °C.

The position of the initial interface and the number of nodes in both models are the same as in the Al-Mg-Si system. The time-step lengths in the TDA and PFM are 1×10^{-1} s and 2×10^{-4} s, respectively.

The interface positions during isothermal DC dissolution of the Al_2CuMg phase in the aluminium phase at three homogenisation temperatures are presented in Fig.(4.8(a)). The interface concentrations of alloying components in aluminium computed by the models are presented in Fig.(4.8(b)). The numerical results of interface positions and relative differences between the results are written in Tab.(4.8). The relative differences between the results computed by the models are negligible from the engineering point of view.

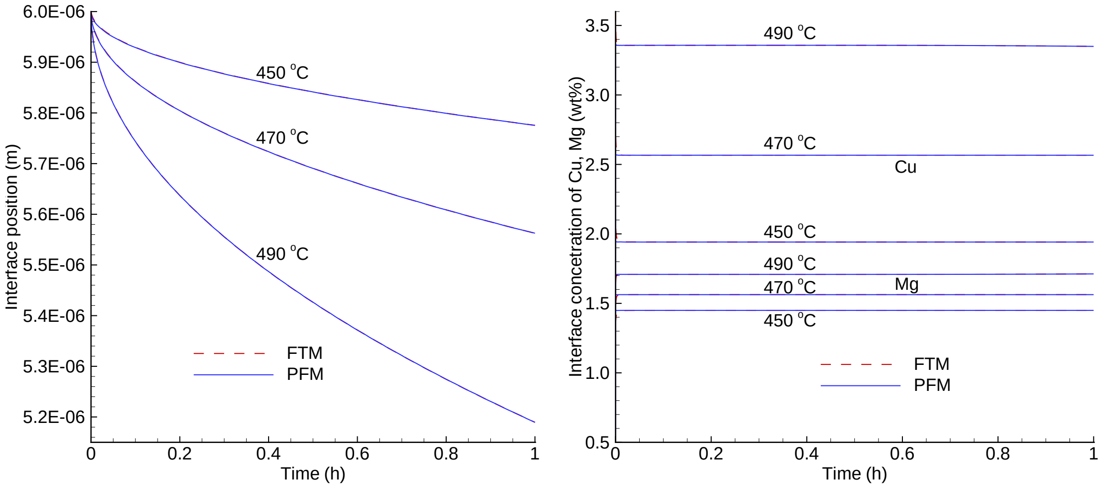

(a) The interface positions during homogenisation.

(b) The interface concentrations of Cu and Mg in the Al phase during homogenisation.

Figure 4.8: Isothermal DC dissolution of the Al_2CuMg in the aluminium phase at three homogenisation temperatures.

Summary

The physical modes are validated by comparison of the numerical results computed by the TDA and PFM. The comparison is performed for isothermal DC phase transformations. The whole spectra of represented numerical results, computed by both physical approaches are in very good agreement. The dissolution of the stoichiometric Al_3Mg_2 and nonstoichiometric θ phase into the aluminium phase for Al-Mg and Al-Cu binary system is solved, respectively. The dissolution of the second stoichiometric and nonstoichiometric phase in the aluminium phase for binary system is successfully modelled by the FTM and PFM.

Furthermore, the good agreement between the results computed by the presented PFM and the Vermolen model [Vermolen and Vuik, 2000] for the dissolu-

Table 4.8: The numerical data for Fig.(4.8(a)) and the relative differences between the results of both methods.

	450 °C			470 °C			490 °C		
t [s]	FTM	PFM	$\Delta\times$	FTM	PFM	$\Delta\times$	FTM	PFM	$\Delta\times$
	$l[\mu\text{m}]$	$l[\mu\text{m}]$	$10^3[\%]$	$l[\mu\text{m}]$	$l[\mu\text{m}]$	$10^3[\%]$	$l[\mu\text{m}]$	$l[\mu\text{m}]$	$10^3[\%]$
360	5.929	5.929	7.494	5.862	5.862	0.440	5.744	5.744	0.240
720	5.900	5.900	6.071	5.804	5.804	0.302	5.637	5.637	3.684
1080	5.877	5.877	7.304	5.760	5.760	1.871	5.556	5.555	2.998
1440	5.858	5.858	5.893	5.723	5.724	1.579	5.487	5.487	3.746
1800	5.842	5.841	0.966	5.691	5.691	1.860	5.426	5.426	4.404
2160	5.826	5.826	0.428	5.661	5.661	0.767	5.372	5.372	0.041
2520	5.812	5.812	4.087	5.634	5.634	3.728	5.321	5.321	3.645
2880	5.799	5.799	3.098	5.609	5.609	0.704	5.274	5.274	1.934
3240	5.787	5.787	0.612	5.585	5.585	3.138	5.231	5.231	0.742
3600	5.776	5.775	5.022	5.562	5.563	2.829	5.190	5.190	1.885

tion of a Mg_2Si particle in an aluminium matrix for Al-Mg-Si system is presented. The isothermal DC dissolution of the Al_2CuMg particle in the aluminium phase for Al-Cu-Mg system is computed by both physical models. The dissolution kinetics computed for simulation in a multicomponent system by the physical models are in very good agreement. The general thermodynamic interface condition for this phase transformation is used in the TDA. The interface-kinetic coefficients in the PFM for the DC phase transformations are estimated by such comparisons.

It is evident that there is a huge influence of homogenisation temperature on the dissolution kinetics. Because of the narrow interface thickness, the number of points in the PFM is higher than in the FTM. Consequently, the time-step length is smaller in the PFM. Also, if we use the thermodynamic conditions written in Eq.(4.3) at every node in the interface region, the time-step length is even smaller.

The accuracy of the PFM results depends on the quality of the interpolation scheme for computing the molar driving force in the phase-field equation. Even with finer meshes, the linear interpolation of the driving force as a function of component concentrations does not produce sufficiently accurate results.

The DC phase transformations in one-dimensional geometry are more easily simulated by the TDA only. The preliminary experimental results show that solid-solid phase transformations are between the DC and interface-controlled mode. In the mixed-controlled mode, the interface condition is influenced by the interface velocity. The tracking of the interphase interface in the FTM is very difficult to implement with complex topology. Also, interface curvature influences the interface condition. The curvature computation in the TDA is not a trivial task. The above mentioned reasons confine the implementation of the TDA for the phase transformations in the solid state. In the following of the thesis, the focus is on the PFM.

4.1.3 The PFM in Two-Dimensional Geometry

Phase transformations at the micro level always occur in the presence of complex geometry. The capability of the PFM for solving phase transformations in a complex topology is demonstrated in this section. Results, independence of interface thickness as well as the total number of nodes in one-dimensional geometry, are demonstrated at the start. These facts enable us to solve the PFM on an equidistant mesh with two-dimensional geometry with reasonable computational time. The governing equations are discretized by the second-order finite difference scheme in space and explicit in time, as explained in Section 3.2. The physical and material properties are assumed to be isotropic.

Results Independence of the Interface Thickness

The interface thickness is fixed to a very small value $1.2 \times 10^{-1}\,\mu$m in the previous computations. The interface positions and concentrations are enabled to be very accurate by using a very small value of this model parameter. The interface values in the PFM are obtained indirectly by the PFV. These interface values need to be very accurate, because of the comparison with numerical results obtained by the TDA, where the interface values are explicitly defined in the model.

The DC phase transformations can be computed with much larger interface thicknesses then in previous computations. Results that are independent of the interface thickness parameter in the PFM are demonstrated here. The numerical results are presented for the Al-Mg system, because of its fastest dissolution kinetics and the shortest diffusion length. Consequently, it can be implemented for other binary or multicomponent systems.

The Mg concentration profiles after one hour of isothermal DC dissolution computed by various interface thicknesses are presented in Fig.(4.9(a)). The interface thicknesses are $1.2 \times 10^{-1}\,\mu$m, $6.0 \times 10^{-1}\mu$m and $1.2\,\mu$m. The numerical results that are independent of the interface thickness are clearly presented. Accurate numerical results can be obtained by using interface thicknesses that are ten times larger than in previous examples. Therefore, the results can be obtained by a significantly smaller number of nodes in the phase-change region.

Recent numerical results are computed by the earlier grid with distances between neighbouring nodes inside $\Delta x_{\text{in}} = 2.0 \times 10^{-2}\mu$m and outside the phase-change region $\Delta x_{\text{out}} = 2.0 \times 10^{-1}\mu$m. The numerical results obtained by different distances between neighbouring nodes in the phase-change region are presented in Fig.(4.9(b)). The interface thickness is fixed to be $6.0 \times 10^{-1}\mu$m. It is evident that accurate results can be obtained even when the distances between neighbouring nodes in outside and inside the phase-change regions are equal, $\Delta x_{\text{in}} = \Delta x_{\text{out}} = 2.0 \times 10^{-1}\mu$m. The total number of nodes in the domain is 251. Accurate results can be obtained even when using few nodes over the diffuse interface. The time-step length is fixed on 2.5×10^{-3} s.

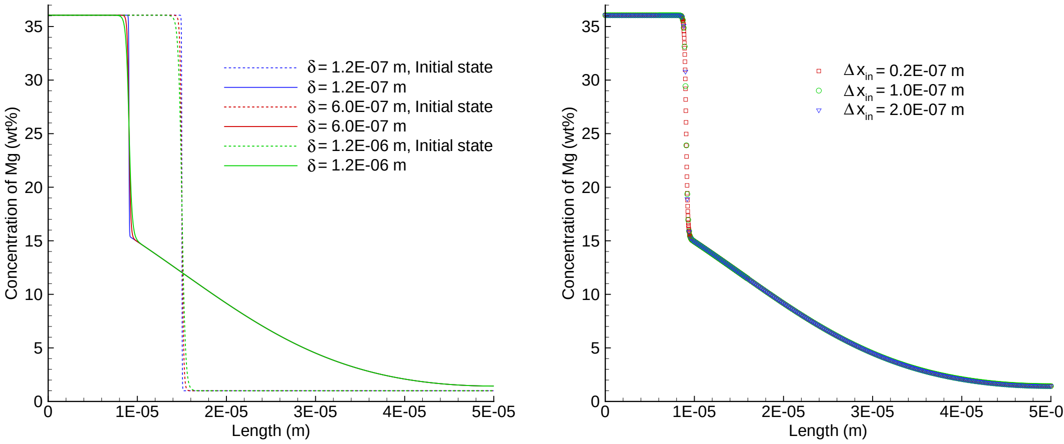

(a) The numerical results computed by the three interface thicknesses with the earlier defined mesh.

(b) The numerical results computed by the three node arrangements with the interface thickness $6.0 \times 10^{-1}\,\mu$m.

Figure 4.9: The Mg concentration profiles of DC dissolution at homogenisation temperature 440 °C computed by different interface thicknesses and different meshes.

Dissolution of Complex Shape Particle

The dissolution of a complex shape Al_2CuMg particle in the aluminium phase is chosen for demonstration. The model parameters of this phase change are: the interface energy 5.0×10^{-1} J/m^2, the interface thickness $6.0 \times 10^{-1}\mu$m and the interface-kinetic coefficient 5.0×10^{-15} m^4/Js. The interface-kinetic coefficient is lower than in the previous example of this phase transformation (5.0×10^{-14} m^4/Js), because we now use a larger time-step length in the computation only. The phase transformation using the selected interface-kinetic coefficient is still in the DC mode.

The arbitrary initial shape of Al_2CuMg phase is presented in Fig.(4.10). The computational domain is $50\,\mu$m × $50\,\mu$m square. The initial uniform concentrations of Cu and Mg in the aluminium phase are 0.50 wt% and 0.50 wt%, respectively. The boundary conditions are assumed to be of the Neumann type with zero flux. The governing equations are discretized by the FDM on the equidistant 251 × 251 mesh. The time-step length is 5×10^{-3} s.

The DC dissolution of a Al_2CuMg particle in the aluminium phase is computed at a homogenisation temperature 490 °C. The Cu and Mg concentration fields during homogenisation are presented in Fig.(4.11). The concentration fields after one hour of heat treatment (Fig.(4.11(a),4.11(b))), two hours (Fig.(4.11(c),4.11(d))) and three hours (Fig.(4.11(c),4.11(d))) are presented. In the first stage of homogenisation, the dissolution is dominant. Later, when the component concentration gradients become smaller, rounding is also pronounced. The curvature effect is more evident when the particle becomes smaller. The dissolution of concave surfaces is slower than the dissolution of convex interfaces. In the presented example, the particle is approximately a circle after three hours

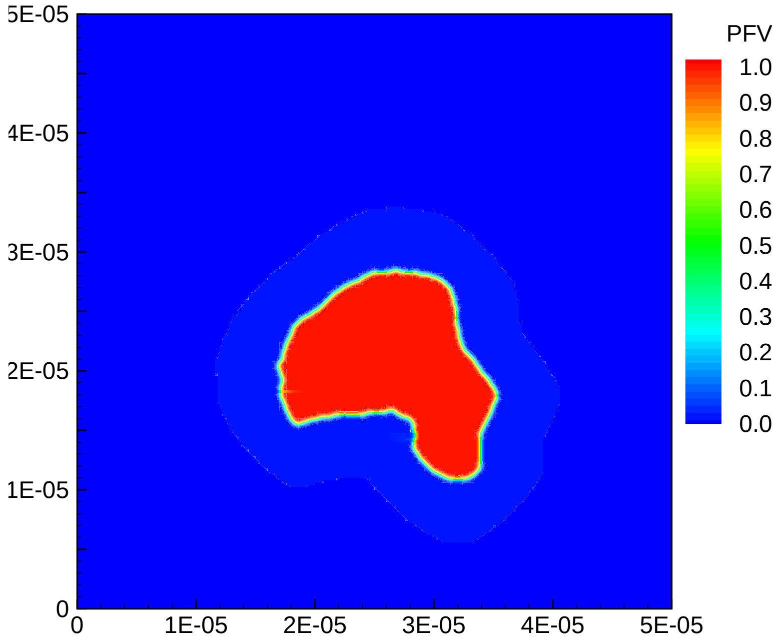

Figure 4.10: The initial shape of Al_2CuMg particle, obtained from the PFV.

of dissolution. The particle is completely dissolved after 3 h 40 min at heating treatment temperature.

The dissolution of the complex shape particle is computed. The PFM has been implemented for phase transformation using various particle topologies, where the soft impingement diffusion mechanism has been also considered.

Summary

The major problem in the PFM is the determination of the model parameters. Interface thickness, as a model parameter, has to be small in comparison with the diffusion length of the component in the particular phase transformation. The results that are independent of interface thickness are demonstrated in the dissolution of Al_3Mg_2 in the aluminium phase example. Thicker interfaces enable the use of fewer nodes in the system. Such a problem is computed on an equidistant grid with one-dimension geometry without losing accuracy. This conclusion enables the use of equidistant grids with the two-dimensional geometry. Also, the interface thickness has to be small in comparison with interface curvature. The capability of the PFM is demonstrated in the dissolution of an arbitrary complex shape Al_2CuMg particle into the aluminium phase. On this simple example, one can see that particle curvature influences the dissolution kinetics. During the dissolution, the particle also becomes round. All necessary physical parameters for solid-solid phase transformation modelling are incorporated in the PFM.

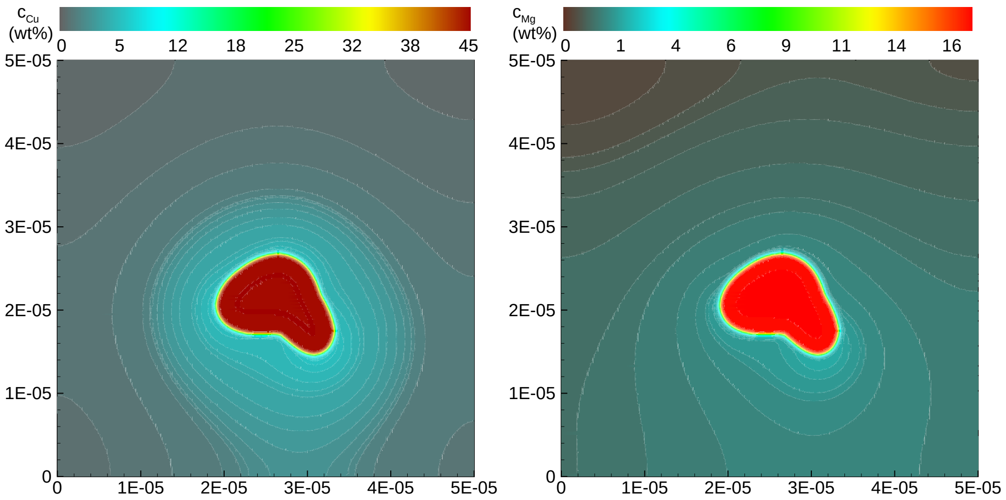

(a) The Cu concentration field, one hour. (b) The Mg concentration field, one hour.

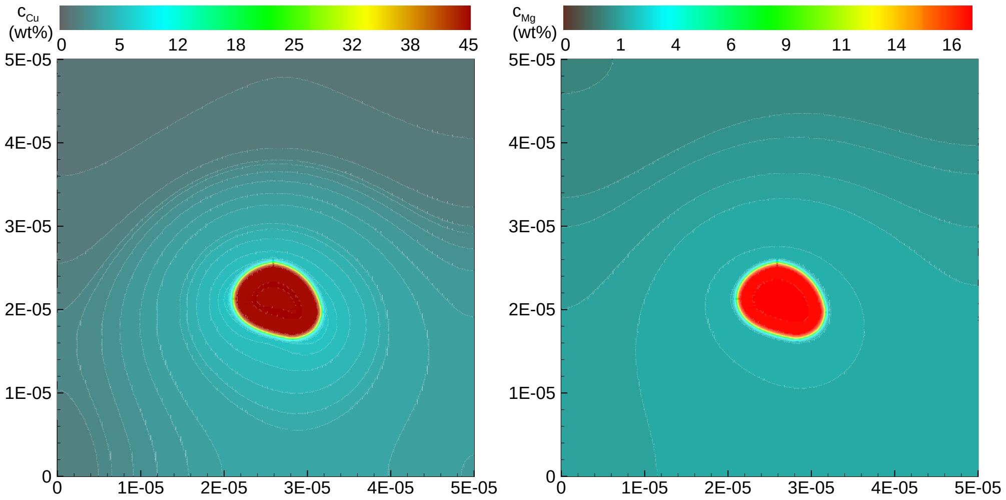

(c) The Cu concentration field, two hours. (d) The Mg concentration field, two hours.

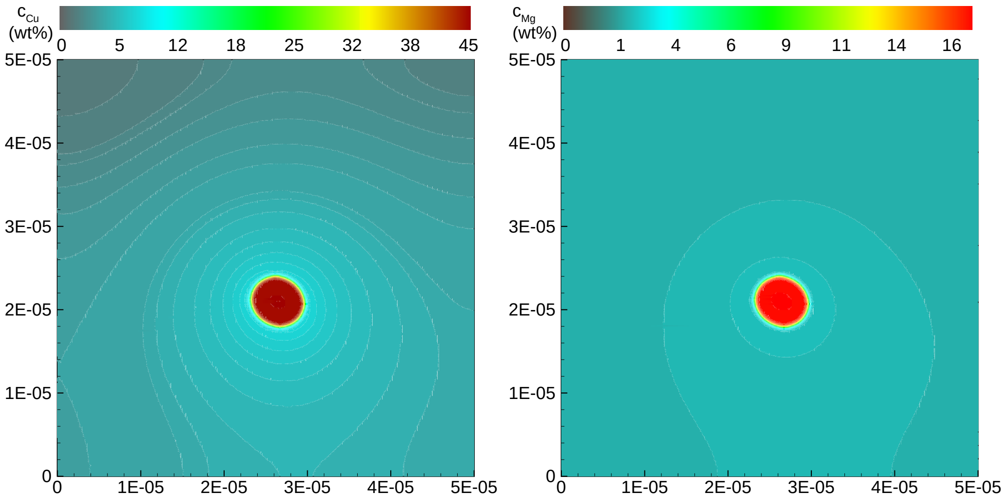

(e) The Cu concentration field, three hours. (f) The Mg concentration field, three hours.

Figure 4.11: The isothermal DC dissolution of the artificial shape Al_2CuMg particle in the aluminium phase at the homogenisation temperature 490 °C.

4.1.4 Comparison of Different Solution Procedures using the PFM

The numerical results simulated by the PFM and solved by the local r-adaptive strong-form MFM are compared with and the results computed by the fine-grid FDM. The isothermal DC dissolution of Al_3Mg_2 particles in the aluminium phase is simulated. The Al-Mg binary system is selected, because the solubility of Mg is highest in the aluminium phase, and the dissolution kinetics are the fastest out all alloying elements in commercial aluminium production. The interface energy and the interface-kinetic coefficient are $3.0 \times 10^{-1}\,\mathrm{J/m^2}$ and $3.0 \times 10^{-14}\,\mathrm{m^4/Js}$, respectively. The constant concentration of Mg in the aluminium phase is used as the initial state. The concentration field and the interface position through time are computed by the previously explained solution procedure in Section 3.3. The procedure and its performance are considerably different in the one and two-dimensional geometry; because of this, the numerical results are presented separately.

One-dimensional Geometry

The system length and the initial interface position are again $50\,\mu\mathrm{m}$ and $15\,\mu\mathrm{m}$, respectively. The initial concentration of Mg in the aluminium phase is the equilibrium concentration at temperature 20 °C. This concentration is computed by the JMatPro software for aluminium alloys, and takes on the value 0.35 wt%Mg. The interface thickness is $1.2 \times 10^{-1}\,\mu\mathrm{m}$.

The total number of nodes used for presentation of the numerical procedure is chosen to be 151. The number of nodes in the local support is three, the simplest possible. The control function is computed by Eq.(3.108), where the transition zone thickness in Eq.(3.109) is $6\,\mu\mathrm{m}$. Generally, the control function for node distribution can be written analytically in the one-dimensional geometry, therefore the node distribution is much easier. The maximum value of the control function is 30. The time-step length is $1 \times 10^{-3}\,\mathrm{s}$. The transition time is 5 s, and therefore the grid is redistributed every 5 s. The computational method for the node positions is explained in Section 3.3.5. The collocation based on the local standard interpolation is used for the computation. The values at the new node positions are computed by the global interpolation with RBFs.

The Mg concentration profiles computed by the r-adaptive local collocation with RBFs during one hour of isothermal dissolution for three homogenisation temperatures are presented in Fig.(4.12). The concentration profiles are presented every 720 s. Homogenisation temperatures are 400 °C, 420 °C and 440 °C. The interface positions during the dissolution for three homogenisation temperatures are presented in Fig.(4.13). The results obtained by the r-adaptive LRBFCM and the FDM are plotted by solid blue and dashed red lines, respectively. The interface positions and the relative difference between the results computed by both numerical methods every 360 s are written in Tab.(4.9).

The numerical results are compared with the results obtained by the fine-grid

FDM, used as the reference solution. The purpose of this comparison is to verify the equivalence of the new numerical procedure. The agreement between numerical results obtained by the proposed numerical procedure and the reference solution is very good. The r-adaptive numerical procedure derived for the solution of phase-change problems gives very accurate results in the one-dimensional geometry. These accurate results are obtained with a significantly less number of total nodes even if the interface thickness is small.

The major advantage of the presented procedure is better shown in the next example, where the same problem is solved by only 101 nodes in the computational domain. The comparison of the Mg concentration profiles after 720 s, 2160 s and 3600 s at homogenisation temperature 440 °C are presented in Fig.(4.14(a)). Again, agreement between the r-adaptive LRBFCM results and the fine-grid FDM is very good. The input parameters in the r-adaptive node arrangement are the same as in the previous example.

Table 4.9: The interface positions in time at three homogenisation temperatures computed by the LRBFCM and the FDM.

	$T = 440\,^\circ\mathrm{C}$			$T = 420\,^\circ\mathrm{C}$			$T = 400\,^\circ\mathrm{C}$		
t	$l\,[\mu\mathrm{m}]$		$\Delta\times$	$l\,[\mu\mathrm{m}]$		$\Delta\times$	$l\,[\mu\mathrm{m}]$		$\Delta\times$
[s]	FDM	MFM	10^2[%]	FDM	MFM	10^2[%]	FDM	MFM	10^2[%]
360	13.064	13.063	0.278	13.749	13.749	0.204	14.209	14.209	0.117
720	12.260	12.259	0.459	13.230	13.231	0.483	13.881	13.881	0.028
1080	11.643	11.642	1.180	12.832	12.832	0.182	13.630	13.629	0.278
1440	11.123	11.121	1.723	12.496	12.496	0.024	13.417	13.417	0.014
1800	10.665	1.0663	1.627	12.201	12.200	0.516	13.230	13.230	0.214
2160	10.251	10.248	2.381	11.933	11.932	0.755	13.062	13.061	0.474
2520	9.870	9.866	3.293	11.688	11.687	0.966	12.906	12.905	0.743
2880	9.515	9.511	4.014	11.459	11.457	1.303	12.762	12.761	0.715
3240	9.182	9.178	5.226	11.244	11.242	1.883	12.626	12.625	0.822
3600	8.867	8.862	6.295	11.041	11.038	2.065	12.497	12.496	0.618

The component concentration profiles after 720 s, 2160 s and 3600 s of the isothermal dissolution in one-dimensional geometry, computed by three different maximum values of the control function, are presented in Fig.(4.14(b)). The results are presented for the maximum values of the control function of $10, 30$ and 50. The initial node arrangements computed by the same three maximum values of the control function are presented in Fig.(3.8). The interface positions computed by the LRBFCM and the FDM are written in Tab.(4.10). Also, the relative difference between the results computed by the LRBFCM with the three maximum values of control function and the reference values are written in the same table. The numerical results are clearly independent of the maximum values of the control function that controls the node arrangements.

Table 4.10: The interface positions during one hour of dissolution for three maximum values of control function of r-adaptive LRBFCM and the FDM.

	FDM	MFM, $\bar{\kappa}_{\max} = 10$		MFM, $\bar{\kappa}_{\max} = 30$		MFM, $\bar{\kappa}_{\max} = 50$	
t [s]	l [μm]	l [μm]	$\Delta \times 10^2$ [%]	l [μm]	$\Delta \times 10^2$ [%]	l [μm]	$\Delta \times 10^2$ [%]
360	13.064	13.067	2.620	13.061	2.049	13.060	3.211
720	12.260	12.257	2.409	12.256	2.820	12.254	4.482
1080	11.643	11.642	1.252	11.640	2.490	11.636	6.163
1440	11.123	11.120	2.694	11.120	2.984	11.114	7.785
1800	10.665	10.662	2.843	10.661	3.430	10.655	9.308
2160	10.251	10.246	4.329	10.247	3.715	10.240	10.360
2520	9.870	9.862	7.423	9.866	4.251	9.858	11.385
2880	9.515	9.506	9.642	9.511	4.576	9.504	11.583
3240	9.182	9.173	9.974	9.177	5.453	9.171	12.010
3600	8.868	8.860	8.127	8.862	6.048	8.856	12.470

Two-dimensional Geometry

The computational domain is a square with size 15 μm. The initial particle shape of Al_3Mg_2 phase is taken arbitrarily from the micrograph. The initial concentration of Mg in the aluminium phase is 1.00 wt%Mg. The initial PFV and initial concentration of Mg are presented on Figs.(4.15(a),4.15(b)), respectively. The positions of nodes are computed on equidistant 76×76 grids with a total number of nodes equal to 5776.

The node arrangement from the procedure explained in Section 3.3.5 is computed by Eq.(3.102). The collocation by a local standard interpolation scheme without a additional polynomial term is implemented for solving these equations. The local supports for the boundary nodes with the only one boundary nodes are necessary for accurate computation of the Neumann boundary conditions (Fig.(3.6(b))). A collocation is made by local support with five supporting nodes on equidistant grids (Fig.(3.4(b))).

The phase-field equation and the concentration equation are solved by the collocation with RBFs on the r-adaptive node distributions. All boundary conditions in the phase-field and the concentration equation are of Neumann type with zero flux. These boundary conditions have a crucial influence on the stability of results computed by the collocation methods on an r-adaptive arrangement. The results computed by collocation based on the local standard interpolation scheme using adaptive node distribution are not correct on the boundaries, even if only one boundary node is used in the local support. The high gradients in the fields have an influence this condition. Therefore, double consideration of boundary nodes for the collocation based on Hermite-type interpolation is necessary for computation on the r-adaptive node distribution.

The polynomial term is necessary for obtaining the interpolation without noise in the region with flat fields. The results are without noise even with a constant polynomial term. By increasing the order of the polynomial augmentation at the same time as the matrix size increases, the computation time is also increased. Because of this, the length of the polynomial term is chosen to be one. The local supports are determined by the procedure described in Section 3.3.4 and presented in Fig.(3.5).

The interface thickness is $8.0 \times 10^{-1}\,\mu$m. The control function is computed by Eq.(3.108), where the norm in Eq.(3.109) is computed by Eq.(3.110). In Eq.(3.110), the diffusion time is 1. The maximum value of the control function is 2. The time-step length is 5×10^{-3} s. The transition time is 25 s, and the grid is redistributed every 25 s. The values at new node positions are interpolated by the local interpolation explained in Section 3.3.6. The field transformation from a one node distribution to another is easy and very straightforwardly related to the strong-form MFMs.

The PFVs and the Mg concentration fields during one hour of dissolution of Al_3Mg_2 particle into the aluminium phase, computed by the collocation with RBFs on r-adaptive node arrangement, are presented in Fig.(4.15). The temporal node arrangements are presented by black circles. The dissolution kinetics are the highest at the start because of the high gradient of component concentration in the aluminium phase. Later on, the particle curvature influences this phase transformation and the interphase interface becomes flatter. The transformation ends, when the component concentration is equal to the equilibrium concentration at a high process temperature and the interface is a straight line.

The results computed by the collocation with RBFs on r-adaptive node distribution are compared with the results computed by FDM on a fine equidistant 251×251 grid. The interface position comparisons are presented in Fig.(4.16). The 0.5 contour of the PFV is used as the interface position and the agreement between the positions is very good.

The maximum value of the control function may be higher and the majority of nodes could be in the phase-change region, whereas a relatively small number of nodes are outside of the phase-change region. This node distribution influences that Neumann boundary conditions on the boundaries are not accurately solved, because a small number of nodes is in the vicinity of the boundary. Consequently, the phase transformation is not accurately solved, as well. The higher value of the control function can be used for the higher total number of nodes. The initial Mg concentration field on the node arrangement, when the maximum value of the control function is five, is presented in Fig.(4.17).

The transition time ensures that the interface position does not move outside the fine-grid region. Very nice agreement is obtained by using different transition times 10 s, 25 s and 50 s. Therefore, we can conclude that the results are independent of the transition time. The transition time is in relation to the parameters for controlling node arrangements. The transition zone decrease is achieved by increasing the maximum value of the control function or/and decreasing the diffusion time.

Summary

The collocation by RBFs and the development of an r-adaptive strong-form MFMs represent one of the principal goals of this thesis. The procedure is implemented for solution of phase-change problems. The automatic elliptic generator for computation of node positions is used. The control function in the elliptic generator controls the node distribution and remains in relation to the interface position. The node arrangement is controlled by two parameters: the maximum value of the control function and the transition zone thickness in one-dimensional geometry, or the diffusion time in the two-dimensional geometry. The node distribution is easily controlled by the chosen method. The collocation by RBFs based on a local standard interpolation scheme on an equidistant grid is used for the solution of the elliptic generator. The field transformation from one node distribution to another is very straightforwardly related to the strong-form MFMs.

The numerical procedure is implemented for phase-change simulation by the phase-field model. The r-adaptive numerical procedure derived for solution of phase-change problems gives very accurate results in the one-dimensional geometry. The computations are performed by three nodes in the supporting domain. Accurate results are obtained with a significantly smaller number of the total nodes even if the interface thickness is small. There are two reasons that explain this fact. The r-adaptive node arrangement is easily controlled, and the approximations of derivatives and functions by the local standard collocation using RBFs with three supporting nodes are very accurate. The derivative boundary conditions do not influence the stability of the results in the one-dimensional geometry.

The stability of the collocation by RBFs based on the local standard interpolation method is not sufficient at boundary nodes where the derivative boundary conditions exist. The stability is significantly improved by using only one boundary node for the boundary local support. The collocation with RBFs by using the double consideration of boundary nodes based on Hermite-type interpolation enables computation on the r-adaptive node arrangement. It improves the stability and accuracy of the results at the derivative boundary nodes. A useful and quick approach for determination of the local support for domain reference nodes in arbitrary node arrangements is developed. Local supports with only five nodes are considered. The addition polynomial term is necessary for obtaining the interpolation without noise for flat fields, such as the PFV for example. The result computed by the collocation using RBFs is in agreement with the results computed by the fine-grid FDM.

The present development of the mesh free technique is more time consuming, so that the main results presented in the forthcoming simulations have been obtained with the FDM.

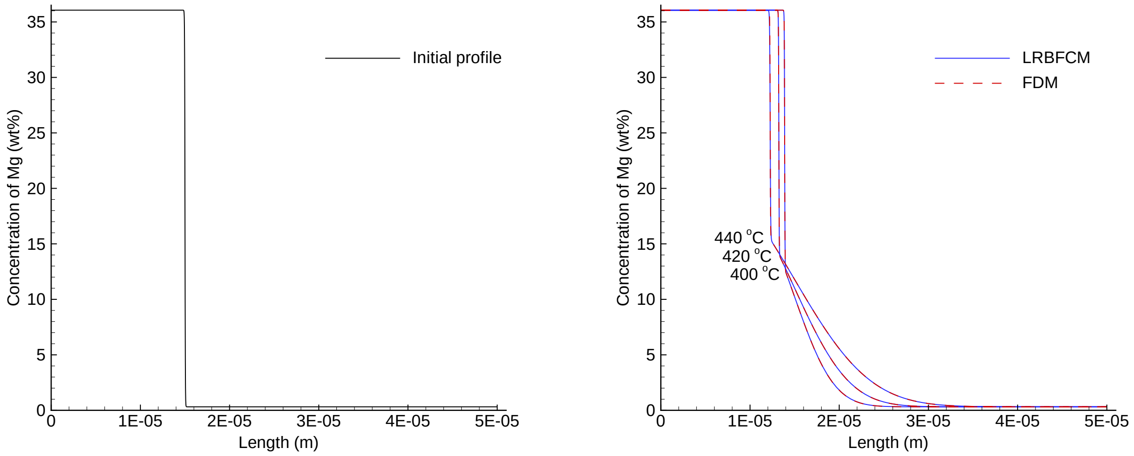

(a) The initial Mg concentration profile.

(b) $t = 720\,\mathrm{s}$.

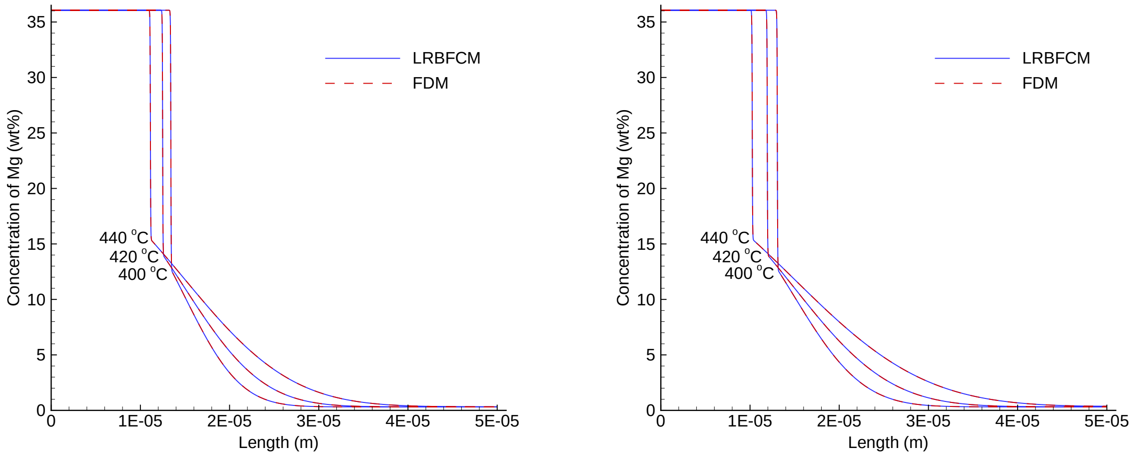

(c) $t = 1440\,\mathrm{s}$.

(d) $t = 2160\,\mathrm{s}$.

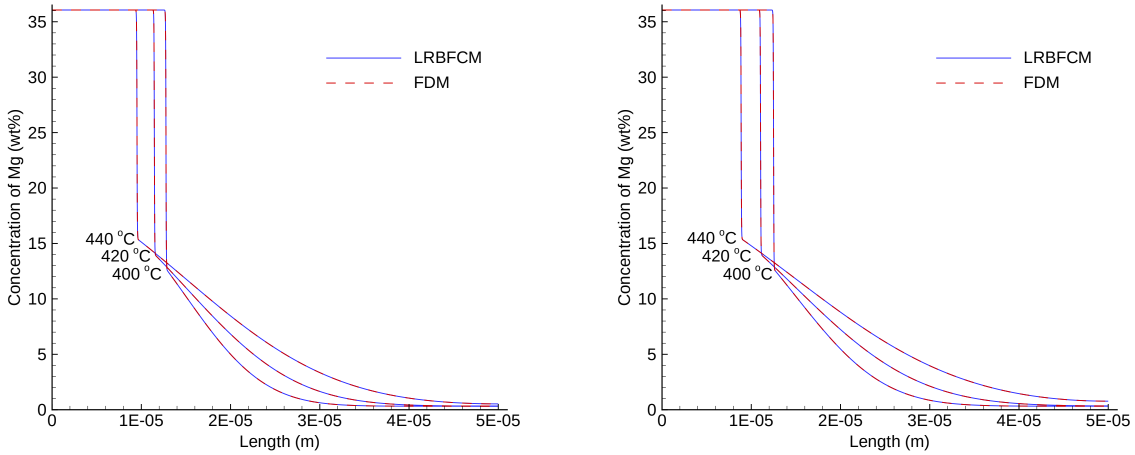

(e) $t = 2880\,\mathrm{s}$.

(f) $t = 3600\,\mathrm{s}$.

Figure 4.12: The Mg concentration profiles during one hour of dissolution at three homogenisation temperatures computed by the LRBFCM and the FDM.

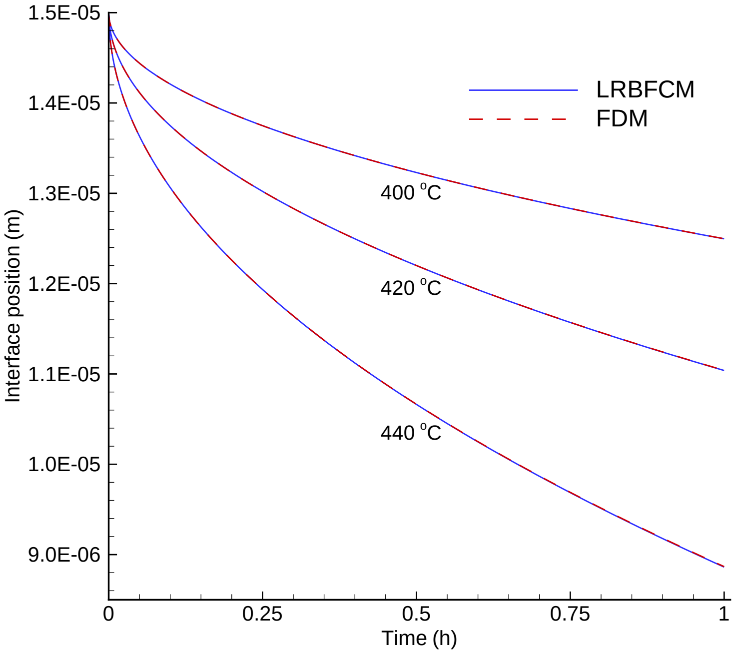

Figure 4.13: Interface positions in time at three homogenisation temperatures computed by the LRBFCM and the FDM.

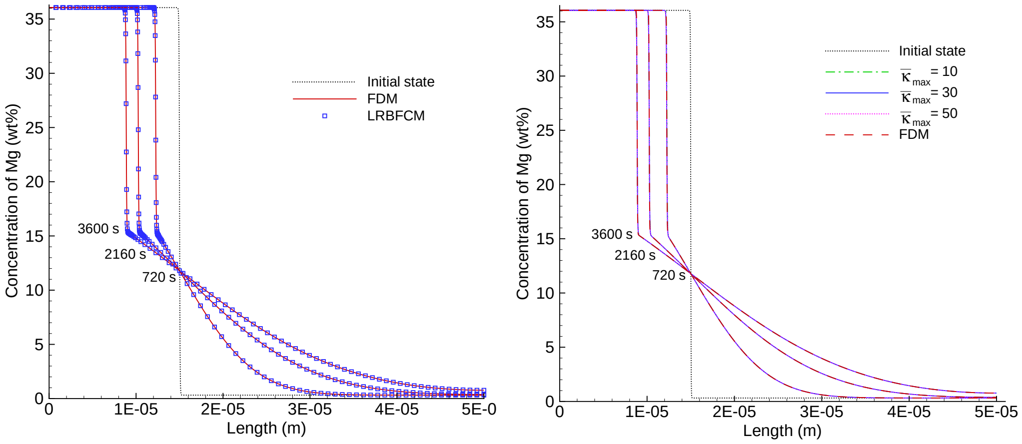

(a) The numerical results computed by the total 101 nodes in the LRBFCM.

(b) The numerical results computed by for three maximum values of the control function in r-adaptive LRBFCM.

Figure 4.14: The Mg concentration profiles during one hour of dissolution at homogenisation temperatures 440 °C computed by the LRBFCM and the fine-grid FDM.

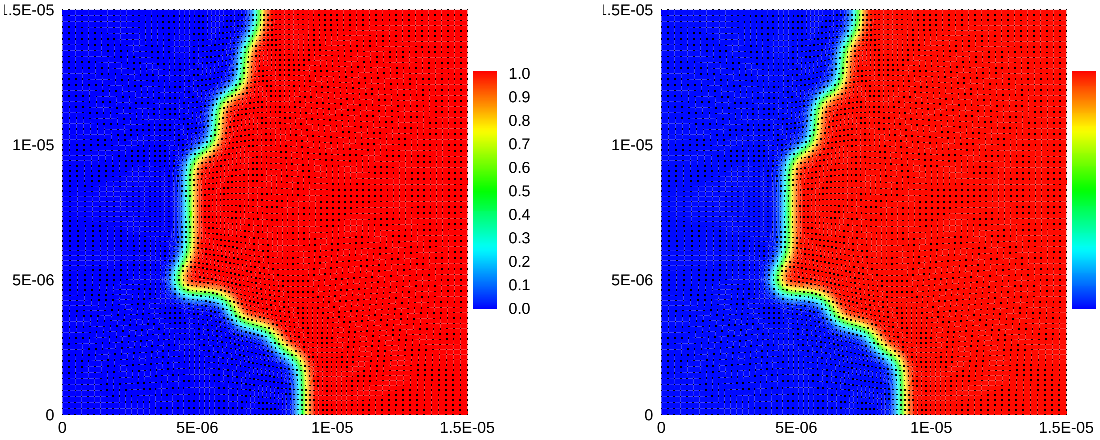

(a) Initial the PFV.

(b) Initial concentration field of Mg.

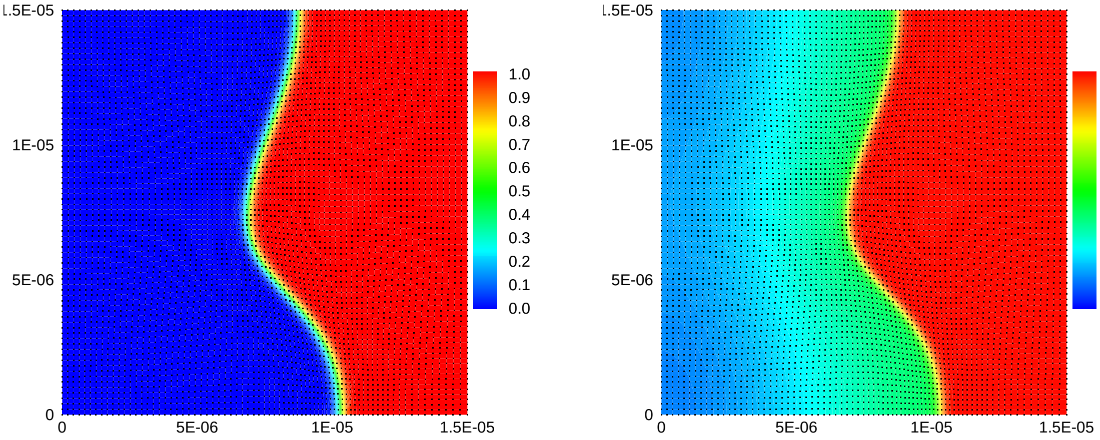

(c) $t = 360\,\mathrm{s}$.

(d) $t = 360\,\mathrm{s}$.

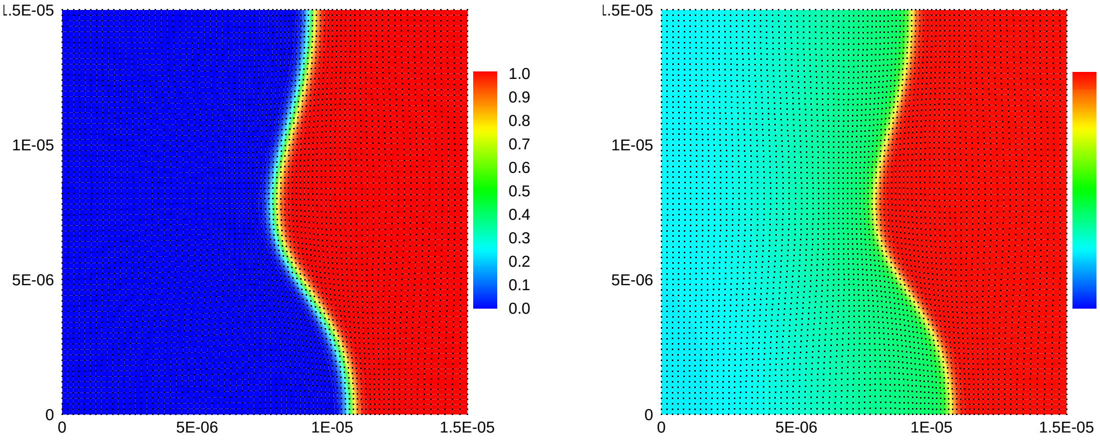

(e) $t = 720\,\mathrm{s}$.

(f) $t = 720\,\mathrm{s}$.

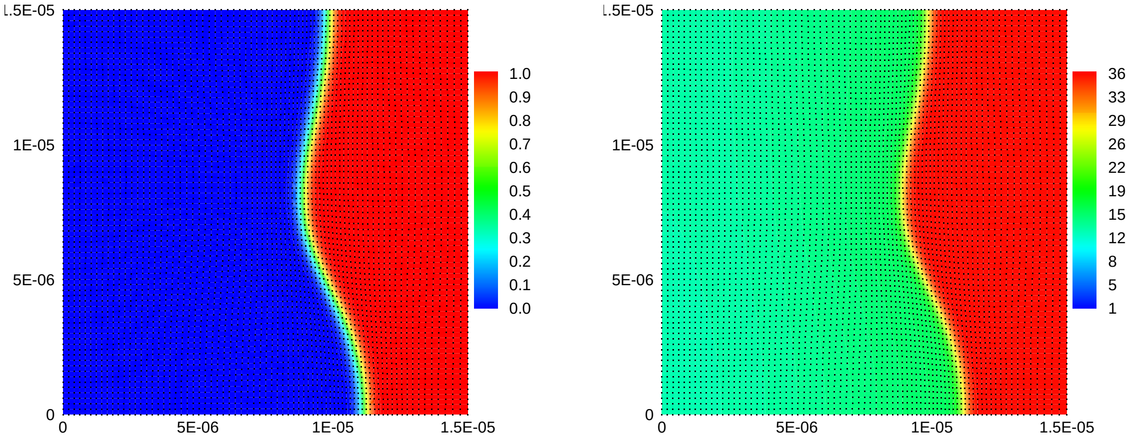

(g) $t = 1440\,\mathrm{s}$. (h) $t = 1440\,\mathrm{s}$.

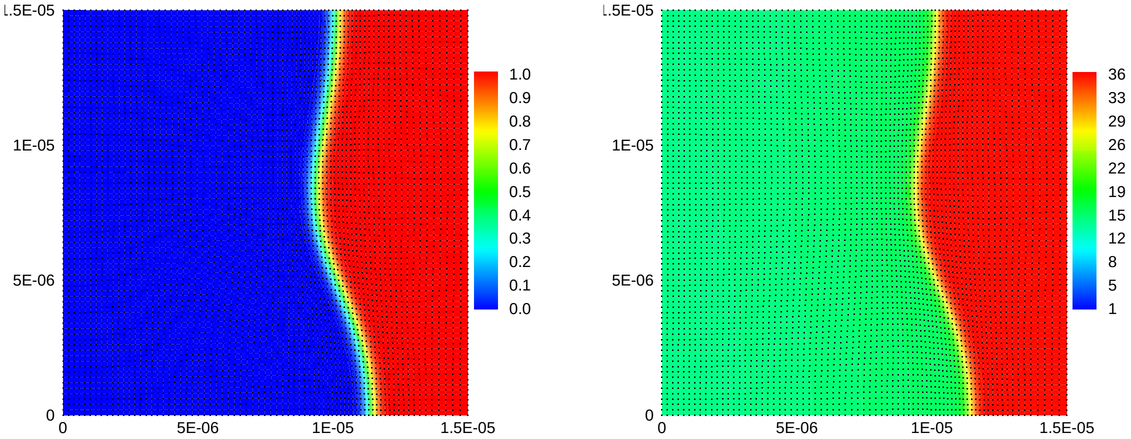

(i) $t = 2160\,\mathrm{s}$. (j) $t = 2160\,\mathrm{s}$.

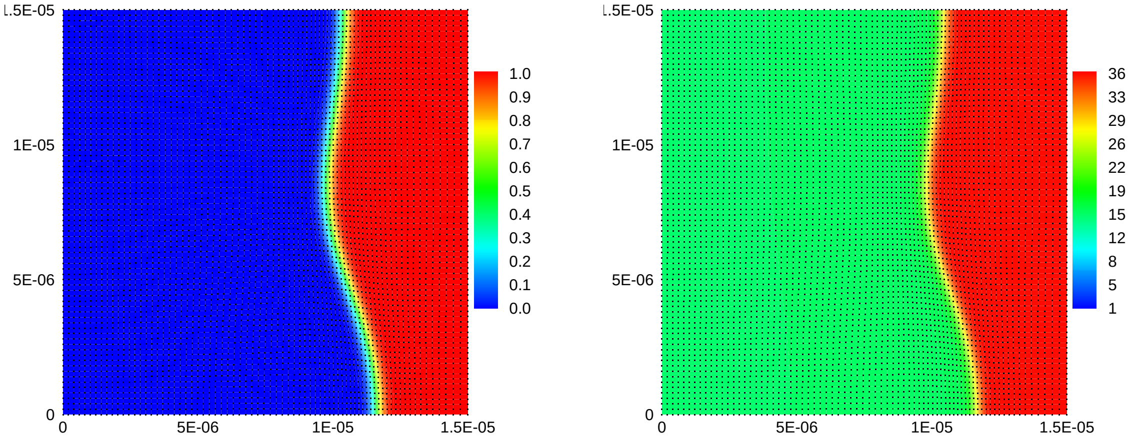

(k) $t = 3600\,\mathrm{s}$. (l) $t = 3600\,\mathrm{s}$.

Figure 4.15: The PFVs and the Mg concentration fields during one hour of isothermal dissolution of Al_3Mg_2 in the aluminium phase at homogenisation temperature 440 °C.

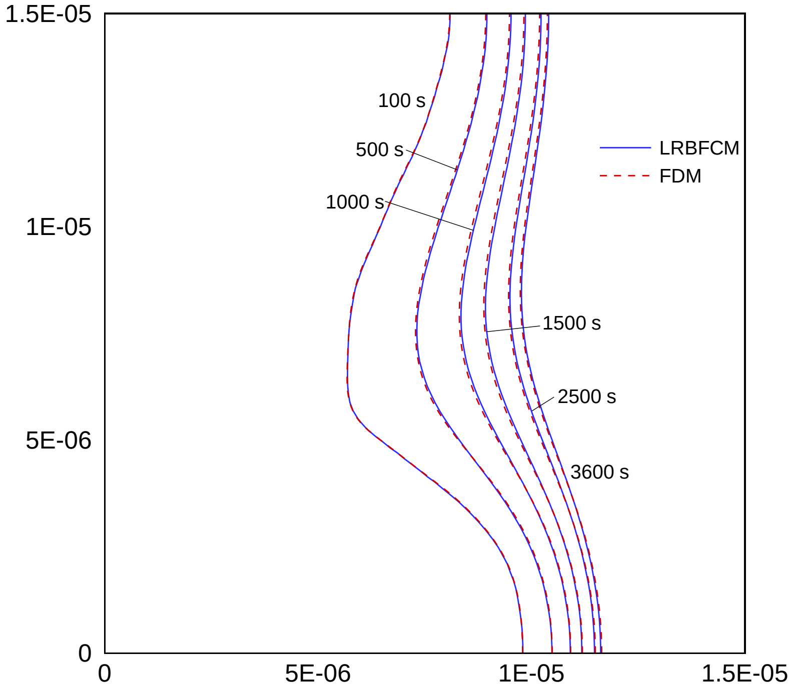

Figure 4.16: Interface positions during one hour of dissolution computed by the LRBFCM (75 × 75) and the fine-grid FDM (251 × 251) at homogenisation temperature 440 °C.

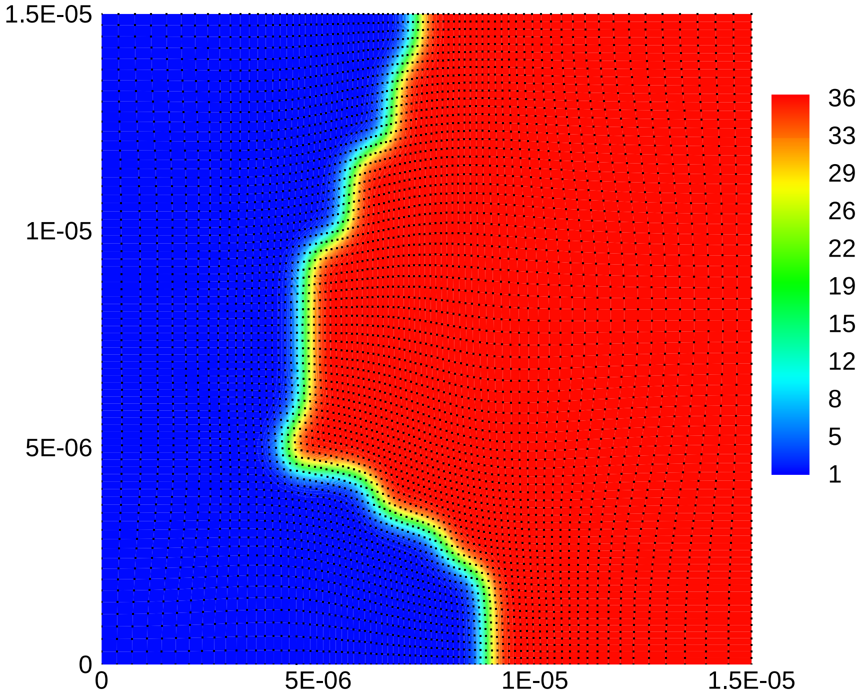

Figure 4.17: The initial Mg concentration field approximated on the node arrangement obtained by the maximum value of the control function five.

4.2 Interface-Controlled Dissolution

In the DC mode, the main assumption is that the interface reaction proceeds sufficiently fast with respect to long-distance diffusion in the phases. Therefore, interface concentrations are determined through the thermodynamic equilibrium state (Fig.(1.3)). If the interface reaction proceeds slower than long-distance diffusion in the phases, the phase transformations are mixed-controlled or Interface-Controlled (IC). The theoretical background of the influence of the interface reaction influences on the interface condition has already been explained in Section 1.3.4.

IC dissolution can be simulated by the TDA and PFM. In the PFM, the phase-field mobility is proportional with the interface-kinetic coefficient in the sharp-interface limit (Eq.(2.109)). The interface-kinetic coefficient quantifies the interface reaction mobility. The PFM copes with all necessarily physics for the simulation of phase transformations in different modes.

The TDA is explained for the DC phase transformations in Section 2.2. The interface conditions for a two-phase binary A-B system is determined throughout the thermodynamic equilibrium state:

$$\mu_{\alpha}^{\mathrm{A}}\left(T, c_{\alpha\mathrm{eq}}\right) = \mu_{\beta}^{\mathrm{A}}\left(T, c_{\beta\mathrm{eq}}\right), \quad \mu_{\alpha}^{\mathrm{B}}\left(T, c_{\alpha\mathrm{eq}}\right) = \mu_{\beta}^{\mathrm{B}}\left(T, c_{\beta\mathrm{eq}}\right), \tag{4.6}$$

where $c_{\varphi\,\mathrm{eq}}$ represents the equilibrium interface concentration in the phase φ.

A variety of atomic attachment mechanisms have been proposed [Aaron and Kotler, 1971] to account for the observed interface reaction into the TDA. Various relationships between the interface velocity magnitude v and the departure from interface equilibrium conditions Δc_{α} are proposed, where the assumption that the second phase β is intermetallic compound ($c_{\beta\mathrm{eq}} = c_{\beta}^{\mathrm{st}}$) is used. Since the interface reaction reduces the flux of atoms which crosses the interphase interface, the actual interface concentration $c_{\alpha\mathrm{I}}$ during dissolution is less than the equilibrium interface concentration $c_{\alpha\mathrm{eq}}$. It is convenient to define a positive departure Δc_{α} as

$$\Delta c_{\alpha} = c_{\alpha\mathrm{eq}} - c_{\alpha\mathrm{I}}. \tag{4.7}$$

The appropriate relationships between interface velocity magnitude v and the departure Δc_{α} for dissolution has been developed in [Aaron and Kotler, 1971]. One of them is the uniform atomic detachment

$$v = -\bar{K}\Delta c_{\alpha}, \tag{4.8}$$

where the parameter $\bar{K}$ is related to the interface mobility. From the Gibbs-Thomson relation, one can obtain the relationship between the parameter $\bar{K}$ and the interface-kinetic coefficient μ_{k}:

$$\bar{K} = \mu_{\mathrm{k}}\left(X_{\beta\mathrm{eq}} - X_{\alpha\mathrm{eq}}\right)\frac{\mu_{\alpha\mathrm{I}} - \mu_{\alpha\mathrm{eq}}}{X_{\alpha\mathrm{I}} - X_{\alpha\mathrm{eq}}}. \tag{4.9}$$

Now, the interface concentration, including interface reaction influence, is $c_{\alpha\mathrm{I}} = c_{\alpha\mathrm{eq}} - \Delta c_{\alpha}$. For the uniform detachment mechanism, one can get

$$c_{\alpha\mathrm{I}} = c_{\alpha\mathrm{eq}} + \frac{v}{\bar{K}}. \tag{4.10}$$

The interface concentration is a function of the interface velocity for simulation of IC phase transformations by the TDA.

The interface-kinetic coefficient influences of the dissolution of Al_3Mg_2 in the aluminium phase in the binary Al-Mg system computed by the PFM are presented in Fig.(4.18). If the interface-kinetic coefficient is high, the interface reaction is fast enough that the dissolution is DC. If the interface-kinetic coefficient is higher than $5.0 \times 10^{-14}\,\mathrm{m^4/Js}$, the dissolution kinetics does not dependent on the interface mobility. The interface concentration converges to the equilibrium concentration ($c_{\alpha\mathrm{I}} \rightarrow c_{\alpha\mathrm{eq}}$), when $v/\bar{K} \rightarrow 0$ as is evident from Eq.(4.10). The Mg concentration profiles after one hour of isothermal dissolution with different interface-kinetic coefficients are presented in Fig.(4.18(a)). Homogenisation temperature and the interface energy are $440\,^{\circ}\mathrm{C}$ and $5.0 \times 10^{-1}\,\mathrm{J/m^2}$, respectively. The time-step length is $5 \times 10^{-4}\,\mathrm{s}$ in computations, except for the interface-kinetic coefficient $5 \times 10^{-13}\,\mathrm{m^4/Js}$ where the time-step length is $1 \times 10^{-4}\,\mathrm{s}$.

Decreasing the interface-kinetic coefficient, increasing the interface reaction influences of the dissolution (Fig.(4.18(b))). Therefore the dissolution kinetics is slower. In the example with the interface-kinetic coefficient $5.0 \times 10^{-20}\,\mathrm{m^4/Js}$, the dissolution is in the IC mode. The interface-kinetic coefficients between these two extremes ($5.0 \times 10^{-16}\,\mathrm{m^4/Js}, 5.0 \times 10^{-17}\,\mathrm{m^4/Js},\ 5.0 \times 10^{-18}\,\mathrm{m^4/Js}$) define the dissolution in the mixed-controlled mode. The interface-kinetic coefficient easily controls the transformation mode.

The interface position changes by square root law with time in the example of the DC dissolution, as in classical Stefan problem. In the IC and the mixed-controlled mode, the interface position changes linearly with time. Comparison of interface positions with time as a function of the interface-kinetic coefficient is presented in Fig.(4.18(b)).

A recent study of austenite decomposition to ferrite during the cooling of steel was performed by experiments and the PFM [Mecozzi *et al.*, 2005]. The interface-kinetic coefficient was used as a fitting parameter to optimise the agreement between the experimental and simulated ferrite-fraction curve. Is was found that this phase transformation is in a mixed-mode character, situated between two extremes of the DC and IC mode. At the initial stage, the transformation is predominantly IC, but gradually shifts toward DC mode with a degree that depends on the cooling rate. Consequently, the interface-kinetic coefficient in the PFM does not have to be a uniform parameter during the phase transformation simulation.

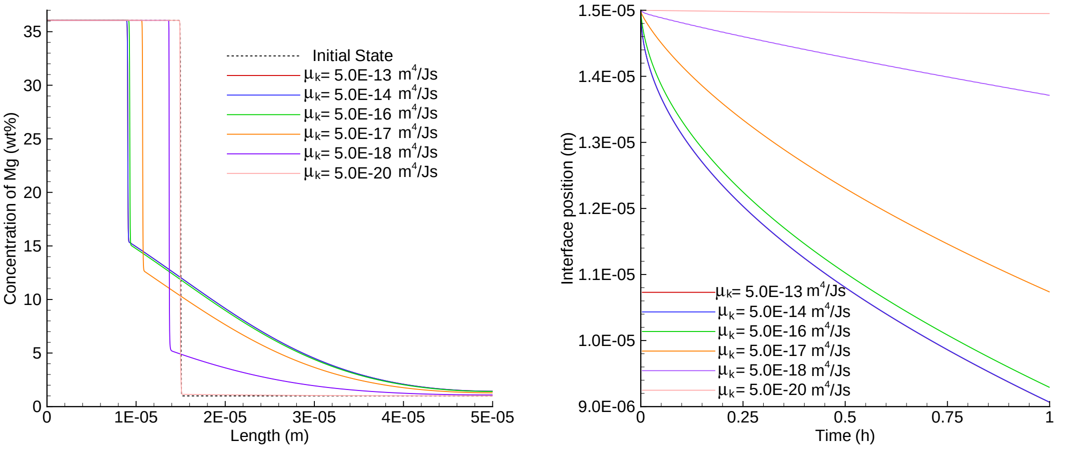

(a) The Mg concentration profiles after one hour of homogenisation.

(b) The interface positions during homogenisation.

Figure 4.18: The dissolution of Al_3Mg_2 in the aluminium phase as a function of the interface-kinetic coefficient at temperature 440 °C.

5 Si-particle Spheroidisation

Modelling of the spheroidisation of elongated Si-particles during high-temperature treatment is elaborated in this chapter. Application of the PFM for spheroidisation or rounding of undissolvable particles during annealing of aluminium alloys is pointed out. The driving force for spheroidisation is the minimization of the total free energy of the system or the minimization of the ratio between the interface areas and the particle volumes. The theoretical background of the solubility dependence on the particle curvature is described in Section 1.3.3. The influence of interface energy anisotropy on the particle shape simulated by the PFM is presented at the end of this chapter.

The ductility of Al-Si alloys depends on the dendrite grain size and the size and shape of the Si-particles. The ductility of the large grain size is low, since it is dominated by the large elongated Si-particles. The dendrite grain size as well as the size of the Si-particles are influenced by the solidification rate. By increasing the solidification rate, the grain size and the size of Si-particles decreases, consequently the ductility increases [Cáreras *et al.*, 1995]. Mg and Cu elements, alone or together, increase the strength and reduce the ductility of Al-Si alloys [Dons *et al.*, 2005].

The as-cast microstructure of Al-12 wt%Si alloy is presented in Fig.(5.1). The micrograph was obtained from the Micrograph Library of the University of Cambridge [Micrograph Library, University of Cambridge, 2007]. The eutectic comprises large elongated plates of silicon in the aluminium matrix. Such alloy has a poor ductility due to the brittleness of large elongated Si-particles. The typical Al-Si eutectic is closer to a lamellar structure than to a fibrous one. This is usually attributed to the strong anisotropy of the growth of silicon and to the relatively low interface energy between silicon and aluminium.

For the commercial Al-Si alloys, microstructural modifications have been made by adding strontium (Sr) to the melt as a modifier in order to obtain a low aspect ratio of silicon plates. Also, the size of the Si-particles is low, and is much less affected by the solidification rate than the unmodified alloy. The micrograph comparison between the unmodified and modified Al-Si alloys is presented in [Mondolfo, 1976].

The changes of eutectic silicon during high-temperature treatment can roughly be divided into three steps:

- Disintegration,
- Spheroidisation and
- Growth of Si-particles.

The beginning of the disintegration of Si-particles is provoked by small fluctuations of its faceted interfaces. The spheroidisation and later coarsening are driven by the solubility dependence of the particle curvature. Also, because the solubility of Si is low even at high temperature, Si-particles grow into the aluminium matrix in Al-Si alloys.

Following the increasing demands of the automotive industry, safety parts should have a minimum fracture elongation of 15 % and a minimum yield strength of 180 MPa, so some relatively new alternative casting technologies are under development. The huge hurdle for Al-Si cast alloys is the 15 % fracture elongation which cannot be reached by conventional sand or semicontinuous casting. Thixocasting as a semi-solid process yields encouraging ductility values [Ogris, 2002].

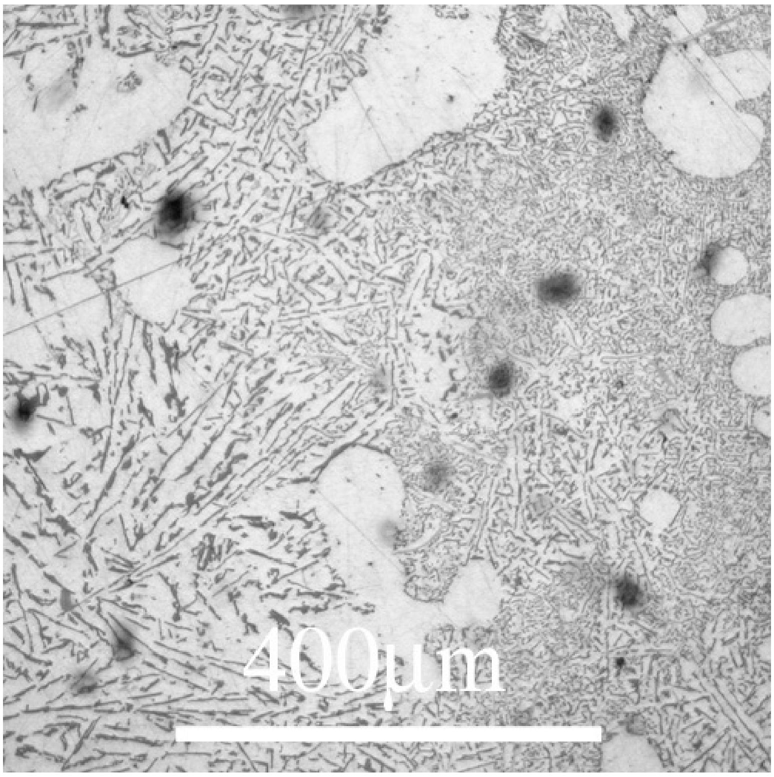

Figure 5.1: The as-cast micrograph of Al-12 wt%Si alloy obtained from [Micrograph Library, University of Cambridge, 2007].

5.1 Rounding Kinetics

The disintegration of Si-particles is provoked by small fluctuations of its faceted interfaces, so a fluctuation term must be included in the model in order to model this effect. This fluctuation is incorporated into the PFM by the additional source term in the phase-field equation [Hechta *et al.*, 2004]. This model is the most frequently used for the simulation of the grain nucleation during solidification. The nucleation and growth during the non-isothermal heat treatment conditions simulated by the PFM is presented in [Simmons *et al.*, 2004].

Our model does not include any fluctuation term, and is used for the estimation of the rounding kinetics of the single elongated particle. The isotropic material and isotropic interface energy (interface energy is constant around the particle) are assumed for simulations. The single Si plate with a large aspect ratio embedded in the surrounding aluminium matrix is chosen for demonstration. The initial length, width and aspect ratio are $5\,\mu$m, $2 \times 10^{-1}\,\mu$m and 25, respectively. The shape of elongated Si consists of two faceted, horizontal interfaces and two particle tops. The initial size and shape of the particle is presented in Fig.(5.2). The initial concentration of Si in the aluminium matrix is equal to the equilibrium concentration of Si at temperature 560 °C. This concentration is computed by the JMatPro software for aluminium alloys, and takes on the value 1.36 wt%Si. The interface thickness and the interface-kinetic coefficients for each computation are $1 \times 10^{-1}\,\mu$m and $5.0 \times 10^{-17}\,\mathrm{m^4/Js}$, respectively. Homogenisation temperature and the interface energy in the first example are 560 °C and $8.0 \times 10^{-1}\,\mathrm{J/m^2}$, respectively.

The computations are performed on one half of the particle. The computational domain is $3\,\mu$m wide and $2\,\mu$m high. The phase-field and concentration equation are discretized by the FDM on the 150×100 equidistant mesh with the spatial step $2 \times 10^{-2}\,\mu$m. Neumann-type boundary conditions are defined at the symmetric and the exterior boundaries. The time-step length is 8×10^{-5} s.

The size and shape of the Si-particles and the Si concentration field in the aluminium matrix during rounding at high-temperature treatment are presented on the left and right sides of Fig.(5.3), respectively. The particle shape is determined by the isovalue 0.50 of the PFV. The results are presented at every hour of the heat treatment. The rounding kinetics of the Si-particle are evident. The aspect ratio rapidly decreases over the course of homogenisation. The higher solubility of Si at the top of the particle is effected by its curvature. This is evident in the concentration field in Fig.(5.3). This higher concentration from the particle top diffuses into the aluminium matrix. The concentration above the solubility at the planar interface results in the growth of faceted interfaces into the aluminium matrix.

In the computations, the interface thickness is high and equal to the Si-particle curvature at the start of computations. Because of that, the computation on the 300×200 equidistant mesh with double thinner interface thickness $5 \times 10^{-2}\,\mu$m is performed. A comparison is made between the results computed on the previously

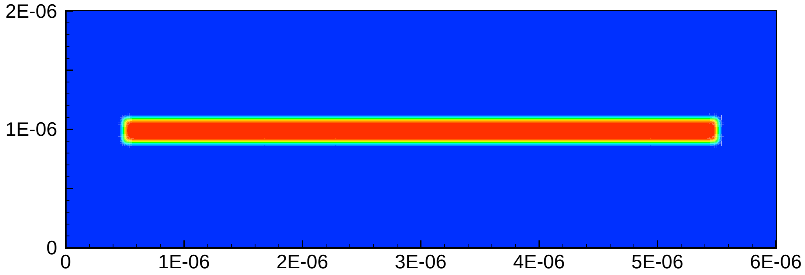

Figure 5.2: The initial shape of elongated Si-particle.

defined mesh with the interface thickness $1 \times 10^{-1}\,\mu$m and the results computed on double denser mesh with the interface thickness $5 \times 10^{-2}\,\mu$m. The results are in well agreement, which enables us to conclude that the computed rounding kinetics do not depend on the interface thickness as the selected model parameter.

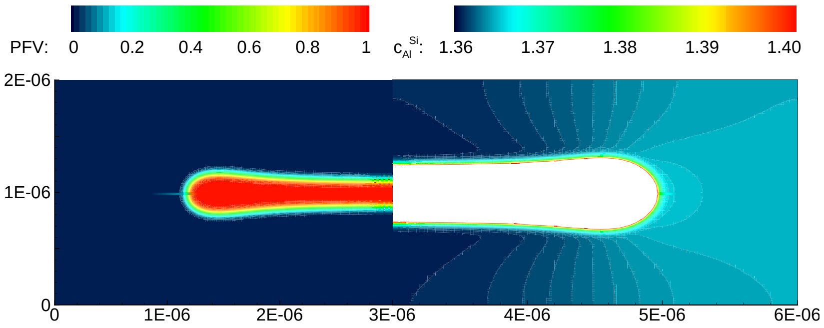

(a) The PFV and Si concentration field after one hour.

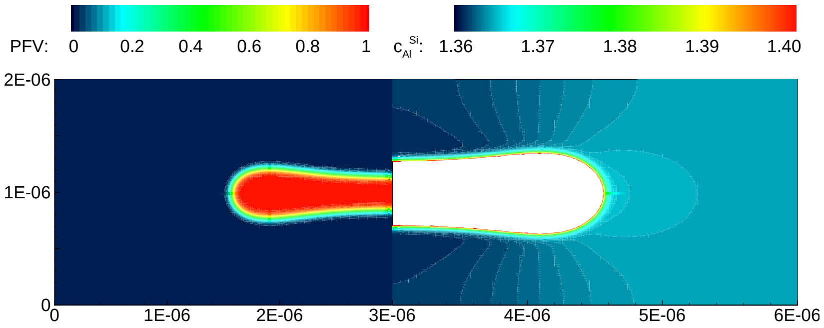

(b) The PFV and Si concentration field after two hours.

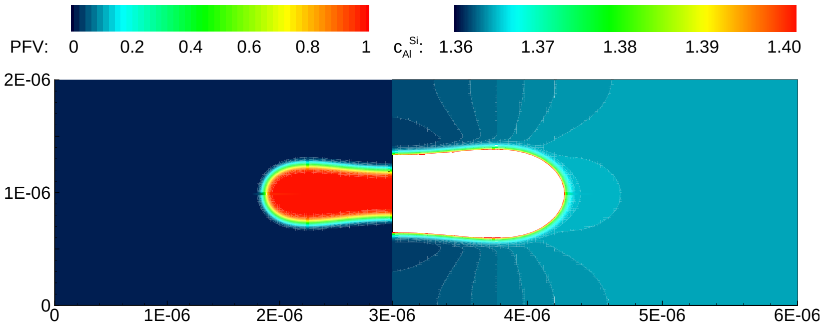

(c) The PFV and Si concentration field after three hours.

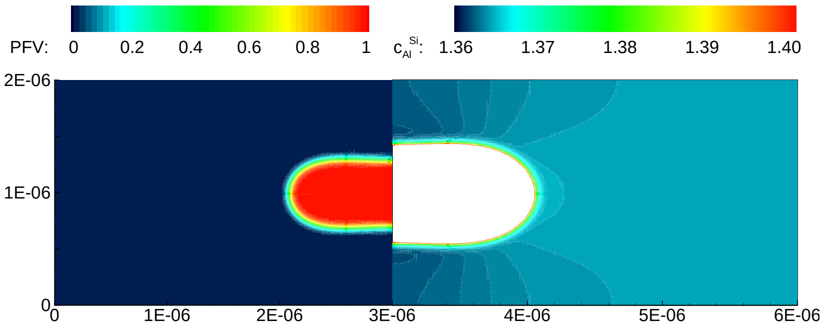

(d) The PFV and Si concentration field after four hours.

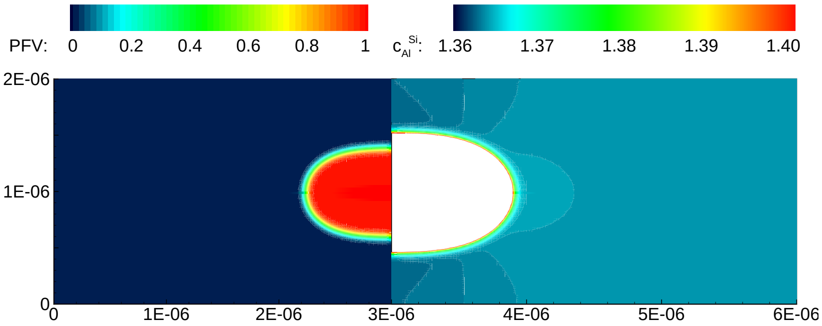

(e) The PFV and Si concentration field after five hours.

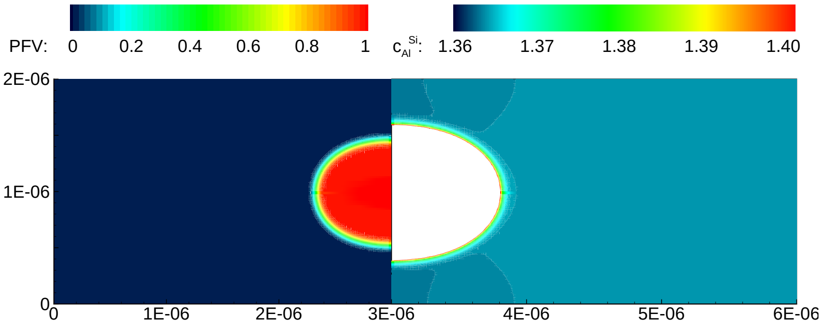

(f) The PFV and Si concentration field after six hours.

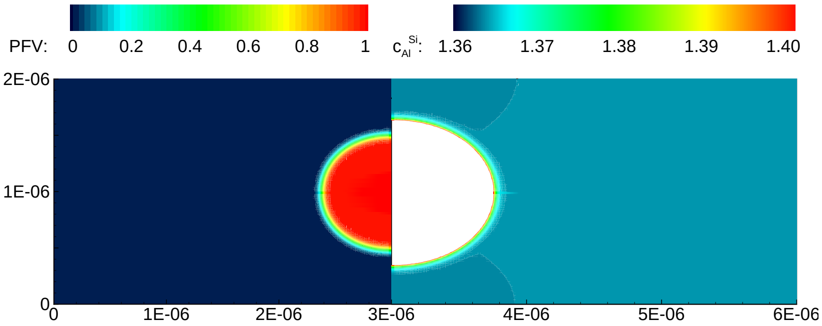

(g) The PFV and Si concentration field after seven hours.

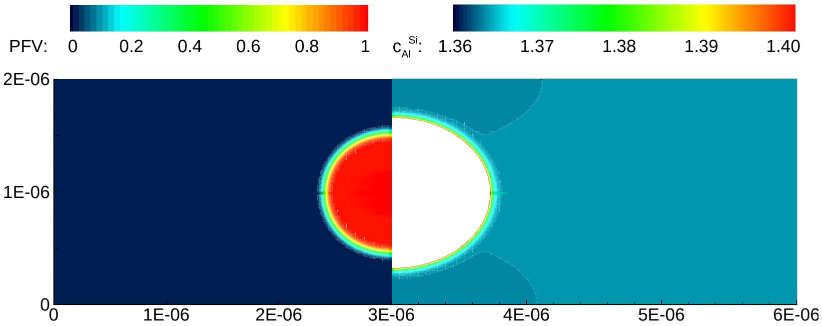

(h) The PFV and Si concentration field after eight hours.

Figure 5.3: Rounding of Si particles during homogenisation at temperature 560 °C with interface energy $8.0 \times 10^{-1}\,\mathrm{J/m^2}$.

5.1.1 Influence of the Parameters of Rounding Kinetics

The influence of the interface energy as a physical interface property and the influence of homogenisation temperature as a process parameter on the rounding kinetics are demonstrated here. The interface energy influence on the rounding kinetics is analysed first.

Interface Energy Influence

The increase in the molar free energy of the particle caused by its local curvature κ is

$$\Delta g_{\kappa} = 2\sigma V_{\mathrm{m}} \kappa \, . \tag{5.1}$$

The interface energy in the solid phase is not a well researched physical property. The interface energy depends on the type of the particle-aluminium interface: for coherent interfaces, the energy ranges up to 2×10^{-1} J/m^2, for semicoherent interfaces the energy is in the range 2-5 $\times 10^{-1}$ J/m^2 and for incoherent interfaces it is in the range 5-10$\times 10^{-1}$ J/m^2 [Porter and Easterling, 1990]. More information related to the interface energy in the solid state can be found in [Howe, 1997].

The interface energy influences the rounding kinetics of the Si-particle at homogenisation temperature 560 °C, as presented in Fig.(5.4). The three interface energies used in the computation are 6×10^{-1} J/m^2, 8×10^{-1} J/m^2 and 1.0 J/m^2. The higher interface energy has the influence that the molar free energy of the particle is higher due to the curvature (Eq.(5.1)), and consequently the solubility of Si in the aluminium matrix increases (Fig.(1.4)). The higher concentration gradient results in an increased driving force for diffusion in the aluminium matrix, and in a higher influence of concentration on the growth of the faceted particle-matrix interface. The aspect ratio of the particle for three interface energies during high-temperature treatment is presented in Fig.(5.6(a)). The particles are roughly spheroidisated in the cases with interface energies 8×10^{-1} J/m^2 and 1.0 J/m^2 after eight hours at high-temperature treatment at 560 °C.

Temperature Influence

The influence of temperature on the rounding kinetics of the defined Si-particle with the fixed interface energy of 1.0 J/m^2 is presented in Fig.(5.5). The three homogenisation temperatures used in the computations are: 520 °C, 540 °C and 560 °C. Homogenisation temperature influences: (i) the molar free energies of the phases present, (ii) the driving force for the phase transformation and (iii) the component diffusion coefficient into the aluminium matrix. For temperatures lower than 560 °C, the driving force is negative and the Si particle along the faceted interface grows into the aluminium matrix. This results in the spheroidisation of the Si-particle. The driving force influenced by the curvature for each temperature is roughly constant because the initial particle geometry as well as the interface energy is fixed. This driving force changes by molar volume only. The aspect ratio of the particle for three temperatures is presented in Fig.(5.6(b)).

The most important parameter for the rounding kinetics during high-temperature treatment is temperature, which is responsible for the component diffusion coefficient into the aluminium matrix. The particle is not completely rounded after eight hours of heat treatment at temperature 520 °C. The aspect ratio of the particle after heat treatment at this temperature is approximately 4.

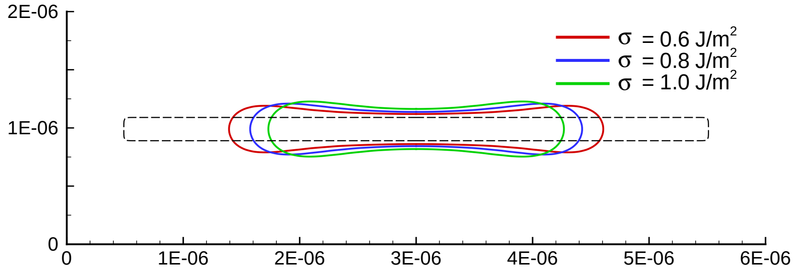

(a) The size and shape of the Si particle after two hours.

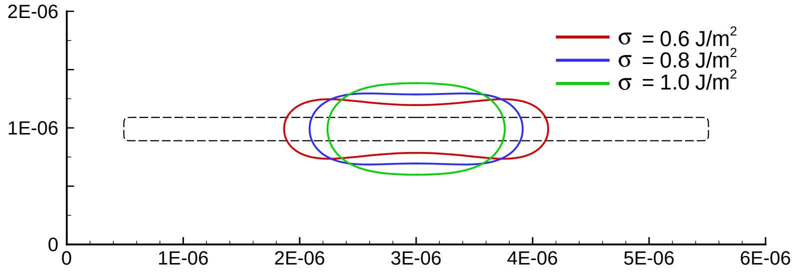

(b) The size and shape of the Si particle after four hours.

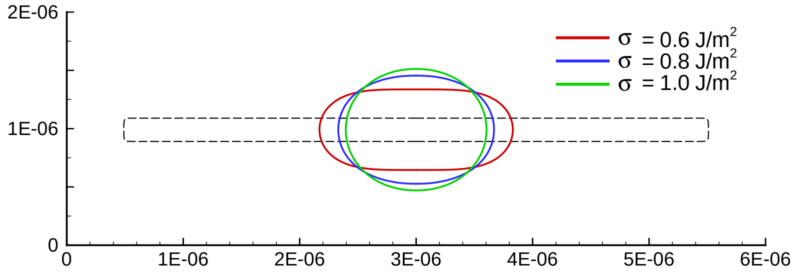

(c) The size and shape of the Si particle after six hours.

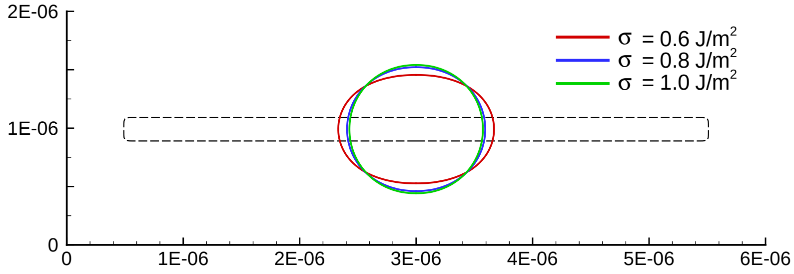

(d) The size and shape of the Si particle after eight hours.

Figure 5.4: The influence of the interface energy on the rounding kinetics of the Si-particle at a homogenisation temperature of 560 °C at different interface energies.

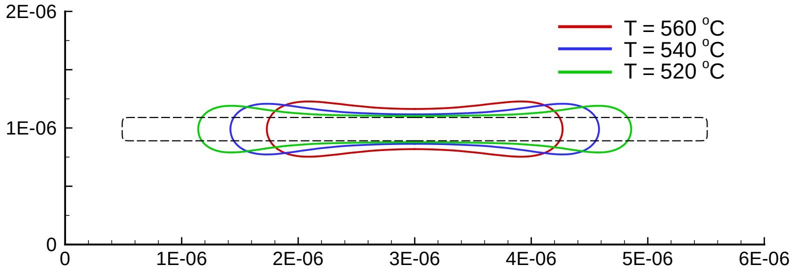

(a) The size and shape of the Si particle after two hours.

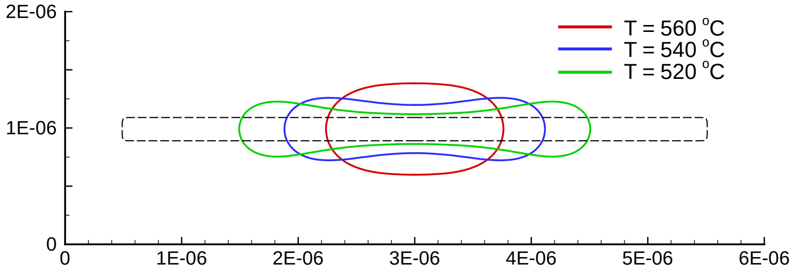

(b) The size and shape of the Si particle after four hours.

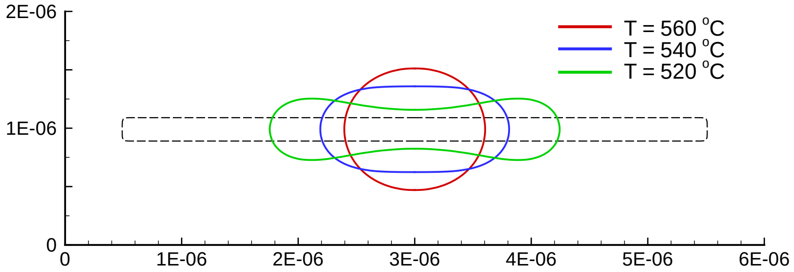

(c) The size and shape of the Si particle after six hours.

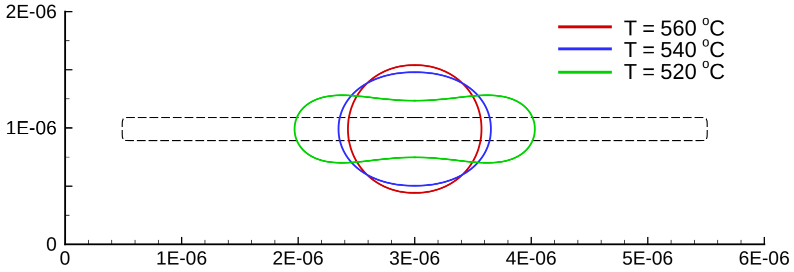

(d) The size and shape of the Si particle after eight hours.

Figure 5.5: The influence of the temperature on the rounding kinetics of the Si-particle with a fixed interface energy of $1.0\,\mathrm{J/m^2}$ at different temperatures.

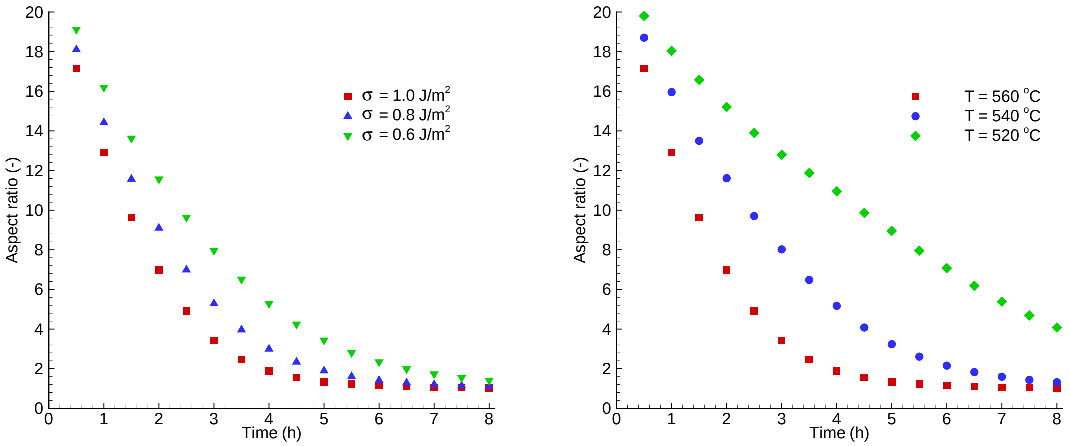

(a) The influence of interface energy on the aspect ratio of the Si particle at a homogenisation temperature of 560 °C.

(b) The influence of temperature on the aspect ratio of the Si particle with a fixed interface energy of 1.0 J/m^2.

Figure 5.6: The aspect ratio of the Si particle during high-temperature treatment.

5.2 Anisotropy

Secondary particles nucleate during all three homogenisation steps. The phase transformations of the secondary particles are nucleation, precipitation or growth, dissolution and coarsening. The majority of secondary particles nucleate on the grain boundaries because of the heterogenous nucleation. The purpose of the secondary particles is to control grain size during further mechanical treatment such as extrusion or rolling. This section introduces the basic understanding and modelling of the anisotropic growth of dispersoids.

The isotropic material and isotropic interfaces give rise to spherical precipitates, since the sphere has a minimal interface area with respect to its volume. The anisotropy in properties leads to a deviation from spherical morphology, and the shape of the precipitates depends on the degree of anisotropy.

The anisotropy in materials originates from different properties, the most influential of which are [Hu, 2004]:

- the interface energy,
- the interface-kinetic coefficient,
- the elastic modulus of the phases,
- the stress-free strain.

The anisotropy in the elastic modulus is observed even for cubic systems, and is related to the bond strength along different directions. The elastic energy anisotropy is determined not only by the elastic modulus contribution but also through the contribution of stress-free strain contribution. The anisotropy can also be introduced by differences in the growth behavior of the interfaces. Growth processes are related to the presence or absence of good atomic fit across the interface. If the interface is incoherent, then atom transfer across the interface by thermally activated jumps is easier. The presence of good atomic fit across one of the precipitate interfaces poses a significant growth barrier for the coherent interface. This growth barrier favors growth perpendicular to these interfaces [Howe, 1997].

5.2.1 Influence of the Interface Energy Anisotropy on the Particle Shape

The interface energy anisotropy is not prevalent in iso-structural systems, especially for the high-temperature treatment. This effect is more pronounced during age hardening treatment at low temperatures. Anisotropies arise between phases with different structures, leading to coherent and/or semi-coherent interfaces. The equilibrium morphology based on the interface energy anisotropy can be obtained by the Wulff's shape construction. The Wulff's shape construction constructs the particle shape that minimizes the amount of total free energy affected by the interface energy [Porter and Easterling, 1990]. Coherent interfaces lead to faceted interfaces, while incoherent interfaces are not faceted.

Here, the concept of the interface energy anisotropy in the PFM is introduced. The total free energy for binary systems, expressed in Eq.(2.55), is

$$\mathcal{F} = \int\limits_V \left[f^{\mathrm{ch}}\left(\phi, c, T\right) + \frac{\varepsilon_\phi^2}{2} \left|\nabla\phi\right|^2 \right] dV. \tag{5.2}$$

The interface energy anisotropy is usually taken into account throughout the energy-gradient coefficient. The energy-gradient coefficient depends on the orientations of the interface

$$\varepsilon_\phi = \varepsilon_\phi\left(\theta\right), \tag{5.3}$$

where θ is the angle between the interface normal and a reference axis, for example the x axis. The angle θ is introduced as

$$\theta = \mathrm{atan}\left(\frac{\partial\phi/\partial y}{\partial\phi/\partial x}\right). \tag{5.4}$$

Because of that, the phase-field equation in Eq.(2.54) is reinterpreted as

$$\frac{\partial\phi}{\partial t} = -M_\phi \left[\frac{\partial f^{\mathrm{ch}}}{\partial\phi} - \nabla^2\left(\varepsilon_\phi^2\phi\right) + \frac{\partial}{\partial x}\left(\varepsilon_\phi \frac{d\varepsilon_\phi}{d\theta}\frac{\partial\phi}{\partial y}\right) - \frac{\partial}{\partial y}\left(\varepsilon_\phi \frac{d\varepsilon_\phi}{d\theta}\frac{\partial\phi}{\partial x}\right) \right]. \tag{5.5}$$

The phase-field modelling of the highly anisotropic interface energy growth of Widanstätten ferrite in binary Fe-C is introduced in [Loginova, 2003].

In crystalline materials, the interface energy always depends on the orientation. The dependence of orientation on the interface energy is represented by a radial vector whose magnitude is proportional to the interface energy. This is the so-called interface energy gamma-plot.

The two interface energy gamma plots are used as input parameters for the PFM. The first gamma plot determines the intermediate θ' phase in Al-Cu alloys [Hu, 2004], and it is presented in Fig.(5.7(a))). The second gamma plot determines a theoretical six surface precipitate, and is presented in Fig.(5.7(b)).

A circular particle with radius $0.1\,\mu$m is used as the initial shape. The thermodynamic driving force for the phase transformation is set up for a constant negative value (10^9 J/mol). The interface thickness and the interface-kinetic coefficient are $7.0 \times 10^{-2}\mu$m and $1.0 \times 10^{-17}\,\mathrm{m}^4/\mathrm{Js}$, respectively. The interface energies are used from the gamma plots in Fig.(5.7). The computational domain is $2.56 \times 10^{-1}\mu$m square. The phase-field equation is discretized on the equidistant 513×513 mesh. The time-step length is 1×10^{-2} s, the particle shapes are presented after 5 s of the simulations.

The secondary particle grows with the equilibrium shape, influenced by the interface energy anisotropy. The equilibrium shapes of the θ' phase and the six surface precipitate are presented in Fig.(5.8(a)) and Fig.(5.8(b)), respectively. The shapes obtained by the PFM are in good agreement with Wulff's construction shapes.

5.3 Summary

The rounding kinetics of the elongated Si particles are estimated by the PFM. The spheroidisation can be roughly divided into three separate physical phenomena:

- The solubility of Si at the top of the particle is highly affected by the particle curvature;
- The Si diffuses according to a concentration gradient into the aluminium matrix;
- The concentration above solubility at the planar interface has the influence that the faceted interface starts to grow into the aluminium matrix.

The influence of the interface energy as a physical property of the interface and the influence of homogenisation temperature as a process parameter on the rounding kinetics have been shown to both strongly influence the rounding kinetics.

The interface energy anisotropy on the equilibrium shape of the secondary particles is computed by the PFM. The computed equilibrium shapes are in good agreement with the equilibrium shapes obtained by the Wulff's shape construction.

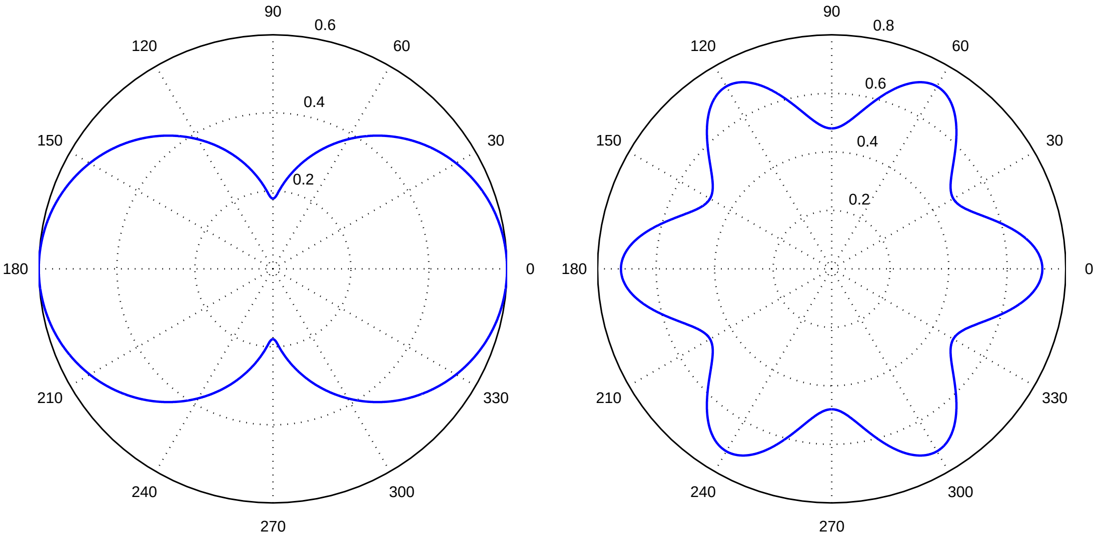

(a) The gamma plot for the intermediate θ' phase in Al-Cu alloys.

(b) The gamma plot for the theoretical six surface precipitate.

Figure 5.7: The interface energy gamma plots. The interface energy is expressed in [J/m^2].

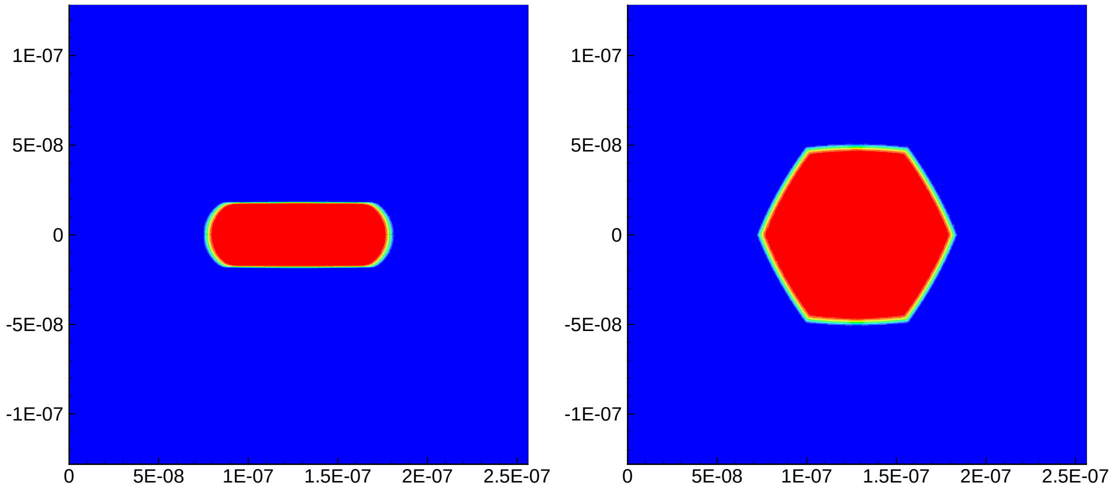

(a) The intermediate θ' phase in Al-Cu alloys.

(b) The six surface precipitate.

Figure 5.8: The equilibrium particle shapes as a function of the interface energy gamma plots sketched in Fig.(5.7).

6 Application to Commercial Aluminium Alloys

The application of the PFM for simulations of homogenisation of commercial aluminium alloys is focused in this chapter. The model is concentrated on the dissolution kinetics of the interdendritic eutectic phase in the aluminium matrix. The eutectic phase is treated as the homogeneous phase, where its molar free energy is computed as the heterogeneous mixture of eutectic phases present.

In aluminium alloys, the as-cast microstructure consists of the cored dendrites of the aluminium matrix, with a variety of constituents at the grain boundaries or interdendritic spaces. Specifically, in the interdendritic spaces of Al-Cu alloys, a brittle, more or less continuous network of the eutectic is formed. By increasing the copper content, there is a continuous increase in the hardness, but the strength and especially the ductility depend on the shape of the copper-rich θ phase. The difference is between spheroidised and evenly distributed particles and a continuous network at grain boundaries. Dissolved copper produces the highest increase in strength. The network of the copper-rich phase has a strong negative influence on ductility. The dissolution of this network represents a key issue in successful homogenisation of binary aluminium alloys [Mondolfo, 1976].

The as-cast micrograph of the commercial Al-5 wt%Cu alloy is presented in Fig.(6.1). It is obtained from the Micrograph Library of University of Cambridge [Micrograph Library, University of Cambridge, 2007].

The basic purpose of homogenisation of 2xxx aluminium alloys is to dissolve the interdendritic eutectic network, the mixture of the aluminium and the θ phase. The regular, lamellar eutectic is formed during an eutectic reaction of Al-Cu alloys. The microstructure [Micrograph Library, University of Cambridge, 2007] of Al-33 wt%Cu, eutectic alloy, is presented in Fig.(6.2). The phase transformations in high-temperature treatment of the observed eutectics are: disintegration, spheroidisation and coarsening of θ lamellae. The total-free energy affected by the interface energy tends to be minimized in the interdendritic eutectic during the homogenisation.

The intention is to derive a model for the dissolution of the eutectic phase, as a homogeneous phase, in the aluminium phase. This assumption ignores all phase transformations in the lamellar eutectic. This assumption is only necessary, because the phase transformations in the eutectic and on grain size occur on different scales, and by using the uniform grid it is not possible to catch all the mentioned phase transformations.

The concept of the eutectic phase allows a connection between the microsegregation solidification and the homogenisation model. The effects of homogenisation temperature, grain size and macroscopic concentration on dissolution kinetics are analysed. The initial concentration profile in the primary aluminium phase is obtained by the Scheil-Gulliver solidification model [Kurz and Fisher, 1998]. This concept of the eutectic phase was presented in [Kovačević and Šarler, 2006a].

The as-cast micrograph of the commercial Al-5 wt%Cu alloy is used as a realistic initial condition for the homogenisation model with two-dimensional geometry. Breaking of the interdendritic eutectic network is estimated by the model.

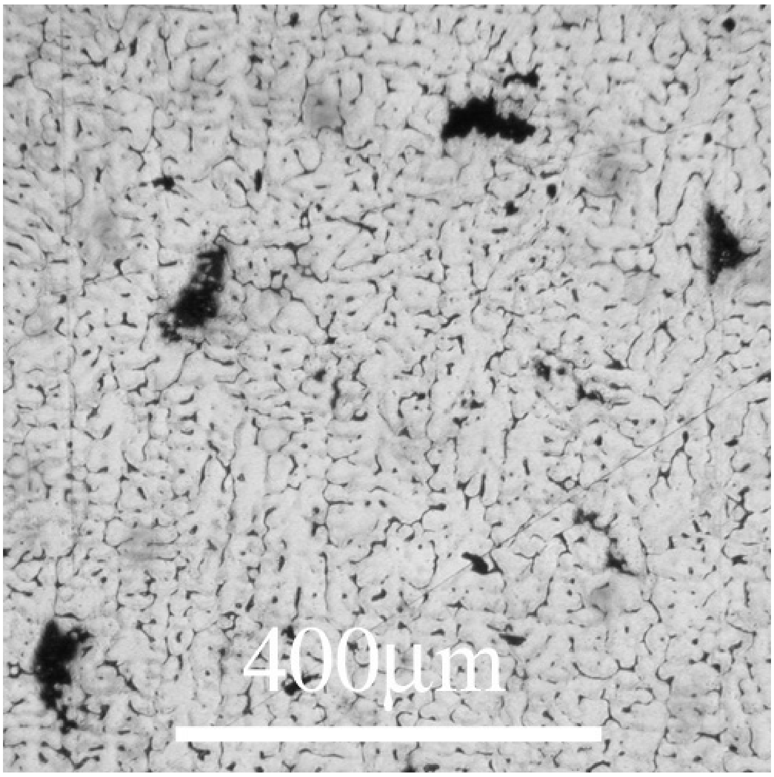

Figure 6.1: The as-cast micrograph of Al-5 wt%Cu alloy obtained from [Micrograph Library, University of Cambridge, 2007].

The dissolution of the regular, lamellar eutectic by taking into account the realistic spatial layout of eutectic phases in the one-dimensional geometry is simulated by the PFM. After that, a new concept of the eutectic phase is introduced.

6.1 Dissolution of the Lamellar Eutectic

The eutectic reaction in Al-Cu binary system occurs at $T = 548.01\,^{\circ}\mathrm{C}$, where the molar concentrations in the aluminium, θ and liquid are:

$$X_{\mathrm{Al}} = 2.52 \text{ at\%Cu}, \quad X_{\theta} = 31.72 \text{ at\%Cu}, \quad X_{\mathrm{Liq}} = 17.43 \text{ at\%Cu}, \tag{6.1}$$

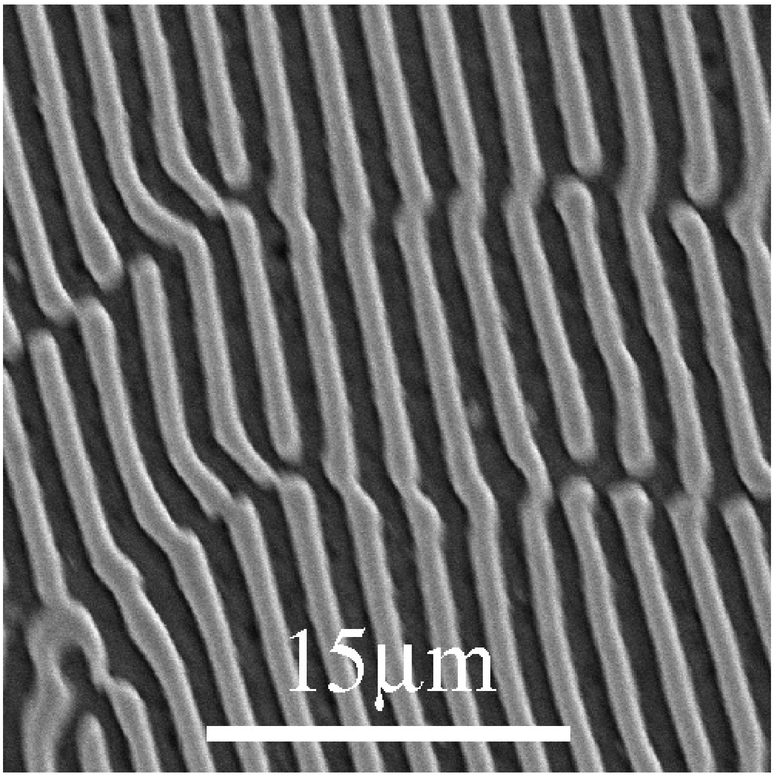

Figure 6.2: The regular, lamellar eutectic after casting of eutectic alloys Al-33 wt%Cu obtained from [Micrograph Library, University of Cambridge, 2007].

respectively.

The dissolution of the lamellar eutectic during homogenisation is simulated by the PFM. The phase transformations are in the DC mode, where the aluminium lamellae and aluminium matrix are treated as the same phase. Therefore, the phase transformation between these phases is ignored. The geometry assumption that the lamellae are parallel to the aluminium dendrite is used. The thermodynamic condition that the phase diffusion potentials are equal in phases in the interface region is implemented (Eq.(4.3)).

A Cu concentration profiles during dissolution of the lamellar eutectic at homogenisation temperature 520 °C are presented in Fig.(6.3). The system length is 50 μm, whereas the eutectic is placed in 6.0 μm on the left side of the system. Results with five (coarser) and ten (finer) lamellae in eutectic of the same size are demonstrated. Interlamellar spacing with five and ten lamellar eutectic are 1.2 μm and 6.0×10^{-1} μm, respectively.

The concentrations of Cu in the aluminium and θ lamellae are equal to the eutectic concentrations of these phases. The initial concentration in the aluminium phase is constant and equals 1.00 wt%Cu. The initial concentration profiles are presented in Figs.(6.3(a),6.3(b)). The concentration profiles with five and ten lamellae in the eutectic are presented on the left and right side of Fig.(6.3), respectively. The interface thickness is 6×10^{-2} μm in both cases. The interface energy and the interface-kinetic coefficient are $6.0{\times}10^{-1}$ J/m^2 and $5{\times}10^{-15}$ m^4/Js, respectively. The boundary conditions are assumed to be of the Neumann type with zero flux.

Two equidistant meshes are used in computation. The first mesh is inside the eutectic and the coarser one is outside of the eutectic region. The boundary between the meshes is $7\,\mu$m from the left boundary of the system. The distance between neighbouring nodes are in the first $1.0 \times 10^{-2}\,\mu$m and in the second mesh $2.0 \times 10^{-1}\,\mu$m. The total number of nodes is 916. The time-step length is 5.0×10^{-4} s.

The computed concentration profiles are presented after one hour (Figs.(6.3(c),6.3(d))), four hours (Figs.(6.3(e),6.3(f))) and eight hours (Figs.(6.3(g),6.3(h))) of the homogenisation. Very fast after the start of the heat treatment, the concentrations in both lamellae become equal to the equilibrium concentrations at high process temperatures.

6.2 The Eutectic Phase

The eutectic reaction in a multicomponent system occurs when the chemical potentials of components in the liquid and solid phases become equal. During the eutectic reaction, the number of solid phases is equal to the number of components and the number of phases is $\mathrm{P} = \mathrm{M} + 1$. The number of degrees of freedom in the eutectic reaction, for an isobaric system, is

$$\mathrm{F} = \mathrm{M} - \mathrm{P} + 1 = \mathrm{M} - (\mathrm{M} + 1) + 1 = 0. \tag{6.2}$$

Therefore, the eutectic reaction occurs at a fixed, eutectic temperature.

In general, the remaining liquid in the system solidifies during the eutectic reaction. It can be written as:

$$\mathrm{Liq}\left(\mathbf{X}_{\mathrm{Eu}}\right) \rightarrow \sum_{i=1}^{\mathrm{M}} \mathrm{s}_i\left(\mathbf{X}_{\mathrm{s}_i}\right), \tag{6.3}$$

where s_i represents a solid phase in the alloy. For example, the eutectic reaction in the binary Al-Cu can be written as:

$$\mathrm{Liq}\left(X_{\mathrm{Eu}}\right) \rightarrow \mathrm{Al}\left(X_{\mathrm{Al}}\right) + \theta\left(X_{\theta}\right). \tag{6.4}$$

From a thermodynamic point of view, the eutectic is a heterogeneous mixture of solid phases. In this section, a new, artificial, homogenous, eutectic phase is introduced. The thermodynamic values and properties of this new eutectic phase are computed from the thermodynamic values and properties of solid phases in the eutectic. The molar free energy and molar volume of such a defined eutectic phase needs to be defined for incorporation into the PFM. Two definitions are presented here.

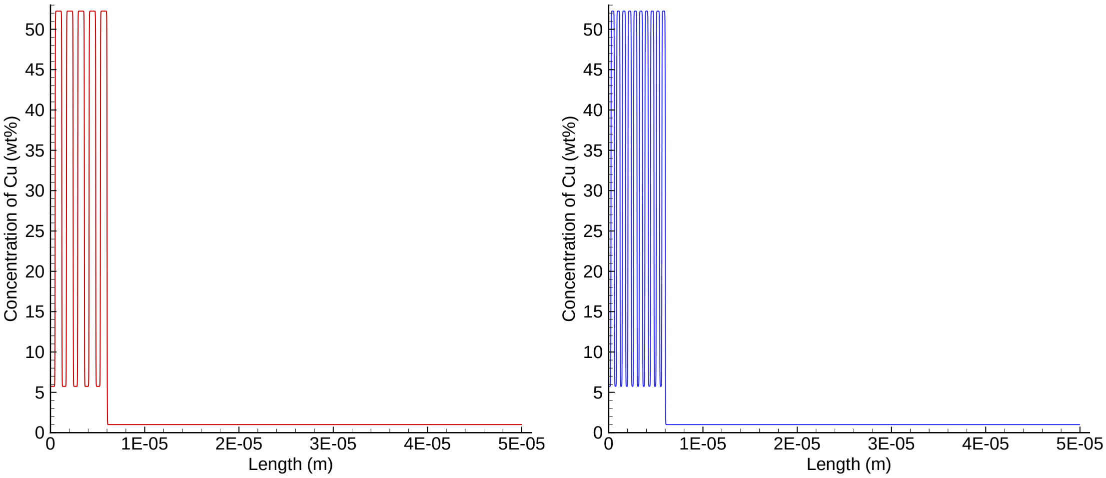

(a) Five lamellae in eutectic, initial state.

(b) Ten lamellae in eutectic, initial state.

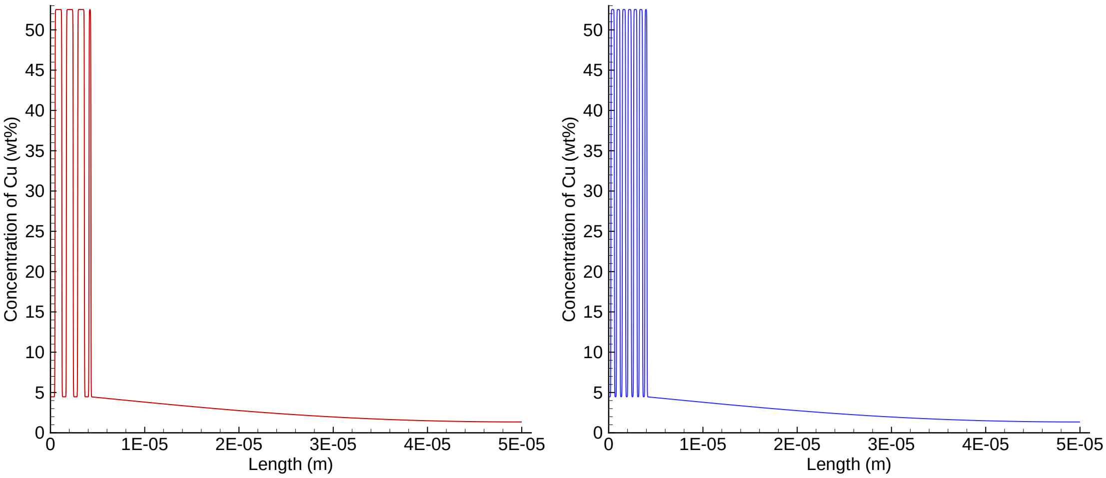

(c) Five lamellae in eutectic, one hour.

(d) Ten lamellae in eutectic, one hour.

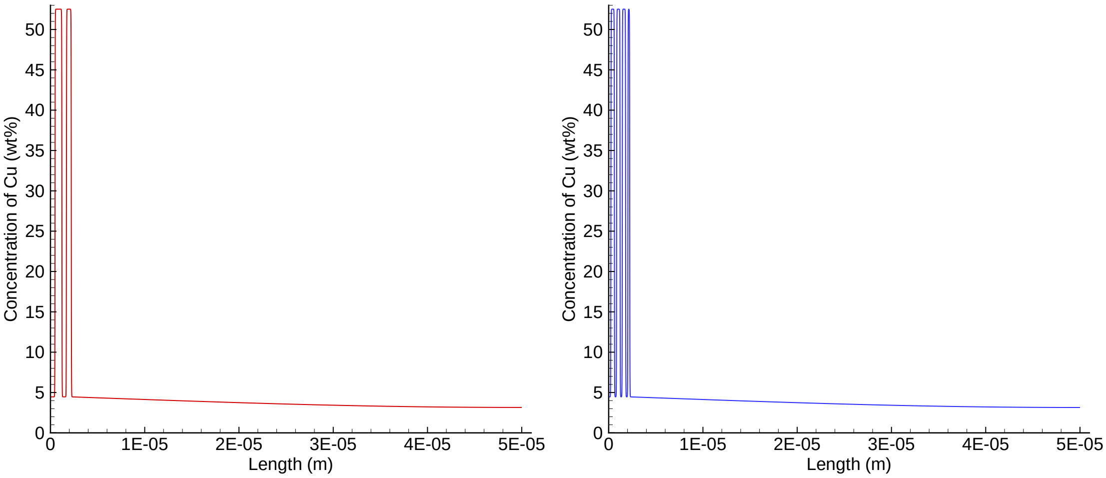

(e) Five lamellae in eutectic, four hours.

(f) Ten lamellae in eutectic, four hours.

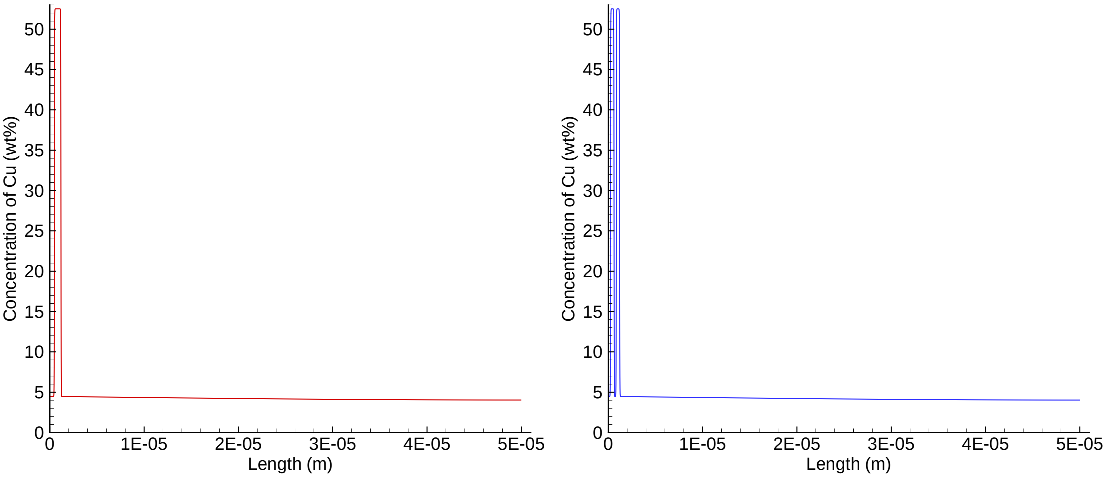

(g) Five lamellae in eutectic, eight hours.

(h) Ten lamellae in eutectic, eight hours.

Figure 6.3: The Cu concentration profiles during eight hours of isothermal dissolution of the lamellar eutectic at homogenisation temperature 520 °C.

Case 1. If an assumption is made that industrial solidification is fast enough, that the solid phases in the eutectic do not interact with each other, the phase transformations into the eutectic, after its formation, are ignored. The concentrations in the solid phases are the same concentrations as during the eutectic reaction. In this case, the Case 1, the molar free energy of eutectic phase g^1_{Eu} is defined by

$$g^1_{\mathrm{Eu}}\left(\mathbf{X}_{\mathrm{Eu}}, T\right) = \sum_{i=1}^{\mathrm{M}} \bar{x}_{\mathrm{s}_i} g_{\mathrm{s}_i}\left(\mathbf{X}_{\mathrm{s}_i}, T\right), \tag{6.5}$$

where $\bar{x}_{\mathrm{s}_i}$ and g_{s_i} are the molar fraction and the molar free energy of phase s_i, respectively. In the Case 1, the concentrations in the solid phases are equal to the concentrations during the eutectic reaction:

$$\mathbf{X}_{\mathrm{s}_i}\left(T\right) = \mathbf{X}_{\mathrm{s}_i\mathrm{eq}}\left(T_{\mathrm{Eu}}\right). \tag{6.6}$$

The molar free energy of the phase s_i at a constant concentration $\mathbf{X}_{\mathrm{s}_i}$ as a function of temperature are available from a thermodynamic database. The schematic presentation of the proposed concept for definition of the molar free energy of the eutectic phase in binary aluminium alloys with two solid phases α and β is presented in Fig.(6.4). In the example of the binary Al-Cu system, the molar fraction of phases are calculated by the lever rule as:

$$\bar{x}_{\mathrm{Al}} = \frac{X_\theta - X_{\mathrm{Eu}}}{X_\theta - X_{\mathrm{Al}}}, \quad \bar{x}_\theta = \frac{X_{\mathrm{Eu}} - X_{\mathrm{Al}}}{X_\theta - X_{\mathrm{Al}}}. \tag{6.7}$$

The molar free energy of eutectic phase, calculated by Eq.(6.5), is used as the second phase in the PFM. The molar volume of eutectic phase is defined as a linear combination of the molar volumes of phases in eutectic, weighed by its molar fractions:

$$V_{\mathrm{mEu}}\left(\mathbf{X}_{\mathrm{Eu}}, T\right) = \sum_{i=1}^{\mathrm{M}} \bar{x}_{\mathrm{s}_i} V_{\mathrm{ms}_i}\left(\mathbf{X}_{\mathrm{s}_i}, T\right) \ . \tag{6.8}$$

The Cu concentration profiles during homogenisation computed by the artificial eutectic phase, defined in this paragraph, are presented in Fig.(6.5). The system length is 50 μm, whereas the eutectic is placed in 6.0 μm on the left side of the system. The initial concentration in the aluminium phase is constant and equals 1.00 wt%Cu. The boundary conditions are assumed to be of the Neumann type with zero flux. The interface thickness, the interface energy and the interface-kinetic coefficient are $1.2\times10^{-1}\,\mu$m, 6.0×10^{-1} J/m^2 and 5×10^{-15} m^4/Js, respectively.

Two equidistant fixed meshes are used for discretization. The boundary between the meshes is 7 μm from the left boundary of the system. The total number of nodes is 566. Distances between neighbouring nodes are for the first $\Delta x_{\mathrm{in}} = 2 \times 10^{-2}\,\mu$m and the second mesh $\Delta x_{\mathrm{out}} = 2 \times 10^{-1}\,\mu$m. The time-step

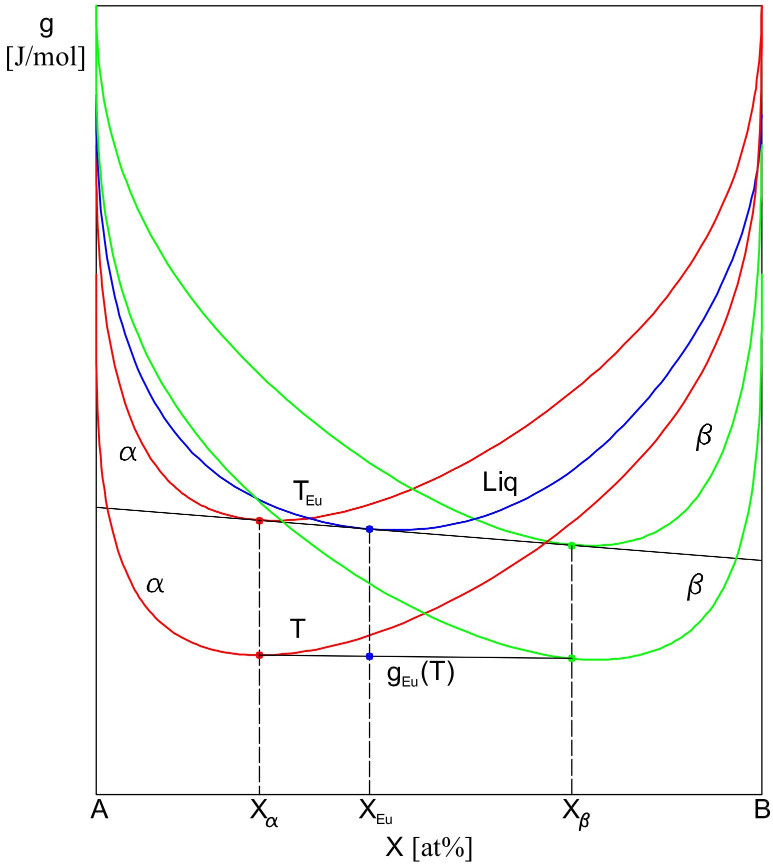

Figure 6.4: Case 1: The definition of the free energy of eutectic phase in free energy-concentration diagram.

length is 5.0×10^{-3} s.

The equilibrium state in the lamellar eutectic is very rapidly reached. The concentrations of both phases in the eutectic become equal to the equilibrium concentrations at the homogenisation temperature. Because of this, the second concept for definition of the eutectic phase is introduced.

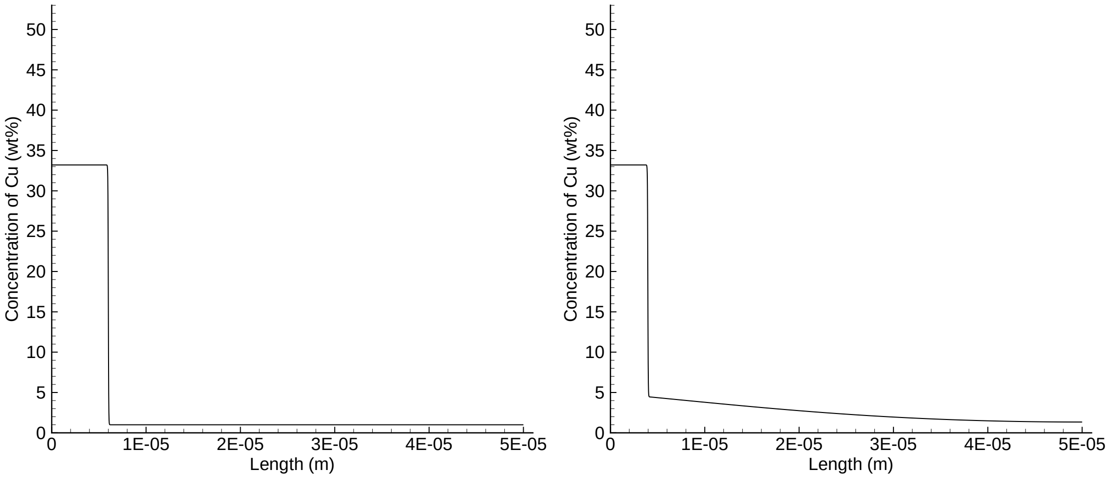

(a) The eutectic phase, initial state.

(b) The eutectic phase, one hour.

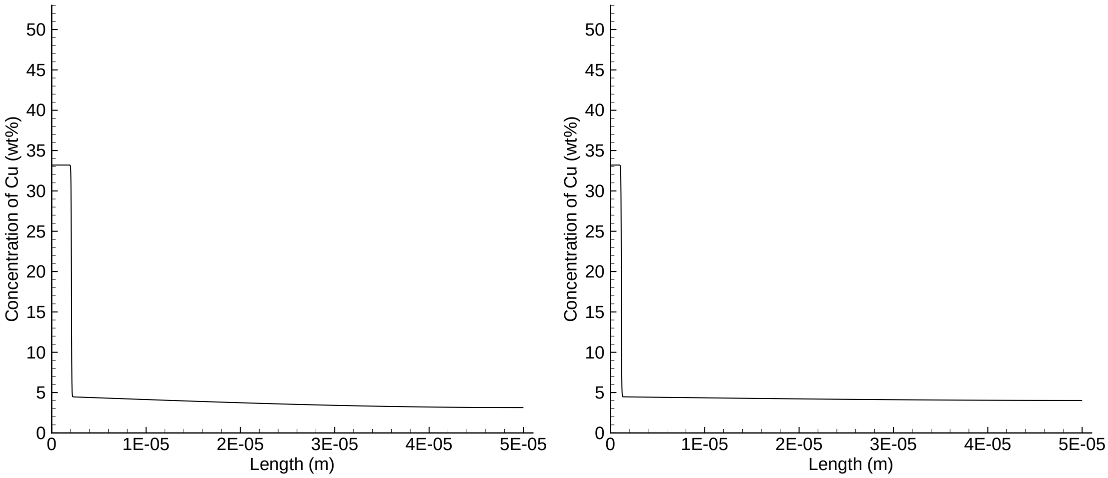

(c) The eutectic phase, four hours.

(d) The eutectic phase, eight hours.

Figure 6.5: The Cu concentration profiles during eight hours of isothermal dissolution of the eutectic phase defined by the Case 1.

Case 2. The diffusion phase transformations in the lamellar eutectic perform very fast because the interlamellar spacing is small. In the second method eutectic phase definition incorporates this fact. The molar free energy of the eutectic phase is in this case defined as:

$$g^2_{\mathrm{Eu}}\left(\mathbf{X}_{\mathrm{Eu}}, T\right) = \sum_{i=1}^{\mathrm{M}} \bar{x}_{\mathrm{s}_i} g_{\mathrm{s}_i}\left(\mathbf{X}_{\mathrm{s}_i\mathrm{eq}}, T\right) . \tag{6.9}$$

The eutectic phase is in Case 2 also stoichiometric. The only difference between these cases is in the determination of the concentrations in phases. The concentrations in phases are equal as during the eutectic reaction in Case 1, whereas in Case 2, the concentrations in the phases are equal to the equilibrium concentrations at the homogenisation temperature:

$$\mathbf{X}_{\mathrm{s}_i}\left(T\right) = \mathbf{X}_{\mathrm{s}_i\mathrm{eq}}\left(T\right) . \tag{6.10}$$

The molar free energy definition of the eutectic phase is in this case presented in Fig.(6.6). Concentrations in phases at process temperature are determined by the common tangent line construction.

The molar free energy in Case 2 is lower than in Case 1, consequently, the driving force for dissolution of the eutectic phase in the aluminium phase is lower and the dissolution kinetics are slower. The difference between the two cases grows when the difference between the eutectic and homogenisation temperature increases, as is evident from the definitions of the eutectic phase. Interface positions during the isothermal dissolution of the eutectic phase, computed by both concepts, at three homogenisation temperatures, are presented in Fig.(6.7). The interface positions are computed implicitly from the PFV ($\phi = 0.50$).

6.2.1 Comparison with the Lamellar Eutectic

Interface positions during homogenisation computed by the concept of the eutectic phase and the lamellar eutectic are compared in Fig.(6.8). The eutectic phase computed by Case 2 is compared with five and ten lamellae in the eutectic at homogenisation temperature 520 °C. Interface position of lamellar eutectic during time is a step-like function whereas the lamellae of the eutectic phase θ and lamellae of the aluminium phase are subsequently and alternatively dissolved. The interface position during dissolution of the phase θ is a roughly parabolic function of time, whereas the interface position drops rapidly when dissolution of this phase is completed. This vertical line is a consequence of the assumption that the aluminium lamellae are in the same phase as the aluminium grain. The comparison with the eutectic phase is acceptable when the dissolution of the whole eutectic lamellae, Al and θ, is only completed. When the number of lamellae in the eutectic increases, the artificial homogeneous eutectic phase becomes more suitable for simulation.

6.3 Influence of Homogenisation Parameters

The definition of the eutectic phase is essential for connection to homogenisation with the solidification model. The numerical results obtained from the solidifi-

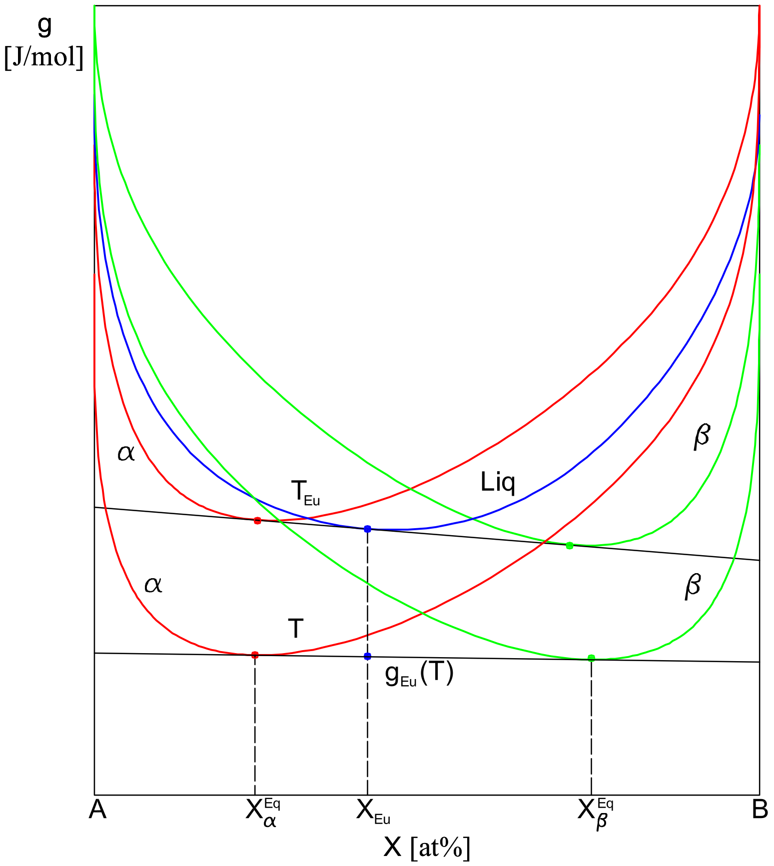

Figure 6.6: Case 2: The definition of the free energy of eutectic phase in free energy-concentration diagram.

cation model, is the initial condition for the homogenisation model. Here, the Scheil-Gulliver model is implemented as the solidification model [Kurz and Fisher, 1998], whereas other models can be implemented as well. The formation of an initial profile from the solidification model is done by using the assumption that the phase densities are equal. In this section, high temperature is instantly reached in computations. Again, the binary Al-5 wt%Cu alloy is in the focus.

The physical parameters used in the computations are as follows. The interface thickness, the interface energy and the interface-kinetic coefficient are $1.2 \times 10^{-1}\,\mu$m, 6.0×10^{-1} J/m^2 and 5×10^{-15} m^4/Js, respectively.

The boundary conditions are assumed to be of the Neumann type with zero flux. Two equidistant fixed meshes are used for discretization. The boundary between the meshes is 7 μm from the left boundary of the system. Distances between neighbouring nodes are for the first $\Delta x_{\text{in}} = 2 \times 10^{-2}\,\mu$m and the second mesh $\Delta x_{\text{out}} = 2 \times 10^{-1}\,\mu$m. The time-step length is 5.0×10^{-3} s.

The homogenisation parameter H_p for quantified estimating of the dissolution kinetics is introduced as

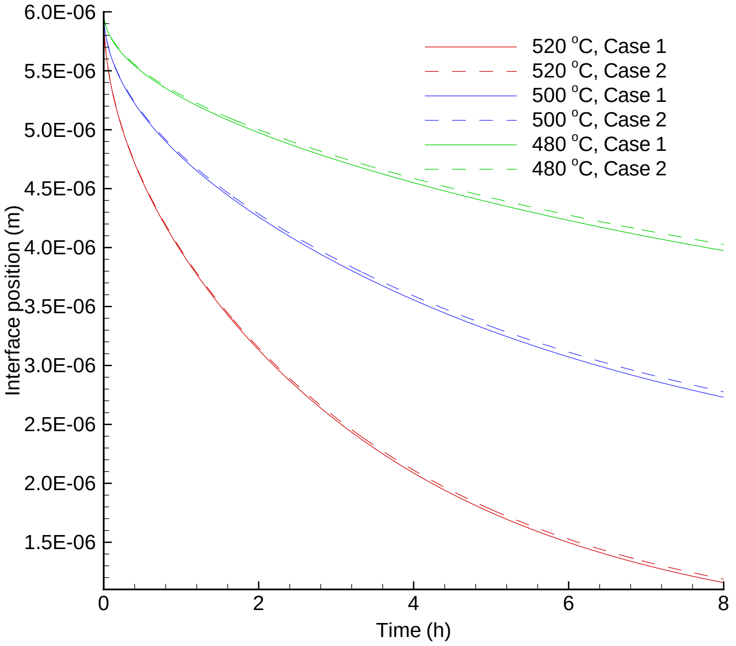

Figure 6.7: Comparison of interface positions computed by the definitions of the eutectic phase at three homogenisation temperatures.

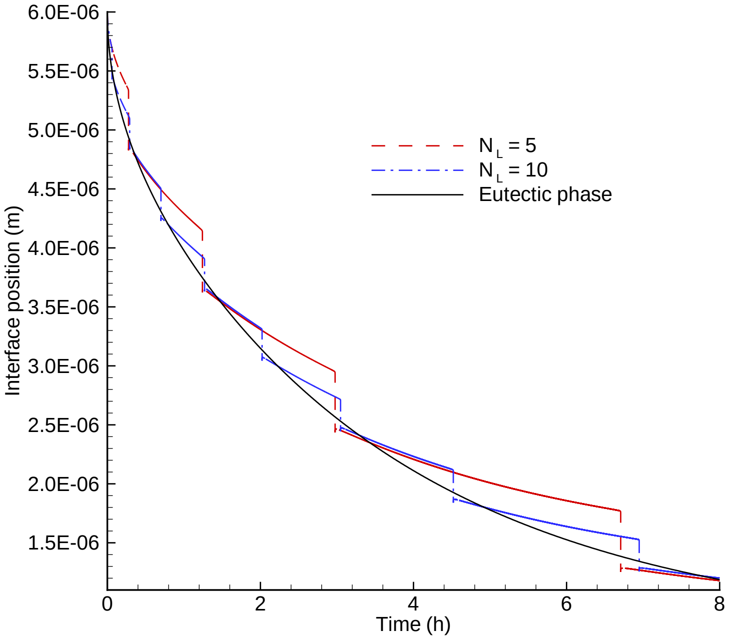

Figure 6.8: Comparison of interface positions computed by the concept of the eutectic mixture phase and the lamellar eutectic.

$$H_p(T) = \frac{c_{\max} - c_{\min}}{c_{\max}}, \tag{6.11}$$

where $c_{\max}$ and $c_{\min}$ are the maximum and minimum concentrations of Cu in the aluminium phase [Vermolen *et al.*, 1998b]. Concentrations in the aluminium phase are determined in the region where the PFV is lower then 0.50.

6.3.1 The Homogenisation Temperature

The temperature influence on dissolution kinetics, as the most important process parameter, is estimated at the beginning. The influence is demonstrated at three homogenisation temperatures: 480 °C, 500 °C and 520 °C. The system length is 50 μm. The Cu concentration profiles during isothermal homogenisation are presented in Fig.(6.9). The initial concentration profile obtained by the Scheil-Gulliver solidification model is presented in Fig.(6.9(a)). The Cu concentration profiles after one (Fig.(6.9(b))), four (Fig.(6.9(c))) and eight hours (Fig.6.9(d)) of homogenisation are presented. The homogenisation parameters in time during solution heat treatment at three temperatures are presented in Fig.(6.10). The temperature influence on dissolution kinetics has been already demonstrated in Fig.(6.7).

Obviously, the influence of homogenisation temperature on dissolution kinetics is enormous. If the homogenisation temperature is higher, the dissolution is faster, and vice versa. The homogenisation temperature is limited by the melting temperature of the presented solid phases which is the eutectic temperature in this example. The easiest way to estimate temperature influence is to compare the homogenisation parameter after homogenisation. The homogenisation parameters for temperatures 480 °C, 500 °C and 520 °C are approximately 0.40, 0.24 and 0.10, respectively.

The temperature influence on the dissolution kinetics is twofold:

- The solubility of the second phase increases with temperature,
- The diffusion coefficient exponentially increases with temperature (Eq.(4.1)).

At the beginning of the isothermal homogenisation, the eutectic phase grows, because the aluminium phase is supersaturated with Cu, i.e. the concentration in the vicinity of the interface is higher than the solubility of the eutectic phase in the aluminium phase. The initial growth is more pronounced with lower homogenisation temperature, because solubility depends on temperature.

6.3.2 The Grain Size

The grain size influence on the homogenisation time is considered next. The as-cast grain size is a function of the solidification rate during casting. The homogenisation times for the required homogenisation parameters for grain sizes 30 μm, 50 μm, 70 μm and 90 μm are written in Tab.(6.1). The homogenisation temperature is 520 °C. The system length with the grain and the eutectic phase is denoted as l_Γ. The huge influence of the grain size on the homogenisation time is demonstrated. The homogenisation times are higher for larger grain

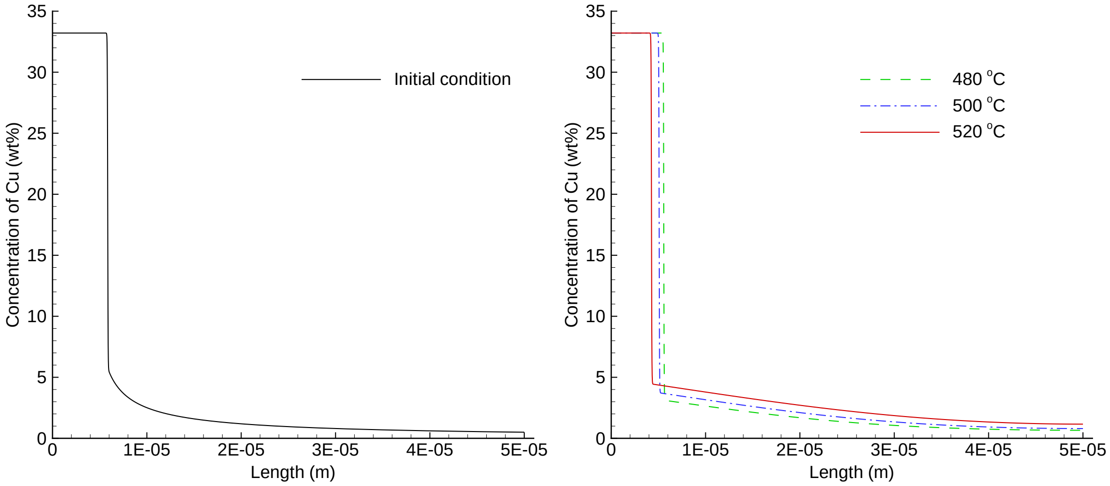

(a) The initial concentration profile. (b) The concentration profiles after one hour.

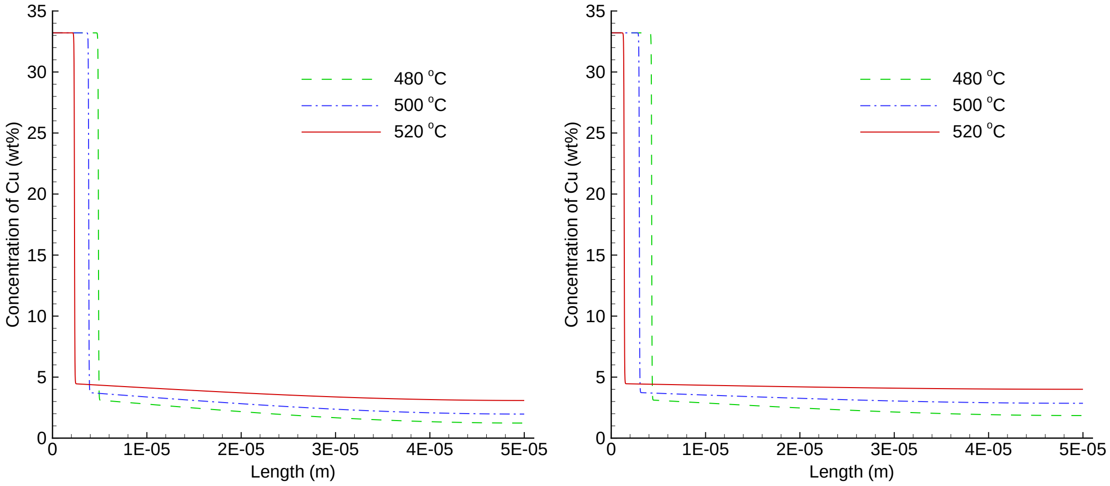

(c) The concentration profiles after four hours. (d) The concentration profiles after eight hours.

Figure 6.9: Concentration profiles of Cu after one, four and eight hours of isothermal dissolution of the eutectic phase at three homogenisation temperatures.

sizes, as expected. If the homogenisation parameter needs to be lower than 0.10, homogenisation has to last more than one day when the average as-cast grain size is 90 μm.

6.3.3 The Macroscopic Concentration

The influence of the macroscopic concentration on the dissolution kinetics of the eutectic phase in the aluminium phase is estimated. The numerical results for three macroscopic concentrations 4 wt%Cu, 5 wt%Cu and 6 wt%Cu are presented in Fig.(6.11). The homogenisation temperature and grain size are 520 °C and 50 μm, respectively. The macroscopic concentration influences the fraction of the

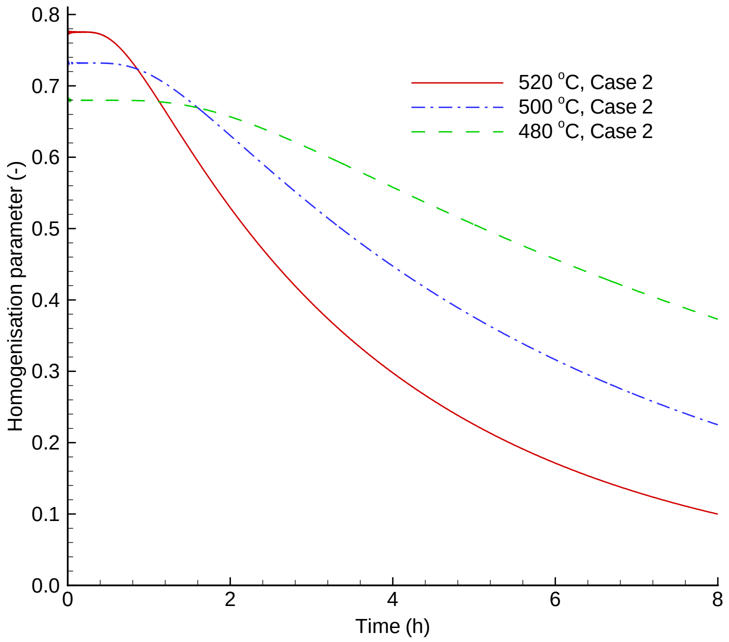

Figure 6.10: Homogenisation parameters during homogenisation computed at three homogenisation temperatures.

H_p [−] l_Γ [μm]	0.70	0.50	0.30	0.10
30	0 h 26 min	0 h 50 min	1 h 26 min	2 h 55 min
60	1 h 12 min	2 h 20 min	4 h 06 min	8 h 05 min
70	2 h 21 min	4 h 35 min	8 h 02 min	15 h 52 min
90	3 h 53 min	7 h 34 min	13 h 17 min	26 h 13 min

Table 6.1: The grain size influence on the dissolution kinetics of the eutectic phase in the aluminium phase for Al-5 wt%Cu alloy.

eutectic phase after solidification, as presented in Fig.(6.11(a)). The initial concentration profiles and the concentration profiles after one (Fig.(6.11(b))), four (Fig.(6.11(c))) and eight (Fig.(6.11(d))) hours of homogenisation are displayed. The dissolution of the eutectic phase is completed after eight hours of homogenisation with macroscopic concentration 4 wt%Cu.

6.4 Dissolution of the Eutectic Phase in Realistic Geometry

Modelling of the phase transformations in a realistic microstructure with complex geometry is demonstrated here. The dissolution of the network of the eutectic phase in a Al-5 wt%Cu alloy is simulated. The representative micrograph of this

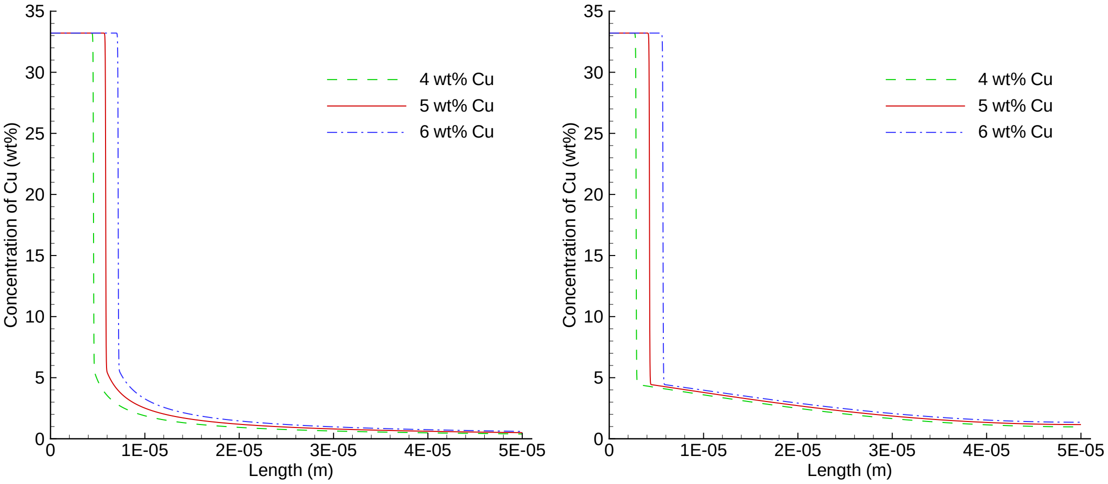

(a) The initial concentration profiles. (b) The concentration profiles after one hour.

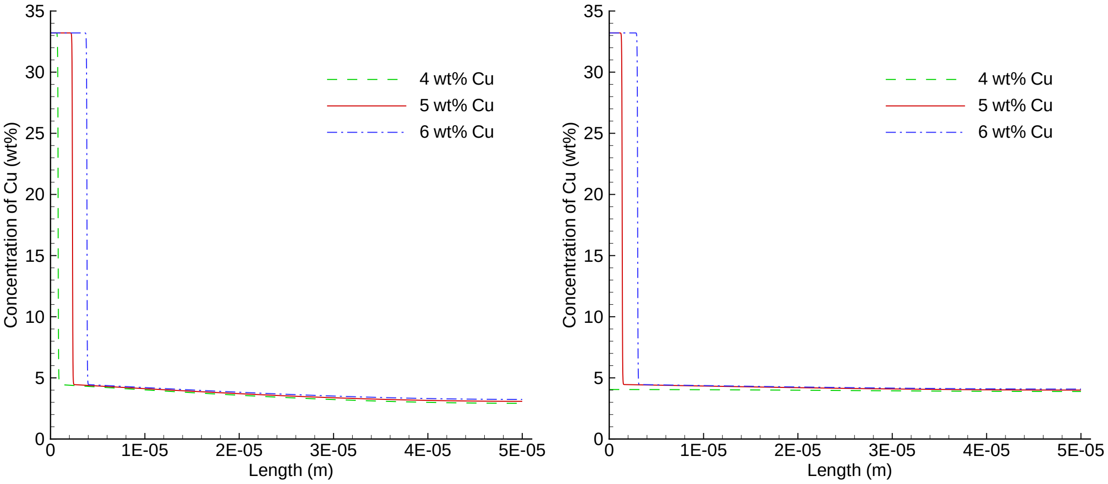

(c) The concentration profiles after four hours. (d) The concentration profiles after eight hours.

Figure 6.11: The macroscopic concentration influence on the dissolution kinetics of the eutectic phase in the aluminium phase in Al-5 wt%Cu alloy at homogenisation temperature 520 °C.

alloy is presented in Fig.(6.1). A closer look at the microstructure was achieved by the Slovenian aluminium company IMPOL, d.d. and is represented in Fig.(6.12). The 53 μm computational square domain is emphasized by the transparent blue colour. The homogenisation temperature is 520 °C. The interface thickness, the interface energy and the interface-kinetic coefficient are $6 \times 10^{-1}\,\mu$m, 6.0×10^{-1} J/m^2 and 5×10^{-15} m^4/Js, respectively.

The initial condition of the PFV is presented in Fig.(6.13(a)). The eutectic and aluminium phases are represented by red and blue colours, respectively. The initial Cu concentration field is obtained by using the Scheil-Gulliver solidification path. The most distant point from the eutectic phase is the lower left corner of the computation domain. This point is established as the center of the aluminium grain. The initial Cu concentration field is represented in Fig.(6.13(b)). The boundary conditions are assumed to be of the Neumann type with zero flux. The governing equations are discretized by the FDM on the equidistant 266 × 266 mesh. The time-step length is $5.0 \times 10^{-3}\,\mathrm{s}$.

The PFV and Cu concentration field after each hour of homogenisation are presented in Fig.(6.13). The dissolution of the network of the eutectic phase is clearly demonstrated and one can observe that after four hours of homogenisation the network of the eutectic phase is broken.

For more precise computation of the dissolution kinetics of the eutectic phase during homogenisation, the model can be upgraded in two ways:

- The initial profile can be computed with a more sophisticated solidification model in which the diffusion in the solid phase during solidification can be included;

- Temperature profile during the heating step of homogenisation can be incorporated in the model.

The second upgrade of the model is demonstrated in the following.

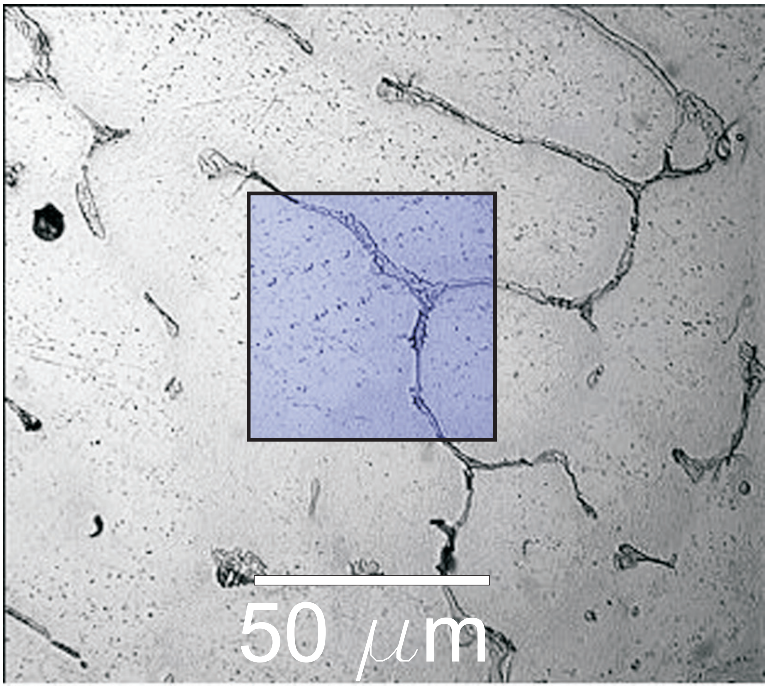

Figure 6.12: The as-cast micrograph of the Al-5 wt%Cu alloy. The micrograph is obtained from the Slovenian aluminium company IMPOL, d.d..

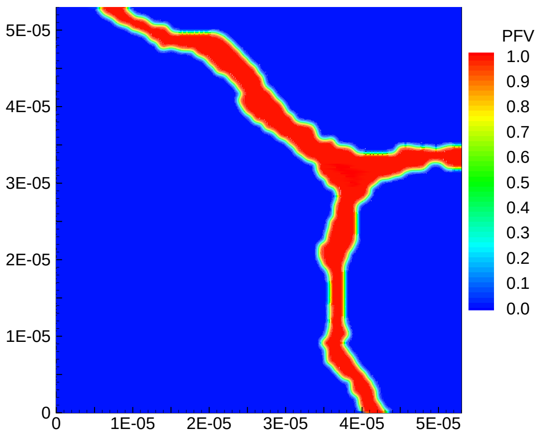

(a) The PFV, initial state.

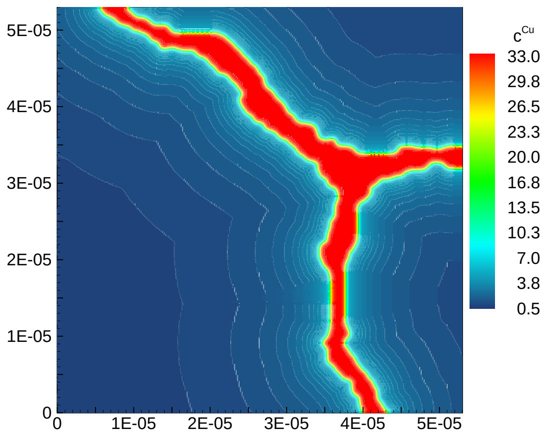

(b) The Cu concentration field, initial state.

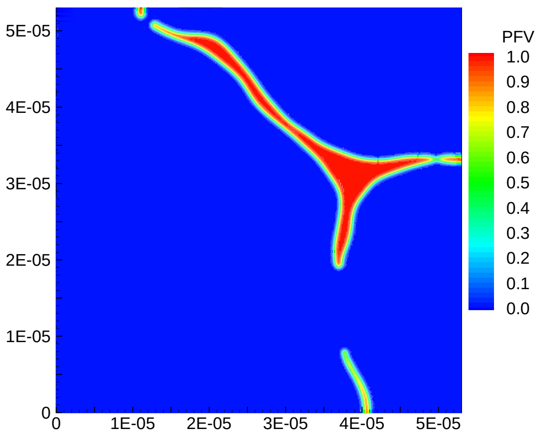

(c) The PFV, one hour.

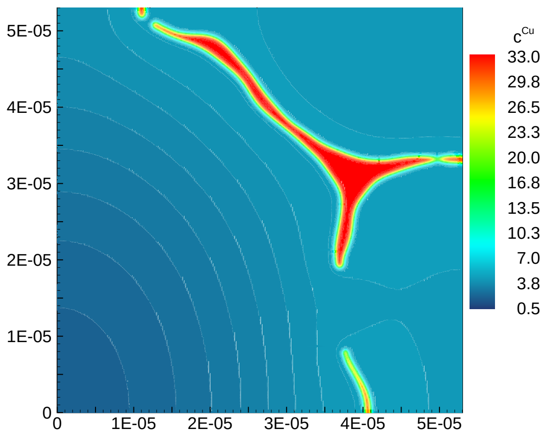

(d) The Cu concentration field, one hour.

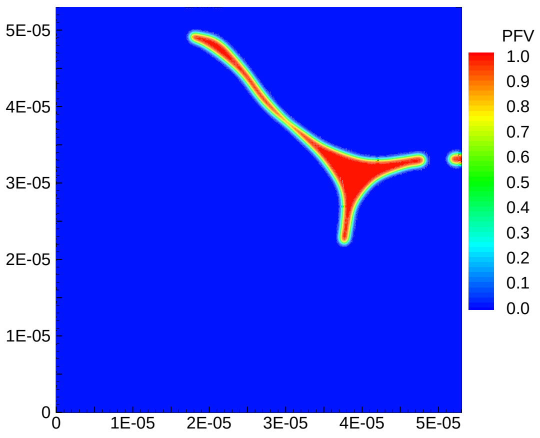

(e) The PFV, two hours.

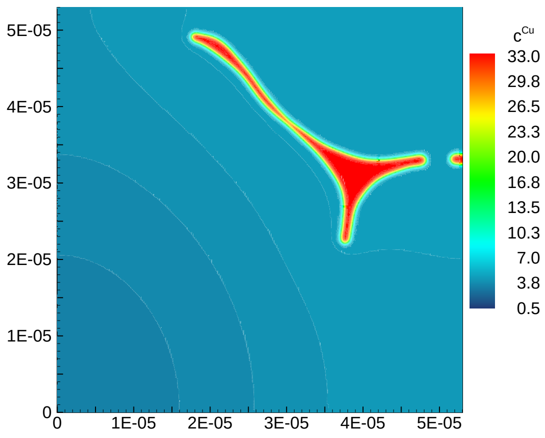

(f) The Cu concentration field, two hours.

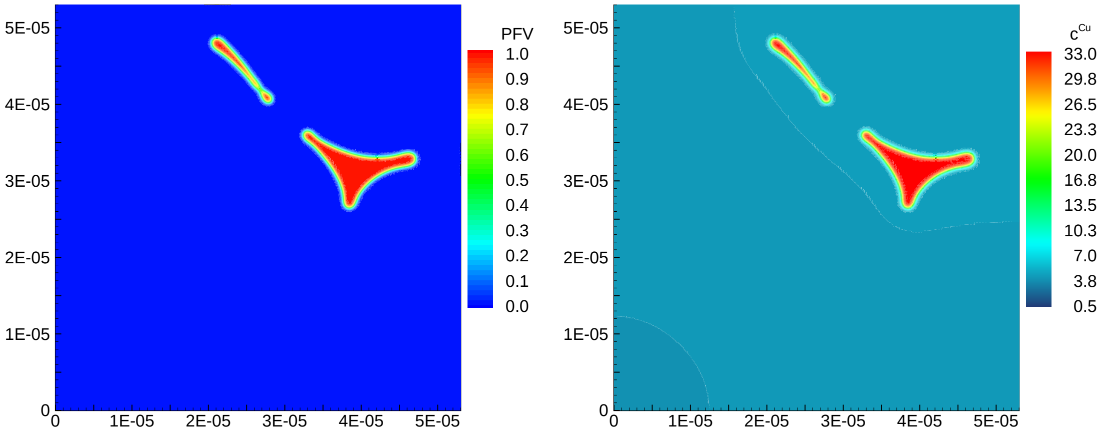

(g) The PFV, four hours.

(h) The Cu concentration field, four hours.

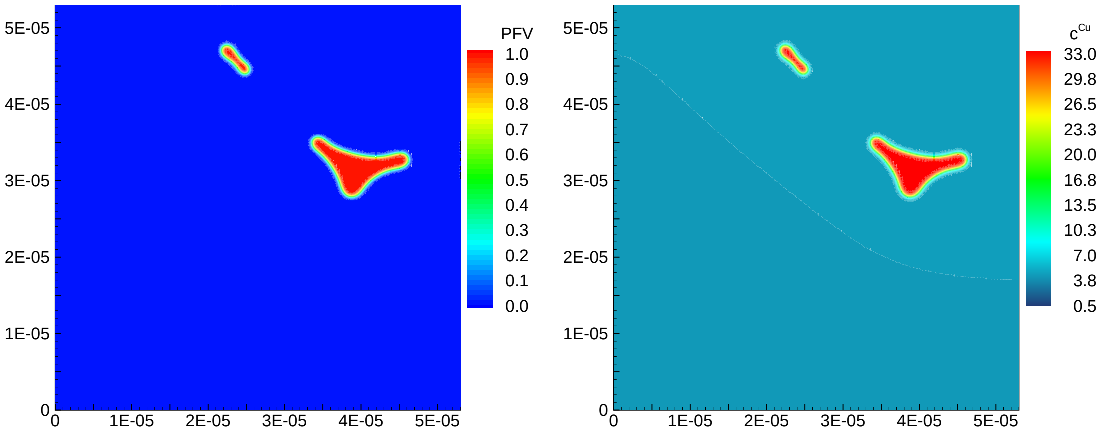

(i) The PFV, six hours.

(j) The Cu concentration field, six hours.

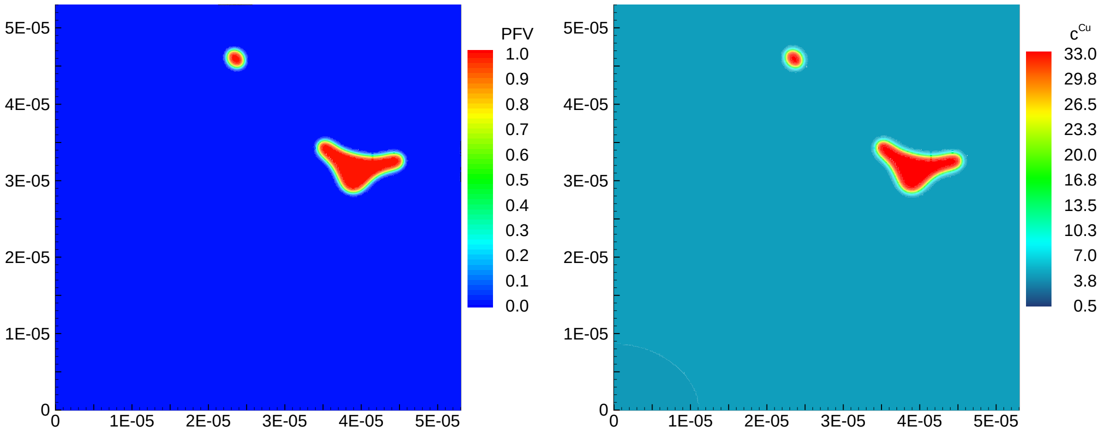

(k) The PFV, eight hours.

(l) The Cu concentration field, eight hours.

Figure 6.13: The PFV and the concentration field of Cu during homogenisation of Al-5 wt%Cu at homogenisation temperature 520 °C.

6.5 Heating Step of Homogenisation

Consider that a homogenisation furnace is continuously supplied by billets. Every billet passes from the input to output door throughout the preheating and holding chamber. The furnace is designed such that every billet spends half of the homogenisation time in the preheating chamber. In the preheating chamber, the billet temperature increases to the homogenisation temperature. During the holding step, the billet temperature is equal to the homogenisation temperature in the holding chamber of the homogenisation furnace.

The idea is to estimate the dissolution of the eutectic phase during the heating step of homogenisation. Because of this, the numerical model for computing temperature field during heating at the macro level is derived.

The input parameters for the macroscopic model are:

- alloy type,
- billet dimension, length and diameter,
- homogenisation temperature and
- homogenisation time.

The macroscopic temperature field is an input for the previously derived PFM for dissolution of the eutectic phase at the micro level.

6.5.1 Macroscopic Temperature Field in Aluminium Billet

Temperature field in a billet during heating step of homogenisation can be prescribed by the classical heat diffusion equation:

$$\rho c_p \frac{\partial T}{\partial t} = \nabla \cdot (k \nabla T), \tag{6.12}$$

where ρ, c_p, k, T, t represent density, specific heat, thermal conductivity of a material, temperature and time, respectively [Incropera and DeWitt, 2002]. The boundary conditions are described by the convective heat transfer

$$h_{\mathrm{ef}} (T_{\mathrm{A}} - T_{\mathrm{S}}) = -\left(\frac{\partial T}{\partial r_c}\right)_{\mathrm{S}}, \tag{6.13}$$

where h_{ef}, T_{A} and T_{S} represent the effective heat transfer coefficient, temperature of the surrounding air in the furnace and temperature of billet surface, respectively. The effective heat transfer coefficient includes the correction influenced by the radiation from the furnace wall to the billets.

The heat conduction in billets is postulated as an axisymmetric problem, and the governing equation Eq.(6.12) can be rewritten in cylindrical coordinates as

$$\rho c_p \frac{\partial T}{\partial t} = \frac{1}{r_c} \frac{\partial}{\partial r_c}\left(k r_c \frac{\partial T}{\partial r_c}\right) + \frac{\partial}{\partial z}\left(k \frac{\partial T}{\partial z}\right), \tag{6.14}$$

where r_c and z represent radial and axial coordinate, respectively. The governing equation (Eq.(6.14)) with the prescribed boundary condition (Eq.(6.13)) is discretized by the finite volume method [Versteeg and Malalasekera, 1996; Patankar, 1980].

The thermophysical macroscopic properties, ρ, c_p and k, as a function of temperature are for Al-5 wt% Cu obtained from the JMatPro software for aluminium alloys [JMatPro, 2004]. The only unknown in the macroscopic model is the effective heat transfer coefficient (h_{ef}) in the preheating chamber of the homogenisation furnace. The velocity field of air in the furnace is very complex and the theoretical determination of the convective heat transfer coefficient is not a trivial task. Also, radiation from the furnace wall to billets is not easy for estimation. Because of this, in-situ temperature measurements in billets during homogenisation are carried out. Two basic conclusions from the measurements [Kovačević and Šarler, 2005] are:

- Heat transfer coefficient varies with the billet position in preheating chamber of the homogenisation furnace.
- The radiation from the furnace wall to billet tops is not negligible in the first hour of heating.

The effective heat transfer coefficient as a function of billet position in the preheating chamber is tuned throughout the measurement results. These values are written in Tab.(6.2). Temperature field in a Al-5 wt%Cu alloy billet after first hour of heating in the preheating chamber of the furnace is computed by the macroscopic model. It is presented in Fig.(6.14(a)). The billet length and diameter are 5.90 m and 2.82×10^{-1} m, respectively. The initial temperature in aluminium billet on the furnace entry is equal to 25 °C. Homogenisation parameters are 520 °C and 8 h. The homogenisation model is implemented at two points, points 1 and 2 depicted in Fig.(6.14(a)). Point 1 is placed 90 mm and 500 mm from the billet surface and top, respectively, whereas point 2 is placed in billet centre. Temperature profiles during the heating step of homogenisation at these points are presented in Fig.(6.14(b)).

6.5.2 The PFM for Non-Isothermal Phase Transformations

Until now, the PFM has been derived for isothermal phase transformations. For the implementation of a model for non-isothermal phase transformation, the physical properties related to model parameters as functions of temperature need to be estimated. The phase-field equation rewritten from Eq.(2.113) is

$$\frac{\partial \phi}{\partial t} = \frac{\mu_{\mathrm{k}}}{\delta}\left\{\sigma\left[\delta\nabla^2\phi - \frac{36}{\delta}\phi\,(1-\phi)\,(1-2\phi)\right] - 30\phi^2\,(1-\phi)^2\,\frac{\Delta g_{\beta\mathrm{Al}}}{V_{\mathrm{m}}}\right\}. \tag{6.15}$$

The physical properties included in the PFM are:

Table 6.2: The effective heat transfer coefficient as a function of billet position in the preheating chamber of the homogenization furnace.

Pos.	Time interval	h_{ef} [J/m^2]		Pos.	Time interval	h_{ef} [J/m^2]	
-	[s]	Surface	Top	-	[s]	Surface	Top
1	0-960	31.9	200.2	9	7681-8640	74.1	74.1
2	961-1920	40.9	160.5	10	8641-9600	73.3	73.3
3	1921-2880	53.2	120.9	11	9601-10560	70.0	70.0
4	2881-3840	58.2	81.2	12	10561-11520	67.0	67.0
5	3841-4800	61.4	61.4	13	11521-12480	61.7	61.7
6	4801-5760	63.6	63.6	14	12481-13440	59.4	59.4
7	5761-6720	71.9	71.9	15	13441-14400	56.9	56.9
8	6721-7680	74.2	74.2				

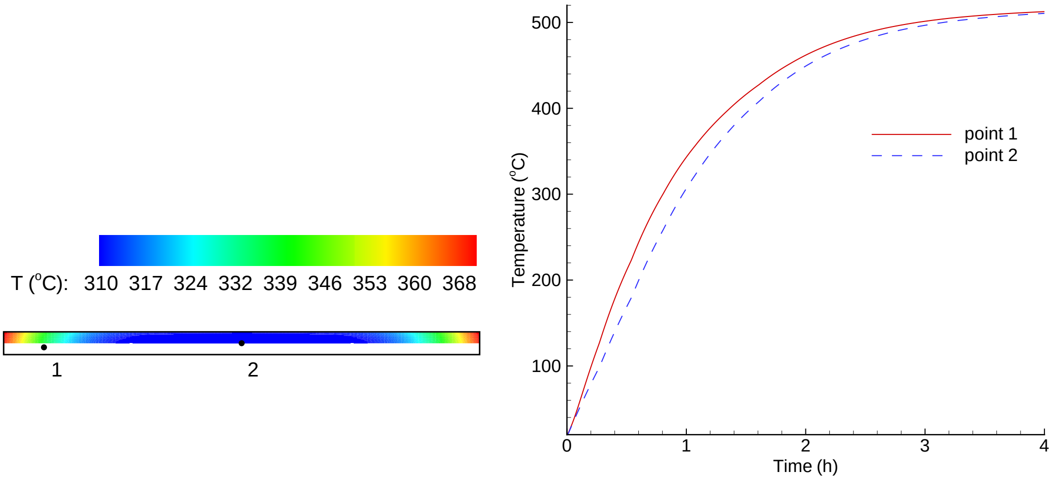

(a) Temperature field in Al-5 wt%Cu alloy billet after the first hour of heating in a preheating chamber of the homogenisation furnace. Two points where the homogenisation model is implemented are depicted.

(b) Temperature profiles during heating step of homogenisation at points 1 and 2.

Figure 6.14: Temperature field in aluminium billet during the heating step of homogenisation, computed by the macroscopic numerical model.

- the interface energy,
- the interface-kinetic coefficient and
- the driving force for phase transformation.

Interface Energy. Interface energy does not depend on temperature in present approximation. The diffusion coefficient as a function of temperature is written in Eq.(4.1) with parameters in Tab.(4.1).

Interface-Kinetic Coefficient. The interface-kinetic coefficient as a function of temperature is postulated as:

$$\mu_{\mathrm{k}} = \mu_{\mathrm{k0}} \exp\left(-\frac{Q_{\mu_{\mathrm{k}}}}{RT}\right), \tag{6.16}$$

where the activation energy $Q_{\mu_{\mathrm{k}}}$ is equal to 140 kJ/mol. This value was experimentally obtained in the study of $\gamma \rightarrow \alpha$ phase transformation in a Fe-Mn steel alloy [Mecozzi *et al.*, 2005]. The constant μ_{k0} is calculated from the condition that the interface-kinetic coefficient is equal to $5.0 \times 10^{-15}\,\mathrm{J/m^4K}$ at temperature 520 °C.

Driving Force for Phase Transformation. In pure material, the driving force for freezing is equal to the difference between the molar free energies of the solid and liquid phase. It is proportional with undercooling ΔT

$$\Delta g_{\mathrm{sl}} = \frac{L_{\mathrm{M}}}{T_{\mathrm{M}}}\Delta T, \tag{6.17}$$

where L_{M} and T_{M} represent the latent heat of melting and melting temperature, respectively. The difference in specific heat between the solid and liquid and the specific heat as a function of temperature are ignored [Porter and Easterling, 1990].

The statement that the driving force for phase transformations is linearly proportional with temperature may be extended for alloys. The theoretical proof is presented in the two-phase α-β system of binary A-B alloy [Rollet, 2001]. The molar free energy versus concentration and the equilibrium phase diagram for presentation of the driving force as a function of temperature is depicted in Fig.(6.15). The two phase system is in thermodynamic equilibrium at the initial temperature T_0. After that, temperature is instantly increased by ΔT. The driving force for dissolution of the phase β into the phase α is the difference between the chemical potentials of components B:

$$\Delta g_{\beta\alpha} = \mu^{\mathrm{B}}_{\mathrm{eq}} - \mu^{\mathrm{B}}_{0} = RT\ln\frac{a^{\mathrm{B}}_{\mathrm{eq}}}{a^{\mathrm{B}}_{0}}, \tag{6.18}$$

where it is assumed that the phase β is a pure component. By using the assumption that the phase α is a dilute solution, the molar free energy difference is:

$$\Delta g_{\beta\alpha} = RT\ln\frac{X_{\mathrm{eq}}}{X_0}\,. \tag{6.19}$$

The solubility is often approximated by an Arrhenius expression

$$X_{\mathrm{eq}} = A\exp\left(-\frac{Q_{\mathrm{M}}}{RT}\right), \tag{6.20}$$

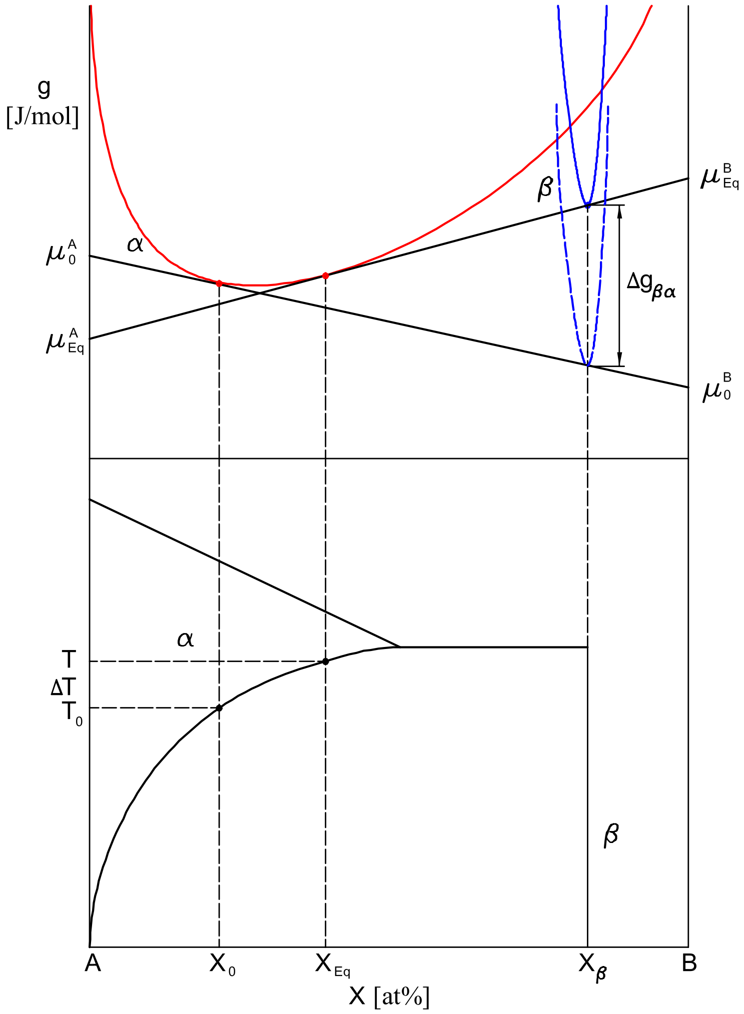

Figure 6.15: Estimation of the driving force for dissolution of phase β into phase α as a function of temperature. The molar free energy versus concentration and the equilibrium phase diagram of a binary A-B system are demonstrated.

where Q_M is heat absorbed (enthalpy) when one mole of the phase β is dissolved in a dilute solution of the phase α. From Eqs.(6.19,6.20), can be obtained that the driving force is linearly increasing with temperature difference:

$$\Delta g_{\beta\alpha} = \frac{Q_\mathrm{M}}{T}\Delta T. \tag{6.21}$$

The driving force for phase transformation is linearly proportional with temperature, Eq.(6.21), by using the assumption that the phase α is the dilute solution.

The driving force for phase transformation of silicon in aluminium for fixed concentrations of Si in the aluminium phase as function of temperature is presented in Fig.(6.16). The results obtained from the thermodynamic database confirm the previous statement that the driving force for phase transformation is linearly proportional with temperature.

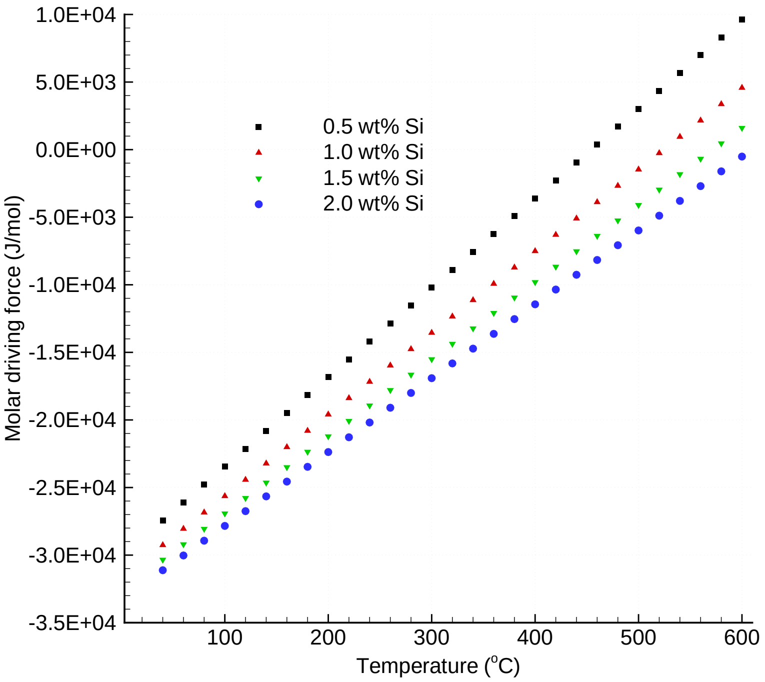

Figure 6.16: The driving force of silicon in the aluminium phase as a function of temperature for four fixed concentrations of Si in the aluminium phase (c_{Al}^{Si}).

6.5.3 Dissolution of Eutectic Phase during Heating Step of Homogenisation

The unsteady temperature field during the heating step of homogenisation is computed by the macroscopic model. Temperature profiles at points 1 and 2 (Fig.(6.14(b))) as the inputs for the dissolution of the eutectic phase at the micro level are incorporated into the PFM. The non-isothermal PFM described in the previous section is used for computation.

The driving force for phase transformation at the homogenisation temperature and the temperature slopes for fixed concentration in the aluminium phase are obtained from the thermodynamic database. In this way, the driving force for phase transformation as a function of concentration in the aluminium phase as well as temperature is calculated. Also, the molar volume of the second phase is a function of temperature.

The system length is 50 μm. The interface thickness and the interface energy are 1.2×10^{-1} μm and 6.0×10^{-1} J/m^2, respectively. The boundary conditions are assumed to be of the Neumann type with zero flux.

Two equidistant meshes are used in computation. The boundary between the meshes is 7 μm from the left boundary of the system. The distance between neighbouring nodes are in the first 1.0×10^{-2} μm and in the second mesh 2.0×10^{-1} μm. The total number of nodes is 566. The time-step length is 5.0×10^{-3} s.

The Cu concentration profiles after one (Fig.(6.17(a))), two (Fig.(6.17(b))), three (Fig.(6.17(c))) and four hours (Fig.(6.17(d))) of heating in the preheating chamber of the furnace are presented. The grain size and homogenisation times are 50 μm and 8 h, respectively. The concentration gradient in the aluminium phase at the interface is positive after the first hour of heating, and therefore the eutectic phase grows during this period. The growth of the eutectic phase is more evident in the next graph, where the interface positions during heating step of homogenisation at points 1 and 2 are presented in Fig.(6.18). During the first hour of the heating step of homogenisation, interface positions do not move. After this period, the eutectic phase starts to grow, because the solubility of component is lower then the concentration of Cu in the interface vicinity. After this short period, the eutectic phase continuously dissolves into the aluminium phase.

After heating step of homogenisation, 31 % and 28 % parts of the eutectic phase are dissolved at points 1 and 2, respectively. The comparison of the homogenisation parameters after the heating step with isothermal homogenisation at 520 °C, the heating part of homogenisation is equal to 63 min and 51 min of the isothermal homogenisation at points 1 and 2, respectively (Fig.(6.10)). The effect of four hours of heating step of homogenisation on the eutectic phase is similar as the effect of one hour of the holding step at a temperature of 520 °C.

6.6 Summary

The new concept of the eutectic phase for application in commercial aluminium alloys is introduced. The eutectic phase is treated as a homogeneous phase, where the properties of this artificial phase are computed as the heterogeneous mixture of the solid eutectic phase present. This assumption ignores all phase transformations inside the eutectic. The dissolution kinetics of the interdendritic eutectic phase in the aluminium matrix is enabled by this model. Such a definition of the eutectic phase enables the use of the microsegregation solidification model as the initial profile for the new homogenisation model. Here, the initial concentration profile in the aluminium phase is obtained by the Scheil-Gulliver solidification model.

The two stoichiometric eutectic phases are postulated here. In Case 1, the concentrations in the solid phases are the same concentrations as during the eutectic reaction. In Case 2, concentrations in the phases are equal to the equilibrium concentration at the homogenisation temperature. The molar free energy in Case 2 is lower than in Case 1, consequently the driving force for the dissolution of the eutectic phase in the aluminium phase is lower and the dissolution kinetics are slower.

The dissolution of the eutectic phase is compared with the regular lamellar eutectic in the one-dimensional geometry. By decreasing the interlamellar spacing in the regular eutectic, the concept of the eutectic phase becomes more suitable for the estimation of dissolution kinetics.

The effects of homogenisation temperature, grain size and macroscopic con-

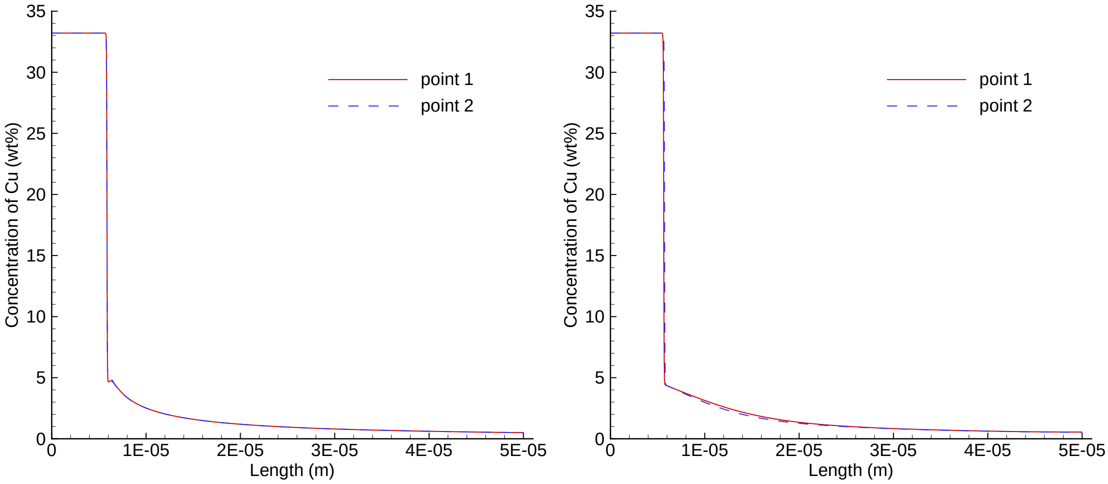

(a) Concentration profile, one hour.
(b) Concentration profile, two hours.

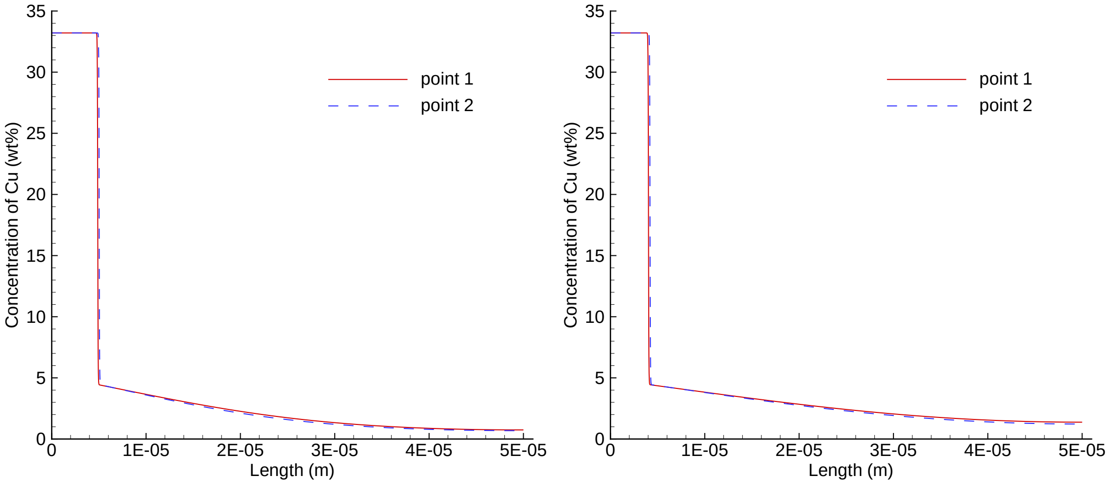

(c) Concentration profile, three hours.
(d) Concentration profile, four hours.

Figure 6.17: Cu concentration profiles during the heating step of homogenisation of Al-5 wt%Cu alloy at points 1 and 2 . The homogenisation parameters are 520 °C and 8 h.

centration on dissolution kinetics are analysed. The tremendous influence of homogenisation temperature and grain size on the homogenisation times is demonstrated.

The possibility of the PFM for solving the realistic phase-change problems in complex geometries such as in industrial homogenisation of aluminium alloys is clearly demonstrated. The model is capable of estimating when the dissolution of network of the interdendritic eutectic phase breaks.

The unsteady temperature field in the billet during the heating step of homogenisation is computed by the macroscopic model. In-situ temperature measurements in aluminium billets during the heating step of homogenisation are carried out for estimation of the effective heat transfer coefficient from the sur-

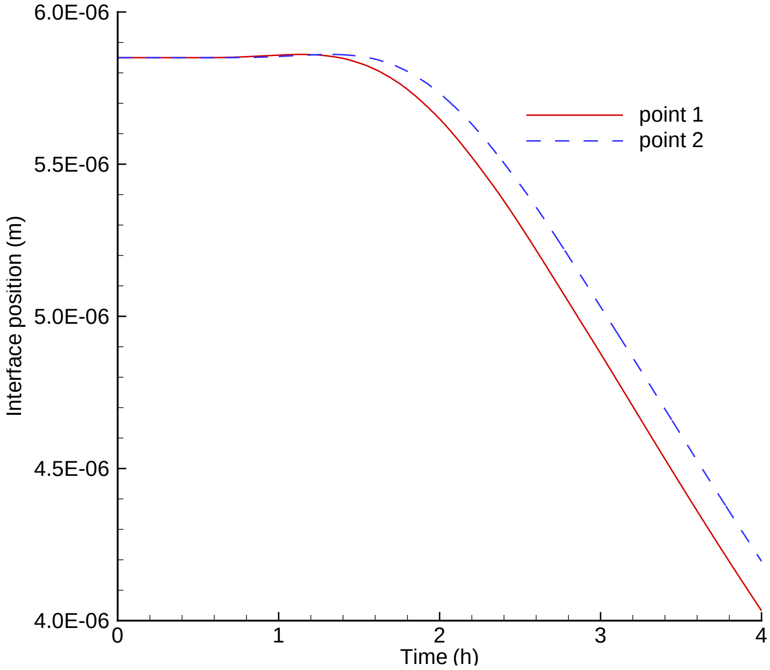

Figure 6.18: Interface position during heating step of homogenisation at points 1 and 2.

rounding air to the billet surface.

The PFM for non-isothermal phase transformations is derived. It is demonstrated that the driving force for phase transformation is linearly proportional with temperature for a constant concentration in the aluminium matrix. The dissolution kinetics of the eutectic phase during the heating step of homogenisation is estimated by this PFM. The effect of four hours of heating on the eutectic phase is similar as the effect of one hour of the holding step of homogenisation at a temperature of 520 °C.

7 Conclusions and Further Developments

The main contribution of this thesis is the application of the phase-field approach to specific phase transformations observed during the homogenisation of aluminium alloys. The explicit phase-field model for such phase transformations is developed. Furthermore, the numerical procedure based on the strong-form meshfree method on r-adaptive node arrangements for solving governing equations of the phase-field model is derived.

7.1 Conclusions

The conclusions of the presented work can be summarized in the following points.

7.1.1 Model Developments

- Phase transformations in heat treatment processes are modelled by the two-domain approach and phase-field model. Thermodynamic data needed for the physical models are obtained from the JMatPro software for aluminium alloys. The general physical model based on the two-phase approach for diffusion-controlled phase transformations in multicomponent alloys is derived.

- The phase-field model is a very strong tool for modelling solid-solid phase transformations under industrial conditions in microstructure topology.

- In the presented phase-field model, the mixture of two phases with different compositions and same local phase diffusion potentials are assumed in the diffuse-interface region. The model connection with the thermodynamic database is established via the driving force for phase transformation.

- The phase-field model for non-isothermal solid-solid phase transformations is derived. The driving force for phase transformation between a phase and aluminium phase is linearly proportional to temperature for constant concentrations in the aluminium matrix.

- In dealing with the stoichiometric second phase, the driving force is a function of concentrations in aluminium phase only. An accurate approximation of this function is essential for accurate computation of phase transformations by the phase-field model. In dealing with the nonstoichiometric second phase, the concentrations in phases have to be computed with the condition that phase diffusion potentials in both phases are equal. This condition has to be satisfied at each node in the diffuse-interface region.

- The interpolation by multiquadric radial basis functions for an accurate approximation of the driving force as a function of component concentrations in aluminium phase in the example of phase transformation between stoichiometric phases and aluminium matrix is implemented. The same interpolation is used for the interpolation of the chemical potentials of each component in both phases in the example of phase transformation between nonstoichiometric phase and the aluminium matrix.

- The isothermal diffusion-controlled dissolution of the primary nonstoichiometric and stoichiometric particles in aluminium phase is successfully simulated by the two-phase approach and phase-field approach. The physical models are validated by a comparison of numerical results computed for the isothermal diffusion-controlled phase transformations. The whole spectrum of represented numerical results, computed by both physical approaches are in very good agreement.

- The very accurate agreement between the results computed by our phase-field model and the Vermolen model for the dissolution of Mg_2Si particle in the aluminium matrix in Al-Mg-Si system is presented. The phase-field model is straightforwardly applied in multidimensional geometry with complex topology.

- The interface-kinetic coefficient in the phase-field model for the diffusion-controlled phase transformation is estimated by the comparison between the two-domain approach and the phase-field model. The interface-kinetic coefficient in the phase-field model easily controls the transformation mode.

7.1.2 Numerical Developments

- The local radial basis function collocation method is implemented for the computation of phase transformations described by the phase-field model. The method is efficient because it does not require a solution to a large system of equations like in the previous global collocation method. Instead, small systems of linear equations have to be solved in each time step for each node in associated local support. Solutions are computed on three and five nodes in local support in one-dimensional and two-dimensional geometry, respectively. Even with the smallest possible local supports, the accuracy of results is sufficient.

- The r-adaptive numerical procedure for the collocation by radial basis functions is derived. The automatic elliptic generator for the computation of node positions is used. The control function in the elliptic generator controls the node distribution and it has to be in relation with the interface position. The collocation by radial basis functions based on the local standard interpolation scheme on the equidistant grid is used for the solution of the elliptic generator. The field transformation from a node distribution to other is very straightforwardly related to the strong-form meshfree methods.

- The stability of the collocation by radial basis functions based on the local standard interpolation method is not sufficient at boundary nodes where the derivative boundary conditions exist. The stability is significantly improved by using only one boundary node for the boundary local support. The collocation with radial basis functions by using the double consideration of boundary nodes, based on Hermite-type interpolation enables the computation on the r-adaptive node arrangement. It improves the stability and accuracy of the results at the derivative boundary nodes.

- A quick model of determining local support for domain reference nodes in arbitrary node arrangements in two-dimensional geometry is developed. Local supports with only five nodes are considered.

- Accuracy of numerical results computed by derived numerical procedure is very high even with the small total number of nodes considered.

- Results computed by the collocation with radial basis functions on r-adaptive node arrangements are in agreement with the result computed by the fine grid FDM.

7.1.3 Phase Transformations Simulated by the Developed Phase-Field Model

- The dissolution of the stoichiometric Al_3Mg_2 and nonstoichiometric θ phase into the aluminium phase for Al-Mg and Al-Cu binary system are simulated, respectively. The isothermal diffusion-controlled dissolution kinetics of Al_2CuMg particle in the aluminium phase for Al-Cu-Mg system is estimated. The dissolution of complex shaped Al_2CuMg particle into the aluminium phase is simulated.

- The spheroidisation kinetics of needle-like undissolvable particles can be estimated by the phase-field model. The rounding kinetics of the elongated Si-particle is presented in this thesis. The spheroidisation is in fact a diffusion process of components in the aluminium matrix. The driving force is the solubility dependence on particle curvature. Because of that, the particle part with smaller particle curvature dissolves, whereas the faceted interface grows into the aluminium matrix. Consequently, the geometrical aspect ratio and the ratio between volume and area interface are reduced. The influences of the interface energy and homogenisation temperature on the rounding kinetics of the elongated Si-particle are simulated. Homogenisation temperature strongly influences the rounding kinetics. For these simulations, the isotropic material and the isotropic interface energy are assumed.

- The concept of the eutectic phase for application in commercial binary aluminium alloys is introduced. The eutectic phase is treated as a homogeneous phase, where the properties of this artificial phase are computed as the heterogeneous mixture of solid eutectic phases present. The spheroidisation and coarsening of eutectic lamellae by the artificial eutectic phase are omitted. Because of the eutectic phase defined in this way, the initial profile for the homogenisation model can be obtained from the microsegregation solidification model. The tremendous influence of the homogenisation temperature and the as-cast grain size on the homogenisation times are demonstrated. The possibility of employing the phase-field model in solving the realistic phase-change problems in complex geometry such as in industrial homogenisation of aluminium alloys is clearly demonstrated. The breaking of the interdendritic eutectic network is estimated by the model. After four hours of isothermal homogenisation of Al-5 wt%Cu, the interdendritic eutectic network is broken.
- The dissolution kinetics of the eutectic phase during the heating step of homogenisation is also estimated. The effect of the four-hour heating step of homogenisation on the eutectic phase is similar to the effect of one-hour holding step of homogenisation at the temperature of 520 °C.
- The unsteady temperature field in the billet during the heating step of homogenisation is computed by the macroscopic model. The in-situ temperature measurements in the aluminium billets during the heating step of homogenisation are carried out for the estimation of the heat transfer coefficient from the surrounding air to the billet surface and the radiation from furnace wall to the billet surface.

7.2 Recommendations for Further Developments

Recommendations for further developments of the presented work can be emphasized in the following points.

7.2.1 Model Developments

- The phase-field model can be extended to multiphase systems, because phase transformations in heat treatments of commercial, multicomponent alloys occur between more phases simultaneously.

- The elastic strain energy can be incorporated into the presented phase-field model. The influence of elasticity on the solid-solid transformation kinetics can be estimated.

- The source terms can be included into the phase-field model. The nucleation of dispersoids during heat treatments can be modelled by this model.

7.2.2 Numerical Developments

- The phase-field model can be solved also by a h-adaptivity node distribution. The number of nodes can be added into the diffuse-interface region, where the control function for the node density can be in relation with the gradient of the phase-field variable.

- Solving the model with the elastic strain energy included with the local collocation by radial basis functions is a very interesting and promising task. By using this numerical procedure, the governing equations of the phase-field model can be solved directly in their strong forms.

7.2.3 Industrial Relevance

- The realistic shape and size of primary particles can be included as initial conditions for the simulation of phase transformations during the homogenisation of aluminium alloys. The dissolution between different primary particles and the aluminium matrix during homogenisation can be simulated by the multiphase-field model.

- The spheroidisation of Si-particle can be observed by a relevant experiment. A comparison between numerical and experimental results can be a tool for estimation of the value of the interface energy as well as the magnitude of the interface energy anisotropy between Si-particle and the aluminium matrix. Furthermore, interaction between elongated Si-particles in Al-Si eutectic can be modelled.

- The concept of eutectic phase can be extended to multicomponent systems. The Gibbs free energies of the phases solidified between the primary aluminium and the final eutectic are functions of component concentrations. The number of independent concentrations for computing the Gibbs free energy of these artificial mixture phases is equal to the number of the degrees of freedom during solidification.

- Kinetics of the β-AlFeSi to α-Al(FeMn)Si transformation in Al-Mg-Si alloy can be simulated by the multiphase-field model. The advantage of using the multiphase-field model for the simulation of this phase transformation in a realistic geometry can be demonstrated.

- The presented phase-field model is applied to aluminium alloys. The model can be adapted and extended for simulations of phase transformations in other metallic systems.

Bibliography

Aaron, H. B. and Kotler, G. R. (1971). Second phase dissolution. *Metallurgical Transactions*, 2:393–408.

Alexander, D. T. L. and Greer, A. L. (2002). Solid-state intermetallic phase tranformations in 3XXX aluminium alloys. *Acta Materialia*, 50:2571–2583.

aluMATTER (2007). *http://aluminium.matter.org.uk*.

Atluri, S. N. (2004). *The Meshless Method (MLPG) for Domain, Bie Discretizations*. Tech Science Press, Forsyth, GA USA.

Ballufi, R. W., Allen, S. M., and Carter, W. C. (2005). *Kinetics of Materials*. John Wiley & Sons, Inc., Hoboken, NJ USA.

Baty, D. L., Tanzilli, R. A., and Heckel, R. W. (1970). Solution kinetics of $CuAl_2$ in an Al-4Cu alloy. *Metallurgical Transactions*, 1:1651–1656.

Beckermann, C., Diepers, H. J., Steinbach, I., Karma, A., and Tong, X. (1999). Modeling melt convection in phase-field simulations of solidification. *Journal of Computational Physics*, 154:468–496.

Boettinger, W. J., Warren, J. A., Beckermann, C., and Karma, A. (2002). Phase-field simulation of solidification. *Annual Review of Materials Research*, 32:163–194.

Brandes, E. A. and Brook, G. B. (1992). *Smithells Metals Reference Book*. Butterword–Heinemann, Oxford, UK.

Cahn, J. W. and Allen, S. M. (1977). A microscopic theory of domain wall motion and its experimental verification in Fe-Al alloy domain growth kinetics. *Journal de Physique*, 38:C7–51.

Cahn, J. W. and Hilliard, J. E. (1958). Free energy of a nonuniform system. I. interfacial free energy. *Journal of Chemical Physics*, 28:258–267.

Callister, W. D. (2003). *Materials Science and Engineering: An Introduction*. John Wiley & Sons, Inc., New York, NY USA.

Cáreras, C. H., Davidson, C. H., and Griffiths, J. R. (1995). The deformation and fracture behaviour of an Al-Si-Mg casting alloy. *Materials Science and Engineering A*, 197:171–179.

Cha, P. R., Yeon, D. H., and Yoon, J. K. (2001). A phase-field model for isothermal solidification of multicomponent alloys. *Acta Materialia*, 49:3295–3307.

Cha, P. R., Yeon, D. H., and Yoon, J. K. (2005). Phase-field model for multicomponent alloy solidification. *Journal of Crystal Growth*, 274(1-2):281–293.

Chen, W. (2002). New RBF collocation schemes and kernel RBFs with application. *Lecture Notes in Computational Science and Engineering*, 26:75–86.

Crank, J. (1984). *Free and Moving Boundary Problems.* Oxford Science Publications, Oxford, UK.

Crank, J. (1995). *The Mathematics of Diffusion.* Oxford Science Publications, Oxford, UK.

DeHoff, R. T. (1993). *Thermodynamics in Materials Science.* McGraw-Hill International Editions, Singapore, Singapore.

DICTRA (2007). *http://www.thermocalc.se/Products/Dictra.html.*

Ding, H., Shu, C., and Tang, D. B. (2005). Error estimates of local multiquadric-based differential quadrature (LMQDQ) method through numerical experiments. *International Journal for Numerical Methods in Engineering*, 63:1513–1529.

Dons, A. L. (2001). The Alstruc homogenization model for industrial aluminium alloys. *Journal of Light Materials*, 1:133–149.

Dons, A. L., Heiberg, G., Voje, J., Mæland, J. S., Løland, J. O., and Prestmo, A. (2005). On the effect of additions of Cu and Mg on the ductility of AlSi foundry alloys cast with colling rate of approximatelly 3 K/s. *Materials Science and Engineering A*, 413–414:561–566.

Eiken, J., Böttger, B., and Steinbach, I. (2006). Multiphase-field approach for multicomponent alloys with extrapolation scheme for numerical application. *Physical Review E*, 73:066122–1–066122–9.

Fasshauer, G. E. (1997). Solving partial differential equations by collocation with radial basis functions. In Méhauté, A. L., Rabut, C., and Schumaker, L. L., editors, *Surface Fitting and Multiresolution Methods*, pages 131–138, Nashville, TN USA. Vanderbilt University Press.

Franke, R. (1982). Scattered data interpolation: tests of some methods. *Mathematics of Computation*, 38:181–200.

Glicksman, M. E. (2000). *Diffusion in Solids: Field Theory, Solid-State Principle, and Applications.* John Wiley & Sons, Inc., New York, NY USA.

Grafe, U., Böttger, B., Tiaden, J., and Fries, S. G. (2000). Coupling of multicomponent thermodynamic databases to a phase field model: application to solidification and solid state transformations of superalloys. *Scripta Materialia*, 42:1179–1186.

Hechta, U., Gránásy, L., Pusztai, T., Böttger, B., Apel, M., Witusiewicz, V., Ratke, L., Wilde, J. D., Froyen, L., Camel, D., Drevet, B., Faivre, G., Fries, S. G., Legendre, B., and Rex, S. (2004). Multiphase solidification in multicomponent alloys. *Materials Science and Engineering R*, 46:1–49.

Hillert, M. (1998). *Phase Equilibria, Phase Diagrams and Phase Transformations, Their Thermodynamic Basis.* Cambridge University Press, Cambridge, UK.

Howe, J. M. (1997). *Interfaces in Materials: Atomic Structure, Thermodynamics and Kinetics of Solid-Vapor, Solid-Liquid and Solid-Solid Interfaces.* John Wiley & Sons, Inc., New York, NY USA.

Hu, S. (2004). *Phase-Field Models of Microstructure Evolution in a System with Elastic Inhomogenity and Defects.* PhD thesis, Department of Materials Science and Engineering, The Pennsylvania State University, University Park, PA USA.

Incropera, F. P. and DeWitt, D. P. (2002). *Fundamentals of Heat and Mass Transfer.* John Wiley and Sons, Inc., New York, NY USA.

Jackson, K. A. (2004). *Kinetic Processes: Crystal Growth, Diffusion, and Phase Transitions in Materials.* Wiley-VCH Verlag GmbH & Co. KgaA, Weinheim, Germany.

Jacot, A. and Rappaz, M. (1997). A two dimensional diffusion model for the prediction of phase transformations: application to austenitization and homogenization of hypoeutectoid Fe-C steels. *Acta Metallurgica*, 45(2):575–585.

Jacot, A. and Rappaz, M. (1999). A combined model for the description of austenitization, homogenization and grain growth in hypoeutectoid Fe-C steels during heating. *Acta Metallurgica*, 47(5):1645–1651.

Jacot, A. and Rappaz, M. (2002). A pseudo-front tracking technique for the modelling of solidification microstructures in multi-component alloys. *Acta Materialia*, 50:1909–1926.

Javierre, E., Vuik, C., Vermolen, F. J., and Segal, A. (2007). A level set method for three dimensional vector Stefan problems: Simulations of particle dissolution in multi-component alloys. *Journal of Computational Physics*, 224(1):222–240.

JMatPro (2004). JMatPro the materials property simulation package, version 3.0, Sente Software Ltd., Guildford, UK. Computer program.

JMatPro (2007). *http:/www.sentesoftware.co.uk/jmatpro.html.*

Jumarhon, B., Amini, S., and Chen, K. (2000). The Hermite collocation methods using radial basis functions. *Engineering Analysis with Boundary Elements*, 24:607–611.

Juric, D. (1996). *Computations of Phase Change.* PhD thesis, The University of Michigan, Ann Arbor, MI USA.

Kammer, C. (1999). *Aluminium Handbook, 1 Fundamentals and Materials.* Aluminium-Verlag, Markering & Kommunikation GmbH, Düsseldorf, Germany.

Kansa, E. J. (1990a). Multiquadrics - a scattered data approximation scheme with application to computational fluid dynamics - i. *Computers & Mathematics with Applications*, 19:127–145.

Kansa, E. J. (1990b). Multiquadrics - a scattered data approximation scheme with application to computational fluid dynamics - ii. *Computers & Mathematics with Applications*, 19:147–161.

Kansa, E. J. and Hon, Y. C. (2000). Circumventing the ill-conditioning problem with multiquadtic radial basis functions: Applications to elliptic partial differential equations. *Computers & Mathematics with Applications*, 39:123–137.

Karma, A. and Rappel, W. J. (1998). Quantitative phase-field modeling of dendritic growth in two and three dimensions. *Physical Review E*, 57(4):4323–4349.

Khachaturyan, A. G. (1983). *Theory of Structural Transformations in Solids.* John Wiley & Sons, Inc., New York, NY USA.

Kim, S. G., Kim, W. T., and Suzuki, T. (1999). Phase-field model for binary alloys. *Physical Review E*, 60(6):7186–7197.

Kostorz, G. (2001). *Phase Transformations in Materials.* Wiley-VCH Verlag GmbH, Weinheim, Germany.

Kovačević, I., Poredoš, A., and Šarler, B. (2003). Solving the Stefan problem with the radial basis function collocation method. *Numerical Heat Transfer B*, 44:575–599.

Kovačević, I. and Šarler, B. (2005). Solution of a phase-field model for dissolution of primary particles in binary aluminum alloys by an r-adaptive mesh-free method. *Materials Science & Engineering A*, 413–414:423–428.

Kovačević, I., Šarler, B., and Chen, C. S. (2004). A mesh-free solution of temperature in direct-chill cast slabs and billets. In *Moving boundaries VII: Computational Modelling of Free and Moving Boundary Problems*, volume 10, pages 271–280, Southampton, UK. WIT Press.

Kovačević, I. and Šarler, B. (2004). Phase-field model for homogenization process of binary aluminium alloys. In Talijan, N., editor, *2nd International Symposium Light Metals and Composite Materials*, pages 45–48, Beograd, Serbia. Association of Metallurgical Engineers SCG.

Kovačević, I. and Šarler, B. (2005). Numerično modeliranje procesa homogenizacije, prvi del: makroskopski model, zlitine: D50,D60,AC30,AC41,AC42. Technical Report, University of Nova Gorica, Nova Gorica, Slovenia.

Kovačević, I. and Šarler, B. (2006a). Dissolution of eutectic phase in binary aluminium alloys during homogenization. In M. Bellet, C., editor, *Modeling of Casting, Welding and Advanced Solidification Processes - XI*, pages 561–568, Opio, France. TMS.

Kovačević, I. and Šarler, B. (2006b). Modelling of phase transformations in heat treatment processes. In J. Périaux, P. E., editor, *ECCOMAS CFD 2006, European Conference on Computational Fluid Dynamics*, pages 590:1–20, Egmond aan Zee, The Netherlands.

Kovačević, I. and Šarler, B. (2006c). Solid-solid phase transformations in aluminium alloys described by a multiphase field model. *Matereials Science Forum*, 508:579–584.

Kurz, W. and Fisher, D. J. (1998). *Fundamentals of Solidification.* Trans Tech Publication LTD, Zurich Switzerland.

Lazzaro, D. and Montefusco, L. B. (2002). Radial basis function for the multivariate interpolation of large scettered data sets. *Journal of Computational and Applied Mathematics*, 140:521–536.

Lee, C. K., Liu, X., and Fan, S. C. (2003). Local multiquadric approximation for solving boundary value problems. *Computational Mechanics*, 30:396–409.

Li, Y. J. and Arnberg, L. (2003). Quantitative study on the precipitation behavior of dispersoids in DC-cast AA3003 alloy during heating and homogenization. *Acta Materialia*, 51:3415–3428.

Liu, G. R. (2003). *Mesh Free Methods, Moving Beyond the Finite Element Method.* CRC Press, Boca Raton, FL USA.

Liu, G. R. and Gu, Y. T. (2003). A meshfree method: meshfree weak-strong (MWS) form method, for 2-D solids. *Computational Mechanics*, 33:2–14.

Liu, G. R. and Gu, Y. T. (2005). *An Introduction to Meshfree Methods and Their Programming.* Springer, Dordrecht, The Nederlands.

Liu, G. R., Kee, B. B. T., and Chun, L. (2006). A stabilized least-squares radial point collocation method (LS-RPCM) for adaptive analysis. *Computer Methods in Applied Mechanics and Engineering*, 195:4843–4861.

Loginova, I. (2003). *Phase-Field Modeling of Diffusion Controlled Phase Transformations.* PhD thesis, Department of Mechanics, Royal Institute of Technology, Stockholm, Sweden.

Mai-Duy, N. and Tran-Cong, T. (2001). Numerical solution of Navier-Stokes equations using radial basis function networks. *International Journal for Numerical Methods in Fluids*, 37:65–86.

Matrin, J. W., Doherty, R. D., and Cantor, B. (1997). *Stability of Microstructure in Metallic Systems.* Cambridge University Press, Cambridge, UK.

McFadden, G. B., Wheeler, A. A., Braun, R. J., Coriell, S. R., and Sekerka, R. F. (1993). Phase-field models for anisotropic interfaces. *Physical Review E*, 48(3):2016–2024.

Mecozzi, M. G., Sietsma, J., van der Zwaag, S., Apel, M., Schaffnit, P., and Steinbach, I. (2005). Analysis of the $\gamma \rightarrow \alpha$ transformation in a C-Mn steel by phase-field model. *Metallurgical and Materilas Transactions A*, 36A:2327–2340.

Mencinger, J. (2001). *Numerical Simulation of Melting and Solidification using Self-Adaptive Grid.* PhD thesis, Faculty of Mechnical Engineering, University of Ljubljana, Ljubljana, Slovenia.

Micrograph Library, University of Cambridge (2007). *http://www.doitpoms.ac.uk/miclib/index.php.*

Mondolfo, L. F. (1976). *Aluminium Alloys, Structure and Properties.* Butterworth & Co, London, UK.

MTDATA (2007). *http://www.npl.co.uk/mtdata/.*

Murray, W. D. and Landis, F. (1959). Numerical and machine solutions of transient heat conduction problems involving melting or freezing. *Journal of Heat Transfer*, 81:106—-112.

Nestler, B., Danilov, D., and Galenko, P. (2005). Crystal growth of pure substances: Phase-field simulations in comparison with analytical and experimental results. *Journal of Computational Physics*, 207:221–239.

Nestler, B. and Wheeler, A. A. (2000). A multi-phase-field model of eutectic and peritectic alloys: numerical simulation of growth structures. *Physica D*, 138:114–133.

Ogris, E. (2002). *Development of Al-Si-Mg Alloys for Semi-Solid Processing and Silicon Spheroidization Treatment (SST) for Al-Si Cast Alloys.* PhD thesis, Swiss Federal Institute of Technology Zurich, Zurich, Switzerland.

Pariser, G., Schaffnit, P., and Steinbach, I. (2001). Simulation of the $\gamma - \alpha$ transformation using the phase-field model. *Steel Research*, 72:1179–1186.

Patankar, S. V. (1980). *Numerical Heat Transfer and Fluid Flow.* Hemisphere Publishing Coorporation, Washington, D.C. USA.

Pedersen, L. and Arnberg, L. (2001). The effect of solution heat treatment and quenching rates on mechanical properties and microstructures in AlSiMg foundry alloys. *Metallurgical and Materials Transactions A*, 32A:525–532.

Pérez, E. J. (2006). *Numerical Methods for Vector Stefan Models of Solid-State Alloys.* PhD thesis, Delft Universitiy of Technology, Delft, The Netherlands.

Perko, J. (2005). *Diffuse Approximate Method for Transport Phenomena.* PhD thesis, School of Applied Sciences, University of Nova Gorica, Nova Gorica, Slovenia.

Perko, J., Chen, C. S., and Šarler, B. (2001). A polygon-free numerical solution of steady natural convection in solid-liquid systems. In Šarler, B. and Brebbia, C. A., editors, *Moving Boundaries VI: Computational Modelling of Free and Moving Boundary Problems*, volume 4, pages 111–122, Southampton, UK. WIT Press.

Porter, D. K. and Easterling, K. E. (1990). *Phase Transformations in Metals and Alloys.* Chapman and Hall, London, UK.

Power, H. and Barraco, V. (2002). A comparison analysis between unsymmetric and symmetric radial basis function collocation methods for the numerical solution of partial differential equations. *Computers & Mathematics with Applications*, 43:551–583.

Provatas, N., Goldenfeld, N., and Dantzig, J. (1999). Adaptive mesh refinement computation of solidification microstructures using dynamic data structures. *Journal of Computational Physics*, 148:265–290.

Qin, R. S. and Wallach, E. R. (2003). A phase-field model coupled with a thermodynamic database. *Acta Materialia*, 51:6199–6210.

Rabczuk, T. and Belytschko, T. (2005). Adaptivity for structured meshfree particle methods in 2D and 3D. *International Journal for Numerical Methods in Engineering*, 63:1559–1582.

Ragone, D. V. (1992). *Thermodynamics of Materials, Volume I and II.* John Wiley & Sons, Inc., New York, NY USA.

Özisik, M. N. (1994). *Finite Difference Method in Heat Transfer.* CRC Press, inc., Boca Raton, FL USA.

Rollet, A. D. (2001). Materials Science and Engineering, Microstructure and Properties I, research activities.

Sheppard, T. (1999). *Extrusion of Aluminium Alloys.* Kluwer Academic Publishers, Dordrecht, The Nederlands.

Shu, C., Ding, H., and Yeo, K. S. (2003). Local radial basis function-based differential quadrature method and its application to solve two-dimensional incompressible Navier-Stokes equations. *Computer Methods in Applied Mechnics and Engineering*, 192:941–954.

Simmons, J. P., Wen, Y., Shen, C., and Wang, Y. Z. (2004). Microstructural development involving nucleation and growth phenomena simulated with the Phase Field method. *Materials Science and Engineering A*, 365A:136–143.

Stead, S. E. (1984). Estimation of gradients from scattered data. *Rocky Mountain Journal of Mathematics*, 14:265–279.

Steinbach, I. and Apel, M. (2006). Multi phase field model for solid state transformation with elastic strain. *Physica D*, 217:153–160.

Steinbach, I. and Pezzolla, F. (1999). A generalized field method for multiphase transformations using interface fields. *Physica D*, 134:385–393.

Steinbach, I., Pezzolla, F., Nestler, B., Seeßelberg, M., Prieler, R., Schmitz, G. J., and Rezende, J. L. (1996). A phase field concept for muptiphase systems. *Physica D*, 94:135–147.

Tarwater, A. E. (1985). A parameter study of hardy's multiquadric method for scattered data interpolation. Technical Report UCLR-53670, Lawrence Livermore National Laboratory.

Thermocalc (2007). *http://www.thermocalc.se/Products/TCW.html.*

Thompson, J. F., Boni, B. K., and Weatherill, N. P. (1999). *Handbook of Grid Generation.* CRC press, Boca Raton, FL USA.

Tiaden, J. (1999). Phase field simulations of the peritectic solidification of Fe-C. *Journal of Crystal Growth*, 198/199:1275–1280.

Tiaden, J., Nestler, B., Diepers, H. J., and Steinbach, I. (1998). The multiphase-field model with an integrated concept for modelling solute diffusion. *Physica D*, 115:73–86.

Usta, M., Glicksman, M. E., and Wright, R. N. (2004). The effect of heat treatment on Mg_2Si coarsening in aluminum 6105 alloy. *Metallurgical and Materials Transactions A*, 35A:435–438.

Vermolen, F. J., Javierre, E., Vuik, C., Zhao, L., and van der Zwaag, S. (2007). A three dimensional model for particle dissolution in binary alloys. *Computational Materials Science*, 39(4):767–774.

Vermolen, F. J. and Vuik, C. (1998). A numerical method to compute the dissolution of second phases in ternary alloys. *Journal of Computational and Applied Mathematics*, 93:123–143.

Vermolen, F. J. and Vuik, C. (2000). A mathematical model for the dissolution of particles in multi-component alloys. *Journal of Computational and Applied Mathematics*, 126:233–254.

Vermolen, F. J., Vuik, C., and van der Zwaag, S. (1998a). The dissolution of a stoichiometric second phase in ternary alloys: a numerical analysis. *Materials Science and Engineering A*, 246:93–103.

Vermolen, F. J., Vuik, C., and van der Zwaag, S. (1998b). A mathematical model for the dissolution kinetics of Mg_2Si-phases in Al-Mg–Si alloys during homogenisation under industrial conditions. *Materials Science and Engineering A*, 254:13–32.

Vermolen, F. J., Vuik, C., and van der Zwaag, S. (2002). A mathematical model for the dissolution of stoichiometric particles in multi-component alloys. *Materials Science and Engineering A*, 328:14–25.

Versteeg, H. K. and Malalasekera, W. (1996). *An Introduction to the Computational Fluid Dynamics, The Finite Volume Method.* Prentice Hall.

Vertnik, R. (2007). Local Collocation Method for Phase Change Problems. Master's thesis, University of Nova Gorica, Nova Gorica, Slovenia.

Vertnik, R. and Šarler, B. (2006). Meshless local radial basis function collocation method for covective-diffusive solid-liquid phase change problems. *International Journal of Numerical Methods for Heat* & *Fluid Flow*, 16(5):617–640.

Vitek, J. M., Vitek, S. A., and David, S. A. (1995). Numerical modeling of diffusion-controlled phase transformations in ternary systems and application to the feritte/austenite transformation in the Fe-Cr-Ni system. *Metallurgical and Materials Transactions A*, 26A:2007–2024.

Šarler, B. (1995). Stefan's work on solid-liquid phase changes. *Engineering Analysis with Boundary Elements*, 16:83–92.

Šarler, B., Perko, J., Chen, C. S., and Kuhn, G. (2001). A meshless approach to natural convection. In Atluri, S. A., Nishioka, T., and Kikuchi, M., editors, *Advances in Computational Engineering* & *Sciences, International Conference on Computational Engineering* & *Science*, pages 271–276, Palmdale, CA USA. Tech Science Press.

Šarler, B. and Vertnik, R. (2006). Meshfree local radial basis function collocation method for diffusion problems. *Computers & Mathematics with Applications*, 51:1269–1282.

Wang, J. G. and Liu, G. R. (2002). On the optimal share parameters of radial basis functions used for 2-D meshless methods. *Computer Methods in Applied Mechanics and Engineering*, 191:2611–2630.

Warren, J. A. and Boettinger, W. J. (1995). Prediction of dendritic growth and microsegregation patterns in a binary alloy using the phase-field model. *Acta Metallurgica Materialia*, 43:689–703.

Wheeler, A. A., Boettinger, W. J., and McFadden, G. B. (1992). Phase-field model for isothermal phase transitions in binary alloys. *Physical Review E*, 45(10):7424–7439.

Yeon, D. H., Cha, P. R., Kim, J. H., Grant, M., and Yoon, J. K. (2005). A phase field model for phase transformation in an elastically stressed binary alloy. *Modelling and Simulation in Materials Science and Engineering*, 13(3):299–319.

Zerroukat, M., Djidjeli, K., and Charafi, A. (2000). Explicit and implicit meshless methods for linear advection-diffusion-type partial differential equations. *International Journal for Numerical Methods in Engineering*, 48:19–35.

Zerroukat, M., Power, H., and Chen, C. S. (1998). A numerical method for heat transfer problems using collocation and radial basis functions. *International Journal for Numerical Methods in Engineering*, 42:1263–1278.

Zhang, X., Song, K. Z., Lu, M. W., and Liu, X. (2000). Meshless methods based on collocation with radial basis functions. *Computational Mechanics*, 26:333–343.